Multi-instrument investigation of mineral dust particle size from fine to giant at a desert emission source

Zur Erlangung des akademischen Grades eines
DOKTORS DER NATURWISSENSCHAFTEN (Dr. rer. nat.)
von der KIT-Fakultät für Physik des
Karlsruher Instituts für Technologie (KIT)

genehmigte

DISSERTATION

von

M.Sc. Hannah Meyer
aus Buxtehude

Tag der mündlichen Prüfung:	16.05.2025
Referentin:	TT-Prof. Dr. Martina Klose
Korreferent:	Prof. Dr. Peter Knippertz

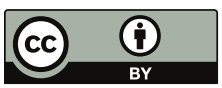

Abstract

Mineral dust particles emitted from dry, uncovered soil can be transported over vast distances, thereby influencing atmospheric processes such as radiation, cloud formation, and biogeochemical cycles, which ultimately affects both regional and global climates. These effects are highly size-dependent. For example, larger particles tend to warm the atmosphere through radiation interactions, while smaller particles generally contribute to cooling. To accurately understand how dust particle sizes evolve during transport, it is crucial to characterize the particle size distribution (PSD) at emission. Large particles with diameters $d_p > 10\,\mu\text{m}$ are particularly understudied, despite their significant environmental effects. However, measuring them poses challenges due to their expected low number concentrations and the limited sampling efficiencies of many instrument inlets.

This PhD thesis characterizes the dust PSD at an emission source during the Jordan Wind Erosion and Dust Investigation (J-WADI) campaign, conducted near Wadi Rum, Jordan, in September 2022, focusing on super-coarse ($10 < d_p \leq 62.5\,\mu\text{m}$) and giant ($d_p > 62.5\,\mu\text{m}$) particles. This study is the first to consistently cover the full range of diameters from $d_p = 0.4$ to $200\,\mu\text{m}$ by using a suite of aerosol spectrometers with overlapping size ranges. This enables a systematic intercomparison and validation across instruments for the campaign and forthcoming measurements, improving PSD reliability and addressing challenges in detecting larger particles such as inlet efficiencies or size range restrictions.

Results show significant PSD variability over the course of the campaign. During periods with friction velocities (u_*) above $0.22\,\text{m}\,\text{s}^{-1}$, the approximate threshold for local dust emission by saltation, both dust concentrations and the contributions of super-coarse and giant particles typically increased with increasing u_*, especially under neutral to unstable atmospheric stability conditions. These large particles accounted for about 85% of the total mass concentration during dust emission events, emphasizing the importance of including super-coarse and giant particles in PSD analyses. A prominent mass concentration peak was observed near $d_p = 60\,\mu\text{m}$ in geometric diameter. While particle concentrations for $d_p < 10\,\mu\text{m}$ show good agreement among most instruments, discrepancies appear for larger d_p due to reduced instrument sensitivity at the size range boundaries and sampling inefficiencies. Despite these challenges, physical samples collected using a flat-plate sampler largely confirm the PSDs derived from the aerosol spectrometers.

These results advance the characterization of the dust PSD over a wide particle size range at emission sources and contribute to (1) a better process-level understanding of the emission and transport of super-coarse and giant dust particles, (2) a robust and transferable measurement and evaluation framework for

future campaigns, and (3) improved observational constraints that can support the refinement of dust parameterizations in atmospheric models.

Zusammenfassung

Mineralische Staubpartikel, die von trockenen, unbedeckten Böden emittiert werden, können über weite Entfernungen transportiert werden und dadurch atmosphärische Prozesse wie Strahlung, Wolkenbildung und biogeochemische Kreisläufe beeinflussen, was sich letztlich sowohl auf das regionale als auch auf das globale Klima auswirkt. Diese Auswirkungen sind stark größenabhängig. So erwärmen beispielsweise größere Partikel die Atmosphäre durch Strahlungswechselwirkungen, während kleinere Partikel im Allgemeinen zur Abkühlung beitragen. Um genau zu verstehen, wie sich die Größe von Staubpartikeln während des Transports entwickelt, ist es entscheidend, die Partikelgrößenverteilung (PSD) bei der Emission zu charakterisieren. Große Partikel mit Durchmessern $d_p > 10\,\mu\text{m}$ sind trotz ihrer erheblichen Auswirkungen auf die Umwelt besonders wenig erforscht. Die Messung dieser Partikel stellt jedoch aufgrund ihrer erwarteten geringen Anzahlkonzentrationen und der begrenzten Probenahmeeffizienz vieler Instrumenteneinlässe eine Herausforderung dar.

Diese Doktorarbeit charakterisiert die Staub-PSD an einer Emissionsquelle während der J-WADI-Kampagne (Jordan Wind Erosion and Dust Investigation), die im September 2022 in der Nähe von Wadi Rum, Jordanien, durchgeführt wurde und konzentriert sich dabei auf supergrobe ($10 < d_p \leq 62,5\,\mu\text{m}$) und riesige ($d_p > 62,5\,\mu\text{m}$) Partikel. Diese Studie ist die erste, die konsequent den gesamten Durchmesserbereich von $d_p = 0,4$ bis $200\,\mu\text{m}$ abdeckt, indem sie mehrere Aerosolspektrometer mit überlappenden Größenbereichen verwendet. Dies ermöglicht einen systematischen Vergleich und eine Validierung der Instrumente für die Kampagne und die kommenden Messungen, wodurch die PSD-Zuverlässigkeit verbessert und die Herausforderungen bei der Erkennung größerer Partikeln, wie z. B. Einlass-Effizienzen oder Einschränkungen des Größenbereichs diskutiert.

Die Ergebnisse zeigen eine erhebliche PSD-Variabilität im Verlauf der Kampagne. Während der Zeiträume mit Schubspannungsgeschwindigkeiten (u_*) über $0{,}22\,\text{m}\,\text{s}^{-1}$, dem ungefähren Schwellenwert für lokale Staubemissionen durch Saltation, stiegen typischerweise sowohl die Staubkonzentrationen als auch die Beiträge von supergroben und riesigen Partikeln mit zunehmendem u_*, insbesondere unter neutraler bis instabiler atmosphärischer Schichtung. Diese großen Partikel machten währenddessen etwa 85% der Gesamtmassenkonzentration aus, was die Bedeutung der Einbeziehung supergrober und riesiger Partikel in PSD-Analysen unterstreicht. Ein markanter Peak der Massenkonzentration wurde in der Nähe von $d_p = 60\,\mu\text{m}$ geometrischem Durchmesser beobachtet. Während die Partikelkonzentrationen für $d_p < 10\,\mu\text{m}$ bei den meisten Instrumenten gut übereinstimmen, treten bei größeren d_p Diskrepanzen auf, die auf die verringerte Empfindlichkeit der Instrumente an den Grenzen des Größenbereichs und die ge-

ringe Effizienz der Probenahme zurückzuführen sind. Trotz dieser Probleme bestätigen die mit einem Flachplattensammler gesammelten physikalischen Proben weitgehend die von den Aerosolspektrometern abgeleiteten PSDs.

Diese Ergebnisse verbessern die Charakterisierung der Staub-PSD über einen weiten Partikelgrößenbereich an Emissionsquellen und tragen dazu bei (1) die Emission und den Transport von supergroben und riesigen Staubpartikeln auf Prozessebene besser zu verstehen, (2) einen robusten und übertragbaren Mess- und Auswertungsrahmen für zukünftige Kampagnen zu schaffen und (3) verbesserte Beobachtungsdaten zu schaffen, die die Verfeinerung von Staubparametrisierungen in atmosphärischen Modellen unterstützen können.

Contents

Preface

This doctoral dissertation was carried out under the supervision of TT-Prof. Dr. Martina Klose and Prof. Dr. Peter Knippertz and funded by the Helmholtz Association's Initiative and Networking Fund (grant no. VH-NG-1533) within the Helmholtz Young Investigator Group "A big unknown in the climate impact of atmospheric aerosol: Mineral soil dust" led by TT-Prof. Dr. Martina Klose.
This dissertation is largely based on a manuscript based on a manuscript published in Atmospheric Measurement Techniques (Meyer et al., 2026),

- Meyer, H., Kandler, K., Dupont, S., Escribano, J., Girdwood, J., Nikolich, G., Alastuey, A., Etyemezian, V., González-Flórez, C., González-Romero, A., Hussein, T., Irvine, M., Knippertz, P., Möhler, O., Querol, X., Stopford, C., Vogel, F., Weis, F., Wieser, A., Pérez García-Pando, C., & Klose, M. (2025). From fine to giant: multi-instrument assessment of the dust particle size distribution at an emission source during the J-WADI field campaign, Atmos. Meas. Tech., 19, 21–61, https://doi.org/10.5194/amt-19-21-2026, 2026.

with the exception of Chapter 2, which provides additional context and literature review. I wrote the text of this manuscript with advice from TT-Prof. Dr. Martina Klose and Prof. Dr. Peter Knippertz. I acknowledges the use of ChatGPT (OpenAI) for assistance in refining the wording of certain sections of this manuscript.
The data presented in this work were collected during the Jordan Wind Erosion and Dust Investigation (J-WADI) field campaign in Wadi Rum, Jordan (`https://www.imk-tro.kit.edu/english/11800.php`, last accessed 5 Mar. 2025) and is available under: Meyer et al. (2025b). The data analysis presented in this thesis has been accomplished using Python. Valuable insights into instrument performance, data acquisition, and processing techniques were gained through prior involvement in an earlier campaign in Iceland (`https://gomera.geo.tu-darmstadt.de/wordpress/about-hilda-2`, last accessed 2 April 2025), which served as a test for some of the instruments. My contributions before both field campaigns included: preparation and testing of some aerosol and meteorological instruments, participation in technical meetings, and support in instrument logistics. I contributed to the enhancement of data acquisition techniques for both meteorological and aerosol spectrometer systems and developed a new data logging routine for the scintillometer based on the legacy software. I was present for the entire J-WADI campaign and half of the Iceland campaign, actively participating in the deployment, operation, and dismounting of instruments and supporting the daily maintenance of the instrumentation.

After the campaigns, the work focused on processing and analyzing the meteorological and aerosol spectrometer data. This included the development and implementation of robust correction and harmonization methods, which were crucial not only for ensuring data consistency across instruments with overlapping size ranges, but also represent a key scientific contribution of this thesis. These methods laid the foundation for deriving reliable particle size distributions and enabled the subsequent analysis of them.

Many of the results and insights presented here stem from collaborative efforts presented in Meyer et al. (2025a) and the following key contributions can be attributed to the authors of the aforementioned research paper: I processed the aerosol spectrometer and most of the meteorological data, performed the majority of the analysis and the final interpretations, created most of the figures, and wrote the manuscript. TT-Prof. Dr. Martina Klose supervised the work with contributions from Prof. Dr. Peter Knippertz, Prof. Dr. Carlos Pérez García-Pando, and Prof. Dr. Konrad Kandler. Prof. Dr. Konrad Kandler conducted the flat-plate sampler (FPS) sampling, scanning electron microscope (SEM) analysis, and provided the corresponding results. Dr. Sylvain Dupont provided the sonic anemometer data from the 10 m mast. Dr. Jerónimo Escribano provided the transformation from optical to geometric diameters for the Fidas, CDA, and Welas. Dr. Adolfo González-Romero, Prof. Dr. Konrad Kandler, Dr. Sylvain Dupont, Dr. Mark Irvine, Dr. Andrés Alastuey, Dr. Xavier Querol, Prof. Dr. Tareq Hussein, Dr. Andreas Wieser, Dr. Franziska Vogel, TT-Prof. Dr. Martina Klose, and Prof. Dr. Carlos Pérez García-Pando implemented the field campaign. Dr. Jessica Girdwood and Prof. Dr. Chris Stopford provided UCASS bin classification and technical support. Dr. Ottmar Möhler contributed one UCASS and two Welas devices. Dr. Vicken Etyemezian and Dr. George Nikolich provided the SANTRI2 and SANTRI instruments and related support. Dr. Frederik Weis contributed the CDA and provided support for the CDA, Welas, and Fidas. Dr. Cristina González-Flórez assisted in campaign preparation and analysis support. TT-Prof. Dr. Martina Klose performed the calculation of flux densities. The J-WADI field campaign was proposed and designed by Prof. Dr. Carlos Pérez García-Pando and TT-Prof. Dr. Martina Klose with contributions from Dr. Andreas Wieser, Dr. Andrés Alastuey, Dr. Xavier Querol, Dr. Sylvain Dupont, Prof. Dr. Konrad Kandler, and Prof. Dr. Tareq Hussein.

I confirm that the research presented in this thesis contains significant scientific contributions by myself. I confirm that appropriate credit has been given within the thesis where reference has been made to the work of others. This copy has been supplied on the understanding that this is copyright material and that no quotation from the thesis may be published without proper acknowledgment.

1. Introduction

Mineral dust aerosol originates from the suspension of particles of uncovered dry soil through the action of strong winds. It represents the dominant fraction of the global aerosol mass in Earth's atmosphere (Textor et al., 2006), with significant impacts, from emission to deposition, on atmospheric processes and climate dynamics (*e.g.*, Shao et al., 2011b; Kok et al., 2023). Mineral dust affects Earth's energy balance by scattering and absorbing solar and infrared radiation (*e.g.*, Ryder et al., 2013b; Kok et al., 2018; Di Biagio et al., 2020) and influencing cloud formation and precipitation potential (*e.g.*, Kumar et al., 2011; Hoose and Möhler, 2012; Froyd et al., 2022). It also transports nutrients to ecosystems, impacting carbon uptake and atmospheric CO_2 levels (Goudie and Middleton, 2001; Jickells et al., 2005; Schulz et al., 2012). Its overall radiative effect remains highly uncertain, estimated at $-0.2 \pm 0.5\,\mathrm{W\,m^{-2}}$, leaving it unclear whether dust ultimately warms or cools the climate (Kok et al., 2023).

The climate impact of dust aerosol is not only determined by the amount, shape, and mineralogical composition of the particles, but also by their particle size distribution (PSD, Mahowald et al., 2014). For mineral dust, the PSD is divided into different size ranges: fine dust with a diameter smaller than $d_p < 2.5\,\mu\mathrm{m}$, coarse dust with $2.5 \leq d_p < 10\,\mu\mathrm{m}$, super-coarse dust with $10 \leq d_p < 62.5\,\mu\mathrm{m}$, and giant dust with $d_p \geq 62.5\,\mu\mathrm{m}$ (Adebiyi et al., 2023). Whereas fine dust exerts a substantial cooling effect at the top of the atmosphere, coarse, super-coarse, and giant dust particles tend to have a net warming effect in sum of the shortwave and longwave spectra, because the particles' absorption increases more significantly than their scattering as particle size grows (Adebiyi et al., 2023). In contrast, smaller dust particles primarily cool the atmosphere by efficiently scattering solar radiation. Particle size is also important for cloud microphysics and precipitation processes (Min et al., 2009). Large dust particles can act as effective cloud condensation nuclei, promoting the formation of very large cloud droplets that enhance collision-coalescence processes, leading to precipitation (Mahowald et al., 2014).

Regardless of their importance in dust-climate interactions, coarse to giant dust particles have traditionally been presumed to sediment rapidly (*e.g.*, Seinfeld and Pandis, 1998), limiting their atmospheric lifetime and potential for long-range transport. Despite expectations of rapid settling by using traditional sedimentation schemes, studies have sampled giant dust particles up to $450\,\mu\mathrm{m}$ in diameter several thousand kilometers from their source regions (Betzer et al., 1988; van der Does et al., 2018). This prolonged suspension of giant particles suggests that mechanisms must exist to counteract gravitational settling (*e.g.*, turbulence, convective uplift, or electrostatic forces), yet these processes are not fully understood and remain an active area of research (Rosenberg et al., 2014; van der Does et al., 2018; Harper et al.,

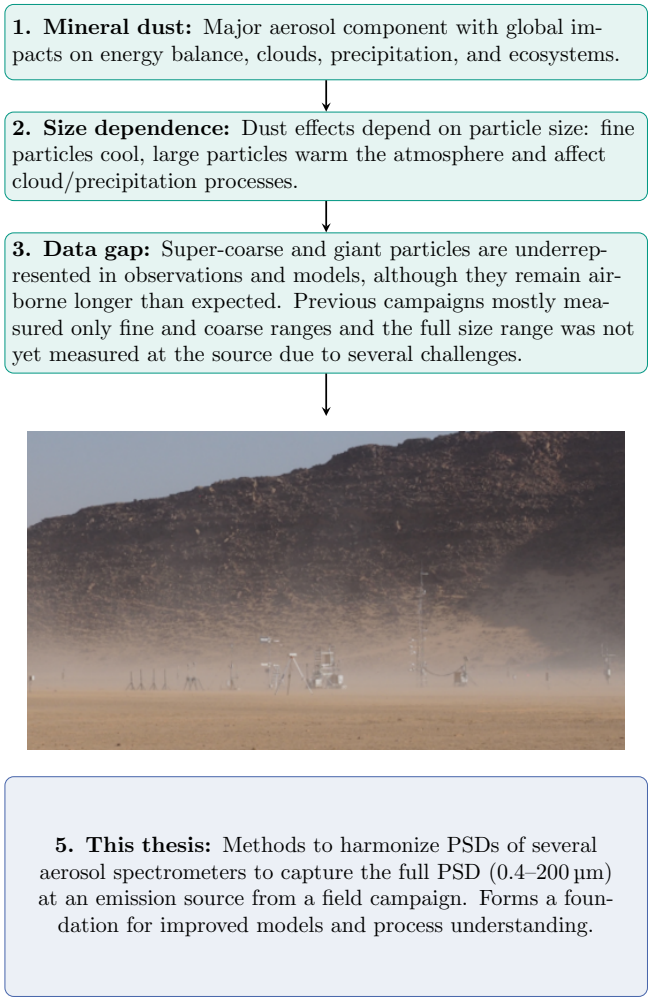

Figure 1.1.: Motivation and aim of this doctoral thesis.

2022; Ratcliffe et al., 2024). Since the mechanisms driving the transport and prolonged suspension of large particles are poorly understood, their emission and transport are either excluded from numerical simulations or their presence in the atmosphere is underestimated (Adebiyi and Kok, 2020). As a result, most models cannot represent the impacts of super-coarse and giant particles on climate, which introduces significant uncertainties into dust-climate impact assessments (Kok et al., 2023).

To better understand the mineral dust cycle and to include its impacts on climate into models, it is essential to accurately quantify and characterize the PSD of mineral dust, including super-coarse and giant particles. Accurately measuring the full PSD of mineral dust remains challenging, as no single instrument can cover its entire size spectrum (Mahowald et al., 2014). Giant dust particles are especially difficult to measure due to their relatively low expected number concentrations and the low sampling efficiencies of instrument inlets (Adebiyi et al., 2023; Schöberl et al., 2024). To mitigate these issues, some aircraft measurement campaigns have avoided inlets altogether or explicitly quantified their losses, allowing for more accurate retrievals of super-coarse and giant dust particles (*e.g.*, Rosenberg et al.,

2014; Ryder et al., 2019). These studies give important insights into the PSD evolution during transport of mineral dust. However, as measured in several hundred meters height, they cannot provide information about the PSD of dust directly after its emission.

Ground-based measurements at emission sources have predominantly targeted the fine and coarse fractions ($< 10\,\mu m$; Formenti and Di Biagio, 2024), and no campaign has yet comprehensively captured the full size range from fine to giant mineral dust directly at an emission source. In addition to this gap, the variability of the emitted dust PSD is not yet fully understood, *e.g.*, how it depends on wind speed (*e.g.*, Alfaro et al., 1997; Shao, 2004; Kok, 2011b) and stability (Khalfallah et al., 2020; Shao et al., 2020; Dupont, 2022).

In Fig. 1.1, the motivation and aim of the thesis is pictured. To address the gap in measuring the full PSD of mineral dust, including (super-) coarse and giant particles , and to capture its variability at a dust emission source, field measurements using a comprehensive suite of aerosol spectrometers were conducted and compared with physical probes. Several of the instruments covered the super-coarse and giant particle size ranges and collectively, the measurements covered a particle size range from approximately $d_p = 0.4$ to $200\,\mu m$. By overlapping the size ranges of different instruments, the measurements enabled a systematic intercomparison and validation of the PSDs, thereby enhancing confidence in the reliability of the observed data. Key challenges in measuring large dust particles at emission are addressed by minimizing the use of inlets, accounting for inlet efficiencies, and quantifying inter-instrument uncertainties. This thesis provides insights into the behavior of the full-range dust concentration PSD at emission and should form a basis for more reliable and more comprehensive future measurements of mineral dust, a deeper understanding of the processes driving its emission and near-surface transport, and the integration of large-particle effects into climate models, ultimately enhancing our comprehension of dust's broader environmental and climatic impacts.

Overview of the thesis structure

This thesis is structured as follows:

- **Chapter 1: Introduction** - Provides background, motivation, literature, and overall goal of this doctoral thesis.
- **Chapter 2: State-of-the-art**: - Reviews existing research on mineral dust, its climatic impacts, and measurement techniques, conducted campaigns, debated questions about mineral dust emission, and it identifies gaps that this study addresses.
- **Chapter 3: Objectives and scope** - Provides motivation, overall goal and objectives of this doctoral thesis.

- **Chapter 4: Data from the J-WADI field campaign and applied methods** - Describes the J-WADI field campaign, meteorological and aerosol spectrometer instrumentation, data collection procedures, developed methods to correct individual instruments and retrieve a harmonized and unified PSD across instruments.

- **Chapter 5: Results** - Presents the uncorrected and corrected PSDs of all aerosol spectrometers, discusses possible reasons for discrepancies and uncertainties between different PSDs, analyzes the variation of the unified PSDs with friction velocity u_* and stability, compares the aerosol spectrometer PSDs with that from physical samples, and from other field campaigns.

- **Chapter 6: Conclusions and Outlook** - Summarizes the main findings, their significance, and broader implications, along with suggestions for future research.

- **Appendix** - Includes supplementary material, such as additional figures and tables.

2. State-of-the-art

This chapter provides an overview of the current understanding and challenges related to the PSD of mineral dust. First, the mineral dust cycle (Sect. 2.1) is explained and the impacts of mineral dust are outlined (Sect. 2.2). The importance of measuring the full PSD is highlighted, including super-coarse and giant particles, due to their environmental and climatic relevance. Present measurements techniques to obtain the dust PSD and evidence for the long-range transport of large particles (Sect. 2.3.1) are given as well as theoretical and observational gaps in our understanding of their emission and transport are discussed. The limitations of current measurement and modeling approaches are outlined, especially with regard to large particle sizes. Section 2.3.2 reviews efforts to extend the measured PSD range by combining multiple instruments. Section 2.3.3 focuses on the PSD at the emission stage and how it may depend on meteorological conditions. Section 2.3.4 concludes by identifying critical research needs to close knowledge gaps and improve the representation of large dust particles in models.

2.1. Mineral dust cycle

North African source regions such as the Sahara Desert are the largest emittents of mineral dust (Kok et al., 2021, ~50%). However, other deserts and regions, such as the Middle East and parts of Asia (~40% Kok et al., 2021), also contribute significantly to the atmospheric dust amount. A small portion comes from North American and Southern Hemisphere regions (~10%, Kok et al. 2021). This is illustrated in Fig. 2.1, which shows that Dust Optical Depth (DOD), a proxy for dust amount, is greatest near dust sources.[1]

The formation of the soil of which mineral dust is emitted is governed by a combination of geological, climatic, and anthropogenic processes. Initially, physical, chemical, and biological weathering break down parent rocks into finer material, producing silts, clays, and sands (Pye, 1987; Wright et al., 1998; Shao, 2008). These materials can then be transported and deposited by aeolian and fluvial processes, accumulating in arid and semi-arid regions where dust emission is most prevalent (Goudie and Middleton, 2006; Kok et al., 2012). These major dust emission regions are characterized by specific geomorphological features that facilitate dust generation, including dry lake beds, sandy deserts, and areas with sparse vegetation (Baddock et al., 2016). Over time, pedogenic processes such as leaching, mineral transformations, and organic matter incorporation further modify soil composition (Claquin et al., 1999; Perlwitz

[1] In Fig. 2.1, the DOD as proxy for dust amount is shown as presented in Gkikas et al. (2021). The paper introduces the MIDAS dataset, which provides global DOD from 2003 to 2017 using MODIS-Aqua and MERRA-2 data. DOD is a type of Aerosol Optical Depth (AOD) and measures how much dust in the atmosphere extincts light at a given wavelength.

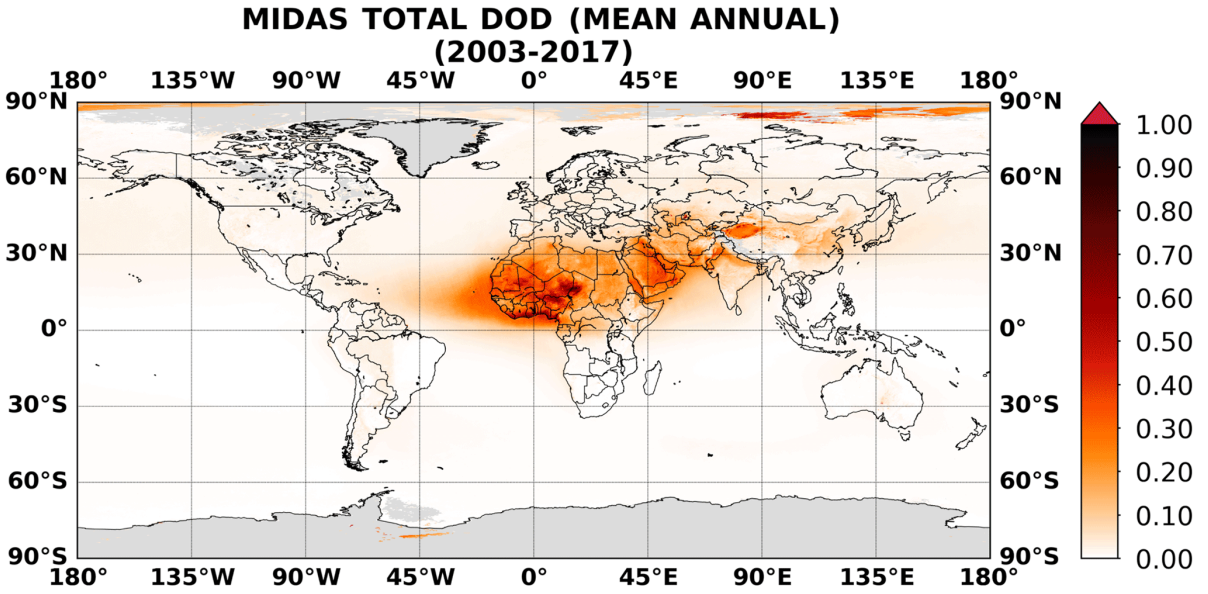

Figure 2.1.: Annual geographical distribution of climatological DOD at 550 nm from the MIDAS dataset for the period 2003–2017. Higher DOD values indicate regions with persistent dust activity, such as the Sahara, Middle East, and parts of Asia. Gray areas represent regions with no available data. Figure from Gkikas et al. (2021)/ CC BY.

et al., 2015a). The mineralogical composition of mineral dust varies by region; for example, Saharan dust is predominantly composed of clay and quartz minerals, while Asian dust contains significant amounts of illite and chlorite (Kandler et al., 2009; Panta et al., 2023; Jeong, 2024). However, most mineral dust samples are generally dominated by (alumino) silicates such as quartz, feldspar, and clay minerals, with varying amounts of carbonates, sulfates, and iron-bearing minerals (Scheuvens and Kandler, 2014). Surface processes, including wind erosion and crust formation through wetting-drying cycles, regulate the availability of erodible material. Additionally, human activities such as agriculture, overgrazing, and deforestation disturb soil structure, increasing its susceptibility to wind erosion (Huang et al., 2015; Chen et al., 2019). The resulting mineralogical composition, soil PSD, and soil erodibility ultimately shape the characteristics of mineral dust emissions into the atmosphere (Nickovic et al., 2012; Mahowald et al., 2014).

One of the primary prerequisites for mineral dust emission is the presence of loose, dry soil that can be eroded by wind (Webb and Strong, 2011). The emission of mineral dust particles is fundamentally influenced by the threshold friction velocity (u_{*t}). The wind friction velocity (u_*) describes the wind stress acting on a horizontal surface and u_{*t} represents the minimum u_* required to initiate particle motion by overcoming forces such as gravity and interparticle cohesion. The forces dominating particle motion strongly depend on particle size, with soil particles ranging in diameter from less than 0.1 µm to over 1 mm (Bullard et al., 2004).

Larger particles are primarily influenced by gravity, whereas smaller particles are dominated by cohesive forces such as van der Waals and electrostatic interactions (Iversen and White, 1982; Shao and Lu, 2000; Shao, 2008; Shao and Klose, 2016). Experimental studies, including wind tunnel experiments (Bagnold, 1937; Chepil, 1945; Zingg, 1952; Iversen et al., 1976; Fletcher, 1976a,b; Greeley et al., 2003), have analyzed u_{*t}. Most of the studies have shown a minimum u_{*t} for particles around 60-100 µm, with increasing u_{*t} for smaller and larger particles due to cohesive and gravitational forces (the increase for smaller particles was not observed in Bagnold 1937). In line with experimental research, several theoretical expressions were developed (Iversen et al., 1976; Shao and Lu, 2000; Shao and Klose, 2016). In addition to gravitational and interparticle forces, environmental factors significantly influence u_{*t}. Increased soil moisture enhances particle cohesion, thereby raising u_{*t} (McKenna-Neuman and Nickling, 1989; Fécan et al., 1999; Klose et al., 2014) and surface roughness, such as vegetation and terrain features, modifies the wind flow, therefore decreases dust emission in comparison to flat terrain (Raupach et al., 1993; Marticorena and Bergametti, 1995; Callot et al., 2000; Klose et al., 2014; von Holdt et al., 2019).

Mineral dust emission

The mechanisms driving mineral dust emission are aerodynamic entrainment, saltation bombardment, and the disintegration of soil aggregates (Fig. 2.2; Shao, 2008). As smaller soil particles are primarily

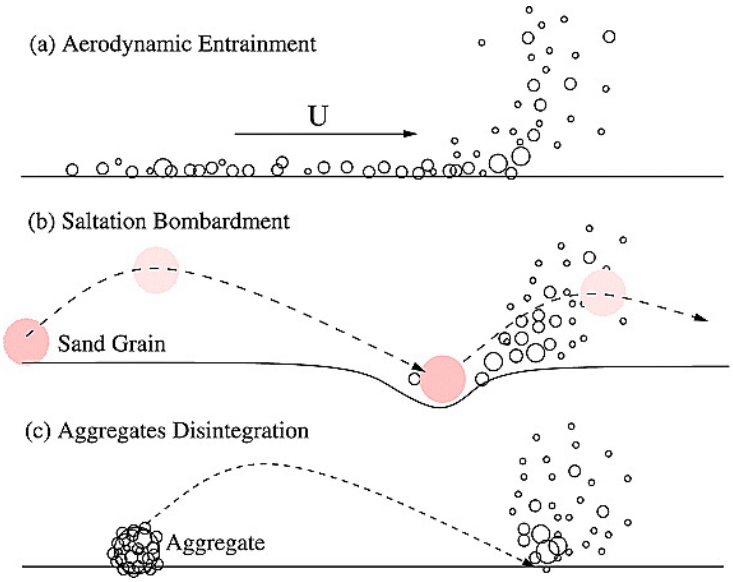

Figure 2.2.: Mechanisms for dust emission. (a) Dust emission by aerodynamic entrainment, (b) by saltation bombardment, and (c) through aggregate disaggregation. Figure from Shao et al. (2011a)/ Copyright 2011 by the American Geophysical Union.

held together by cohesive forces, their direct emission rate under wind action is limited (aerodynamic entrainment; Fig. 2.2a; Shao and Klose 2016). However, a small subset of particles with interparticle forces lower than the mean, which are more easily detached (Klose and Shao, 2012), can be entrained

by the wind. This mechanism can occur even under weak mean wind conditions due to turbulence (Klose et al., 2014). However, the initiation of saltation, *i.e.,* the hopping motion of particles, is a necessary precursor for the majority of the release of dust particles (Sow et al., 2009; Shao et al., 2011a). Saltation bombardment, also known as sandblasting, is the key mechanism of dust emission (Gomes et al., 1990; Shao et al., 1993; Alfaro et al., 1997). Here, sand-sized particles propelled by wind are lifted and brought back to the surface due to their high gravitational forces. Upon impact, a saltating particle transfers energy to surrounding grains (Bagnold, 1941; Shao et al., 2011a; Marticorena, 2014). This energy can eject additional particles that can either be suspended or brought back to surface and eject further particles, contributing to the saltation layer (Gillette et al., 1997). The saltation layer has a height of 30-50 cm, above which suspended particles dominate (Gillette et al., 1997). This process can effectively release fine dust particles from the soil into suspension, whereas sand-sized particles were expected to predominantly contribute to the saltation layer (Marticorena, 2014, Fig. 2.2b). However, also sand-sized particles could enter suspension (Sect. 2.3.1). Another dust emission mechanism involves the lifting of aggregates composed of differently sized particles held together by cohesive forces. After being lifted, if these aggregates strike the surface, the impact provides sufficient energy to overcome cohesive forces, resulting in their disintegration. This process can liberate individual or aggregated particles, some of which may enter suspension (Shao et al., 2011a; Marticorena, 2014, aggregate disintegration, Fig. 2.2c).

Mineral dust transport

Dust can be lifted into the atmosphere and remain suspended for days to weeks, traveling thousands of kilometers before settling to the surface (Schepanski, 2018). The transport of mineral dust is influenced by meteorological conditions, including wind speed and direction, as well as atmospheric stability (Knippertz and Todd, 2012) but also by particle size (Ryder et al., 2013b; Kok et al., 2021). Transport pathways are often complex, involving both horizontal and vertical movements within the atmosphere. They are influenced by atmospheric circulation patterns, including the trade winds and mid-latitude westerlies, which can carry dust from arid regions to urban areas and even across oceans (Goudie and Middleton, 2001). For instance, dust emitted from the Sahara can travel across the Atlantic Ocean, reaching as far as the Caribbean and even the southeastern United States (Goudie and Middleton, 2001; Kok et al., 2021). Similarly, Asian dust can travel over the Pacific Ocean to North America and the Arctic, while also contributing significantly to dust deposition in various ocean basins such as the North Pacific, South Pacific, and Indian Ocean (Kok et al., 2021).

Mineral dust deposition

The deposition of mineral dust can be either dry or wet. Dry deposition is influenced by gravitational settling and atmospheric turbulence. The spatial distribution of dust deposition is highly variable, with

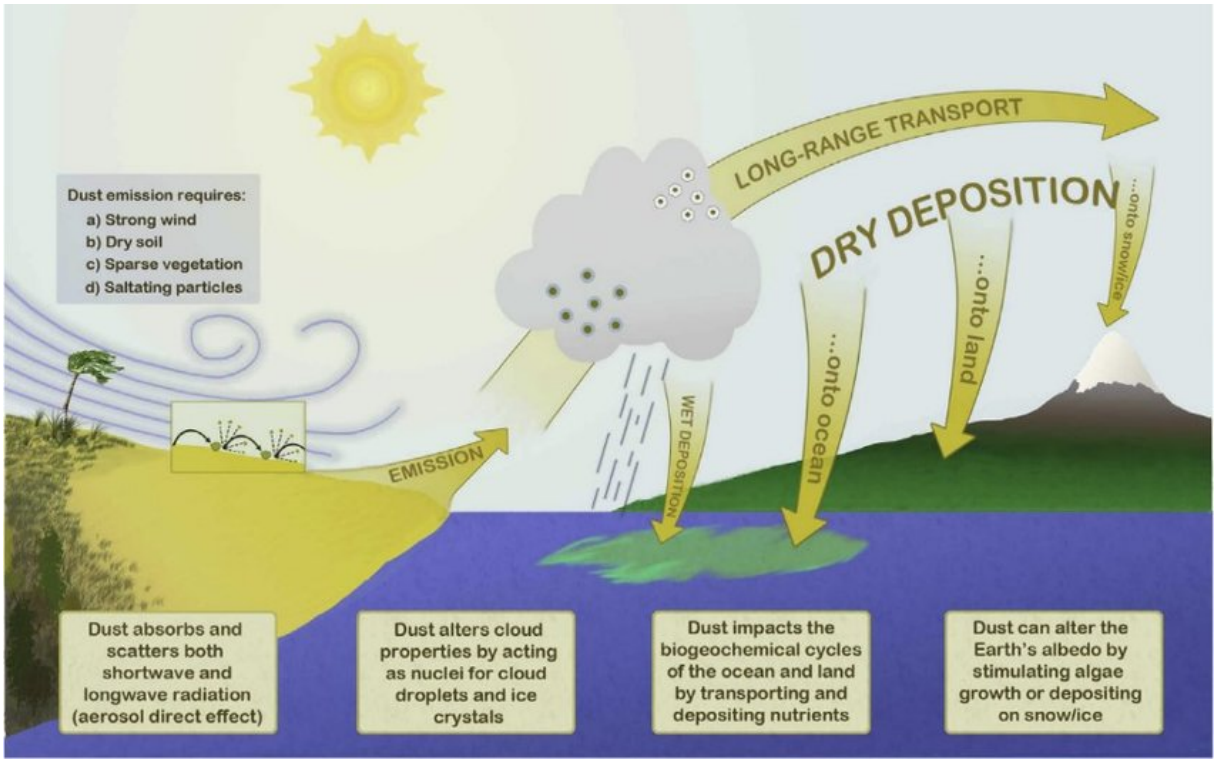

Figure 2.3.: Schematic of the mineral dust cycle and the interactions between dust and climate and biogeochemistry. Figure from Mahowald et al. (2014)/ CC BY-NC-SA.

regions downwind of and close to dust sources as the Atlantic Ocean and the Americas receiving substantial amounts of dust, while others remain relatively unaffected (Bergametti and Forêt, 2014). Larger particles are expected to settle quickly due to the greater influence of gravitational forces compared to friction *i.e.*, their higher ratio of mass to surface, while smaller particles are expected to remain airborne for extended periods (Bergametti and Forêt, 2014). Deposition can also be wet during precipitation events that wash dust from the atmosphere (Seinfeld and Pandis, 1998).

Key Message: Mineral dust, primarily emitted from arid regions such as the Sahara and the Middle East, accounts for the majority of the global aerosol mass. Its emission is governed by wind-driven mechanisms, including aerodynamic entrainment, saltation bombardment, and aggregate disintegration, all of which are affected by soil properties, meteorological conditions, and surface characteristics. Once airborne, dust can be transported over vast distances before settling through dry and wet deposition processes (Fig. 2.3). Larger particles are expected to fall out quickly.

2.2. Impact of mineral dust

Mineral dust plays a crucial role for society, in Earth's biogeochemistry, and the climate system (Prospero, 1996). It affects various socio-economic sectors, including aviation, where dust particles can impair visibility and cause engine damage, and solar energy management, where dust deposition on solar panels reduces their efficiency and increases maintenance costs (Nemuc et al., 2020). Health effects include respiratory, cardiovascular, and cardiopulmonary diseases (Longueville et al., 2012; Kotsyfakis et al., 2019), particularly caused by particles smaller than 2.5 µm, which can penetrate deep into the lungs and even enter the bloodstream (Baluchova et al., 2019). Coarse particles primarily affect the upper respiratory tract but their effect remains inconclusive (Marker, 2012).
The impact of mineral dust on the Earth's climate is multifaceted. Dust aerosols can directly scatter and absorb radiation (direct radiative effect), influence the development of clouds and the potential subsequent precipitation, interact with atmospheric chemistry and biogeochemistry on Earth's surface and oceans and can alter the albedo of surfaces (Fig. 2.3), and thus indirectly influence climate. These effects are explained in the following.

Direct radiative effect

The direct radiative effect of mineral dust refers to its impact on Earth's radiation balance at the top of the atmosphere by scattering and absorbing solar and terrestrial radiation. Dust generally cools by scattering shortwave radiation and warms by absorbing both longwave and shortwave radiation (Seinfeld and Pandis, 1998). The direct radiative effect depends on dust optical properties, *e.g.*, particle size, shape, and composition (Di Biagio et al., 2020; Huang et al., 2021), which vary with source region (*e.g.*, Huang et al., 2014; Ansell et al., 2014; Kuwano et al., 2024) and chemical aging (Klingmüller et al., 2019), but it also depends on the time of the day due to the Sun's position (Banks et al., 2014; Ansell et al., 2014; Meloni et al., 2018). Larger dust particles tend to warm the atmosphere because their absorption increases more significantly than their scattering as particle size grows. They absorb a substantial fraction of the extinguished shortwave radiation, with single-scattering albedos (SSA; ratio of scattered to total extinguished radiation) of ~ 0.80 at diameters $d_p = 10\,\mu\text{m}$ in the shortwave spectrum, and even lower for particles larger than this size (Tegen et al., 1996; Adebiyi et al., 2023). Furthermore, larger dust particles primarily absorb longwave radiation, further contributing to atmospheric warming (Tegen et al., 1996; Dufresne et al., 2002). In contrast, smaller dust particles primarily cool the atmosphere by efficiently scattering incoming radiation, with a SSA close to 1 for particles $d_p < 1\,\mu\text{m}$ decreasing to approximately 0.95 at $d_p = 2\,\mu\text{m}$ at 550 nm (Kok et al., 2023) . Thus, smaller particles dominate cooling effects, while larger particles contribute to atmospheric warming (Kok et al., 2017; Ryder et al., 2019; Kok et al., 2023, Fig. 2.4). However, it is important to note that the actual effect of particle size is also debated and might be less size-dependent and more composition driven (Ryder et al., 2018). Therefore it is important

to know the full size distribution of mineral dust particles in the atmosphere to further investigate its importance.

Due to, for example, not taking the full size distribution of mineral dust into consideration and uncertainties in the optical properties of mineral dust, the net global direct radiative effect of mineral dust exhibits large uncertainties and is estimated to be slightly cooling with $-0.15 \pm 0.35\,\mathrm{W\,m^{-2}}$ but could also slightly warm the planet (Kok et al., 2023).

Interaction with clouds

Mineral dust alters cloud formation by acting as both cloud condensation nuclei (CCN) and ice nucleating particles (INP) and therefore influencing the formation of liquid water droplets and ice crystals (Kumar et al., 2011; Hoose and Möhler, 2012). It significantly influences mixed-phase, warm, and cirrus clouds (Nenes et al., 2014; Sokolik, 2015; Froyd et al., 2022). Consequently, dust aerosols modify cloud lifetime, and can therefore influence precipitation. They alter cloud droplet number concentrations, leading to smaller (larger) droplets that enhance (decrease) cloud albedo, depending on the cloud type (Zimmermann et al., 2008; Kumar et al., 2011; Hoose and Möhler, 2012).

Particle size, which is often interconnected with the composition of mineral dust, is also important for the interaction with clouds (Min et al., 2009). Large dust can act as effective cloud condensation nuclei, promoting the formation of very large cloud droplets that enhance collision-coalescence processes, leading to precipitation (Mahowald et al., 2014). Supermicron particles ($> 1\,\mu\mathrm{m}$) show higher ice nucleation activity compared to submicron particles ($< 1\,\mu\mathrm{m}$), possibly due to differences in composition (Fig. 2.4; Welti et al., 2009; Niemand et al., 2012; Reicher et al., 2019). Additionally, the absorption of both solar and terrestrial radiation by large dust, which can lead to a warming of the air, impacts cloud distribution, highlighting its role in modifying atmospheric dynamics (Fig. 2.4; Otto et al., 2011; Adebiyi and Kok, 2020; Adebiyi et al., 2023).

As these aspects are often not fully taken into consideration (Kok et al., 2023), *e.g.*, only parts of the PSD are taken into account, large uncertainties in the climate effect of mineral dust with regard to clouds exist. The cloud impact on the radiative effect, (*i.e.*, indirect radiative effect) of mineral dust depends on cloud type and altitude. For instance, it is estimated to be negative for cirrus clouds ($-0.4 \pm 0.1\,\mathrm{Wm^{-2}}$) but positive for mixed-phase clouds ($0.1 \pm 0.1\,\mathrm{Wm^{-2}}$; Kok et al., 2023).

Biogeochemical interaction

Dust impacts ocean and land biogeochemistry both directly, by supplying nutrients to ecosystems, and indirectly, by altering precipitation patterns, temperature, and radiation (Kok et al., 2023). When mineral dust is deposited, it delivers essential micronutrients, such as iron and phosphorus, to terrestrial and marine ecosystems, thereby influencing primary productivity and biogeochemical cycles (Moore and Braucher, 2008; Schulz et al., 2012). In oceanic regions where iron is a limiting nutrient, dust deposi-

tion can stimulate phytoplankton growth, enhancing biological productivity and affecting global carbon dynamics (Jickells et al., 2005; Moore and Braucher, 2008; Johnson and Meskhidze, 2013). Especially near source regions, coarse, super-coarse, and giant dust dominates the deposited dust mass, even though its influence is debated (Adebiyi et al., 2023, Fig. 2.4).
Additionally, the supply of nutrients to ecosystems plays a vital role in the carbon cycle and therefore also contributes to climate regulation by influencing atmospheric CO_2 levels. The influence of dust on the radiative effect due to their impacts on biogeochemistry and therefore CO_2 levels is estimated at $-0.12 \pm 0.12\,\mathrm{Wm}^{-2}$ (Kok et al., 2023).

Interaction with atmospheric chemistry

Mineral dust undergoes significant chemical transformations once suspended. Through heterogeneous reactions, photochemistry, and in-cloud processing, mineral dust alters atmospheric composition and oxidation capacity as outlined below (Adebiyi et al., 2023). Mineral dust influences atmospheric chemistry by interacting with trace gases, which can affect the lifetime and concentration of key greenhouse gases such as methane and ozone (Dentener et al., 1996; Usher et al., 2003; Gaston, 2020). For instance, dust provides reactive surfaces for trace gas uptake, influencing nitrogen oxides (NO_x, HNO_3, N_2O_5), sulfur dioxide (SO_2), ozone (O_3), and volatile organic compounds (VOCs) (Dentener et al., 1996; Usher et al., 2003; Gaston, 2020). Iron- and titanium-rich minerals further enhance photochemical activity, promoting NO_2 uptake and OH radical formation under humid conditions (Ndour et al., 2008; Dupart et al., 2012). Additionally, dust plays a role in modifying the concentration and radiative effects of anthropogenic aerosols (Karydis et al., 2016; Klingmüller et al., 2020).
Coarse, super-coarse dust, and giant particles play a dominant role in these processes due to their large reactive surface area, facilitating the condensation of sulfates, nitrates, and organics (Fig. 2.4; Falkovich et al., 2004; Sullivan et al., 2007; Mahowald et al., 2014). Additionally, they promote new particle formation, secondary organic aerosol production, and ocean fertilization through enhanced iron solubility (Meskhidze et al., 2005; Shi et al., 2012). Furthermore, coarse and super-coarse dust particles provide the majority of the reactive surface area available for multiphase processes, such as heterogeneous reactions (Fig. 2.4; Mahowald et al., 2014; Adebiyi et al., 2023).
The impact of dust interactions with atmospheric chemistry on the aerosol direct radiative effect is $0.1 \pm 0.15\,\mathrm{Wm}^{-2}$ (Kok et al., 2023), indicating a range that includes the potential for slight cooling as the lower bound and a more pronounced warming effect as the upper bound.

Alteration of snow albedo

Dust deposition on snow and ice surfaces can significantly reduce their albedo, enhancing melt rates and affecting glacier mass balances (Oerlemans et al., 2009; Wittmann et al., 2017). This process is crucial for ice sheet evolution over glacial cycles (Willeit and Ganopolski, 2018). Dust can be externally

deposited or internally mixed with snow grains, with internal mixing causing greater albedo reduction (He et al., 2019; Shi et al., 2020). The effects are more pronounced at higher dust concentrations and for larger snow grains (He et al., 2019). Additionally, dust can stimulate algae growth on glaciers, further darkening the surface (Oerlemans et al., 2009). Thus, the impact of dust on snow albedo is a critical factor in climate modeling for glacial-interglacial cycles (Warren, 1984; Willeit and Ganopolski, 2018).

Including all the components mentioned above, mineral dust affects the global energy budget with a net cooling effect of $-0.2 \pm 0.5\,\mathrm{W\,m^{-2}}$ (Kok et al., 2023) and has thus a large uncertainty possibly even leading to a warming effect. As mentioned above, the climate impact of mineral dust and therefore its uncertainty is not only determined by the shape, and mineralogical composition of the particles but also by their size distribution (Mahowald et al., 2014). Mineral dust particles are predominantly non-spherical, with shapes best approximated by oblate spheroids (Otto et al., 2011; Woodward et al., 2015) or triaxial ellipsoids (Huang et al., 2020). Their aspect ratios vary depending on composition, with clay minerals exhibiting plate-like structures and higher aspect ratios compared to non-clay minerals (Veghte and Freedman, 2014; Veghte et al., 2015; Jeong, 2024). Therefore, typical aspect ratio (AR) (*i.e.*, length-to-width ratio) and height-to-width ratio (HWR) ratios deviate from unity (Kandler et al., 2007; Huang et al., 2020).

Over the past few decades, significant efforts have been made to incorporate the representation of mineral dust properties in more detail into climate models. The complex mineralogy of dust particles, which is strongly connected to their shape, and depends on the parent soil composition (Claquin et al., 1999; Journet et al., 2014; Li et al., 2021; Ageitos et al., 2023), is now being implemented in models (Scanza et al., 2015; Perlwitz et al., 2015a,b; Kok et al., 2017; Menut et al., 2020; Di Biagio et al., 2020; Anaya et al., 2024; Obiso et al., 2024) and is increasingly retrieved via remote sensing (Green et al., 2020; Zhou et al., 2020; Biagio et al., 2023). However, accurately representing the spatial and temporal variability of the full dust PSD remains a challenge, particularly for particles larger than 20 µm, which are significantly understudied and their dynamics are not well understood. This limited size representation directly affects our ability to represent key processes such as dust emission and deposition, and thus hampers reliable assessments of dust impacts on climate and the Earth system. The following sections elaborate on these gaps and their implications.

Key Message: Mineral dust influences the climate as it affects radiation, modifies clouds and precipitation, and alters atmospheric chemistry. It also delivers nutrients to ecosystems and reduces snow and ice albedo, accelerating melt. These influences are highly size-dependent and large uncertainties remain for the climatic impact of mineral dust, especially due to the uncertainties in the size distribution of mineral dust.

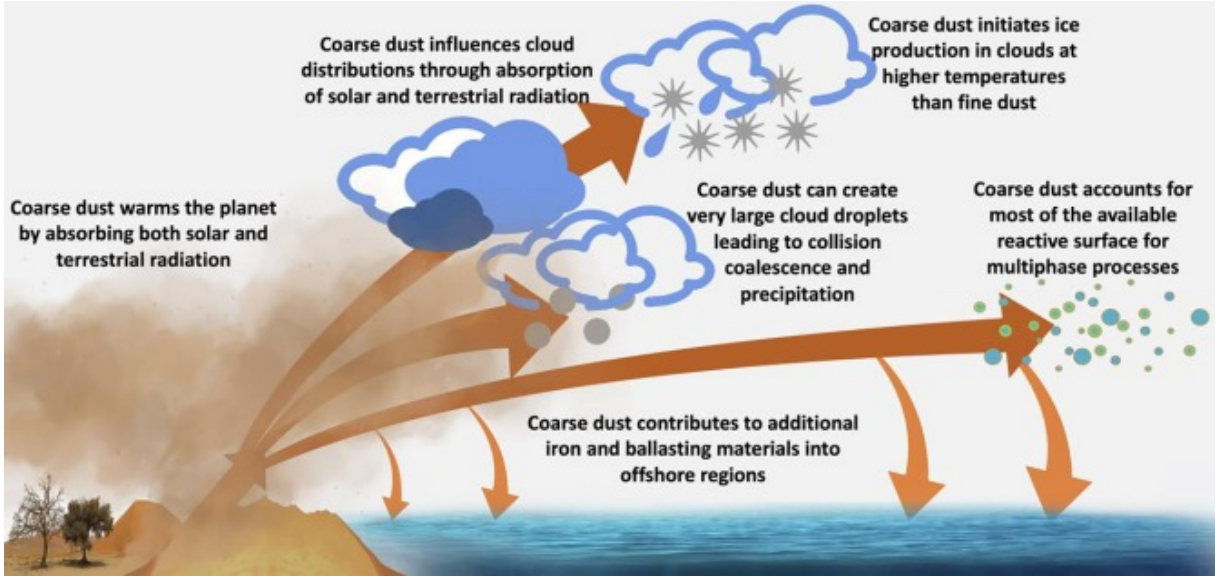

Figure 2.4.: Coarse and super-coarse dust influence multiple components of the Earth system, including radiation balance, cloud formation, precipitation processes, atmospheric chemistry, and biogeochemical cycles. Figure from Adebiyi et al. (2023)/ CC BY.

2.3. Mineral dust particle size distribution (PSD)

Airborne mineral dust spans a wide size range, from particles with a diameter $d_p < 1\,\mu m$ (Baddock et al., 2013) to particles exceeding $d_p = 100\,\mu m$ in diameter (van der Does et al., 2018). The size of mineral dust particles is influenced by factors such as soil composition, wind speed, and surface conditions at emission, and it evolves during transport due to processes like gravitational settling, aggregation, and atmospheric interactions (Scheuvens and Kandler, 2014). As a result, the PSD shifts with distance from the source, with larger particles usually depositing closer to the source and smaller particles remaining suspended over longer ranges (Ryder et al., 2013a,b).

To categorize mineral dust, particle diameters are typically grouped into distinct size ranges. The definitions of these different ranges (*e.g.*, fine, coarse, and giant dust particles) vary in the literature and there is some terminological confusion (Mahowald et al., 2014; van der Does et al., 2018; Ryder et al., 2019). In an effort to unify the terminology, Adebiyi et al. (2023) have provided the following definition for dust diameter ranges: fine dust with a diameter smaller than $d_p < 2.5\,\mu m$, coarse dust with $2.5 \leq d_p < 10\,\mu m$, super-coarse dust with $10 \leq d_p < 62.5\,\mu m$, and giant dust with $d_p \geq 62.5\,\mu m$ (Adebiyi et al., 2023). In this study, their classification is used, unless otherwise stated.

The size of a dust particle is typically defined by its radius or diameter and a collection of dust particles is characterized by a size distribution, which represents particle number, surface area, volume, or mass over a specific diameter range (Seinfeld and Pandis, 1998). To compare particle counts categorized in different size bins, the PSD is commonly normalized by dlogD, the logarithmic width of each size bin.

This normalization accounts for the varying bin widths, providing a more accurate representation of the relative contribution of each size range to the total distribution (*e.g.*, Mahowald et al., 2014).

Due to variations in measurement techniques and disciplines, different types of diameters are used to describe dust aerosols, each defining an equivalent diameter based on specific particle properties or behaviors (Kulkarni et al., 2011; Hinds and Zhu, 2022). Commonly used diameter types for atmospheric dust include aerodynamic, optical, area-equivalent (projected-area), and volume-equivalent (geometric) diameters (Mahowald et al., 2014; Huang et al., 2021; Adebiyi et al., 2023). The aerodynamic diameter represents a sphere with a standard density ($1000\,\mathrm{kg\,m^{-3}}$) that has the same settling velocity as an irregular dust particle and is widely used in air quality standards (Mahowald et al., 2014). The optical diameter refers to the diameter of a sphere with equivalent light-scattering properties (Tegen et al., 1996). This sphere often refers to the diameter of a calibration particle–typically a polystyrene latex sphere or a similar non-absorbing material–that scatters the same amount of radiation as an irregularly shaped dust particle (Hinds, 1999). Area-equivalent (or projected-area) diameter measures the diameter of a circle with the same 2D projected area as the dust particle (Kandler et al., 2007), while the volume-equivalent (geometric) diameter represents a sphere with the same volume as the particle and is commonly used in dust modeling (Mahowald et al., 2014).

The conversion between various diameter types is influenced by particle shape, refractive index (optical measurements), and dust density (aerodynamic diameter, Reid et al., 2003b; Hinds and Zhu, 2022), though these factors have frequently been neglected in past studies (Huang et al., 2020). Huang et al. (2021) have facilitated the development of conversion methods among the four primary diameter types, incorporating the asphericity of dust particles by assuming them as triaxial spheroids. They used the diameter conversions to obtain a consistent observational constraint on the size distribution of mineral dust.This constraint indicates a substantially coarser distribution than those assumed in current global aerosol model parameterizations, which underestimate the emitted dust mass in the range $10 \leq D_{\mathrm{geo}} \leq 20\,\mu\mathrm{m}$ by approximately a factor of two.

Key Message: Airborne mineral dust spans a wide size range, from submicron particles to those exceeding $100\,\mu\mathrm{m}$ and their size distribution evolves during transport. The size can be classified in fine ($< 2.5\,\mu\mathrm{m}$), coarse ($2.5 \leq d_p < 10\,\mu\mathrm{m}$), super-coarse ($10 \leq d_p < 62.5\,\mu\mathrm{m}$) and giant ($> 62.5\,\mu\mathrm{m}$) dust particles. Different diameter definitions for mineral dust exist, including aerodynamic, optical, projected-area, and volume-equivalent diameters, each relevant for specific measurement techniques and fields of interest. Converting between these diameters is essential for aligning observations and models but remains challenging.

2.3.1. Challenges in quantifying super-coarse and giant particles

Accurately measuring the size distribution of mineral dust is essential due to its significant size-dependent influence on atmospheric processes and climate dynamics (Sect. 2.2). Several methods are available to obtain the PSD of mineral dust. While satellite systems like MODIS and CALIPSO offer valuable data on AOD and vertical profiles of aerosols, they cannot directly measure the PSD, even though recent advancements in remote sensing retrievals show progress in this area (Kalashnikova and Kahn, 2008; Song et al., 2022; Sanwlani and Das, 2022).

The PSD of mineral dust can also be retrieved using columnar data from the AErosol RObotic NETwork (AERONET, Formenti and Di Biagio, 2024). It is a globally distributed, ground-based network of sun-photometers designed to measure atmospheric aerosol properties. These measurements provide normalized size distributions for particles with optically equivalent diameters between 0.1 and 30 µm, which are treated as chemically homogeneous (Dubovik and King, 2000; Dubovik et al., 2006; Taylor et al., 2014; Torres and Fuertes, 2021). AERONET data also serve as look-up tables for satellite-based dust retrievals (Cuesta et al., 2015; Zhou et al., 2020) but the measurements are accompanied by large biases and uncertainties in the coarse size range (Ryder et al., 2015). Therefore, in situ measurements of mineral dust are an essential supplement for accurately capturing the full PSD and physical properties, including super-coarse and giant particles, which are often missed by AERONET data that provide only column-integrated retrievals with limited sensitivity to larger particle sizes.

In recent decades, various measurement techniques have been employed to investigate mineral dust processes across its atmospheric cycle, including emission, transport, and deposition, which often occur simultaneously and influence one another. Even though these stages are interconnected, the measurements discussed here are categorized based on the most likely dominant process at the time of observation.

Emission stage: Data in different degree of detail, depending on the focus of the study, on mineral dust size distribution have been collected during the initial stage of the mineral dust cycle. While the early sampling analysis in Texas and Nebraska by Gillette et al. (1972) and Gillette (1974) used deposition samplers to analyze freshly emitted dust, other research focused on ground-based real-time PSD measurement with aerosol spectrometers (Fratini et al., 2007; Rajot et al., 2008; Sow et al., 2009; Shao et al., 2011a; Huang et al., 2019; Khalfallah et al., 2020; González-Flórez et al., 2023, see Table 2.1). Aerosol spectrometers are widely used for real-time PSD measurements. These instruments measure the size distribution and concentration of airborne particles by *e.g.*, analyzing their interaction with light, aerodynamic behavior, or electrical fields, categorizing particles based on their optical, aerodynamic, or electrical properties. Optical Particle Counters (OPCs), a special type of aersosol spectrometer, are commonly used to determine the size and number concentration of mineral dust particles (Table 2.1). They operate on light-scattering principles, where particles passing through a light source scatter light, typically in the forward or sideward direction, and the intensity of the scattered light is used to estimate particle size.

Table 2.1.: Examples of dust measurement campaigns at emission sources.

Reference	Location, field campaign acronym	Measurement technique	d_p measured	d_p size data	Measured size range
Gillette et al. (1972); Gillette (1974)	Texas and Nebraska	Deposition sampler & microscopy	Projected-area	Projected-area	1 - 20 µm
Fratini et al. (2007)	Gobi desert	OPC	Optical	Geometric	0.35 - 9.5 µm
Rajot et al. (2008)	Niger, AMMA - Local erosion	OPC	Optical	Optical	up to 30 µm
Sow et al. (2009)	Niger, AMMA	OPC	Optical	Optical	$\geq$ 0.3 µm
Shao et al. (2011a)	Australia, JADE	OPC	Optical	Geometric	0.3 - 8.4 µm
Huang et al. (2019)	California	OPC	Optical	Optical	0.49 - 7 µm
Khalfallah et al. (2020)	Dar Dhaoui, Tunisia, Wind–O–V's	OPC	Optical	Optical	0.24 - 17.8 µm
González-Flórez et al. (2023)	Morocco, FRAGMENT	OPC	Optical	Geometric	0.2 - 19.1 µm

Transport and deposition stage: Campaigns based on airborne platforms play a crucial role in investigating how the PSD of mineral dust evolves during atmospheric transport. Instruments mounted on research aircraft or drones, such as aerosol spectrometers and cloud probes, provide data on the vertical distribution, composition, and size of transported dust particles (*e.g.*, de Reus et al., 2000; Clarke et al., 2004; Otto et al., 2007; Chou et al., 2008; McConnell et al., 2008; Osborne et al., 2008; Wagner et al., 2009; Weinzierl et al., 2009; Chen et al., 2011; Formenti et al., 2011; Johnson and Osborne, 2011; Weinzierl et al., 2011; Ryder et al., 2013b,a; Meloni et al., 2015; Denjean et al., 2016a; Weinzierl et al., 2017; Renard et al., 2018; Ryder et al., 2018). These measurements are complemented by ground-based (*e.g.*, Maring et al., 2000; Bates et al., 2002; Kandler et al., 2007; Reid et al., 2008; Rajot et al., 2008; Müller et al., 2010; Struckmeier et al., 2016) and more seldom ship-based campaigns, which examine dust transport over oceans, providing critical insights into particle interactions with marine atmospheric conditions (*e.g.*, Schütz et al., 1981).

Long-term monitoring stations, such as the one in Barbados (Delany et al., 1967; Prospero, 1996), provide valuable data on dust deposition and long-range transport far from source regions. Since these stations were installed, various dust deposition stations have been established in regions such as French Guiana (Prospero et al., 1981), Mali (Kaly et al., 2015), Senegal (Skonieczny et al., 2013), Tenerife (Prospero, 1996), Gran Canaria (Torres-Padrón et al., 2002), southeast Australia (Leys et al., 2008), the central North Atlantic (Korte et al., 2017), and the Mediterranean (Rizza et al., 2021). However, not all of these stations routinely provide information about mineral dust PSD because their analysis is time-consuming. Samples from deposition stations can be analyzed by laboratory-based methods, including Scanning Electron Microscopy (SEM) and X-Ray analysis to determine dust size, shape, and composition. Such analyses are essential for characterizing the final stage of the dust cycle, providing insights into the composition of mineral dust, its interactions with atmospheric processes during transport and deposition. Research on the PSD after long-range transport and deposition are also conducted during field campaigns using the same methods as for emission and transport, such as aerosol spectrometer or sample collection,

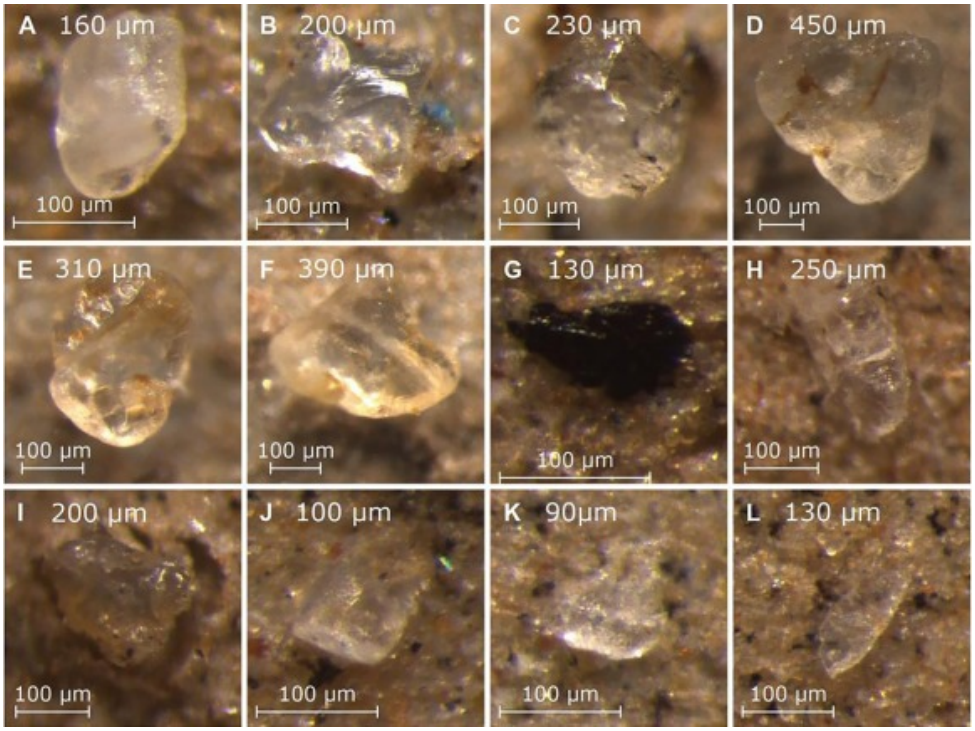

Figure 2.5.: Giant mineral dust particles sampled by van der Does et al. (2018) and the MWAC samplers at 2400 and 3500 km from the west African coast where they originated from in 2014 and 2015, with their approximate diameters. Figure by van der Does et al. (2018)/ CC BY-NC.

conducted ground-based (Formenti et al., 2001; Maring et al., 2003; Reid et al., 2003b; Jung et al., 2013; Denjean et al., 2016a), on airplanes (Reid et al., 2003a,b; Weinzierl et al., 2017), or ship-based (Schütz et al., 1981).

The studies discussed above, focusing on different stages of the mineral dust cycle, offer insights into the relationships between environmental conditions, dust emissions, transport, deposition, their size distribution, and atmospheric transport (overview and further studies are compiled in Table 7.1). In most of the measurement campaigns mentioned, mainly fine and coarse mineral dust is considered, excluding most of the super-coarse and giant particle size range. This omission leaves a substantial portion of the size distribution unaccounted for, despite evidence of the presence and transport of even giant particles in the atmosphere.

Measurements of the PSD and super-coarse and giant dust particles

Evidence for the long-range transport of super-coarse and giant dust particles was first documented by Betzer et al. in 1988 with particles of diameters $d_p > 75\,\mu m$. Since then, recent field campaigns have significantly advanced our understanding of this phenomenon. For example, van der Does et al. (2018) observed giant particles up to a diameter of 450 µm over the Atlantic Ocean, thousands of kilometers from their source (Fig. 2.5). Super-coarse dust has also been recorded in French Guiana (Barkley et al., 2021),

the Carpathian Basin (Varga et al., 2014), and Iceland (Varga et al., 2021), where back-trajectory analyses and granulometric data confirmed Saharan origins (Adebiyi et al., 2023). These and other studies (Reid et al., 2003b; Kandler et al., 2007; Rajot et al., 2008; Chou et al., 2008; Kandler et al., 2009; Wagner et al., 2009; Jeong et al., 2014; Ryder et al., 2015; Denjean et al., 2016b,a; Weinzierl et al., 2017; Ryder et al., 2019; Ratcliffe et al., 2024) collectively reveal that super-coarse, and even giant dust particles are more abundant close to emission sources than previously thought and measured and travel farther than predicted by gravitational settling theory (Seinfeld and Pandis, 1998).

Using traditional gravitational settling theories, coarse to giant dust particles are expected to sediment rapidly (*e.g.*, Seinfeld and Pandis, 1998), limiting their atmospheric lifetime and potential for long-range transport. For instance, van der Does et al. (2018) estimated that 100 µm particles could travel up to 75 km when emitted from an altitude of 3 km at wind speeds of $10\,\mathrm{m\,s^{-1}}$. From a higher altitude of 7 km and at stronger wind speeds of $25\,\mathrm{m\,s^{-1}}$, the travel distance could increase to 438 km assuming a deposition velocity of $400\,\mathrm{mm\,s^{-1}}$. These calculations suggest rapid sedimentation of such large particles, implying that they would not remain in the atmosphere long enough to potentially have a significant impact on the climate, nor to travel such large distances. Therefore, strong winds alone are insufficient to explain their long-distance transport.

To improve the understanding of the size distribution, a much debated question is how (super-) coarse particles can be emitted and remain suspended in the air over time periods longer than a few hours. Previous studies have only discussed possible mechanisms for the (long-range) transport, such as convection, electrification, non-spherical particles, topography, and turbulence, but have failed to prove and quantify them (van der Does et al., 2018; Adebiyi and Kok, 2020; Ryder et al., 2019; Heisel et al., 2021).

Challenges in measuring super-coarse and giant mineral dust: As outlined in Sect. 2.3.1, evidence for the presence and long-range transport of super-coarse and giant dust particles exists. However, the largest dust particles are especially difficult to measure due to their relatively small expected number concentrations, instrumental size range limitations, and the low sampling efficiencies of instrument inlets (Ryder et al., 2019; Adebiyi et al., 2023; Schöberl et al., 2024).

In active instruments, which draw in air, sampling should ideally be isokinetic, meaning the inlet airflow matches the ambient air velocity to preserve the original PSD (Kulkarni et al., 2011). However, perfect isokinetic sampling is rarely achieved due to variable wind speeds and airflow patterns around the inlet. When mismatched, anisokinetic sampling occurs, introducing biases at the nozzle, so that PSDs inside and outside of the nozzle differ. Inside the inlet, in horizontal sampling lines, gravitational settling further contributes to particle losses. In addition, the effect of higher inertia for larger particles, particularly in bends or curved tubing, makes them less responsive to airflow changes, leading to inertial losses. All these effects together often cause under-sampling or exclusion of super-coarse and giant particles (>10 µm), introducing biases in the observed PSD (Kulkarni et al., 2011). Understanding and addressing these issues is crucial to understanding and improving the accuracy of PSD measurements.

Modeling of super-coarse and giant mineral dust

Since the mechanisms driving the transport and prolonged suspension of super-coarse and giant particles are poorly understood and computationally demanding to model, the emission and transport of these larger dust particles are often excluded from numerical simulations (Huneeus et al., 2011) or their deposition is overestimated (Adebiyi and Kok, 2020). Most climate models inadequately represent coarse and super-coarse particles, with recent estimates indicating that more than 75% of particle mass between 5 µm and 20 µm are absent (Adebiyi and Kok, 2020). Based on existing emission schemes such as Kok et al. (2014), efforts have been made to enhance the representation of super-coarse dust at emission and to improve understanding of their climatic impacts, as demonstrated by Meng et al. (2022). Additionally, to model the transport of large dust particles, some researchers have proposed including an upward velocity component or an artificial force counteracting gravity (Maring et al., 2003; Drakaki et al., 2022). However, such approaches are not yet widely implemented as transport and deposition mechanisms are not well understood and observational data at the point of emission for validation remain lacking.
As a result, most models cannot represent the effects of super-coarse and giant particles, and their results on climate, *e.g.*, radiative effect, are at least doubtable (Kok et al., 2017). Consequently, models are not yet capable of providing meaningful insights into the role of super-coarse and giant particles within the mineral dust cycle or accurately assessing their impacts on climate processes. Therefore, more measurements in this large size range need to be conducted.

The impact of super-coarse and giant dust particles differs substantially from that of fine dust (Sect. 2.2). While the individual effects of super-coarse and giant dust, such as radiative interactions or roles in cloud microphysics, have been proposed, their overall influence remains uncertain due to limited knowledge of their abundance, emission, and transport dynamics. Quantifying these aspects is therefore essential to assess their true environmental relevance.

Key Message: Field campaigns have collected data using *e.g.*, aerosol spectrometers or physical samples to obtain the size distribution. Most studies focus on fine and coarse dust, often missing super-coarse and giant particles, which have been observed in long-range transport events. Instrumental limitations, including inlet inefficiencies and anisokinetic sampling, introduce biases that hinder accurate measurement of super-coarse and giant particles. Furthermore, the mechanisms to keep super-coarse and giant particles aloft remain poorly understood and are therefore seldom included in models.

2.3.2. Extending the measured PSD range

Measuring across a wide size range and capturing the full PSD of mineral dust is challenging, as no single aerosol spectrometer is capable of covering the entire size range. Each instrument is typically optimized for a specific range, while mineral dust spans a broad spectrum from submicron to giant particles

(Mahowald et al., 2014; Formenti and Di Biagio, 2024). While size distributions can also be inferred from collected samples, this approach has significant drawbacks, including low temporal resolution, the need for labor-intensive analysis methods, and the necessity to decide for a magnification on specific size fractions, *i.e.*, the limitation to a size range per magnification, *e.g.*, for SEM analysis. Moreover, physical sampling methods are often affected by flow dynamic limitations and are typically optimized for particular particle size ranges, which can introduce biases and hinder the accurate representation of the full size distribution. These challenges necessitate the combination of multiple measurement techniques to achieve a comprehensive view of the dust size distribution.

Several field campaigns have successfully merged data from different aerosol spectrometers and samples to extend the measurable size range. For example, Maring et al. (2000, 2003), Bates et al. (2002), and Müller et al. (2010) combined Differential Mobility Particle Sizer (DMPS) and Aerodynamic Particle Sizer (APS) measurements, while Chen et al. (2011) used OPC and APS. Other studies, including de Reus et al. (2000), Otto et al. (2007), and Denjean et al. (2016a,b), integrated Scanning Mobility Particle Sizer (SMPS) and OPC data. Additionally, multiple OPC instruments were employed in campaigns such as Reid et al. (2003b), McConnell et al. (2008), Johnson and Osborne (2011), Weinzierl et al. (2009), Weinzierl et al. (2011), and Weinzierl et al. (2017). Still, after combining these instruments, all of the campaigns mentioned so far did not extent into the giant size range of mineral dust (Table 2.2) and partly not or barely into the super-coarse range.

As an exception, a more extensive approach was taken by Kandler et al. (2011), who combined DMPS, APS, and microscopy analyzing the size range from $0.04 - 500\,\mu m$ during ground-based measurements in Cape Verde thus probing the transport stage of mineral dust. Additionally, during the FENNEC campaign in June 2011, Ryder et al. (2013a,b) employed multiple optical aerosol spectrometers and cloud probes (OAP, Optical Array Probe) on an airplane to provide size distribution measurements from d_p =0.1 to 100 µm. Despite being measured at some distance from the source (in altitudes below 2–3 km but occasionally between 100 m and 8 km), much of the observed dust was relatively fresh, within 12 hours of uplift. This setup was especially conceived to increase the confidence in the coarse, super-coarse and giant size range, covered by different instruments simultaneously. They demonstrated the ubiquity of coarse and super-coarse particles in Saharan dust plumes in Western Africa. Rosenberg et al. (2014) further extended these size measurements to 300 µm using the eddy covariance technique and used measurements in altitudes ranging between 100 – 1000 m. In another effort, Ryder et al. (2018) conducted airborne in situ measurements near Cape Verde during the AER-D campaign in August 2015. This campaign utilized similar instrumentation as FENNEC, with the addition of cloud imaging probes for measuring particles larger than 10 µm. Wing-mounted aerosol spectrometer and shadow probes covered a size range from 0.1 to 100 µm, further demonstrating the persistence of super-coarse particles during transport.

Table 2.2.: Selection of studies that combined measurements in order to get a larger size range with location, instruments used, size range and transport stage: emission, mid-range transport (MRT) or long-range transport (LRT).

Study	Location	Instruments	Size (µm)	Stage
Bates et al. (2002)	Indian Ocean, ground-based	DMPS, APS	0.02 - 7	MRT
Maring et al. (2000, 2003)	Tenerife, ground-based	DMPS, APS	0.013 - 15	MRT/LRT
Müller et al. (2010)	Cape Verde, ground-based	DMPS, APS	0.01 - 10	MRT
Chen et al. (2011)	Tropical Atlantic, airborne	OPC, APS	0.07 - 5	MRT
de Reus et al. (2000)	Canary Islands, airborne	SMPS, OPC	0.02 - 31	MRT
Otto et al. (2007)	Canary Islands, airborne	SMPS, OPC	0.02 - 31	MRT
Denjean et al. (2016a)	Mediterranean Basin, airborne	SMPS, OPC	0.01 - 12	MRT
Denjean et al. (2016b)	Puerto Rico, ground-based	SMPS, OPC	0.011 - 32	LRT
Reid et al. (2003b)	Puerto Rico, ground-based and airborne	OPC	up to 22	LRT
McConnell et al. (2008)	Senegal, airborne	OPC	up to 40	MRT
Johnson and Osborne (2011)	Western Sahara, airborne	OPC	0.1 - 60	MRT
Weinzierl et al. (2009)	Morocco, airborne	OPC	0.1 - 50	MRT
Weinzierl et al. (2011)	Cape Verde, airborne	OPC	0.1 - 30	MRT
Weinzierl et al. (2017)	Atlantic Ocean, airborne	OPC	0.06 - 50	MRT/LRT
Kandler et al. (2011)	Cape Verde, ground-based	DMPS, APS, Microscopy	0.04 - 500	MRT
Ryder et al. (2013a,b)	Western Africa, airborne	Optical Array Probe (OAP), OPC	0.1 - 100	< 1 day /MRT
Rosenberg et al. (2014)	Western Africa, airborne	0.5 - 300	OAP, OPC	< 1 day
Ryder et al. (2018)	Cape Verde, airborne	OAP, OPC	0.1 - 100	MRT
Kandler et al. (2009)	Morocco, airborne	DMPS, APS, Microscopy	0.02 - 500	emission

The studies mentioned in the paragraph above, which extended the measured size range by combining different instruments focused on the transport or deposition stage of mineral dust. As an exception, Kandler et al. (2009) conducted field measurements in Morocco covering a size range from 20 nm to 500 µm during the SAMUM-2 campaign in May/June 2006. The submicron range was measured using a DMPS, covering particle diameters from 20 to 800 nm. The supermicron range, spanning 850 nm to 5 µm, was characterized using an APS. For even larger particles, a single-stage impactor and a free-rotating wing impactor extended measurements up to 500 µm. By merging data from these instruments, composite size distributions ranging from 20 nm to 500 µm were constructed. However, the dataset of Kandler et al. (2007) was reported to be contaminated by very large saltation grains from the soil (Formenti and Di Biagio, 2024). In addition, the large size range was only represented by samples with an average temporal frequency of about one day, which is often not sufficient to draw conclusions between meteorological conditions and dust emissions.

In contrast to combining instruments at a single location and time to characterize the PSD, another approach to gain insights into the average evolution of the PSD of mineral dust during transport is to

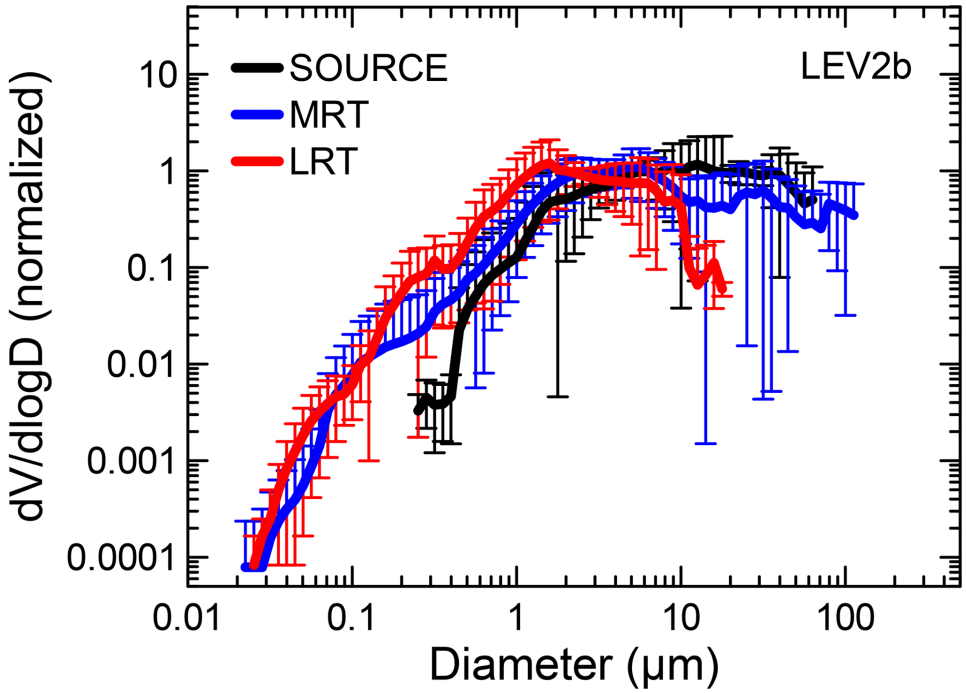

Figure 2.6.: Comparison of the normalized mean volume size distributions for the SOURCE, MRT, and LRT categories in the review study from Formenti and Di Biagio (2024), presented as geometric diameter with aspherical dust data with standard deviation as error bars. The data are normalized to an integral of 1 over the common diameter range of 0.35 – 17.8 µm before normalization with dlogD. Figure by Formenti and Di Biagio (2024)/ CC BY.

integrate measurements from different field campaigns into transport stages. Formenti and Di Biagio (2024) synthesized over 50 years of in situ field observations to compare mineral dust size distributions systematically. These data were categorized into three transport stages: source (SOURCE, within one day after emission), mid-range transport (MRT, one to four days after emission), and long-range transport (LRT, more than four days, Fig. 2.6). The main mode of the dust volume size distribution shifts from approximately 10 µm at SOURCE to 5 µm during MRT and 2 µm under LRT conditions. The normalized size distribution between 0.4 and 10 µm remains relatively stable, particularly in the coarse range, which contributes 34.9 – 44.5% of the total volume across all transport stages. Particles between 0.4 and 2.5 µm increase in prominence at LRT, accounting for 53.5% of the volume compared to 10.8% at SOURCE and 22.0% during MRT. Super-coarse particles ($d_p > 10\,\mu m$) contribute significantly at SOURCE (55%) and MRT (34%), but decrease sharply to only 2% under LRT conditions, reflecting their limited transport range. These findings highlight the variability in dust size distributions throughout their atmospheric lifetime, with notable reductions in larger particles as transport distances increase.

The data presented in Formenti and Di Biagio (2024) gives a good overview over the evolution of mineral dust over distance. However, as depicted in Fig. 2.7, existing data are predominantly from African regions and nearby transport pathways, with many studies focusing on MRT. Additionally, the synthesized dataset is derived from multiple campaigns, meaning that differences between dust events, locations,

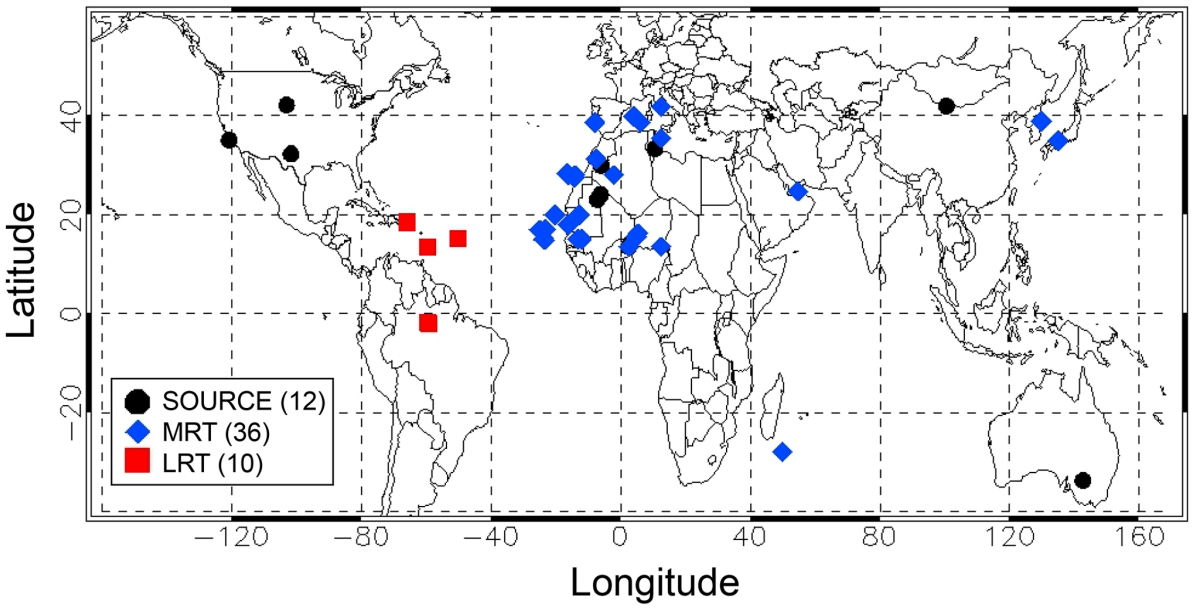

Figure 2.7.: Map of the location of the field measurements conducted considered in Formenti and Di Biagio (2024), ordered by temporal distance to the source (SOURCE, MRT, and LRT). The number of data for each category is indicated in the parentheses in the legend. Figure by Formenti and Di Biagio (2024)/ CC BY.

measurement techniques, and environmental conditions could influence the results and no direct connection between meteorological conditions and dust amount can be deducted. For SOURCE data (thus freshly emitted <1 day after emission), only two measurements (Ryder et al., 2013a; Rosenberg et al., 2014) represent the super-coarse and giant size range, and both were conducted on airplanes in several hundred meters height rather than directly at the source in a few meters height. In the first seconds to hours after emission, the size distribution is expected to change rapidly due to gravitational settling. Consequently, the full PSD immediately following emission remains unknown, especially for super-coarse and giant particles, as conditions and PSDs directly at the source differ significantly from airplane platform observations in several hundred meters height.

The lack of direct, high-frequency measurements of the full size range of dust at the emission source remains a major limitation, as no study has captured the full dust size distribution directly close to the source. Previous emission measurements were either conducted using airborne platforms in several hundred meters height or suffered from limited sampling frequency and instrumental constraints. Addressing these challenges will require dedicated high-resolution measurements of the full emission PSD, particularly for super-coarse and giant particles, to better constrain their role in dust transport and deposition processes.

Key Message: Measuring the full size distribution of mineral dust requires the use of several instruments, as no single instrument can capture the entire range of mineral dust. Most of the studies that combined measurements have focused on fine and coarse dust, rarely covering the super-coarse and giant particle range. Some studies for mid- and long-range transport also covered the super-coarse and giant size range. However, no study has directly measured the complete dust size distribution directly at the emission source.

2.3.3. Variability of the PSD at emission

While the transport and deposition stage provides insights into the evolution of the size distribution, key questions remain regarding the initially emitted PSD. As depicted in Sect. 2.3.2, no study has directly measured the complete dust size distribution including super-coarse and giant particles directly at the emission source. Additionally, some in situ studies, supported by wind tunnel experiments, reveal variability in PSD responses to meteorological conditions (Zhang and Li, 2014) while some studies decline their influence. Consequently, which environmental and physical factors control the size distribution of mineral dust at emission, remains a fundamental question. Wind speed is one of the most debated influences on mineral dust emission to directly govern the PSD of dust particles into the atmosphere.
Some wind tunnel and field studies have shown enrichment of fine particles at higher wind speeds (Alfaro et al., 1997; Ishizuka et al., 2008; Sow et al., 2009; Webb et al., 2021). In agreement with them, some theories predict that higher wind speeds increase the proportion of fine particles during saltation and link the PSD to soil properties (*e.g.*, Alfaro and Gomes, 2001; Shao, 2004). In contrast, Kok (2011b) proposed to use the Brittle Fragmentation Theory (BFT), suggesting that the emitted PSD is largely independent of wind speed, at least in the fine and coarse range. Kok (2011a) and Kok et al. (2014) reuse data from existing measurements and find no significant dependence on PSD in line with Kok (2011b). This independence is explained with findings that saltator impact speeds, key to dust emission, remain largely unaffected by variations in mean wind speed (Durán et al., 2011; Kok et al., 2012).
Atmospheric stability could also influence dust emission by modulating turbulence and saltation bombardment intensity. Shao et al. (2020) and Khalfallah et al. (2020) argue that dust PSD depends on the stability in the atmospheric boundary-layer, with enhanced turbulence leading to increased emission of finer particles. In contrast, Dupont (2022) suggests that PSD variations are more strongly linked to surface soil conditions than to enhanced eddy diffusivity of fine particles.

2.3.4. Full mineral dust PSD at emission

To better understand the mineral dust cycle and its impacts on climate, it is essential to accurately quantify, evaluate, and understand the size distribution of mineral dust at all three stages: Emission, transport, and deposition.

While some effort has been made in understanding full dust size distributions during transport, large uncertainties remain regarding the emitted dust size range. Understanding the emission phase of the dust cycle is crucial: Without understanding the initial stage, it is not possible to predict the subsequent stages and their impact on the environment. In dust models, the emission informs the development of dust transport and deposition, which are essential for assessing the impacts of dust (Bryant, 2013). Uncertainties remain regarding the factors influencing the emitted dust PSD, particularly the role of meteorological conditions in shaping the size distribution (Shao et al., 2011b, Sect. 2.3.3). Most campaigns conducted in the past have primarily focused on fine and coarse dust, often neglecting the coarser part of the PSD for particles with $d_p > 20\,\mu m$ (Kok et al., 2017; Adebiyi et al., 2023; Formenti and Di Biagio, 2024). This leaves a major gap in our ability to quantify the full dust size distribution at emission sources, despite the important size-dependent impacts of mineral dust on the environment. So far, models are not able to accurately represent the PSD. Especially the super-coarse and giant particle size ranges are underrepresented (Drakaki et al., 2022; Ratcliffe et al., 2024) as the mechanisms driving the emission (and transport) are either poorly understood or are under debate (see previous Sect. 2.3.3). Therefore, conducting field campaigns at dust sources to better understand the size-resolved emission processes are key to better understand this transport stage.

Key Message: Understanding the full size distribution of mineral dust at emission is crucial for predicting its transport and environmental impacts, but it has never been measured close to dust sources in high temporal resolution. Large uncertainties remain regarding the connection between atmospheric conditions and emission PSD.

3. Objectives and scope

The overarching aim of this doctoral thesis is to contribute to closing the gaps in the understanding of the full size distribution of mineral dust at emission, especially in the super-coarse and giant range, based on measurements from J-WADI, an intensive dust field campaign conducted in Wadi Rum, Jordan.
In order to achieve this aim, the thesis will focus on the following objectives:

(1) measure the full size-resolved mineral dust concentration near the surface at a dust source in Jordan together with corresponding meteorological conditions,

(2) evaluate and address the challenges in measuring super-coarse and giant particles using a comprehensive suite of aerosol spectrometers,

(3) develop and apply methods to harmonize and merge data from different instruments with overlapping size ranges, in order to derive consistent and reliable particle size distributions,

(4) analyze the occurrence of super-coarse and giant dust particles based on the field data collected in (1),

(5) investigate the variability of the full particle size distribution at a dust source in Jordan under different atmospheric conditions, *i.e.,* friction velocity and atmospheric stability.

Achieving these objectives, will lay the foundation for a future development of a new dust emission parameterization and the subsequent transport.

4. Data from the J-WADI field campaign and applied methods

The goal of this study is to better quantify the full-range mineral dust concentration PSD and its variability at emission. For this purpose, meteorological (Sect. 4.2) and aerosol spectrometer measurements (Sect. 4.4) collected during the J-WADI field campaign (description Sect. 4.1) are used and the threshold friction velocity is calculated (Sect. 4.3). To combine measurements from multiple aerosol spectrometer instruments, a strict correction procedure is developed and applied, methods to quantify sampling efficiencies are presented (Sect. 4.4.6), and the aerosol spectrometer measurements are compared with collected samples as detailed below. To ensure the validity of these merged aerosol spectrometer data, they are systematically compared with physical samples collected during the campaign, using a flat-plate sampler and analyzed with Scanning Electron Microscopy (SEM, Sect. 4.5). A constant deposition velocity approach is applied to reconcile dry deposition rates with real-time concentration measurements.
Some of the approaches were first explored during earlier fieldwork, such as a campaign in Iceland, which provided initial insights into instrument behavior and supported early testing of correction techniques. Building on the insights from the Iceland and the J-WADI field campaign, specific correction procedures were developed as a key part of this thesis and are described in detail in this chapter. These include outlier identification (Sect. 4.4.2), conversion to a common diameter definition (geometric diameter, Sect. 4.4.3), systematic bias correction through intercomparison of instrument types (Sect. 4.4.5), harmonization by scaling concentrations to a reference instrument (Sect. 4.4.5), and a rebinning method to merge PSDs from multiple instruments into a unified format (Sect. 4.4.4).
Together, these methods provide a robust framework for temporally high-resolution, size-resolved dust measurements at emission sources. Beyond their use in this study, the correction methods developed here offer valuable tools for future field campaigns, particularly those targeting the characterization of super-coarse and giant mineral dust particles.

4.1. General information about the J-WADI field campaign

The J-WADI (Jordan Wind erosion And Dust Investigation) field measurement campaign (`https://www.imk-tro.kit.edu/english/11800.php`, last accessed 5 Mar. 2025) was conducted in Wadi Rum, Jordan in September 2022. It was co-organized by the ERC Consolidator Grant FRAGMENT (FRontiers in dust minerAloGical coMposition and its Effects upoN climaTe; earlier studies in this context: González-Flórez et al., 2023; González-Romero et al., 2023; Yus-Díez et al., 2023; González-Romero et al., 2024a,b) at the Barcelona Supercomputing Center (BSC) and the Helmholtz Young Inves-

tigator Group "A big unknown in the climate impact of atmospheric aerosol: Mineral soil dust" (HYIG Mineral Dust) at KIT in collaboration with the University of Jordan.

Scientific scope and objectives of J-WADI

J-WADI aims to improve our understanding of desert dust emissions, specifically the full-range PSD and mineralogical composition of emitted dust, and their dependence on parent soil properties and meteorological conditions.
The primary goals of J-WADI are to enhance our understanding of:

- The mechanisms responsible for the emission and prolonged suspension of super-coarse and giant dust particles.
- The variability of the emitted dust particle-size distribution and its underlying controls.
- The size-resolved mineralogical composition of dust at emission and its relationship with the parent soil.
- The optical and ice-nucleating properties of emitted dust.
- The mineralogical composition of dust based on spectroscopy.

Collaborations and Related Projects

J-WADI is closely linked to MICOS (Dust-induced Ice Nucleation: Effects of Mineralogical Composition and Size), a joint ATMO-ACCESS project between the Barcelona Supercomputing Center and the Karlsruhe Institute of Technology (KIT). MICOS includes laboratory experiments using the renowned Aerosol Interaction and Dynamics in the Atmosphere (AIDA) cloud chamber (`https://www.imk-aaf.kit.edu/AIDA_facilities.php`, last accessed: 13 Mar. 2025).
Additionally, J-WADI is connected to EMIT (Earth Surface Mineral Dust Source Investigation), a NASA mission that has been mapping Earth's surface mineral composition via hyperspectral imaging spectroscopy from the International Space Station (ISS) since August 2022 (`https://earth.jpl.nasa.gov/emit/`, last accessed: 13 Mar. 2025).
In addition to the J-WADI campaign, data from an Iceland campaign in collaboration with the HiLDA project (Iceland as a model for high-latitude dust sources – a combined experimental and modeling approach for characterization of dust emission and transport processes, `https://gepris.dfg.de/gepris/projekt/417012665?language=en`, last accessed 04 April 2025) and FRAGMENT with contributions from the HYIG Mineral Dust were used to support method development and instrument testing. HiLDA addresses the scarcity of observational data on dust emissions and export from Iceland. High-latitude dust sources, including Iceland, cover $> 500.000\,\mathrm{km}^2$ and contribute ~5% of the global dust budget (Bullard et al., 2016). Beyond the previously discussed environmental impacts, Icelandic dust,

primarily basaltic volcanic glass, plays an important role in high-latitude systems. When transported to glaciated regions, it can darken snow and ice surfaces upon deposition, thereby reducing the surface albedo and accelerating melt processes and ultimately affecting local climate and glacier mass balance (Albani, 2021). During an intensive campaign in August 2021, measurements were conducted at an Icelandic dust source using a similar instrument setup as deployed during J-WADI, though with a reduced number of instruments from the HYIG Mineral Dust. Among others, the SANTRI2 (Sect.4.4) and the scintillometer (Sect.4.2) were deployed, allowing further development and validation of the measurement configuration and data acquisition setup for both instruments. Based on the Icelandic dataset and additional outdoor tests in Germany, refinements in the scintillometer data acquisition and processing were established. Similarly, a correction approach for SANTRI2 data were developed based on the field data from Iceland.

Field site and set-up

The field site of the J-WADI campaign was located at 29°44'21"N, 35°22'56"E, in Wadi Rum (Fig. 4.1a) and nearby the village of Rashidiyah and approximately 700 m downwind of the Quweira solar power plant. During the measurement period, no significant human activity occurred at the power plant, and I therefore do not expect that its presence had any influence on the measurements. It was situated within a flat, open landscape surrounded by small hills (< 100 m in altitude, Fig. 4.1b). This configuration created a wide opening facing the expected predominant wind direction, while the opposite side featured a narrow opening where winds typically exited. Despite this surrounding topography, the measurement site was within a flat area that may occasionally be flooded during heavy rainfall periods, and lacked any significant surface roughness features. The location and timing of the campaign were chosen based on analysis of station and remote sensing data, on-site inspection, and local guidance, considering scientific and practical aspects, such as expected dust emission potential and likelihood, accessibility, and logistics. The site setup was similar to previous FRAGMENT campaigns in Morocco and Iceland (González-Flórez et al., 2023; Dupont et al., 2024), but with additional instrumentation emphasizing super-coarse and giant dust as well as atmospheric turbulence. To minimize the potential for instrument shadowing, the instruments were oriented approximately perpendicular to the expected predominant wind direction (Fig. 4.1b, c, d), determined by analysis of measurements at seven stations across Jordan available through the NOAA ISD meteo data (`https://www.ncei.noaa.gov/products/land-based-station/integrated-surface-database`, last accessed 24 Mar. 2025), and observation of local erosion, e.g. ripples. All instruments except one (SANTRI - powered by a photovoltaic panel on top of the device with battery buffering) were powered by a diesel generator placed approximately 200 m north of the measurement setup (see Fig. 1). Consequently, I expect minimal impacts of the generator exhaust on the near-surface PSD measurements, and only during northerly winds and for the smallest particle

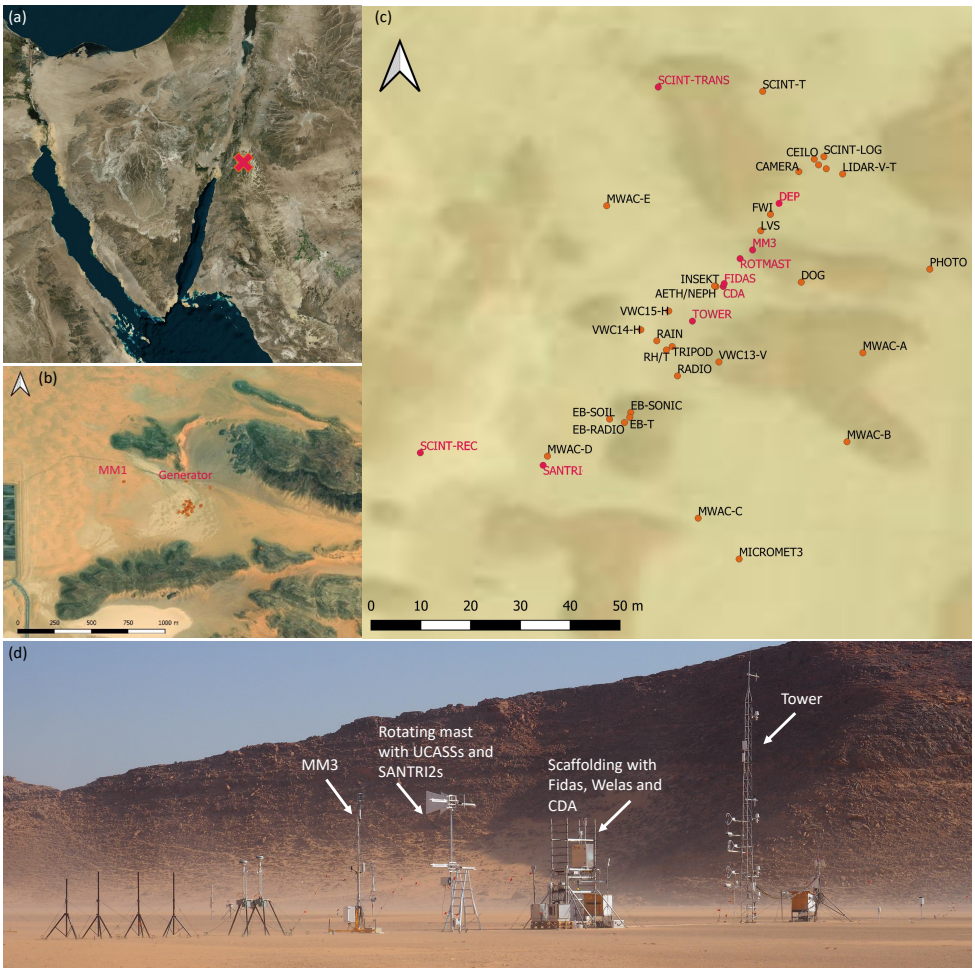

Figure 4.1.: Field location and set-up. (a) Background image from Bing maps with the field site marked with a orange cross, (b) topographic map, field set-up, and surrounding of J-WADI, including mobile mast MM1 and the diesel generator, (c) set-up at the measurement site with the instruments used marked in orange (abbreviations: SCINT-TRANS/-REC = Scintillometer transmitter/receiver, ROTMAST = rotating mast, DEP = deposition sampler, MM3 = mobile mast 3), (d) photo of the site center including most instruments used in this study in their field deployment. Background map copyright for (b) and (c) Esri, Maxar, Earthstar Geographics, and the GIS User Community, generated by M. Klose.

sizes. Here I present only instruments and data used in this study. Other measurements from J-WADI are described elsewhere (e.g., Dupont et al., 2024).

4.2. Meteorological measurements

The meteorological instruments and data used here are summarized in Tab. 4.1. I obtained the momentum flux and Obukhov length (L) using a scintillometer (Scintec SLS-40, 1 min data acquisition rate) positioned parallel to the main instrument line (Fig. 4.2 a). The scintillometer measures the refractive index structure parameter (C_n^2) and sensible heat flux (H), from which u_* and L were derived based on Monin-Obukhov Similarity Theory (MOST). The Obukhov length L characterizes atmospheric stability as the ratio of mechanical turbulence to buoyancy effects, where negative values indicate unstable,

Table 4.1.: Overview of meteorological instruments and measured variables used in this article. Abbreviations: MOST - Monin-Obukhov Similarity Theory; EC - Eddy Covariance; TFEM - Time Fraction Equivalence Method

Instrument (Model)	**Variable(s)**	**Height (m)**	**Temporal resolution**	**Purpose / Usage**
Scintillometer (Scintec SLS-40)	C_n^2, sensible heat flux (H); derived u_* and L	2.54	1 min (logging frequency)	Derivation of u_* and Obukhov length L via MOST; provides spatially representative turbulence measurements; *gaps filled with 3D sonic anemometers (Campbell)*
3D sonic anemometer (Campbell CSAT3)	Wind vectors, temperature (sonic); u_* via EC	3.0 (on 10 m tower)	50 Hz (logging frequency)	Gap-filling for u_* and L when scintillometer data are missing and when wind data from MM3 are missing
3D sonic anemometers (R.M. Young 81000)	Wind speed, direction	2.0 and 4.0 (on MM3 mast)	40 Hz (logging frequency)	Wind input for particle concentration calculations; *gaps filled with 3D sonic anemometer (Campbell)*
Barometer (R.M. Young 61202V)	Air pressure	1.0 (on MM3 mast)	15-min mean (analysis frequency)	Provides pressure data for atmospheric context; *gaps filled with MM1 sensor*
Temperature and humidity sensor (Rotronic MP100)	Temperature and relative humidity	2.0 (on MM3 mast)	15-min mean (analysis frequency)	Used for ambient conditions and to derive humidity; *gaps filled using MM1 sensor*
Saltation sensor (SANTRI)	Saltation counts at three heights; streamwise saltation flux	0.05, 0.15, and 0.3	15-min mean (analysis frequency)	Used to derive threshold friction velocity u_{*t} via TFEM

positive values stable, and large magnitudes near-zero indicate neutral stratification. The original data acquisition software for the Scintillometer used in this study was a legacy application designed exclusively for MS-DOS, presenting significant challenges for integration with modern hardware. During the Iceland campaign, data collection relied on an outdated Windows 98 laptop running the software via the middleware TameDOS. However, this setup was cumbersome, difficult to use in the field and it could not be synchronized with the time server. To modernize the system and enhance reliability, a new approach was implemented: the software was migrated to a Raspberry Pi using the MS-DOS emulator DOSBox-X, which supports hardware emulation and improved integration with serial interfaces. This allowed for synchronization with a time server and provided a more secure approach for data acquisition and a user-friendly platform for field deployment. Necessary configurations were made to enable serial port access, and the emulator environment was adapted to support continuous and stable data acquisition during the campaign. This solution not only facilitated a smoother operation in the field but also extended the usability of the aging scintillometer system for future studies[1]. I assumed a constant air density of $\rho_{\text{air}} = 1.07\,\text{kgm}^{-3}$ (mean over the campaign) for calculating the friction velocity (u_*) from the momentum flux. The instrument itself cannot distinguish stable and unstable conditions and provides data for night (stable) and daytime (unstable) times. The manufacturer advises to use a temperature gradient to distin-

[1]These modifications were employed in cooperation with Bernhard Deny (Karlsruhe Institute of Technology (KIT), Institute of Meteorology and Climate Research Troposphere Research (IMKTRO), Karlsruhe, Germany)

guish between those. I used temperature measurements from a 10 m measurement tower in 2 and 4 m height (Campbell Scientific 43502 fan-aspirated shield with 43347 RTD Temperature Probe, Fig. 4.1d) to retrieve this gradient. Scintillometer data where the percentage of error-free diagnostic periods (`NOK`) was lower than 30 were removed by setting values to `NaN`. The primary reason for the choice for the scintillometer is that the scintillometer provides values representative of a larger surface area, reducing local turbulence biases. The setup of the scintillometer consists of two primary components, both placed at $z = 2.54$ m height: a transmitter, which emits a laser beam, and a receiver (located 97 m away from the transmitter), which captured the transmitted light (Fig. 4.1d). Variations in air temperature along the path of the laser beam cause fluctuations in the intensity of the received light. Detecting these fluctuations gives information about turbulence along the beam's trajectory. Atmospheric stability classes were determined using z/L intervals following the classification by Berg et al. (2011). The classification distinguishes five stability regimes: unstable ($z/L \leq -0.2$), near-unstable ($-0.2 < z/L < -0.04$), neutral ($-0.04 \leq z/L \leq 0.04$), near-stable ($0.04 < z/L < 0.2$), and stable conditions ($z/L \geq 0.2$).

Some data gaps occurred due to scintillometer issues, including high noise levels, power cuts, and overheating. Gaps in u_* and L were filled based on measurements of a 3D sonic anemometer (Campbell Scientific CSAT3, 50 Hz, Fig. 4.2b) mounted on a 10 m tower at 3.0 m height retrieved based on the eddy covariance (EC) method, as presented in Dupont et al. (2024)[2]. To calculate particle concentrations from particle counts detected by the UCASS and SANTRI2 instruments (described in Section 4.4 and mounted on a rotating mast), I used wind speed data at 2 m and 4 m height measured by 3D sonic anemometers (R. M. Young Company, model 81000 Ultrasonic Anemometer, 40 Hz, Fig. 4.2d) mounted on a 4 m mast (mobile mast MM3) located less than 2 m from the rotating mast (ROTMAST, Fig. 4.1c). Pressure was measured using a barometer (R.M. Young Company, Model 61202V) positioned at a height of 1 m on the 4 m mast, while (potential) temperature and relative humidity were measured (and inferred) using a temperature and humidity sensor (Rotronic, Model MP100) mounted at a height of 2 m on the 4 m mast (Fig. 4.2c, 4.1c). Some gaps in the data of the 4 m mast occurred due to power cuts and faulty data acquisition. To fill any gaps in the wind data, I used measurements of the 3D sonic anemometers from the 10 m tower at 2 m and 4 m heights (Fig. 4.2b). Gaps in temperature, relative humidity, and pressure measurements were filled using instruments of the same type mounted on an identical mobile mast located approximately 500 m upwind of the expected dominant wind direction (MM1 in Fig. 4.1b).

[2] u_* and L data of the 3D sonic anemometer was provided by Dr. Sylvain Dupont (INRAE, Bordeaux Sciences Agro, ISPA, Villenave d'Ornon, France).

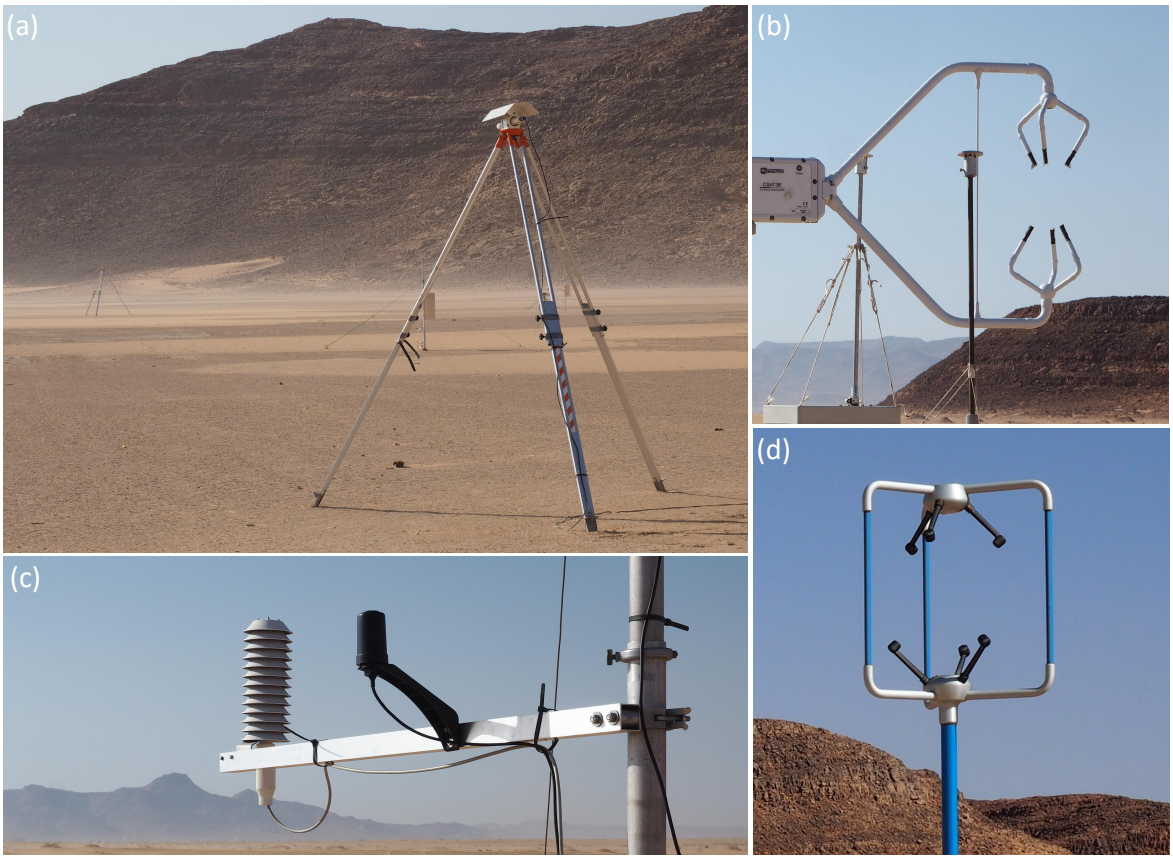

Figure 4.2.: Meteorological instruments deployed during J-WADI and used in this study: (a) Scintillometer SLS40 used to retrieve the friction velocity u_* with transmitter in the foreground and receiver in the background. (b) 3D sonic anemometer Campbell Scientific® CSAT3B used to fill gaps from u_*, L and wind speed. (c) Temperature, humidity and GPS sensor mounted on a 4 m meteorological mast. (d) 3D sonic anemometer R. M. Young Company, model 81000, mounted on the 4 m mast and used to retrieve particle concentrations from UCASS and SANTRI2.

4.3. Threshold friction velocity[3]

The threshold friction velocity u_{*t} represents the minimum friction velocity required to initiate saltation. To retrieve u_{*t}, I used saltation data from the SANTRI (Standalone AeoliaN Transport Real-time Instrument) platform (Etyemezian et al., 2017; Goossens et al., 2018; Klose et al., 2019) and implemented the Time Fraction Equivalence Method (TFEM; Stout, 1998; Barchyn and Hugenholtz, 2011) for 15-min averaged data over the whole campaign period. This method assumes that the time fraction during which saltation is detected is equivalent to the time fraction during which the friction velocity exceeds the threshold. SANTRI measures saltation counts at three heights as described in González-Flórez et al. (2023, Sect. 2.2.3). Here I counted times of active saltation as those during which at least two out of four sensors measured saltation and the height-dependent streamwise saltation flux (calculated as described

[3]TT-Prof. Dr. Martina Klose provided the saltation flux (Karlsruhe Institute of Technology (KIT), Institute of Meteorology and Climate Research Troposphere Research (IMKTRO), Karlsruhe, Germany) provided the saltation flux based on the SANTRI measurements.

Figure 4.3.: SANTRI instrument to measure saltation and retrieve flux density to obtain threshold friction velocity.

in Klose et al. 2019) was non-zero. SANTRI are the original saltation measurement design of which later on the SANTRI2 evolved. It was located approximately 40 m from the tower (Figs. 4.1c, 4.3). For values of u_*, I used the scintillometer data with gaps filled by the 3D sonic anemometer retrieved u_*.

4.4. Aerosol spectrometer

In this study, I analyze a comprehensive set of aerosol spectrometer measurements from the J-WADI campaign to investigate the size distribution of airborne mineral dust particles, with a particular focus on the larger particles (>10 µm). Their set-up during J-WADI, their working principle, and the data treatment are explained in the following. The aerosol spectrometer suite included the UCASS (Universal Cloud and Aerosol Sounding System, designed at the University of Hertfordshire; Smith et al. 2019), the saltation particle counter SANTRI2 (Standalone AeoliaN Transport Real-time Instrument, second edition, designed at the Desert Research Institute; Etyemezian et al. 2017; Goossens et al. 2018), the CDA (Cloud Droplet Analyzer), the Welas 2500 (White Light Aerosol Spectrometer, Kuhli et al. 2010), and the Fidas 200S (González-Flórez et al. 2023; all three manufactured by the Palas GmbH). This multi-instrument approach was chosen to ensure a robust examination of the entire size distribution from approximately 0.4 to 200 µm in terms of optical diameter (except SANTRI2, projected-area diameter). This encompasses the fine to giant particle fractions with significant overlap between the size ranges covered by the instruments as shown in Fig. 4.4. The UCASS and SANTRI2 devices were positioned on the rotating mast (Fig. 4.5) and the two Welas, two Fidas, and CDA next to or on a scaffolding (Fig. 4.6). Key instruments properties are summarized in Table 4.2.

SANTRI2: To explore the giant particle size range, SANTRI2s were employed, which uses optical gate devices to infer time and size-resolved particle counts (Etyemezian et al., 2017; Goossens et al., 2018; Klose et al., 2019). Originally designed to measure saltation, these instruments are normally

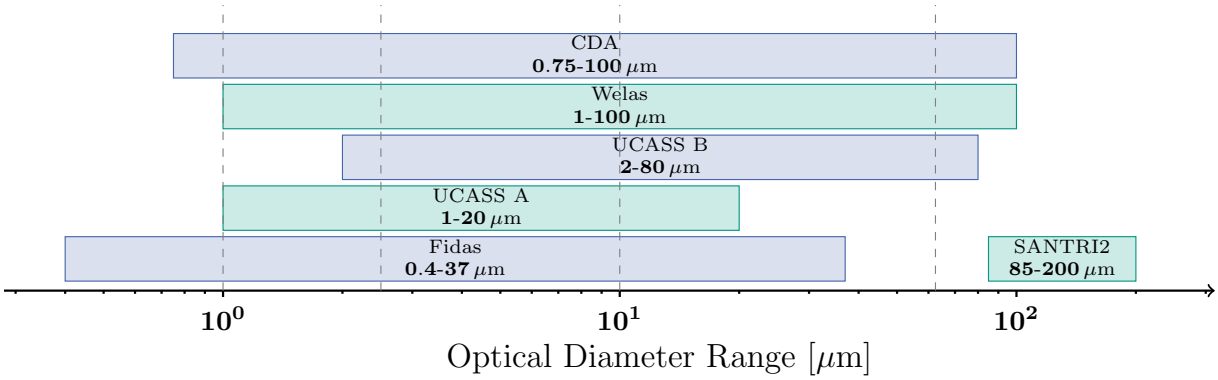

Figure 4.4.: Size ranges covered by the five instrument types in terms of optical diameter (except SANTRI2, projected-area diameter). The multi-instrument strategy covers the full size range from about 0.4 to 200 µm, effectively encompassing fine to giant particle sizes. Dashed lines indicate the size ranges of the dust size classifications (Adebiyi et al., 2023).

Table 4.2.: Characteristics of the aerosol spectrometers used in this study. Diameters are optical diameters (except for SANTRI2: projected-area diameter).

Instrument	Measurement principle	Light source	Inlet	Diameter size range	Scattering angle	Position	# of bins	Height	Number
UCASS	light scattering	laser: 658 nm	nearly open-path	1-20 µm, 2-80 µm	16-104°	rotating mast	16	4 m	2
Welas	light scattering	Xenon light	directional inlet	1-100 µm	90°	scaffolding	256	2/4 m	2
Fidas	light scattering	LED light	directional inlet	0.4-37 µm	90°	scaffolding	256	2/4 m	2
CDA	light scattering	white light	Sigma-2 head	0.75-100 µm	90°	scaffolding	256	4 m	1
SANTRI2	shadowing	diode: 890 nm	open-path	85-200 µm	none	rotating mast	7	2/4 m	4 (5 sensors each)

positioned vertically on the ground to detect particles transported in saltation at different heights. For the purpose of detecting giant dust particles during J-WADI – the size range of which fits to that of typical saltation particles – the SANTRI2s were mounted at greater height (2 m and 4 m) oriented horizontally to have multiple synchronous measurements at the same height. One unit consists of 5 sensors and each comprises a photosensor that is 9.53 mm away from the diode with 890 nm light wavelength. The onboard electronics interpret the reduction in light signal caused by a sand grain or giant dust particle traveling through the beam as voltage drop of a circuit in which the sensor is incorporated when it arrives at the photosensitive sensor. The SANTRI2 therefore measure projected-area diameters. Four SANTRI2 units were employed during J-WADI measuring in the size range d_{PA} ~85 µm to 200 µm (projected-area diameter) in 7 size bins. The four SANTRI2 instruments were mounted on the rotating mast (Fig. 4.5a). It consisted of a wind vane and a rotating pole, so that the instruments were turned toward the wind. Two units were mounted at 2 m height and two at 4 m height with one unit facing upward and one facing downward at each height. This setup was chosen to avoid possible biases in particle detection due

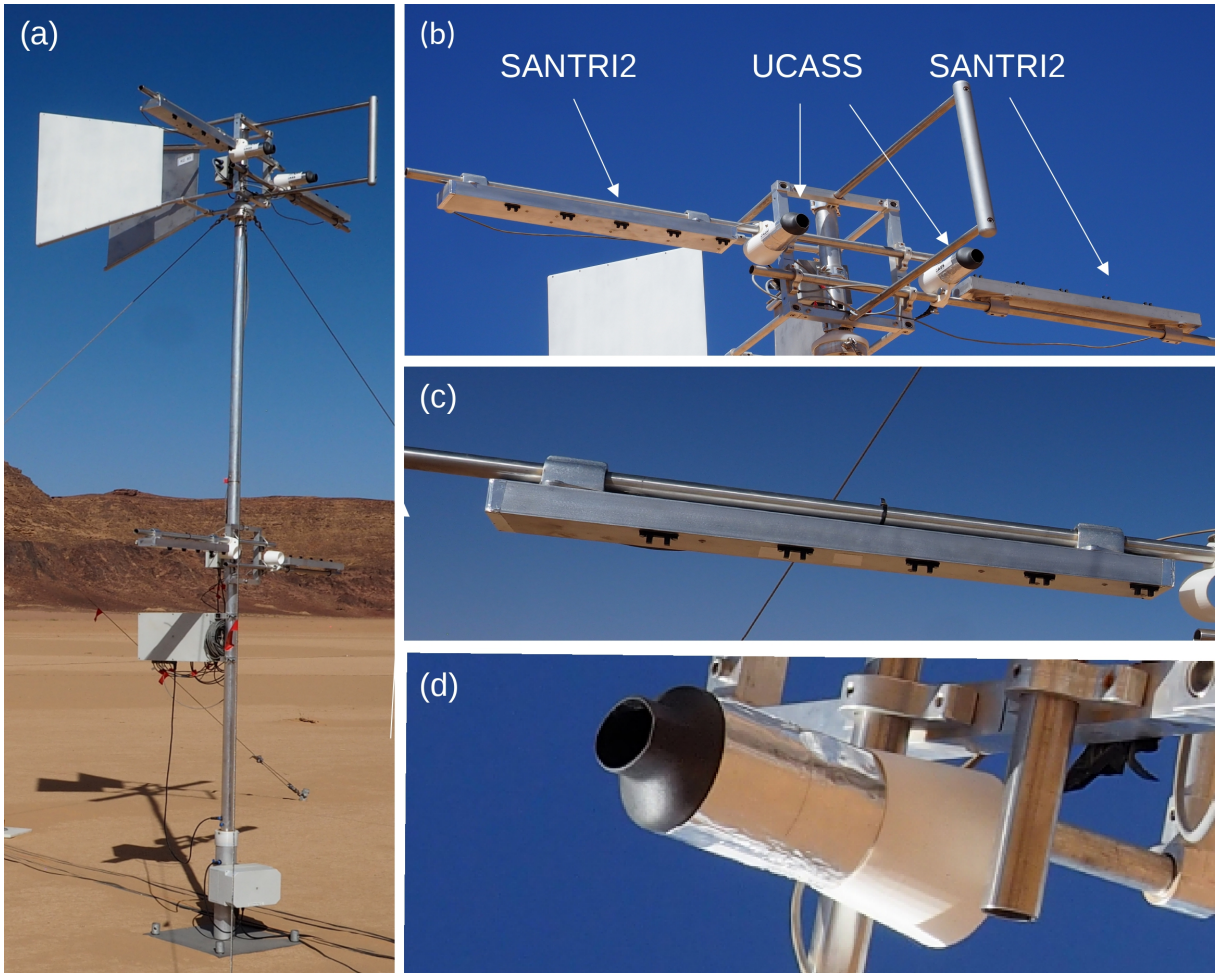

Figure 4.5.: UCASSs and SANTRI2s on the rotating mast: (a) The rotating mast (b) with two UCASS and two SANTRI2 at 4 m height and c) SANTRI2 at 2 m height, (d) view from below the UCASS at 4 m height.

to interference between particle trajectories and flow around the (relatively slim) instruments' bodies. Analysis showed that the downward-facing units exhibited a high level of noise. They were therefore excluded from further analysis. The exact cause of this behavior remains unclear and requires further investigation.

UCASS: UCASS is a low-cost particle counter designed at the University of Hertfordshire. It was used for airborne measurements of aerosol and droplet concentrations and size distributions using, e.g., drones and dropsondes in greater heights (Smith et al., 2019; Girdwood et al., 2020, 2022) while during J-WADI it was used ground-based. Here, the UCASSs were deployed at 4 m on the rotating mast together with the SANTRI2 (Fig. 4.5b). As measurement principle, it uses wide-angle elastic light scattering with a passive open-geometry system (nearly open-path). The input beam is a 658 nm continuous-wave diode laser, operating at 10 mW. The optical setup includes a laser with a collimator, a cylindrical lens, and a 2 mm aperture. The laser beam is directed into the instrument using a front-silvered mirror positioned at a 45° angle. When particles intersect the laser beam, they scatter light. An elliptical mirror then gathers

the light scattered at angles between 16° and 104°, and focuses it onto the detector, where both the pulse height and duration are measured. Two versions of the UCASS were used, measuring in 2 different size ranges: one in a larger size range with diameters d_p from 2 – 80 µm (UCASS B) and the other one in a smaller size range with d_p = 1 – 20 µm (UCASS A) in 16 different size bins each.

Welas and Fidas: The Welas and Fidas systems measure number and size of aerosols through light scattering detection at a 90° angle. Both instruments use a white light source (Fidas: LED; Welas: Xenon) to uniformly illuminate a small, T-shaped measurement volume. This design minimizes optical limitations, border-zone effects, and coincidence errors, ensuring high measurement accuracy. As particles traverse this volume, they scatter light pulses of varying intensities, which are detected and analyzed based on Mie theory, assuming spherical particles. Particle number is determined by counting the number of detected pulses per time unit, allowing simultaneous and independent measurement of both size and quantity. To measure a wide size range within the same air volume, the active instruments Welas 2500 and Fidas 200S were connected through an optical tube, allowing both instruments to sense particles in the same air flow (Fig. 4.6 b). The Fidas 200S measured particles in the size range of 0.4–37 µm (up to 40 µm but with last bin removed, see Sect. 4.4.1), whereas the Welas measured in the range between 1 and 100 µm (after coincidence removal), extending the joint size range of both instruments to include larger particles. Importantly, the pump of the Welas was not used; instead, the pump of the Fidas provided a steady flow rate of 4.8 lmin^{-1}, ensuring consistent sampling conditions for both instruments. This setup, deployed for the first time in a field campaign, allowed simultaneous measurements across an expanded size range, enhancing the characterization of the PSD. Instead of using the standard Palas Sigma-2 passive collector, a custom-made directional inlet was used to align the inlet flow with the mean wind. The exact dimensions of the inlet are provided in Fig. 5.5. After the inlet, the particles are guided through a sampling tube with drying section IADS (Intelligent Aerosol Drying System), avoiding condensation effects. The combined instruments were used at 2.1 m (referred to as Welas_2m/Fidas_2m) and 3.8 m height (Welas_4m/Fidas_4m) on a scaffolding at a distance of about ~5 m from the rotating mast (Fig. 4.6a).

CDA: Next to Fidas_4m and Welas_4m, a CDA was placed at 4 m height on the scaffolding and set to measure in the size range of 0.75 – 100 µm (after coincidence removal) with a flow rate of 5 lmin^{-1}. The CDA uses the same measurement principle as the Fidas and Welas, but unlike the other two instruments, it senses the entire flow volume rather than just a portion of it. This approach was expected to be beneficial for larger particles, as their number concentrations in ambient air are typically much lower than those of smaller particles. By increasing the sensed volume, and thereby the number of detected particles for any given concentration, this setup should improve the statistical robustness at which the larger, less abundant particles are counted.

The measurements of all aerosol spectrometers were time-synchronized by connecting them to a time server. The devices used different sampling frequencies, mostly 1 Hz, but for the analysis I averaged them

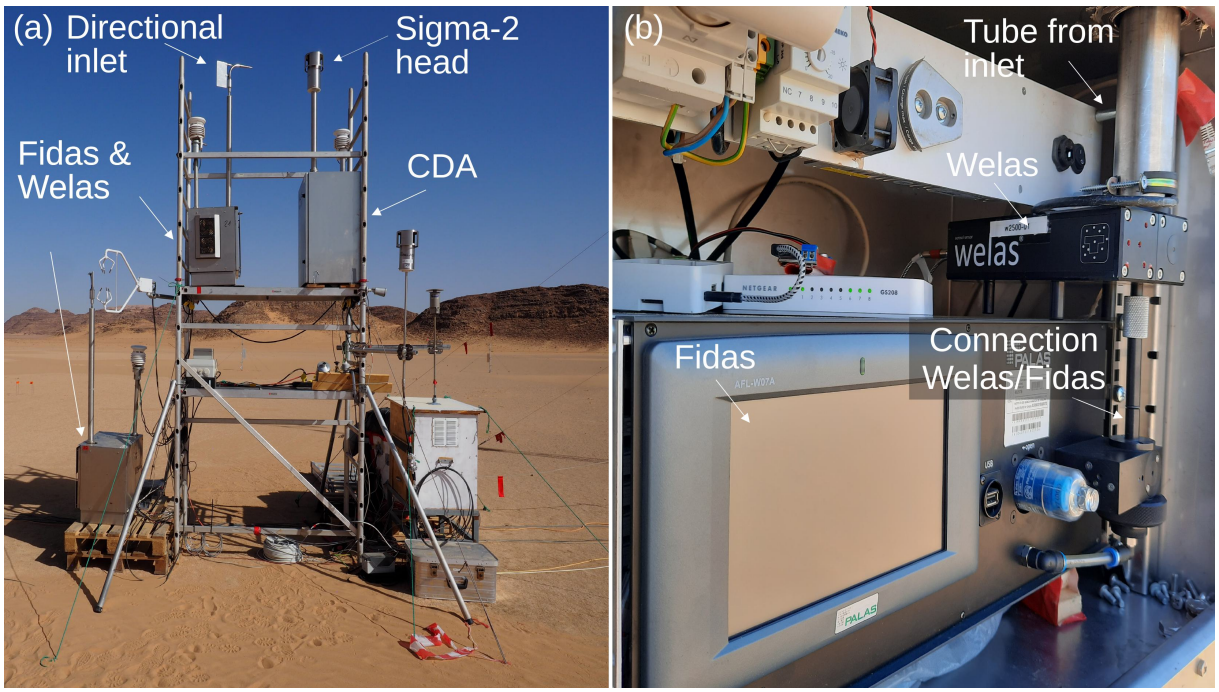

Figure 4.6.: Welas, Fidas, and CDA (a) on and next to the scaffolding, (b) Welas and Fidas sharing the same air flow in the metallic box.

over 15 min (time stamps correspond to the end of the interval) in consistency with earlier campaigns (González-Flórez et al., 2023; Panta et al., 2023; Yus-Díez et al., 2023). Note that Dupont et al. (2024) used time stamps that corresponded to the middle of each interval, but the data used here (e.g. u_*) was re-assigned to match the time stamps used in this study. The time interval of 15 min was chosen as it is still small enough to identify variations, but also large enough to characterize the boundary layer turbulence spectrum. Fidas, Welas, and CDA were calibrated using monodisperse polystyrene latex spheres (PSL, MonoDust 1500, manufactured by Palas GmbH). The Fidas and Welas instruments were calibrated at the start of the campaign, while the CDA and UCASS (Girdwood et al., 2025) were calibrated prior to shipping. As a result, the optical diameters used to describe the original instrument PSD correspond to the diameters of latex spheres that produce the same intensity of scattered light as the dust particles being measured. To make the the measurements comparable, they need to be converted in a common diameter class as described in the following sections (Sections 4.4.1, 4.4.3).

4.4.1. Retrieving PSDs from instrument data

To gain information about the mineral dust emission, dust fluxes are often used to infer the emitted dust PSD (Shao, 2008). This emission PSD at height zero can not be measured directly. The dust fluxes are typically estimated using the flux-gradient (FG) and eddy covariance (EC) methods, but their applicability for particles $d_p > 10\,\mu m$ is limited (Fratini et al., 2007; Shao, 2008; Dupont et al., 2021). Recent experiments confirmed that dry deposition can strongly influence both concentration and diffusive flux

PSDs, modulated by wind-dependent fetch length and friction velocity (González-Flórez et al., 2023), supporting earlier modeling studies (Dupont et al., 2015; Fernandes et al., 2019). Therefore, in this study, as a first step, I approximate the PSD of emitted dust flux by the PSD of near-surface dust concentration during emission, assuming that the latter is shifted toward smaller sizes compared to the actual emission flux PSD due to the removal of large particles by gravitational settling.

Bin retrieval

The counts of aerosol spectrometers are typically categorized into size bins. To obtain their size boundaries and later the PSD, several steps need to be pursued as outlined in the following.

Welas, Fidas, and CDA: During the campaign, single-particle and .promo data, a format which can be analyzed by the PDAnalyze software from the Palas GmbH were recorded. The single-particle data approach provides high-resolution data (>1 Hz) as it detects every particle individually, whereas the .promo data is already time-averaged. Therefore, where possible, I used the single-particle data. The Welas and CDA instruments provide 256 approximately logarithmically spaced raw size bins as defined by the manufacturer. Here, I aggregated the raw 256 bins into 31 approximately logarithmically spaced bins to reduce noise and enhance the clarity of trends in the PSD. A reduction to 31 bins was sufficient to achieve this in case of the Welas. The approach assigns bins based on their logarithmic spacing, maintaining a balanced resolution across the size range. The algorithm iterates through the raw bin data, dynamically adjusting the binning strategy depending on the relative logarithmic differences between consecutive bin boundaries. This method prevents overly large or small bin intervals and ensures a smooth PSD representation. For the largest bin, the method adapts the binning scheme to avoid excessively large last bins.

For the Fidas, only .promo data were recorded. The Fidas data were analyzed with the PDAnalyze software from Palas GmbH and I summarized the 256 bins into 16 logarithmically-spaced bins similar to the approach in González-Flórez et al. (2023). The last bin of the Fidas, Welas, and CDA were removed because they correspond to the respective upper boundaries of the instruments' measurement range, where limitations in size classification accuracy and potential edge effects introduce uncertainties in the recorded data.

UCASS[4]: A data file from the UCASS contains, among other, the counts in every size bin (b0 to b15). To interpret the data, the instrument's bin boundaries must be considered. The UCASS provides 16 bin boundaries, which define the upper limits of each bin.

Each bin boundary corresponds to an instrument response value measured by an analog-to-digital converter (ADC) with a range of 0 to 4095. The lower boundary of bin 0 lies between 3 and 4, but I discarded it due to uncertainties in its lower limit. To determine particle diameters from these values, both the calibration coefficients for the specific instrument and the Mie scattering curve for the sampled material must

[4]Dr. Jessica Girdwood and Prof. Dr. Chris Stopford (Particle Instruments and Diagnostics, University of Hertfordshire, Hatfield) provided the bin classification for the UCASS and corresponding scientific and technical support.

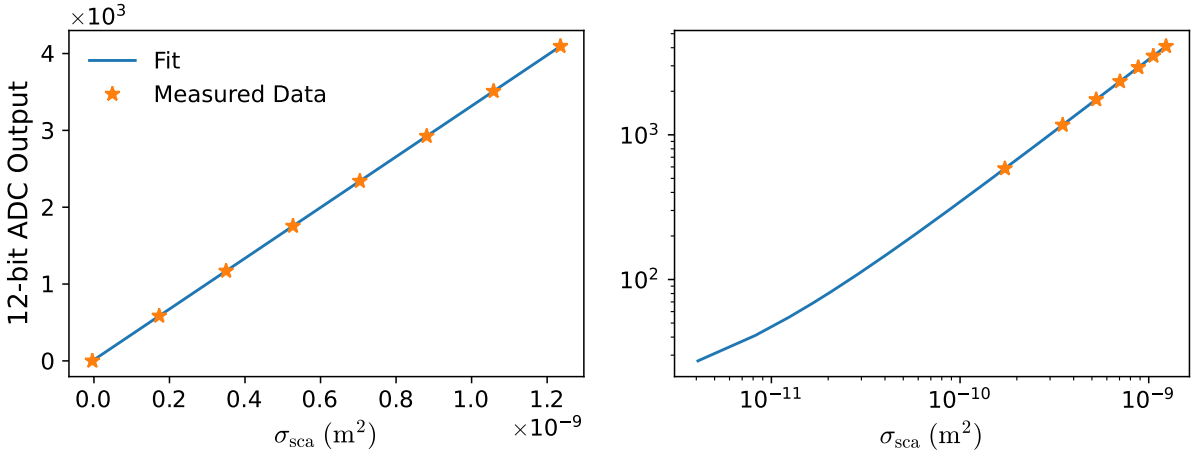

Figure 4.7.: Experimental data and linear regression to receive SL and gain (Eq. 5.1) for the UCASS instrument (linear and logarithmic scale).

be applied. The linear relationship between the ADC response and the scattering cross-section (σ_{sca}) is given by:

$$\sigma_{sca} = \frac{(ADC - SL)}{\text{gain}} \tag{4.1}$$

where *ADC* is the instrument response, *SL* is the first calibration coefficient, and gain is the second calibration coefficient, the latter two retrieved from experimental data by linear regression as shown in Fig. 4.7.

The obtained scattering cross-section σ_{sca} is then used to derive the particle diameter by applying the Mie scattering curve, which depends on the instrument's optical geometry and the refractive index of the particles. This curve is typically precomputed and stored as a lookup table. To retrieve the (optical) particle diameter, Generalized Lorenz-Mie Theory (GLMT, Gouesbet 2019) is used. GLMT extends the classical Lorenz-Mie framework to account for scattering by particles under non-uniform or partial illumination, such as those exposed to focused or structured beams (e.g., Gaussian or Bessel beams). It adapts the incident field's spatial characteristics, modifies scattering coefficients, and uses numerical integration over the illuminated particle region to model these complex interactions. Several of these Mie-curves for different material and polystyrene latex spheres (PSL) were provided by Dr. Jessica Girdwood (Fig. 4.8, different conversion tables). These curves are not monotonically increasing, requiring the application of interpolation techniques to establish a continuous conversion function. Several interpolation methods were tested, including linear interpolation, curve fitting, smoothing techniques, and selecting the first value where the given σ_{sca} threshold is met. Despite these efforts, none of the approaches yielded satisfactory results, as they led to unrealistic PSD characteristics. Specifically, the UCASS PSD exhibited oscillatory behavior or significantly overestimated concentrations for particles smaller than 10 µm. These issues highlight the challenges in accurately interpreting UCASS measure-

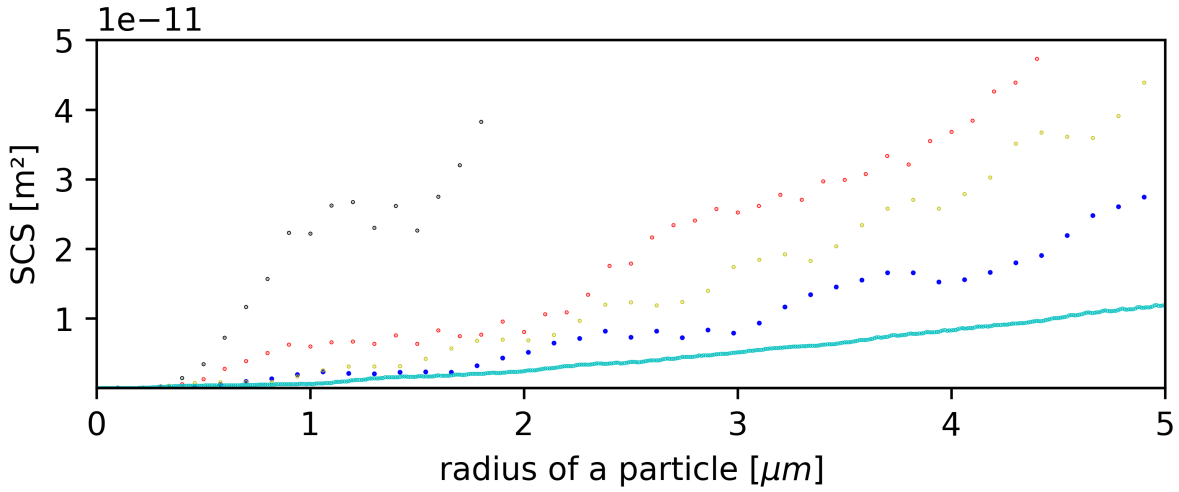

Figure 4.8.: UCASS scattering cross section (SCS) to radius conversion with different conversion curves (material or methods).

ments, necessitating further refinement of the conversion methodology to ensure reliable PSD estimates. For this reason, they are mainly not used for the analysis in this thesis.

SANTRI2: To determine the lower limits of the projected-area diameter bins for the SANTRI2, I applied a method similar to that previously used with the SANTRI instrument (Klose et al., 2019) with the formula:

$$d_{PA} = \sqrt{\frac{4A_s b_i}{\text{Signal1} \cdot \pi}}, \tag{4.2}$$

where d_{PA} is the lower bin boundary for the projected-area diameter, b_i represents the bin levels, given as [10.0, 12.0, 14.0, 18.0, 29.0, 41.0, 76.0], and A_s is the sensor area, set to 1.61 mm^2. The factor $4\pi^{-1}$ accounts for the assumption that particles are circular in projection, ensuring that the diameter calculation corresponds to the equivalent projected-area diameter. Using these values and assuming Signal1 = 3000 mV (for valid measurements, it should lay between 2750 and 3250 mV), I obtained bin boundaries of approximately 83, 91, 98, 111, 141, 168, and 228 µm. Since Signal1 varied over time, these boundaries were not fixed but adjusted dynamically based on the recorded Signal1 values throughout the campaign as shown in Fig. 4.9. The averaged geometric particle diameters from lower and upper bin boundaries obtained are provided in Table 4.3 with the standard deviation in parentheses.

Table 4.3.: Geometric mean of weighted averaged lower and upper bin boundaries of the SANTRI2 over the whole campaign with mean standard deviation in parentheses over all 15-minutes time step. Values are in µm. The bins are named according to the ranges the developers (George Nikolich and Vicken Etyemezian, Desert Research Institute (DRI), NV, USA) gave them (in µm), as the mean sizes differ slightly for both instruments.

	Cnt 73-80	Cnt 80-87	Cnt 87-99	Cnt 99-125	Cnt 125-149	Cnt 149-202
SANTRI2_2U	88.9 (0.06)	97.3 (0.05)	105.0 (0.04)	119.0 (0.04)	150.6 (0.02)	178.7 (0.02)
SANTRI2_4U	89.4 (0.03)	97.8 (0.02)	105.6 (0.02)	119.7 (0.02)	151.4 (0.01)	180.1 (0.02)

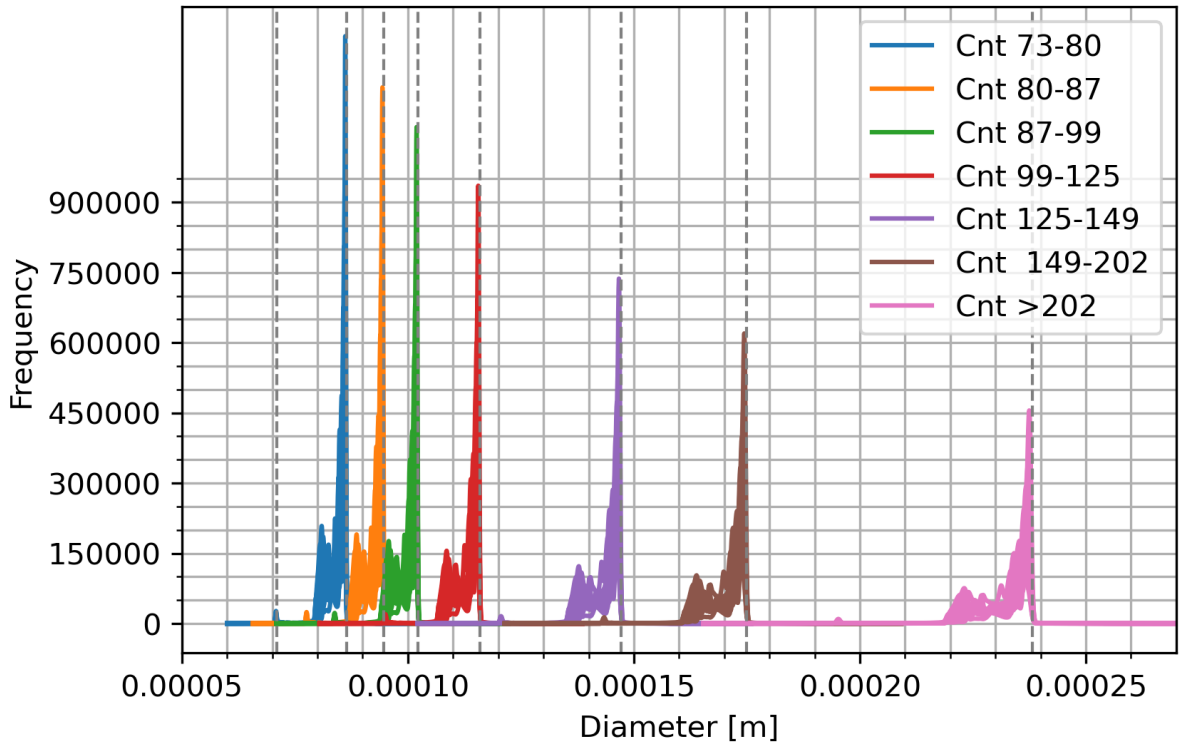

Figure 4.9.: Probability density function for the different SANTRI2 bin diameter lower boundaries from the original time resolution over the course of the campaign. Dashed lines are 99th percentile of each bin, except the one on the left-hand side (1st percentile).

As the largest bin, which extends to diameters $d_{PA} > 200\,\mu m$, has no upper size limit, I do not currently use it. To determine a representative central value for each size bin for all instruments, I used the geometric mean of the upper and lower bin boundaries.

Concentration retrieval

Most aerosol spectrometers record the size and count of particles (#), but the conversion to concentration metrics such as number concentration ($\#\,m^{-3}$) and mass concentration ($kg\,m^{-3}$) requires additional calculations. The specific approach depends on the instrument type: active, aspirated instruments such as the Fidas, Welas, and CDA, or passive instruments such as the SANTRI2 and UCASS. In all cases, the sample flow must be considered, with aspirated instruments relying on controlled flow rates and passive instruments depending on ambient wind flow.

For the Welas instrument, were single-particle data is obtained, *i.e.*, number per size bin, the number concentration is determined using:

$$dC_N = \frac{\# \cdot pl}{odv \cdot dt}, \tag{4.3}$$

where # represents the detected particle counts, pl is the pulse length (averaged over a time period dt), dt represents the sampling time (e.g., 10 s), odv is the optical detection volume calculated as:

$$odv = \text{length} \cdot \text{cross-section} \tag{4.4}$$

with length = 0.0313 cm and cross-section = $(0.0493)^2$ cm^2. For the Fidas, concentration calculations are handled internally by the instrument's software. For the CDA, as it probes the entire flow, the number concentration is calculated as:

$$dC_N = \frac{\#}{\text{flow} \cdot dt}, \tag{4.5}$$

where the flow is assumed to be 5 L/min.

For passive instruments, the sample volume (V_S) is calculated based on the exposed sampling area and the airspeed flowing through the instrument:

$$V_S = A_S \cdot v_{\text{asp}} \cdot dt, \tag{4.6}$$

where A_S is the sample area in m^2 and v_{asp} is the airspeed in ms^{-1}.

The calculation for the UCASS concentration follows this formula with $A_S = 0.5\,\text{mm}^2$. Alternatively, as the wind speed might be altered inside the housing of the UCASS, a more precise approach would be to use the time-of-flight (ToF), which represents the time a particle takes to cross the laser beam:

$$V_S = S_S \cdot w_y \cdot ToF \cdot dt \tag{4.7}$$

where w_y is the laser beam width. However, due to poor correlation between wind speed and ToF and an unrealistic behavior for the ToF, the wind speed (see Sect. 4.2) was applied for the UCASS to retrieve the concentration. The same calculation was used for the SANTRI2, adjusting for different sensor dimensions ($1.27 \cdot 9.53\,\text{mm}^2$).

To derive mass concentration from number concentration, I assumed a particle density of $\rho = 2650\,\text{kg}\,\text{m}^{-3}$ as reported by Tegen and Fung (1994). Particle density was not measured in the field.

4.4.2. Outlier correction

Throughout the research campaign, I observed irregularities in the mineral dust PSD across instruments, which presented two main challenges. Some instruments (UCASS, SANTRI2, occasionally Welas, and CDA) displayed sharp peaks in their size distribution data that were unrealistic and inconsistent with visual observations (e.g., periods of low wind) and did not align with data from other instruments (or other sensors, in the case of the SANTRI2). I attribute these anomalies to outliers.

Outliers are expected due to various instrumental factors: in SANTRI2, light reflected from surfaces can lead to erroneous detections; in UCASS, a occasionally faulty connection could result in recurring high

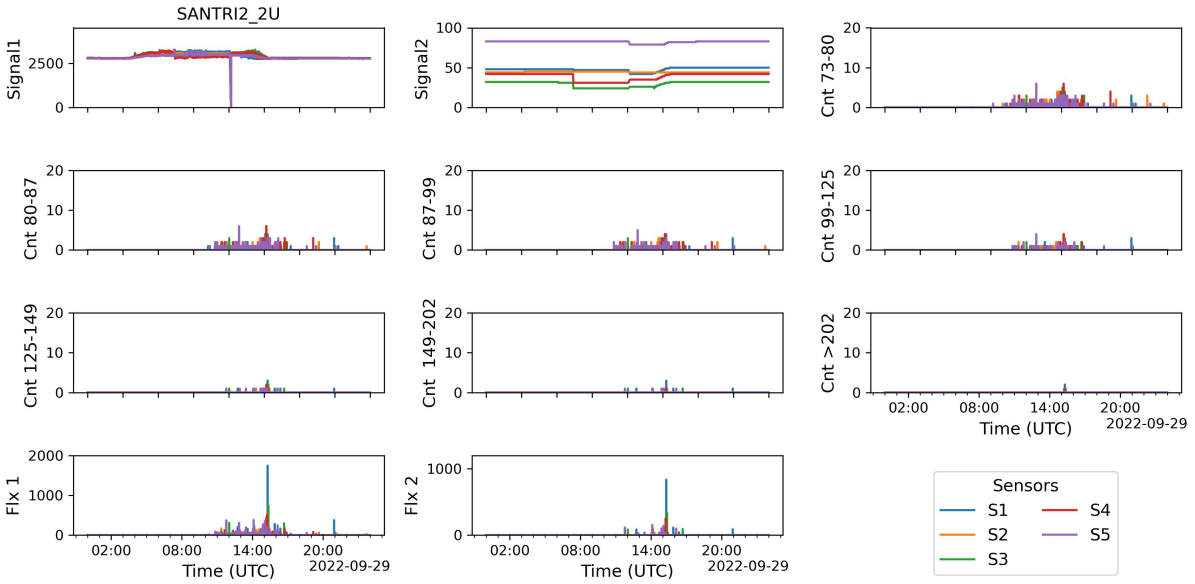

Figure 4.10.: Parameters measured by SANTRI2_2U during 29 Sep. with colors corresponding to the 5 sensors of each unit. The parameters are: Signal 1, Signal 2, and counts (Cnt xx-yy) for the expected bin ranges in µm in an ascending order in all 7 sensors, as well as Flux 1 and Flux 2.

numbers in the counts (without similar values in the surrounding period); and in Fidas, Welas, and CDA, outliers can arise from misclassification errors, where particle counts are incorrectly assigned to adjacent bins. These discrepancies in PSD underscored the necessity of correcting such outliers to ensure the accuracy and reliability of subsequent statistical analyses. This step was crucial for uncovering trends and patterns in the data. To address outliers and harmonize measurements between instruments, various correction methods were applied as described in the following. Outliers were identified and removed in the SANTRI2, UCASS, and, to a lesser extent, in the Welas and CDA data as described in the following.

SANTRI2 outlier correction: Since the SANTRI2 is an open-path instrument, its sensors are directly exposed to environmental factors such as sunlight, shadows, light reflections from nearby metal, and dirt. This exposure can result in artifacts in the data counts in different bins. Additionally, fluctuations in light source intensity may be misinterpreted by the sensors as particles in the air. Outliers in the SANTRI2 data were first identified during the Iceland campaign, providing the basis for the development of the correction methods applied in this study. While the data collected in Iceland proved valuable for understanding instrument behavior under high-latitude dust conditions, the SANTRI2 setup during that campaign was limited to three size bins, with the upper boundary of the largest bin remaining undefined. As a result, no detailed PSD could be retrieved from SANTRI2 data alone. However, by applying the outlier correction techniques developed here and combining SANTRI2 measurements with data from other aerosol spectrometers used during the Icelad campaign, a broad PSD can be reconstructed, though not continuous with a large gap in the super-coarse and giant particle range. This approach could enable the characterization of the PSD at a high-latitude dust source and contributes to closing existing observa-

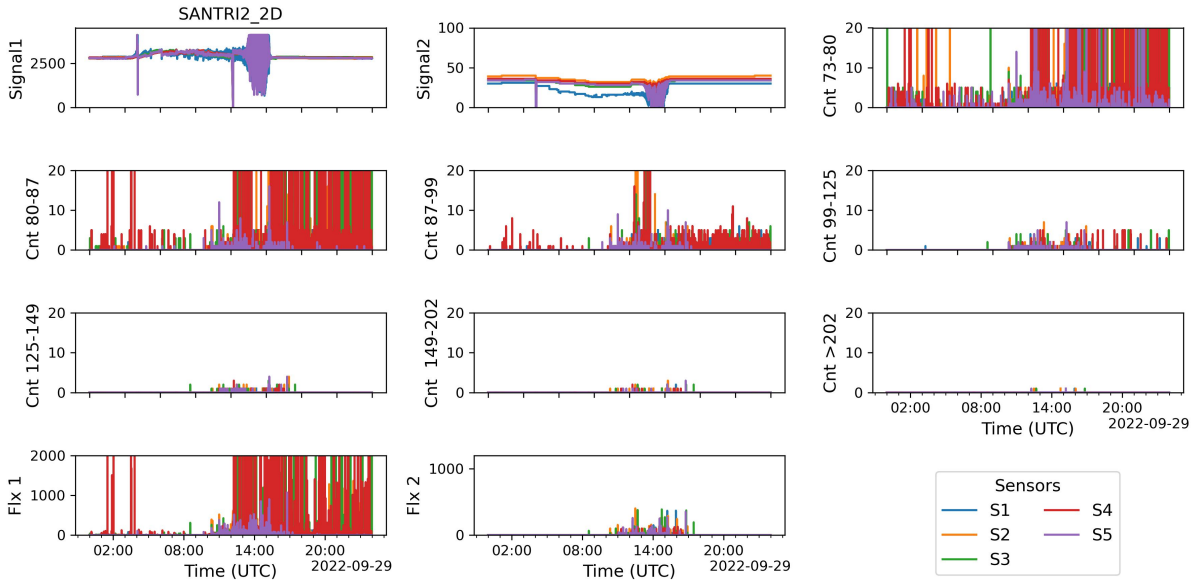

Figure 4.11.: SANTRI2_2D quantities during 29 Sep. with colors corresponding to the 5 sensors of each unit. The quantities are: Signal 1, Signal 2, and counts (Cnt xx-yy) for the expected bin ranges in µm in an ascending order in all 7 sensors, as well as Flux 1 and Flux 2.

tional gaps in this understudied region in the future. Due to the limitation to three size bins and missing upper size limit, I focus exclusively on the data collected during the J-WADI field campaign.

During the J-WADI campaign, both SANTRI2 upfacing units (2U and 4U) exhibited more daytime peaks than nighttime peaks and generally reported fewer counts compared to SANTRI2_2D and 4D, which displayed less systematic behavior with more disordered and ubiquitous high peaks and more counts in general (compare Fig. 4.10 and 4.11). The behavior of the upfacing units (SANTRI2_xU) reflects the observations made by other instruments that dust concentrations during nighttime were generally lower due to calm winds. To better understand this behavior, I investigated whether the elevated counts in the downward-facing SANTRI2 units were due to their orientation toward the light. Consequently, between 13:08 UTC on 19 September and 16:30 UTC on 21 September, the upfacing units were inverted for testing so that they faced downward. No direct correlation was observed between turning the unit and corresponding counts in 2U and 2D. During this period, counts in SANTRI2 2D changed but not immediately after turning the unit (16:08 local time = 13:08 UTC) and persisted even after turning the unit back, suggesting no significant impact. With increasing bin size, outliers became less pronounced, with most outliers disappearing in the 99–125 µm bin (Fig. 4.10 and 4.11). This reduction in outliers may stem from higher noise sensitivity in smaller bins, where the corresponding voltage levels are relatively low. Although noise decreased for larger bins, the downward-facing units still show numerous unrealistic outliers, especially in the smaller bins, and also unrealistically high counts in the larger bins. Consequently, I decided to exclude the downward-facing units from the analysis, as these outliers do not appear to arise from misdirected light reflections but rather from other hardware or software issues.

For the remaining two units, the outliers detected in SANTRI2 data were managed by applying a filter based on comparison between counts registered at the different sensors and outlier statistics and I applied the following steps: (1) time periods of instrument cleaning were removed from the data entirely; (2) I excluded sensors across all bins for the time frames which included highly unrealistic counts exceeding on average four times those recorded by other sensors; (3) Sensor 1 of SANTRI2_4U was removed entirely from the dataset due to persistent unrealistic behavior. After these initial steps, additional outliers were identified and removed using a statistical comparison with measurements of other sensors of the same and of other SANTRI2 devices. The comparison was applied to all data points at their original 1 Hz frequency as discussed below:

I: Intra-Sensor and Intra-Instrument Comparison (Bins and Flux) of the SANTRI2

1. Signal 1 recorded by SANTRI2 corresponds to the voltage obtained by the photosensor. I removed counts which were outside the signal range 2750 to 3250 mV.
2. Signal 2 is the indicator of IR-led light source intensity required to keep the detector (Signal 1) in the range from 2500 - 3500 mV. I did not see any abnormal behavior here for the remaining two units.
3. The flux recorded by SANTRI2 (Fig. 4.11) is proportional to the cross-sectional area (Flux 1 over all bins, Flux 2 only the upper 3 bins) of all particles recorded in the corresponding time. Visual inspection of the time series suggests that Flux 1 values above 1000 may be unrealistic and potentially indicative of measurement error. Therefore, data points for which Flux 1 surpassed this threshold were removed.
4. For a given time step in which a count in the smallest bin was significantly higher than its surrounding counts and which exceeded a predefined threshold, the counts in all bins were set to `NaN`. I considered these counts outliers, as observing numerous giant particles in one second and much fewer in the next was deemed unrealistic. This procedure was applied using two methods:
   a) **Localized Spike in Sum**: An outlier was flagged if the sum of the surrounding 30 data points was at least ten times higher than the sum of the 300 data points around them. Additionally, individual counts were only removed (set to `NaN`) if their value exceeded 2, to prevent the removal of valid low-magnitude data. The correction procedure is shown in Fig. 4.13.
   b) **Local Anomaly in Individual Counts**: An individual count was considered an outlier if it was at least ten times higher than the sum of the surrounding 180 data points ($\pm$90). This method aimed to identify sharp, localized spikes in the data that significantly deviated from their immediate surroundings. The correction procedure is shown in Fig. 4.12.

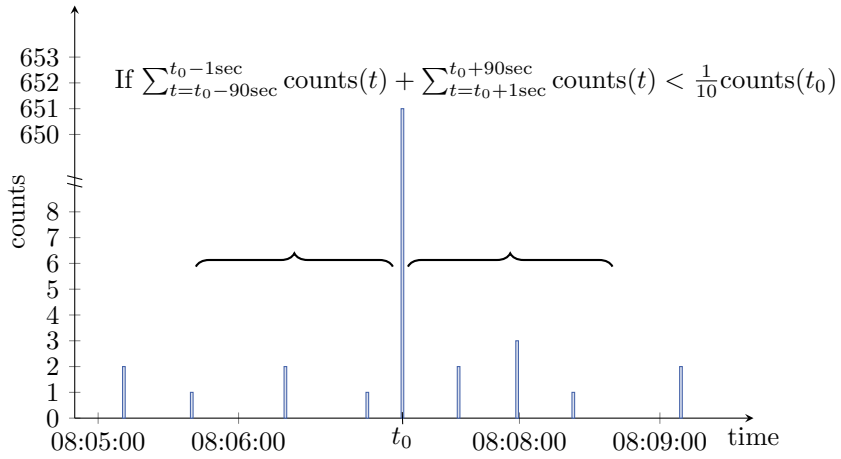

Figure 4.12.: SANTRI2 outlier correction I.4a

II: Inter-Sensor and Inter-Instrument Comparison of the SANTRI2

1. I averaged counts over 3600 points (1 hour, running mean) in the 73-80 µm bin (first bin) and compared it to the mean of the same bin for all other sensors of the two units. If the mean of the 73-80 µm bin was more than 10 times higher than the averaged counts from all other sensors, I set the corresponding count in all bins of the unit under test to `NaN`. Additionally, individual counts were only removed if their value exceeded 3 to prevent the removal of valid low-magnitude data (arbitrary threshold).

The thresholds and time windows for these methods were chosen based on exploratory analysis, as there is no defined standard for identifying outliers in data for such large particles. While somewhat arbitrary, these parameters effectively removed unrealistic spikes without eliminating data I considered realistic based on observatory analysis and in comparison with other instruments.

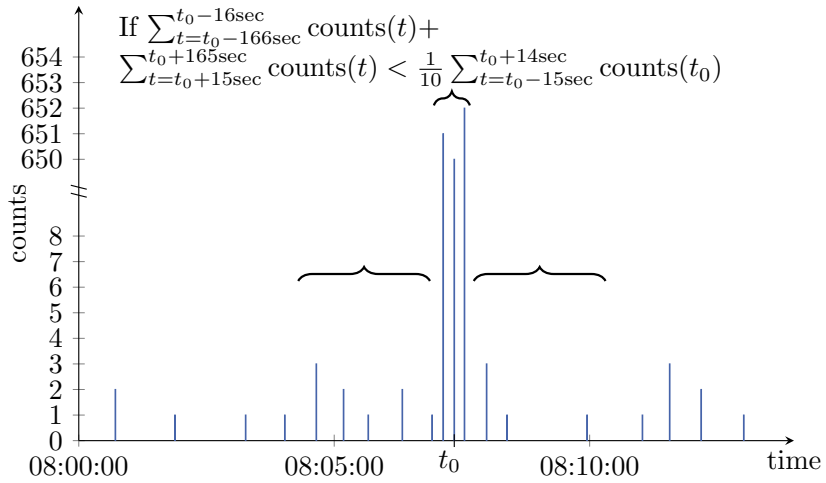

Figure 4.13.: SANTRI2 outlier correction process I.4b

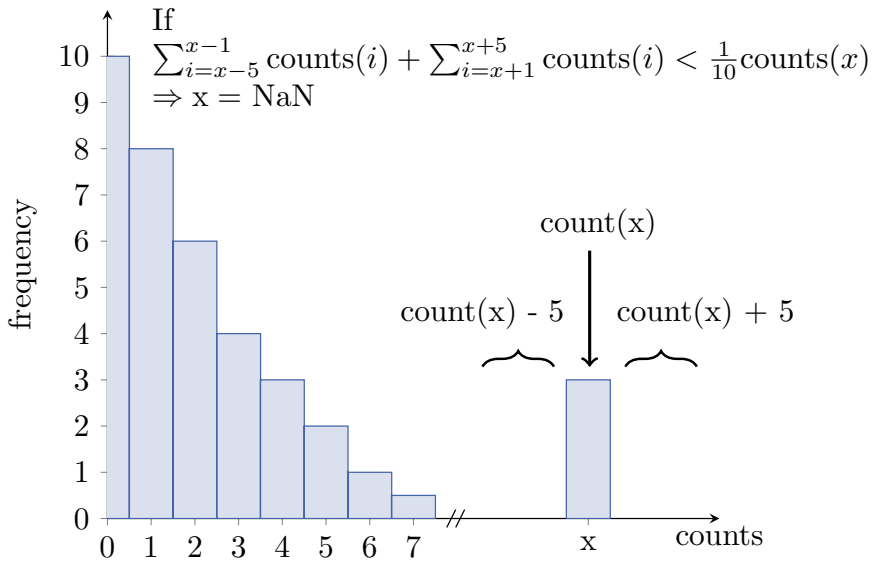

Figure 4.14.: Outlier correction method for UCASS.

UCASS outlier correction: Although the electronics of the UCASS were protected from ambient light by a housing (Fig. 4.5), some light could still enter through the cylindrical opening but this did not result in systematic outliers.

However, I observed a large number of counts with recurring values, such as 243, 512, 514, and 65535 ($2^{16}-1$) but also others. The value 65535 corresponds to $2^{16}-1$, which is the maximum value that can be recorded using a 16 bit variable. However, since the UCASS records data using 12-bit variables, the occurrence of this value indicates an anomaly, specifically suggesting occasionally faulty communication between the UCASS and the Raspberry Pi. Those recurring values were removed from the data. For the remaining data, I used the probability density function of the counts as the basis to remove other recurring count values as outlined below. Firstly, for each instrument, I created a count distribution of detected values for all particle size bins. The maximum observed value in each size bin was determined, and a complete range of integer values up to this maximum was generated. The actual frequency of occurrence for each integer value was then compared against this range, with missing values set to zero. To identify outliers, each detected value was assessed based on its local neighborhood as exemplarily shown in Fig. 4.14. Specifically, for each value, the sum of occurrences in the five preceding and following integer bins was computed. If this sum was less than one-tenth of the observed value, the value was flagged as an outlier. Once the outliers were identified, a thresholding step was applied to remove only those outliers exceeding a minimum value of 2 (as counts of 1 and 2 differed significantly). These flagged values were replaced with `NaN` values. Consequently, I excluded these values from the analysis.

Welas, Fidas, and CDA outlier correction: The concentrations of the CDA differed significantly in some aspects from that of other instruments as outlined in Sect. 5.2. For the CDA, some data gaps from a few seconds to several minutes were observed, which were possibly due to coincidence, *i.e.*, too many

particles in the measurement volume to be analyzed. Due to these data gaps, the averaged measured number of particles likely deviates from the true one. To reduce time periods were this issue was occurring, the smaller bins were successive removed which lead to a decrease of these periods. To analyze the periods were these gaps occurred, several approaches were tested. Even though they are technically no outliers, I list them here. First, I analyzed the time series of pulse lengths and checked if they were in line with the one from the Welas. Second, I compared the CDA data with Welas measurements by removing periods where no data were recorded in the CDA. Third, I examined the flow in the CDA to check for potential pump malfunctions. For all these approaches, I found no connection between these issues. Forth, I compared the number of particles obtained from `.promo` files with that of single-particle data to determine whether the manufacturer's algorithm applied any data correction methods in this format. Although both datasets were largely consistent, small discrepancies were identified, yet they did not provide a solution to the observed data gaps.

In addition to the data gaps in the CDA, there were almost no detectable outliers in Welas, Fidas, and CDA, except that occasionally, they measured counts for large d_p, but not in the smaller sizes. For instance, occasionally, they measured ten counts in a size range $d_p > 60\,\mu m$ but none for $40\,\mu m < d_p < 60\,\mu m$ in a 15 minutes time interval. For Welas and CDA, I applied a filtering criterion for particles larger than $10\,\mu m$, where I removed counts if particles were detected in one size bin but not in the preceding, smaller size bin. This criterion was applied to the integrated size distribution, where approximately eight raw bins were combined, over the 15-minute averaging intervals. Such outliers could arise due to re-entrainment in the inlet, which can lead to inaccurate size measurements, inconsistent particle sampling or wrongly interpreted light scattering.

4.4.3. Conversion from optical to geometric diameter[5]

By deriving the geometric diameter for Welas, CDA, Fidas, and SANTRI2 assuming biaxial ellipsoids, I make the measurements more tailored to dust and the PSDs of the different instruments comparable (Fig. 4.15).

Fidas, Welas, and CDA: Optical diameters for Fidas, Welas, and CDA were converted into geometric (volume-equivalent) diameters by following the approach proposed by Huang et al. (2021) that was implemented in González-Flórez et al. (2023) for the same Fidas instruments as used in this work. I assumed an average complex refractive index (CRI) for the Middle East (1.53 - 0.0011i) from Di Biagio et al. (2019), and a prolate biaxial ellipsoids shape for the dust particles with an aspect ratio (AR, length-to-width) of 1.49, which were obtained from the median diameter from the physical samples introduced in Sect. 4.5. In this diameter conversion procedure, I made use of the single-particle scattering calcula-

[5]Dr. Jerónimo Escribano (Barcelona Supercomputing Center (BSC), Barcelona, Spain) provided the transformation from optical to geometric diameter for the Fidas, CDA, and Welas.

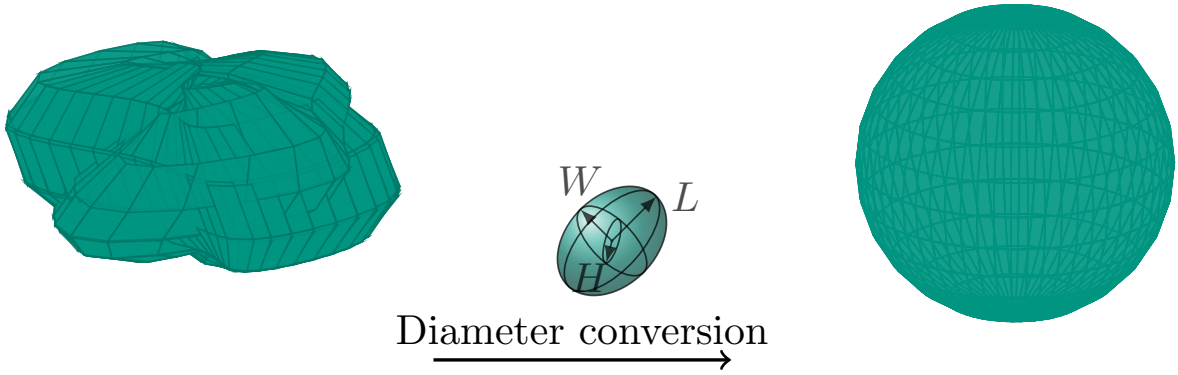

Figure 4.15.: Conversion from measured to geometric diameter. The irregular particle (left, exemplary) is approximated by an ellipsoid to retrieve the geometric diameter (the diameter a sphere with the same volume would have).

tions for biaxial ellipsoids from the Gasteiger and Wiegner (2018) database in this diameter conversion procedure.

It is important to note that dust is assumed to be highly irregular and would be better approximated by triaxial ellipsoids (Huang et al., 2020). However, the triaxial approach is only possible up to ~50 µm diameter of PSL (80 µm dust) for the database of Meng et al. (2010). They indicate a larger size in their work, but this is only for the best case (i.e., spheres). The more the HWR deviates from unity, the more the maximum size possible decreases.

In Fig. 4.16, I compare the resulting geometric diameters (1) assuming biaxial ellipsoids with an aspect ratio of 1.49 (y-axis) and (2) assuming triaxial ellipsoids with the default optical diameters from PSL (x-axis). This shows that optical diameters of PSL tend to underestimate the sizes of biaxial dust particles, particularly for larger particles. In contrast, the transformation for smaller particles is minimal, which can be attributed to the combined effects of dust asphericity and the refractive index.

SANTRI2: To determine the ratio of the volume-equivalent diameter d_{geo} to the projected-area diameter d_{PA}, the following equation was used:

$$d_{geo} = d_{PA} \cdot \sqrt{\mathrm{AR} \cdot \mathrm{HWR}} \cdot \left(\frac{3}{\mathrm{AR}^p + \mathrm{HWR}^p + (\mathrm{AR} \cdot \mathrm{HWR})^p} \right)^{\frac{1}{2p}}. \tag{4.8}$$

In this equation, p is a shape-dependent exponent given by:

$$p = \frac{\log(3)}{\log(2)}. \tag{4.9}$$

This equation was derived based on the surface area of spheres and triaxial ellipsoids, providing a geometric approximation of the relationship between the volume-equivalent and projected-area diameters. For the main analysis, I assumed that mineral dust particles can be approximated as biaxial ellipsoids,

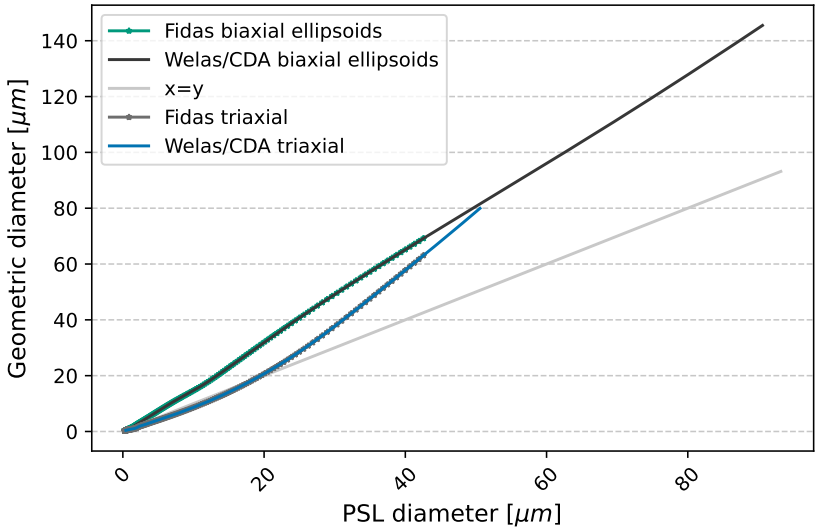

Figure 4.16.: Conversion from optical (retrieval for PSL, x-axis) to geometric diameter (biaxial/triaxial ellipsoids, y-axis) for Welas, Fidas, and CDA.

meaning they exhibit two equal axes and one distinct axis. For $AR = 1.49$ and $HWR = 1$, I computed the ratio d_{geo}/d_{PA} as

$$\frac{d_{geo}}{d_{PA}} = \sqrt{1.49 \cdot 1} \cdot \left(\frac{3}{1.49^p + 1^p + (1.49 \cdot 1)^p} \right)^{\frac{1}{2p}}. \tag{4.10}$$

which led to

$$\frac{d_{geo}}{d_{PA}} \approx 1.055. \tag{4.11}$$

This result provides an estimate of the conversion factor between the volume-equivalent and projected-area diameters, which is essential for relating different measurement techniques in aerosol and dust research. The assumption of biaxial ellipsoids aligns with the assumption for the Fidas, Welas, and CDA. For a more accurate analysis, triaxial ellipsoids should be considered with a HWR-ratio $\neq 1$.
For the UCASS, no conversion to geometric diameter could be performed as no conversion table was provided for these analyses.

4.4.4. Rebinning method for harmonizing and comparing PSDs

To create a unified PSD covering the entire size range out of the two SANTRI2 (with 5 sensors each), the two Welas and the two Fidas instruments (2 and 4 m height), data of these instruments were combined by aligning overlapping size bins. Due to high inconsistencies in two SANTRI2 units (high noise level), the UCASS (oscillation) and CDA (decrease for $d_p > 20\,\mu m$) data, I excluded them from the analysis (for more detail see Sect. 5.2). To harmonize the PSD from different instruments and enable averaging into a single PSD, I applied a rebinning method that calculates bin-weighted averages. Due to differences in the operational size ranges of these instruments, I included the data of the encompassed instruments only

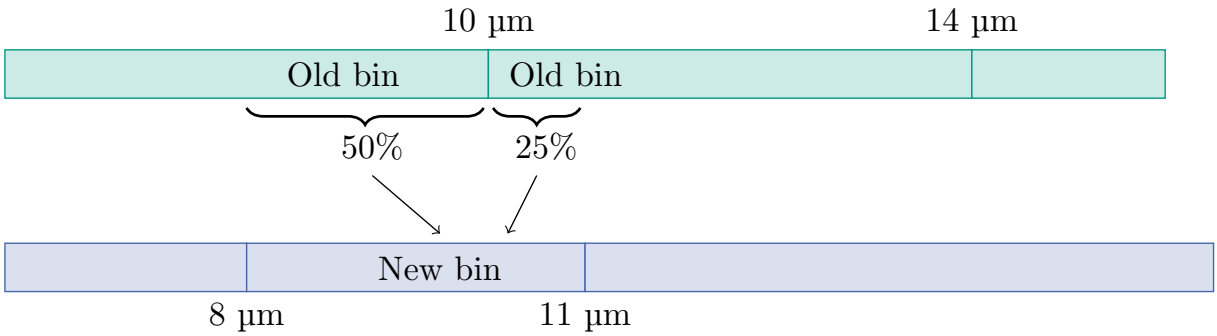

Figure 4.17.: Rebinning method: The old bins (top) are resorted based on the fraction of the old bin that overlaps with the new bin assuming uniform distribution.

above specific size thresholds to avoid inaccuracies near the boundaries of their measurement ranges to obtain an average PSD. For the Welas, data were included from $d_p > 1.5\,\mu m$, for the Fidas from $d_p > 0.5\,\mu m$, and for the SANTRI_xU from $d_p > 80\,\mu m$.

The rebinning method interpolates measurements from the original (old) bin edges to a common set of target (new) bin edges. For each time step, I calculate the contributions of the old bins to the new bins by determining the overlapping bin widths. Specifically, the method computes a bin-weighted average by considering the fraction of the old bin that overlaps with the new bin, weighted by the corresponding particle concentration. This approach accounts for both constant and varying (such as for SANTRI2) bin edges over time, allowing flexibility for instruments with differing size classifications (Fig. 4.17). In cases where no overlap exists between old and new bins, or where contributions to a specific new bin are entirely invalid (*e.g.*, `NaN` values), the resulting value is set to `NaN`. The method ensures that all instruments' outputs are harmonized to a consistent set of size bins, which allows for intercomparison and averaging of the PSD. For some analysis steps (e.g. comparison to other studies or the comparison of different time steps), to make the averaged PSDs' shape from different time steps comparable, they are normalized over a certain diameter range (Sect. 4.4) so that the integral is equal to 1 in every time step. The rebinning method described above was also applied to compare the J-WADI data with results from other field campaigns and was normalized according to the approach outlined by Formenti and Di Biagio (2024).

4.4.5. Intercomparison and bias correction

To establish a baseline for identifying and quantifying systematic differences between the instruments, intercomparison measurements were conducted at the end of the campaign. From 2 October to 5 October, 2022, at the end of the J-WADI measurement period, Welas, Fidas, CDA, and UCASS were installed in close proximity to each other at ~2 m height for comparative analysis. The SANTRI2 units were mounted also next to each other on the ground and vertically, i.e. in their standard setup, to capture more large particles, now transported in saltation. This substantially increased the number of particles they

registered and enabled a more robust statistical comparison. Even though particles were measured in this time period, unfortunately, there were no notable dust events, which posed limitations to the comparative assessment. In this section, I describe three procedures applied to correct for systematic errors.

Systematic x-axis (diameter) correction of the Welas

During the measurement period, the Welas_2m instrument often recorded lower number concentrations than Welas_4m across the full measured size range, especially towards larger sizes. Often, no large particles were measured for Welas_2m but for Welas_4m while their overall shape remained similar. This observation was contrary to expectations, as concentration are supposed to decrease with distance to the source. This trend persisted during the intercomparison period, when both instruments were positioned at the same height. While the Fidas instruments displayed higher concentrations at 2 m compared to 4 m, the Welas instruments did not follow the same pattern. Instead, Welas_4m typically measured higher concentrations than Welas_2m, except for certain nighttime periods, where Welas_2m showed comparable or slightly higher concentrations. To investigate possible explanations for these discrepancies, the influence of wind direction and speed was analyzed by comparing the relative occurrences of Welas_2m exceeding Welas_4m and vice versa. However, no significant dependency on wind conditions was identified.

Additionally, the flow, temperature, and pressure of both instruments were examined, but no clear correlation with the observed differences was found. Cross-correlation analysis between the two Welas instruments was also performed, but it did not reveal a conclusive reason for the unexpected differences in number concentrations.

The Welas instruments utilize a light source with a guaranteed lifespan of 400 hours. Beyond this period, the light spectrum, and therefore also the bin classification, may shift, which I suspect occurred for Welas_2m. During the campaign, the Welas lamps were not exchanged. I assume that degradation of the lamps due to their limited nominal lifetime may have led to a gradual shift in bin classification toward smaller bins over time. Such an effect was likely the cause of the lower number size distributions for the Welas_2m data, which matches with the observation of similar shapes of PSD but lower concentrations in the Welas_2m. To correct this bias, I sought a method to transform the x-axis (bin diameters) of

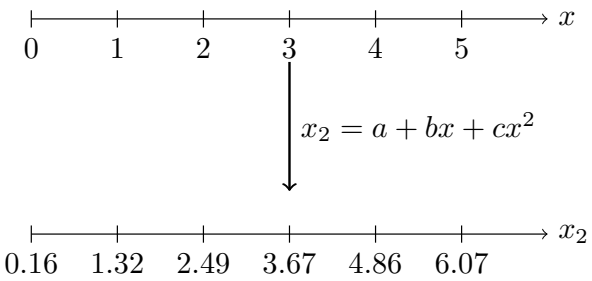

Figure 4.18.: Systematic correction of the Welas by applying a quadratic function on the bin boundaries.

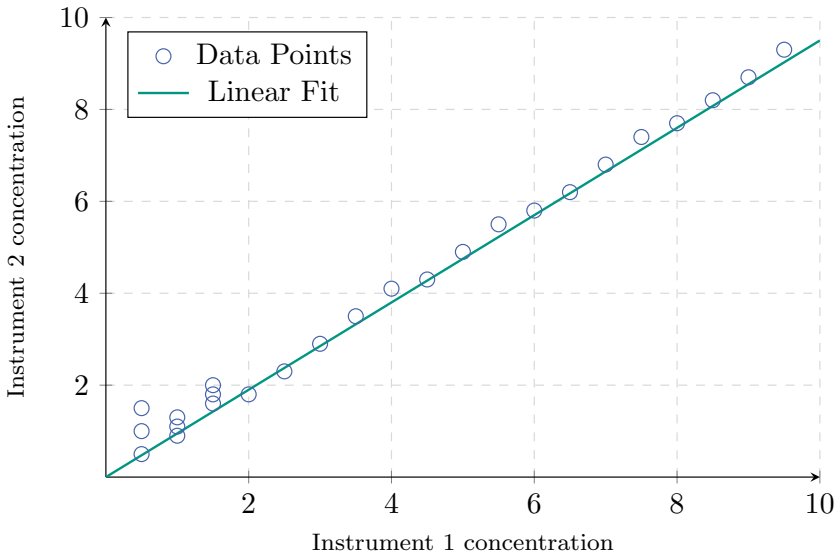

Figure 4.19.: Bin-wise correction via linear regression. For SANTRI2, Fidas, and Welas, for each bin, a linear regression between the number concentration is applied in order to correct their systematic biases between instruments of the same type.

the PSDs by analyzing data collected during the intercomparison period, where both Welas instruments measured next to each other at the same height.

From this analysis, I identified a quadratic relationship of the form $a+bx+cx^2$ to correct the bin boundaries, with the parameters $a = 0.16$, $b = 1.15$, and $c = 0.006$. This correction approach was implemented by optimizing the diameter-wise alignment of the size distributions using data from both instruments (Fig. 4.18). The optimization minimized the discrepancy between the two instruments by comparing the linearly interpolated concentration of Welas_2m with the observed values of Welas_4m across their overlapping size ranges. To account for the influence of larger particles with smaller number concentrations, I weighted the diameter-values using x^2, which further improved the alignment for super-coarse and giant particles. The correction parameters were determined using a global optimization routine, specifically the differential evolution algorithm (SciPy's differential evolution algorithm). By applying this correction to the Welas_2m data, I observed an improvement in the correlation between the size distributions of the two instruments. The Pearson and Spearman correlation coefficients and the Kolmogorov-Smirnov statistic were calculated to evaluate the alignment, showing an increase in agreement after applying the correction (Original Spearman Correlation = 0.978/Scaled Spearman Correlation = 0.987, Original Kolmogorov-Smirnov = 0.161/Scaled Kolmogorov-Smirnov = 0.139). The correction function $a+bx+cx^2$ with the corresponding parameters were then applied to the original bin diameters of Welas_2m.

Systematic error correction via linear regression of Welas, Fidas, and SANTRI2

For instruments of which more than one device was used, such as Fidas, Welas, and SANTRI2, I applied bin-wise linear regression corrections to the counts to eliminate systematic biases between devices of the same type. This approach follows the methodology outlined in González-Flórez et al. (2023) and Dupont et al. (2024). The average dust concentration in each 15-minute bin from one instrument was compared to the corresponding values from the other aerosol spectrometer of the same type. The systematic correction parameter, λ_i, for each bin i, was calculated as the slope of the regression between the concentrations of the compared instrument bins:

$$c_{oc}(d_i) = \lambda_i c_r(d_i), \tag{4.12}$$

where d_i represents geometric mean of upper and lower boundaries for bin i, c_r the concentration from the reference instrument and c_{oc} the concentration from the instrument to be corrected. A $\lambda_i > 1$ indicates that the concentration of the reference instrument is lower, and $\lambda_i < 1$ indicates that the concentration of the reference instrument is higher. A perfect match would yield a correction factor of one. The corrected concentration (c_{om}) was then obtained as:

$$c_{oc}(d_i) = c_{oc}^{\text{uncorr.}}(d_i)/\lambda_i. \tag{4.13}$$

The correction parameter obtained during the intercomparison period was applied to the entire measurement period. The Pearson correlation coefficient r was used to assess the correlation between the instruments. At correlations less than r =0.6, no correction was applied as I assumed this correlation to be too low to represent a meaningful relationship. For the Welas, only a few data points existed above $d_p > 45$µm with low mass concentrations, with many values being 0 in one instrument and small number in the other. Therefore the concentrations across the last bins ($d_p > 45$µm) were averaged and treated together. This procedure was implemented for the different instrument types. Here, Fidas_4m, Welas_4m, and SANTRI2_2 m served as the reference, while Fidas_2m, Welas_2m, and SANTRI2_4 m were corrected and adjusted by the slope determined from the linear regression. The issue of unrealistically large numbers of counts in some bins of the SANTRI2 persisted during the intercomparison period for the SANTRI2s. For correction, I applied the first step of the outlier correction method (Sect. 4.4.2) without adjusting for higher fluxes, as higher fluxes are possible due to SANTRI2 being positioned at ground level.

The retrieved correction parameters λ_i for the different instruments and the corresponding bins (i) are given in Table 4.4, 4.5, and 4.6. For SANTRI2, the sensors closer to the ground (ascending from S1 to S5) and for small bins $\lambda_{i,S}$ were closer to 1, decreasing for sensors in more distance to the ground and larger bins. For the largest bins and the sensors furthest from the ground the correlation was < 0.6, so $\lambda_{i,S}$ was set to 1. For Welas and Fidas, the values were closer to 1, except for Welas $d_i > 45\,\mu$m (= 0.3) and $d_i = 1\,\mu$m (= 0.5).

Table 4.4.: Correction parameter $\lambda_{i,S}$ to bin-wise correct the concentration of SANTRI2_4U (reference SANTRI2_2U). $\lambda_{i,S}$ was set to 1.0 (indicated in red), if the correlation was lower than 0.6. The bins are indicated according to the nominal ranges the developers gave them, as the mean sizes differ slightly for both instruments (Table 4.3).

Sensor	Cnt 73-80	Cnt 80-87	Cnt 87-99	Cnt 99-125	Cnt 125-149	Cnt 149-202	Cnt > 202
S1	0.97	0.97	0.97	0.97	0.96	0.97	0.99
S2	1.05	1.03	1.05	1.05	1.14	1.18	1.2
S3	1.18	1.04	0.86	0.84	0.76	0.69	1.0
S4	0.79	0.61	0.43	0.3	1.0	1.0	1.0
S5	0.45	0.42	0.42	0.19	1.0	1.0	1.0

Table 4.5.: Correction parameter $\lambda_{i,W}$ to bin-wise (i) correct the concentration of Welas_2m (reference Welas_4m). The bins are indicated by the geometric mean of upper and lower bin d_i.

d_i [µm]	1.4	1	2	2.4	2.9	3.6	4.3	5.3	6.5	7.9	9.6	12	14	17	21	26	31	37	>45
λ_i	0.1	0.5	0.8	0.8	0.9	0.7	0.8	0.7	0.7	0.8	0.8	0.6	0.7	0.7	0.8	1.1	1	0.6	0.3

Systematic instrument differences correction via comparison with Fidas_4m

Since all instrument types rely on slightly different measurement principles, harmonizing their outputs is essential to ensure consistent and comparable PSD data. This harmonization minimizes systematic biases and allows for intercomparison across instruments, which is particularly crucial for combining size-resolved dust measurements.

In this study, I use Fidas_4m as the reference instrument due to its reliable performance and broad operational size range, which overlaps to some extent with all other instruments except with the SANTRI2. This makes it well-suited for establishing correction factors for the other instruments. To remove systematic differences between instruments, I applied a constant correction factor relative to the reference instrument after rebinning all instruments to the Fidas bins, as explained in Section 4.4.4. The correction factor for each instrument was obtained by minimizing (SciPy in Python) the squared difference between the instrument's PSD and that of the Fidas_4m during the intercomparison period. The correction factors were determined in a specific size range in which they overlapped with Fidas_4m and which were not too close to the limits of their measurement range. For the Welas, a size range of 2–7 µm was used, while size ranges of 2–10 µm and 4–7 µm were applied for UCASS A and UCASS B, respectively. For the CDA, a size range of 5–10 µm was used. To ensure the statistical robustness of the correction, I calculated the correction factor for every 15 minute time step in the intercomparison period. Then I used a trimmed mean (5% on every end) over the whole time frame for all retrieved correction factors to calculate the scaling factors. The scaling factors obtained were 1.03 for UCASS A, 1.23 for UCASS B, 1.10 for Welas_4m, 1.15 for Welas_2m, and 0.62 for CDA. For the SANTRI2s, no correction factor was applied as they measure outside the Fidas size range.

Following the correction procedures explained in the last sections, the PSDs of all instruments considered for analysis (Welas, Fidas, SANTRI2) could be harmonized. After the initial outlier correction and the

Table 4.6.: Correction parameter $\lambda_{i,F}$ to bin-wise (i) correct the concentration of Fidas_2m (reference Fidas_4m). $\lambda_{i,F}$ was set to 1 (indicated in red), if the correlation was lower than 0.6. The bins are indicated by the geometric mean of upper and lower bin d_i.

d_i in µm	0.36	0.49	0.67	0.92	1.2	1.7	2.4	3.4	4.7	6.4	8.8	12	16	22	30	40
λ_i	0.9	1	0.9	1	1	0.9	0.8	0.8	0.8	0.8	0.9	0.7	0.8	1.0	1.0	1.0

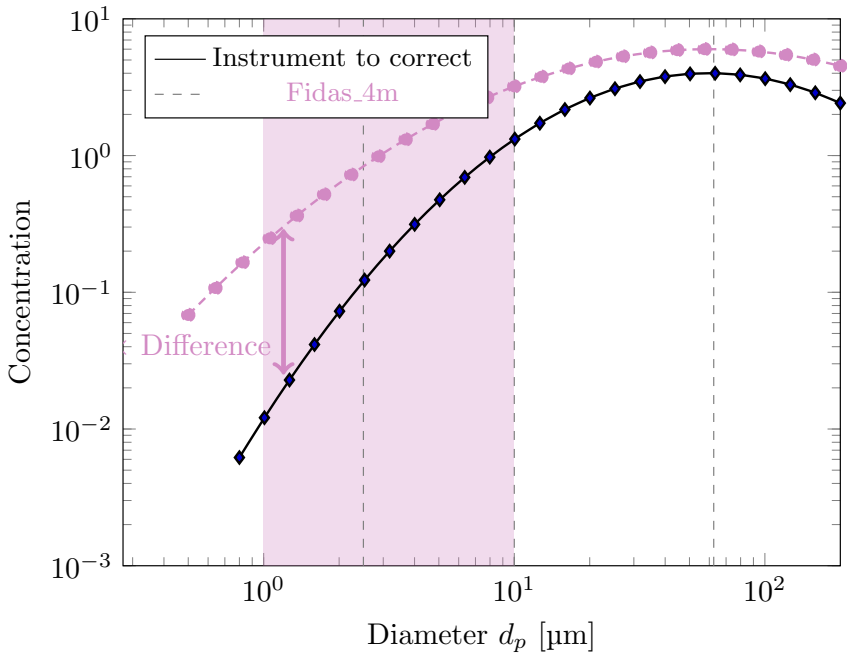

Figure 4.20.: Correction via comparison with Fidas_4m. An optimal factor is retrieved via the optimization of the distance to the Fidas_4m during the intercomparison period.

geometric diameter conversion, all subsequent correction steps based on the intercomparison period were applied as shown in Fig. 4.21, with the applied order indicated by arrows (1 conversion to geometric diameter: SANTRI2, Welas, Fidas; 2 diameter stretching: only Welas_2m; 3 bin-wise linear regression correction: SANTRI2, Welas, Fidas; 4 correction via comparison with Fidas_4m: Welas, Fidas_2m). Each of the methods outlined above was a crucial step in preparing the data for the subsequent analysis of the full PSD directly after emission. Moreover, they provide a transferable framework for future campaigns aiming to investigate the full PSD.

4.4.6. Sampling efficiency

Inlets are critical components of instruments used for aerosol sampling, and they serve the purpose of guiding particles into the measurement system. Aspirating an aerosol sample through an inlet toward a sensor involves several complexities. The sizes of the particles, inlet design as well as wind conditions in comparison to the aspiration airstream inside the inlet determine the occurring particle losses. The sampling efficiency η_{sampling} is used to describe the effectiveness of an inlet system in capturing and

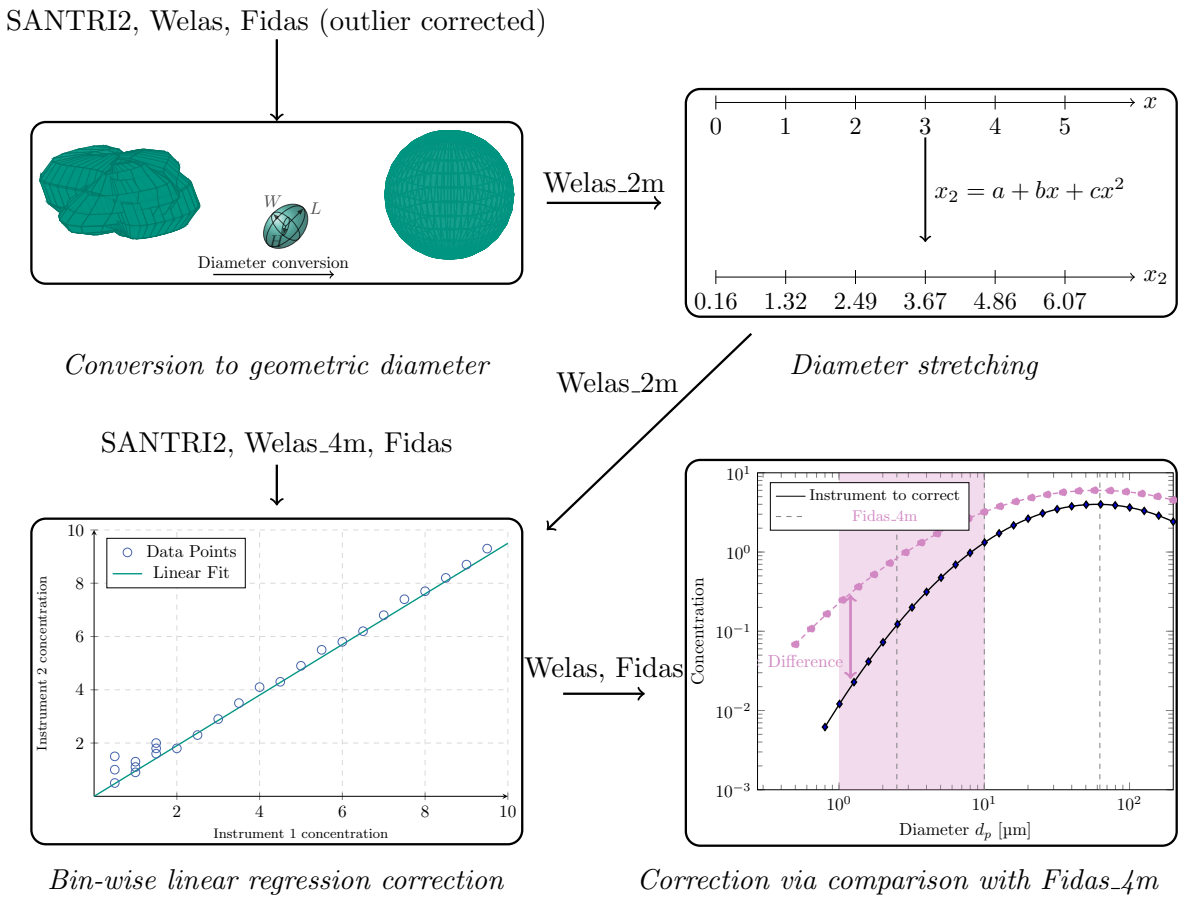

Figure 4.21.: All systematic correction methods applied on the instruments and in the corresponding order: 1) geometric diameter conversion (SANTRI2, Welas, Fidas), 2) diameter stretching (only Welas_2m), 3) bin-wise linear regression correction (SANTRI2, Welas, Fidas), and 4) correction via comparison with Fidas_4m (Welas, Fidas_2m). The sequence in which the correction mechanisms were applied is indicated by the arrows starting after the outlier correction explained in Sect. 4.4.2.

transporting particles from the environment to the measurement chamber. It is defined as the product of inlet and transport efficiencies, η_{inlet} and $\eta_{\text{transport}}$:

$$\eta_{\text{sampling}} = \eta_{\text{inlet}} \cdot \eta_{\text{transport}}. \tag{4.14}$$

When measuring larger particles, such as (super-) coarse and giant mineral dust particles, the choice of inlets can significantly impact the amount of detected particles and is therefore discussed for the different instruments used in this study. These losses are depicted in Fig. 4.22. For this study, especially the losses in the nozzle due to varying flow dynamics outside and inside the inlet, sedimentation, losses in the bend and possibly inertial deposition are of importance as outlined in the following.

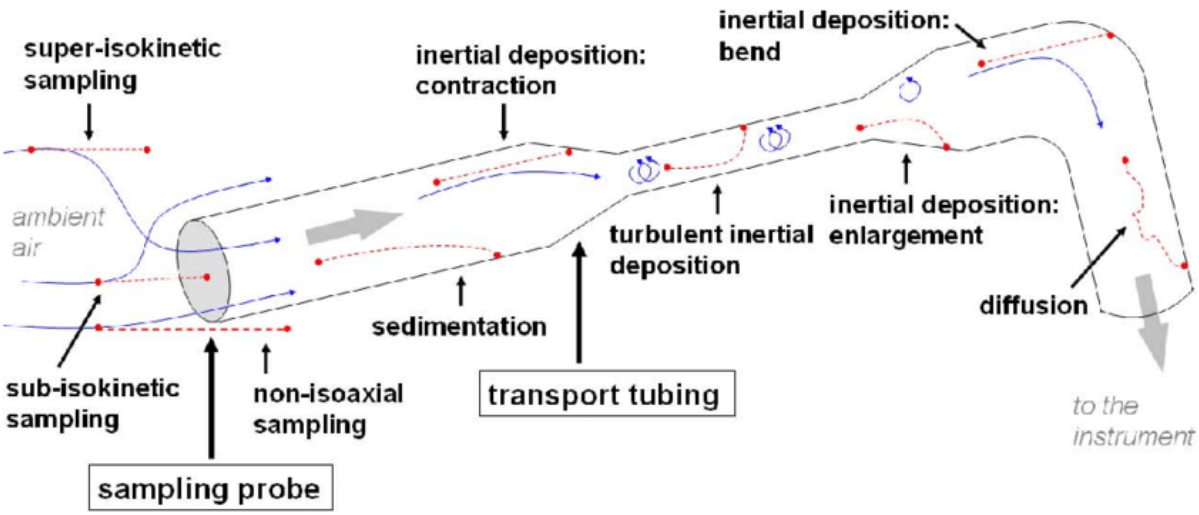

Figure 4.22.: Alteration processes influencing the sampling efficiencies. Figure from Weiden et al. (2009)/ CC BY.

Inlet efficiency

The inlet efficiency (η_{inlet}) is the product of the aspiration and transmission efficiencies, representing the fraction of ambient particles delivered to the sampling system, defined as:

$$\eta_{\text{inlet}} = \eta_{\text{asp}} \cdot \eta_{\text{transm}}. \tag{4.15}$$

For inlets of instruments that actively aspirate air with pumps, *i.e.*, the directional from Fidas and Welas and the Sigma-2 (in other studies used for passive sampling, Waza et al. 2019) inlet of the CDA in this study, measurements suffer from anisokinetic conditions which alter the particle concentration in the nozzle of the inlets compared to the original samples. Super-isokinetic conditions, where the airflow speed in the inlet U exceeds ambient air speed U_0, lead to an underestimation of larger particles. Sub-isokinetic conditions, where the inlet airflow speed U is slower than the surrounding air speed U_0, lead to an overestimation of larger particles. The concentration of particles of given size entering the inlet divided by their concentration in the ambient environment is defined as aspiration efficiency (η_{asp}).
Several studies have investigated sampling from a flowing gas using thin-walled nozzles under various conditions, including isokinetic and anisokinetic sampling in both isoaxial and anisoaxial flows. Summaries of this work are provided by Kulkarni et al. (2011). The developed equations are applied under conditions of constant ambient and sample gas velocities, which are typically much higher than the particle settling velocity, making gravitational effects negligible. Among the various studies, I chose the correlation from Liu et al. (1989) and Zhang and Liu (1989) for the aspiration efficiency (η_{asp}) due to its applicability over a larger Stokes number (Stk) range ($0.01 \leq \text{Stk} \leq 100$) and wind speed range (0.1

$\leq \frac{U_0}{U} \leq 10$) to represent particle sampling under various flow conditions. Aspiration efficiency (η_{asp}) is estimated as:

$$\eta_{\text{asp}} = \begin{cases} 1 + \frac{\left[\frac{U_0}{U} - 1\right]}{\left[1 + \frac{0.418}{\text{Stk}}\right]} & \text{for} \frac{U_0}{U} > 1 \\ 1 & \text{for} \frac{U_0}{U} = 1 \\ 1 + \frac{\left[\frac{U_0}{U} - 1\right]}{\left[1 + \frac{0.506\sqrt{U_0/U}}{\text{Stk}}\right]} & \text{for } \frac{U_0}{U} < 1. \end{cases} \tag{4.16}$$

The transmission efficiency (η_{trans}) is the fraction of aspirated particles transmitted through the inlet (Kulkarni et al., 2011). Inertial transmission losses have been studied by Liu et al. (1989) and Hangal and Willeke (1990). For sub-isokinetic sampling (when $\frac{U_0}{U} > 1$), particles are often deposited on the nozzle walls, resulting in a transmission efficiency of less than 1 (Liu et al., 1989). Liu et al. (1989) proposed the following expression for the inertial transmission efficiency $\eta_{\text{trans,inert}}$ under sub-isokinetic, isoaxial sampling conditions:

$$\eta_{\text{transm,inert,L89}} = \frac{1 + \left[\frac{U_0}{U} - 1\right] \Big/ \left[1 + \frac{2.66}{\text{Stk}^{2/3}}\right]}{1 + \left[\frac{U_0}{U} - 1\right] \Big/ \left[1 + \frac{0.418}{\text{Stk}}\right]}. \tag{4.17}$$

Conversely, Hangal and Willeke (1990) assume no inertial transmission losses for sub-isokinetic isoaxial sampling. For super-isokinetic sampling (when $\frac{U_0}{U} < 1$), Liu et al. (1989) stated that the particle movement is not directed towards the walls, leading to a transmission efficiency of 1.

However, Hangal and Willeke (1990) argue that under super-isokinetic conditions, flow separation occurs at the nozzle inlet, leading to the formation of a constricted jet (vena contracta). This induces turbulence, which enhances particle deposition. They provide the following inertial transmission efficiency for super-isokinetic sampling:

$$\eta_{\text{transm,inert, HW90}} = \exp\left[-75 I_v^2\right], \tag{4.18}$$

where the parameter I_v describes the inertial losses in the vena contracta and is given by:

$$I_v = 0.09 \left(\frac{\text{Stk}}{(U_0/U)^{0.3}} \right). \tag{4.19}$$

Equation (4.17) applies for $0.01 \leq \text{Stk} \leq 100$ and $1 \leq \frac{U_0}{U} \leq 10$ (Liu et al., 1989) and Eq. (4.18) for $0.02 \leq \text{Stk} \leq 4$ and $0.25 \leq \frac{U_0}{U} \leq 1.0$ (Hangal and Willeke, 1990). In this study, I combine the expression for sub-isokinetic sampling conditions from Liu et al. (1989) and for super-isokinetic sampling from Hangal and Willeke (1990) to estimate $\eta_{\text{transm,inert}}$.

A minor issue is that the approximations might not be applicable for calm ($U_0 < 0.5\,\text{m s}^{-1}$) and slow wind conditions ($0.5 < U_0 < 1.5\,\text{m s}^{-1}$) due to an enhanced gravitational force (Kulkarni et al., 2011). I neglect this issue here as I am particularly interested in the large-size range of the PSD, which I assume to be most relevant under higher wind speeds.

Transport efficiency

Transporting the aerosol sample through pipes to the measurement chamber involves bends and other flow elements, with either laminar or turbulent flow. Particle deposition during transport in the pipes can alter aerosol characteristics, influenced by mechanisms such as agglomeration and re-entrainment. These phenomena depend on flow regime, rate, tube size and orientation, temperature gradients, and particle size (Kulkarni et al., 2011). The transport efficiency ($\eta_{\text{transport}}$) for a given particle size is the product of the efficiencies for each deposition mechanism, m, in each flow element, f:

$$\eta_{\text{transport}} = \prod_f \prod_m \eta_{f,m}$$

The different mechanisms and flow elements which lead to transport losses for the inlets considered in this study are explained in the following.

Fuchs (1964) and Thomas (1958) developed expressions for gravitational settling in horizontal tubes with laminar flow. These losses are especially important for the directional inlet due to its horizontal first part. Heyder and Gebhart (1977) extended this to inclined tubes, providing a general correlation for gravitational deposition (η_{grav}) from laminar flow in circular tubes:

$$\eta_{\text{grav}} = 1 - \frac{2}{\pi}\left[2\kappa\sqrt{1-\kappa^{2/3}} - \kappa^{1/3}\sqrt{1-\kappa^{2/3}} + \arcsin(\kappa^{1/3})\right] \tag{4.20}$$

with $\kappa = \varepsilon\cos\theta = \frac{3}{4}\frac{L}{d}\frac{V_{\text{ts}}}{U}\cos\theta$ and $\varepsilon = \frac{3}{4}Z = \frac{3}{4}\frac{L}{d}\frac{V_{\text{ts}}}{U}$ where $\frac{V_{\text{ts}}\sin\theta}{U} \ll 1$ with V_{ts} being the settling velocity, L the length of the pipe element, θ the possible inclination of the element, and d the diameter. This formula applies to various tube orientations and is consistent with experimental results (Kulkarni et al., 2011). It reduces to the case of the horizontal tube when $\theta = 0°$. In vertical tubes, the transport efficiency for gravitational settling is 1 (100%) as particles do not deposit horizontally. Here, V_{ts} is the settling velocity that can be approximated by Stokes settling for small particles. However, as discussed in Adebiyi et al. (2023), this cannot be applied for larger particles. Adebiyi et al. summarize alternative calculations for V_{ts} and I implement Wu and Wang (2006) with a Corey Shape Factor (CSF) of $= 0.8$ (in line with the HWR = 1 and AR = 1.49, I used for the geometric conversions).

Another relevant loss of particles during sampling is the transport efficiency for bends η_{bend}. This is an important part in the directional inlet. I implement a formula based on the experimental work developed in Wang et al. (2024) to calculate η_{bend}, as it shows advantages compared to other experimental data (Pui et al., 1987) and models proposed before (*e.g.*, Pui et al., 1987, *e.g.*, a larger Stokes number range). It is defined as:

$$\eta_{\text{bend}} = \frac{1}{1 + (\text{Stk}/0.17)^{2.73}}. \tag{4.21}$$

Turbulent inertial deposition occurs when large particles, due to their high inertia, cannot follow the curved streamlines of turbulent eddies and are deposited on the walls of a tube. For this study, this is relevant for the UCASS for their large housing diameter (which is similar to the pipe of other inlets) and corresponding high Reynolds numbers but not for the directional inlet in which I assume a laminar flow due to the calculated low Reynolds numbers. This phenomenon is described by the transport efficiency $\eta_{\text{turb-inert}}$ (Kulkarni et al., 2011):

$$\eta_{\text{tube, turb-inert}} = \exp\left(-\frac{\pi d L V_t}{Q}\right) \quad . \tag{4.22}$$

where d is the tube diameter, L is the transport length, V_t is the turbulent inertial deposition velocity, and Q is the volumetric flow rate. Liu and Agarwal (1974) found that the dimensionless deposition velocity (V^+) increases with particle relaxation time (t^+) in the so-called turbulent diffusion–eddy impaction regime and peaks at $t^+ \approx 30$. For larger t^+, deposition velocity decreases in the particle inertia-moderated regime, as reduced turbulence influence allows particles to penetrate the sublayer and deposit directly onto the wall.

The re-entrainment of particles could significantly influence the PSD. To my knowledge, there is no widely accepted approximation for the re-entrainment of particles (Kulkarni et al., 2011). I assume that especially for changing wind conditions and therefore, *e.g.*, a moving directional inlet (Welas, Fidas, or rotating mast) or acceleration in the UCASS, re-entrainment could be a relevant alteration mechanism of the PSD, but this mechanism could not be quantified further. Another effect, the diffusional deposition only becomes relevant for particles $< 0.1\,\mu\text{m}$, and therefore I neglect it here. In addition, the calculation of the pipe enlargement is not included due to inconsistencies in published methods and difficulties in reproducing the reported calculations (Schade et al., 2007).

4.4.7. Impact of topography on the uplift of (super-) coarse particles

Heisel et al. (2021) investigates how gentle topography affects the vertical transport of coarse and super-coarse dust particles in the atmosphere. The study implies that atmospheric dust models need to account for topography effects to accurately represent coarse dust concentrations. The authors suggest that a simple parameterization based on enhanced dispersion due to topography might be sufficient to correct for the underestimation of coarse dust in current models. Aiming to test the hypothesis that elevated terrain might favor the uplift of (super-)coarse particles, an additional UCASS (UCASS E) instrument was mounted on top of a small hill (<100 m) at 4 m height during the J-WADI campaign to explore the influence of topography on the uplift of (super-)coarse particles (Heisel et al., 2021). This unit was mounted on a hill approximately 500 m downwind of the other two units that were installed at the main site (Figure 4.1b). The unit on the hill was configured to cover the same size range as the site-mounted unit UCASS B with only slight differences in geometric mean diameter $d_{\text{UCASS X}}$ of upper and lower bin boundaries (Table 4.7). However, during the intercomparison period, when all UCASS instruments were

operated at 2 m height, UCASS B and UCASS E showed a poor correlation for particles with diameters $d_p > 36\,\mu m$ (Table 4.7). Due to another unresolved general issues for the UCASS, *i.e.*, an unrealistic PSD (Sect. 5.2), which is assumed to stem from a false bin classification, the UCASS data were not included in the combined PSD analysis. Therefore, before this dataset can be used to investigate the influence of topography, the aforementioned challenges, particularly the bin conversion, need to be addressed. Thereafter, the data may still hold potential for future studies, especially for particles $\leq 36\,\mu m$, where the instruments' correlation is good and more particle counts are expected.

Table 4.7.: Correlation coefficients R during the intercomparison period when UCASS B and UCASS E measured next to each other at 2 m height on the rotating mast and mean bin diameters for UCASS B and UCASS E in µm.

Bin	1	2	3	4	5	6	7	8	9	10	11	12	13	14	15	16
$d_{\text{UCASS B}}$ [µm]	–	2.3	3.6	4.7	6	8	10	13	15	19	24	30	36	45	56	70
$d_{\text{UCASS E}}$ [µm]	–	–	1.7	3.4	5	7	10	12	15	19	24	29	36	45	56	70
R	–	–	1	1	1	1	1	1	1	1	0.8	0.7	0.8	0.4	0	0

4.5. Particle sampling and analysis[6]

Dry deposition samplers of a 'flat-plate' type (FPS; Waza et al., 2019; Panta et al., 2023) were used to collect deposited particles directly on pure carbon adhesive substrates (SpectroTabs, Plano GmbH, Wetzlar, Germany) during J-WADI. Briefly, the FPS consists of two circular brass plates, a top plate with a diameter of 203 mm and a bottom plate with a diameter of 127 mm with a distance of 16 mm (Fig. 4.23). Between the plates the wind is channeled and thus turbulence is reduced. A 25 mm aluminum stub is placed in the center of the lower plate with the adhesive surface level with the plate. As a function of wind speed, particles larger than a few hundreds of µm are generally prevented from reaching the sampling surface due to their large settling velocities (Ott and Peters, 2008). The sampler was placed approximately 10 m from the rotating mast and 1.5 m above ground on a tripod. The substrates were typically exposed for 24 hours with some exceptions during high dust loadings (Table 7.2).

Scanning electron microscopy (SEM)

A FEI Quanta 400 FEG ESEM (FEI, Eindhoven, The Netherlands) was used to analyze the morphology, size, and surface features of individual particles by directing a focused beam of electrons onto a sample and detecting the resulting secondary and backscatter electrons (Scanning Electron Microscopy, SEM). The system is operated in a semi-automated way, in which backscatter images are used to detect the particle on the carbon substrate by their higher brightness. For each identified particle, size, shape and an X-ray fluorescence spectrum (using an X-Max 150 energy-dispersive X-ray detector (EDX), Oxford, Oxfordshire, UK) is recorded. The samples were analyzed under high-vacuum conditions without

[6]Prof. Dr. Konrad Kandler (Technical University of Darmstadt, Germany) conducted the Flat-Plate Sampler (FPS) sampling, SEM analysis, and provided the corresponding PSDs.

Figure 4.23.: Flat-plate sampler (FPS) used in the J-WADI campaign, adapted from Ott and Peters (2008). Positioned 10 m from the rotating mast, it consists of two brass plates at a distance of 16 mm and a circular substrate (diameter = 25 mm) in the center of the bottom plate. Figure by TT- Prof. Dr. M. Klose.

pretreatment. An acceleration voltage of 12.5 kV, a beam current of 18 nA, and a working distance of approximately 10 mm were used. Analysis was carried out at two different magnifications (1.28 and 0.16 µm pixel^{-1}). This allowed for the sizing of particles with a minimum projected-area diameter of 0.2 µm at the high magnification. The low magnification enabled the analysis of a large sample area, yielding sufficient counting statistics for larger particles. At higher magnification, analysis locations on the substrates were randomly selected, while at lower magnification the total substrate could be investigated. After the automated analysis, the images were manually inspected for obvious surface defects and the corresponding regions removed from the data (less than 1 % of the surface). Plant fibers found on some samples sized several 100 µm were also disregarded. Also, particles with very low EDX count rates due to shading effects were not included. On average, 3500 particles were analyzed for each sample (min. 1700). The projected area-equivalent diameter, d_{PA}, is derived from a two-dimensional (2-D) projection image of a three-dimensional (3-D) irregularly shaped dust particle with a volume-equivalent diameter d_{geo}. The FPS is expected to collect dust particles in an orientation where their largest surface lies parallel to the collection substrate, meaning the smallest dimension (height H) is aligned perpendicular to the surface (Huang et al., 2021). Consequently, the projected area-equivalent diameter might overestimate the geometric diameter. To convert from the projected area, I assume that all particles deposit in this orientation. In this case, the projected area-equivalent diameter can be approximated as:

$$d_{area} = \sqrt{LW}. \tag{4.23}$$

Thus, the ratio of projected area-equivalent to geometric diameter can be expressed as a function of the aspect ratio ($AR = L/W$) and height-to-width ratio ($HWR = H/W$):

$$\frac{d_{area}}{d_{geo}} = \frac{\sqrt{LW}}{\sqrt[3]{LWH}} = \frac{\sqrt[6]{AR}}{\sqrt[3]{HWR}}. \tag{4.24}$$

This formulation accounts for the systematic overestimation of particle size due to orientation effects in impactor-based measurements. Detection limits were calculated using 2σ of the peak intensity, and a final sorting step was applied to remove particles with low X-ray counts due to shading effects. For details on the procedure, I refer to Kandler et al. (2018) and Panta et al. (2023). Geometric (volume-equivalent) diameters were estimated from the apparent projected area and the particle shape as explained in Appendix 4.4.3.

Deposition velocities to retrieve mass deposition rates

To derive mass deposition rates from the concentration PSDs retrieved from the aerosol spectrometers, assumptions about deposition velocities are required. Because the FPS captures particles that have settled out of the atmosphere, these measurements reflect number deposition rates (in # area^{-1} time^{-1}), not directly the ambient airborne number concentration as for the aerosol spectrometers (in # volume^{-1}). Sedimentation plays a key role in determining the atmospheric lifetime of dust particles. The terminal fall velocity of particles describes the rate at which particles settle onto surfaces and reflects the balance between gravitational and drag forces. Numerous expressions exist to estimate the velocity of particle deposition (*e.g.* Stokes approximation). However, most formulas are poorly suited for super-coarse and giant mineral dust particles ($d_p > 10\,\mu m$) due to their complex aerodynamic behavior, which deviates from Stokes approximation and the idealized spherical shape (Adebiyi et al., 2023). This limitation is compounded by a lack of experimental data to validate their deposition, particularly under natural environmental conditions. Adebiyi et al. (2023) compared several expressions to estimate particle settling velocity and concluded that for $d_p = 450\,\mu m$, which represents the approximate size of the largest particles observed after long-range atmospheric transport (Betzer et al., 1988; van der Does et al., 2018), the measured deposition velocity ranges from approximately 1.5 to 3.5 m s^{-1}. This range aligns with the empirical relationships proposed by *e.g.*, Cheng (1997) and other expressions used in Adebiyi et al. (2023). However, the assumptions underlying the estimates of deposition velocity presented in Adebiyi et al. (2023) may not fully apply to the field conditions. While terminal fall velocity describes the rate at which particles settle under gravitational and drag forces, the actual settling onto the FPS may be influenced by turbulent diffusion outside or inside the sampler which does not have such a strong dependence on particle size (Guha, 2008) and small lifting events before deposition, through, *e.g.*, flow dynamics around the FPS (*e.g.*, the plates) and other instruments. Therefore, the particles might not reach the terminal fall velocity. Consequently, formulas for particle settling velocity, including those reviewed by Adebiyi et al. (2023), might not accurately represent the deposition behavior of the particles. Waza et al.

(2019) and Panta et al. (2023) reported that with none of the traditional deposition velocity expressions the shape of aerosol spectrometer and FPS could be matched, but instead the deposition velocities appeared to have a much lower particle size dependency, i.e., the general shape of aerosol spectrometer concentrations and FPS deposition rates were similar. In this study, I could confirm that none of the formulas could match the shapes of PSDs of FPS and aerosol spectrometer and therefore also assumed a uniform deposition velocity for all particle sizes. A constant deposition velocity of $v_d = 0.0003\,\mathrm{m\,s^{-1}}$ provided the best fit to my data as found by minimizing the mean squared errors.

The methods described in this chapter provide a comprehensive framework for measuring, processing, and analyzing the PSD of mineral dust at an emission source. The combination of multiple aerosol spectrometers with overlapping size ranges, supported by deposition samplers and detailed meteorological measurements, enables a robust characterization of the full size spectrum from fine to giant particles. Key methodological advancements developed during this work include outlier correction routines, bin-wise and intercomparison-based inter-instrument correction, and a rebinning technique to generate consistent PSDs across instruments. These methods contribute directly to the results presented in the subsequent chapter and offer a transferable approach for future measurement campaigns aiming to resolve the full dust size distribution.

5. Results

This chapter provides an overview of meteorological conditions and measured dust mass concentrations during the campaign (Sect. 5.1). Mass concentration PSDs from active dust emission events before and after applying correction methods (Sects. 5.2–5.3) and discrepancies between instruments, including inlet efficiency estimates are discussed (Sect. 5.4). The PSD variability is analyzed in relation to friction velocity and atmospheric stability (Sect. 5.5), followed by a comparison of the aerosol spectrometer PSDs and FPS and SEM results (Sect. 5.6). Finally, I compare my findings with other field measurements (Sect. 5.7). The correction and harmonization procedures developed in Chapter 4 form an integral part of the results presented here, as they enabled the generation of consistent and comparable particle size distributions across instruments.

5.1. Meteorological and dust conditions during J-WADI

The meteorological conditions during the campaign (Fig. 5.1) are characterized by high air temperatures, with mean daily minimum and maximum averages of $\overline{T}_{\text{daily min}} = 18.2\,^{\circ}\text{C}$ and $\overline{T}_{\text{daily max}} = 32.4\,^{\circ}\text{C}$, respectively (Fig. 5.1a). Relative humidity at 4 m height was continuously low, with average daily minimum and maximum averages of $\overline{\text{RH}}_{\text{daily min}} = 20\%$ and $\overline{\text{RH}}_{\text{daily max}} = 61\%$ (Fig. 5.1b). No precipitation was recorded during the campaign. The mean atmospheric pressure during the campaign was 924 hPa, exhibiting a diurnal cycle with the lowest values occurring around 0 and 12 UTC (local time = UTC+03:00 h local time), and two maxima, one around 6 and the other around 21 UTC (Fig. 5.1c).
Local dust emissions predominantly occurred between 12 and 15 UTC at wind speeds of more than about $v_{4\,m} \approx 6\,\text{ms}^{-1}$, with usually north-westerly wind directions (Fig. 5.1 d, e, h, Fig. 5.2). Wind speeds during the campaign were generally relatively low (Fig. 5.2). The 15 minute averaged dust mass concentration time series is shown in Fig. 5.1h. It represents the average of the two SANTRI2 (with 5 sensors on each), the two Welas and the two Fidas instruments (2 and 4 m height), including the correction procedure explained in Sect. 4.4 and in further detail in Sects. 4.4.2-4.4.4. Results obtained with each instrument and more detail on the combined PSDs are presented in Sect. 5.4. Several events with high total mass concentrations ($C_m > 1 \times 10^4\,\mu\text{g}\,\text{m}^{-3}$) were recorded, with significant contributions of particles with diameters greater than 20 µm and also regularly larger than 60 µm. For higher total mass concentrations, typically also more larger particles contributed to the mineral dust mass. The most continuous dust event occurred on 29 September 2022 with intensive dust emission between 10 and 15:30 UTC and high total mass concentrations up to $C_m = 10 \times 10^4\,\mu\text{g}\,\text{m}^{-3}$.

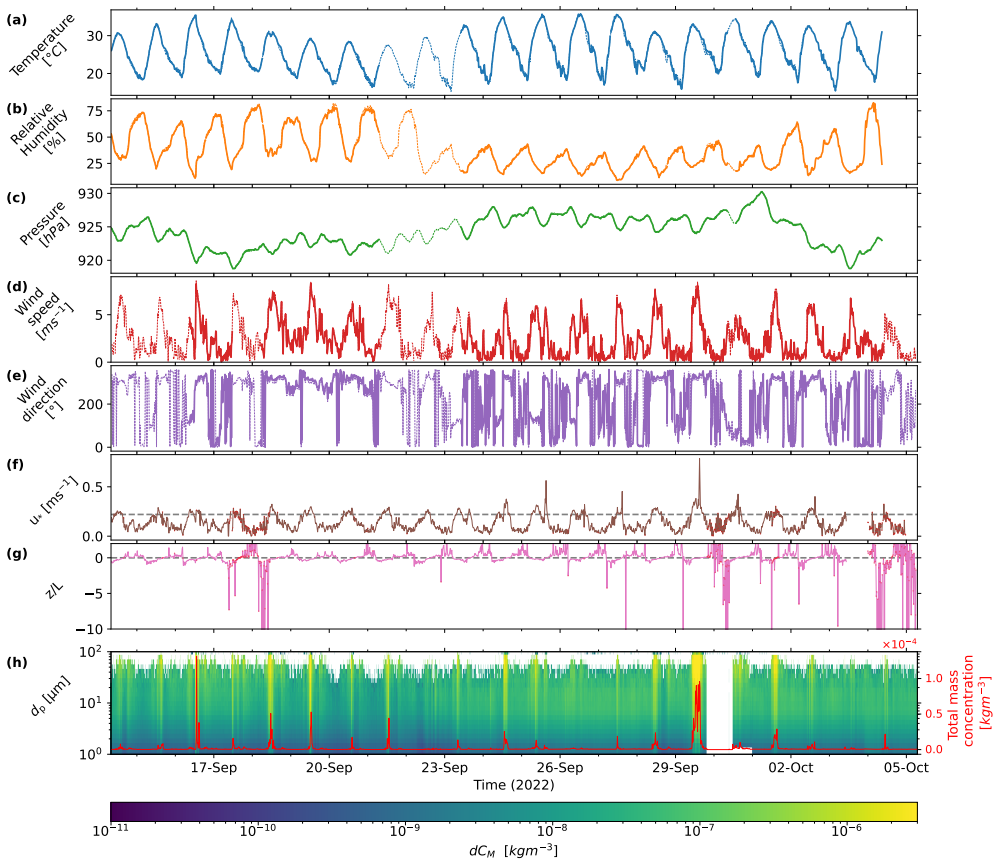

Figure 5.1.: 15-minute averaged meteorological and dust conditions during the campaign. Dashed lines (a-e, mast data) and red dots (f-g, scintillometer data) indicate missing values in the measurements used that were filled with data from other instruments as described in Sect. 4.1. (a) Temperature (4 m), (b) relative humidity (2 m), (c) pressure (1 m), (d) wind speed (4 m), (e) wind direction (4 m), (f) friction velocity u_* from the scintillometer (2.54 m) with the dashed line representing the threshold friction velocity $u_{*t} = 0.22\,\mathrm{m\,s^{-1}}$. (g) Atmospheric stability represented by z/L, where L is the Obukhov length from the scintillometer and z is the reference height 2.54 m. The dashed line represents $z/L = 0$. (h) Particle mass concentration by particle size averaged for Welas, Fidas, and SANTRI2. These data include the corrections explained in Sect. 4.4. Color shading represents the mass concentration in each size bin, whereas the red line indicates the total dust concentration summed over all bins.

I obtained a threshold friction velocity of $u_{*t} = 0.22\,\mathrm{m\,s^{-1}}$ using the Time Fraction Equivalence Method (Sect. 4.2). I note that saltation was occasionally registered already at lower friction velocities as shown in Fig. 5.3 where the flux density from SANTRI4 together with u_* to retrieve u_{*t} is depicted. This discrepancy could be due to intermittent saltation not captured within the 15-min periods used to derive u_{*t}, or localized variations in surface conditions.

During periods when the threshold friction velocity was exceeded ($u_* > 0.22\,\mathrm{m\,s^{-1}}$, typically around noon or in the afternoon in UTC time zone, Fig. 5.1f, gray line), noticeable contributions from particles with diameters (d_p) exceeding 62.5 µm (giant mineral dust particles) were observed. Additionally, several particles > 80 µm in diameter were registered. For unstable and neutral conditions ($z/L \leq 0$), the majority of more intense dust events were observed, particularly during the transition from unstable to neutral

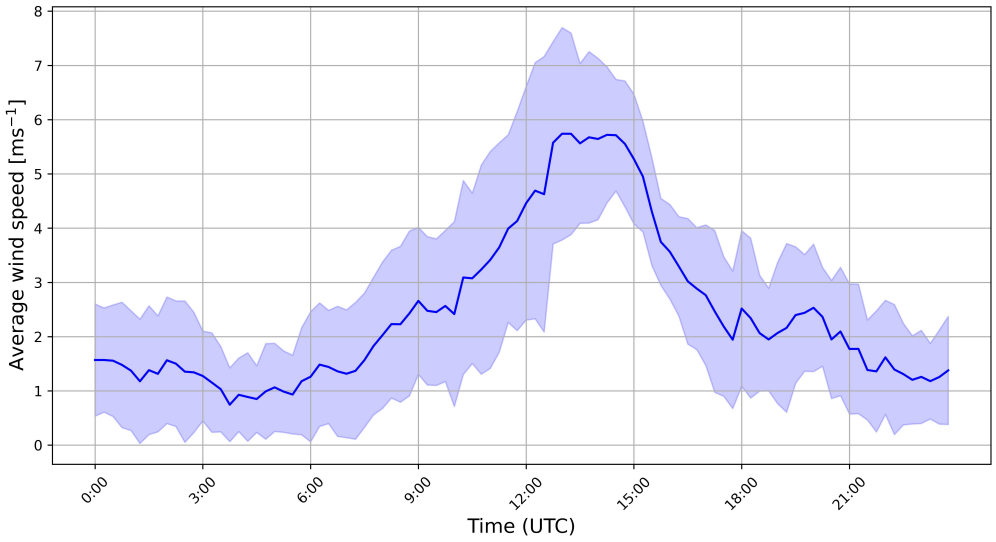

Figure 5.2.: Averaged daily wind speeds during the campaign with shaded areas as standard deviation.

conditions (Fig. 5.1g). A more detailed analysis of the sensitivity of observed dust mass concentrations to stability and friction velocity is presented in Sect. 5.5.

5.2. Uncorrected aerosol spectrometer size distributions

I present the uncorrected 15-minute average PSDs of mass concentration of the two Fidas, Welas, UCASS, and the one from the CDA with optical diameters, and that of the two SANTRI2 with projected-area diameter in Fig. 5.4a. The diameters to which the mass concentrations are assigned are the geometric mean of the upper and lower bin boundaries. The PSDs highlight significant mass concentrations of particles larger than 10 µm, with pronounced peaks between approximately 10 µm and 30 µm in diameter. The 15-minute average PSDs from each instrument demonstrate substantial temporal variability, as indicated by the error bars, which represent the standard errors within the corresponding averaging period, and for SANTRI2s also across the analyzed sensors per instrument.

PSDs from Fidas_4m and Welas_4m are consistent for particle diameters smaller than 7 µm (Fig. 5.4a). However, the diameter corresponding to the peak mass concentration of the PSDs from different instruments varies, ranging in d_p from ~10 µm to 30 µm. Contrary to expectations of higher dust concentrations and larger particles closer to the ground, Welas_2m PSDs show peak mass concentration at a smaller diameter of approximately 20 µm compared to Welas_4m, which peak at around 30 µm (Fig. 5.4a). For particles smaller than 10 µm, Welas_4m and Welas_2m alternate in exhibiting higher mass concentrations. In contrast to the Welas instruments, the behavior of the two Fidas PSDs aligns with expectations, as Fidas_4m generally shows lower concentrations across most of the size range. However, toward the upper end of the size range, the concentration of Fidas_4m partially exceeds that of Fidas_2m (*e.g.*, Fig. 5.4a

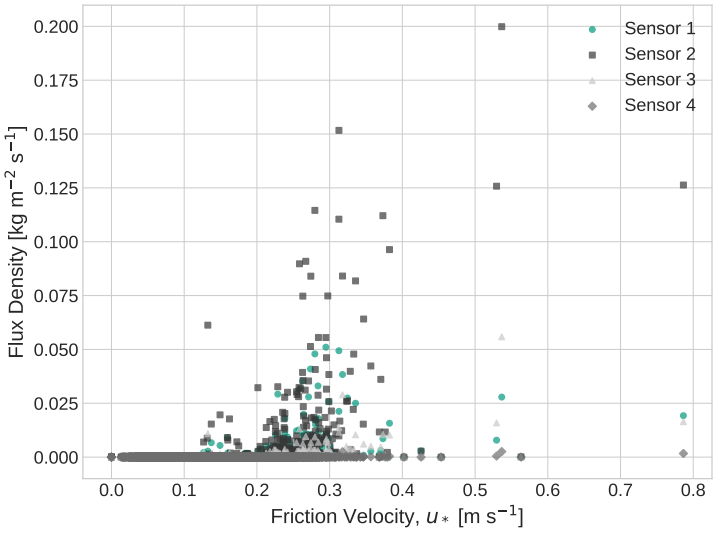

Figure 5.3.: Flux density for the four sensors of the SANTRI4 at 5, 15, and 30 cm height over u_* to retrieve u_{*t}.

2022-09-29 14:45). Another characteristic of the Fidas mass concentration PSDs is the absence of a distinct peak. Instead, their mass concentration appears to be relatively evenly distributed across sizes between approximately 5 – 20 µm in Fig. 5.4a. Mostly, UCASS B and Welas_4m generally show good agreement. The measurements of UCASS B closely match those of Welas_4m for particle diameters $d_p < 4$ µm and up to $d_p \approx 10$ µm. However, the PSD measured by UCASS B exhibits oscillations instead of forming a smooth curve up to approximately $d_p = 10$ µm. Beyond this range, UCASS B shows a more gradual increase in concentration compared to Welas_4m. Both instruments exhibit peak concentrations in the particle size range of $d_p = 20$ to 30 µm, with the peak concentration of UCASS B being roughly an order of magnitude smaller than that of Welas_4m. UCASS A exhibits significant differences in its mass concentration PSD compared to the other instruments. At approximately 1 µm, its mass concentration is comparable to that of the other instruments, but it increases by an order of magnitude for the third bin (around 1.3 µm). For larger particles, the concentration decreases until it matches the concentrations of the other instruments at ~2 µm and increases again at ~3 µm to an order of magnitude higher than the concentrations of other instruments (at ~4 µm) and oscillates around the other instruments' PSDs for d_p up to ~10 µm. At 10 µm, UCASS A's mass concentration aligns well with the UCASS B concentrations. The oscillation of the PSD, *i.e.*, the classification of size bins and the conversion from scattering cross-section to particle diameter, seems to be unrealistic in comparison to the other instruments, and further adjustments may be needed to optimize particle categorization. UCASS A and B are therefore excluded from further analysis. The CDA PSDs (measured at 4 m height) show significant differences compared to the PSDs of the other instruments. Before peaking at around 15 µm, the CDA concentrations generally agree well with those of Fidas_4m and Welas. After the peak, the CDA concentration decreases rapidly, crossing below Fidas' mass concentration and eventually falling below all other measurements. This decrease could not be resolved by any correction method. I suspect that this decrease was due to either a

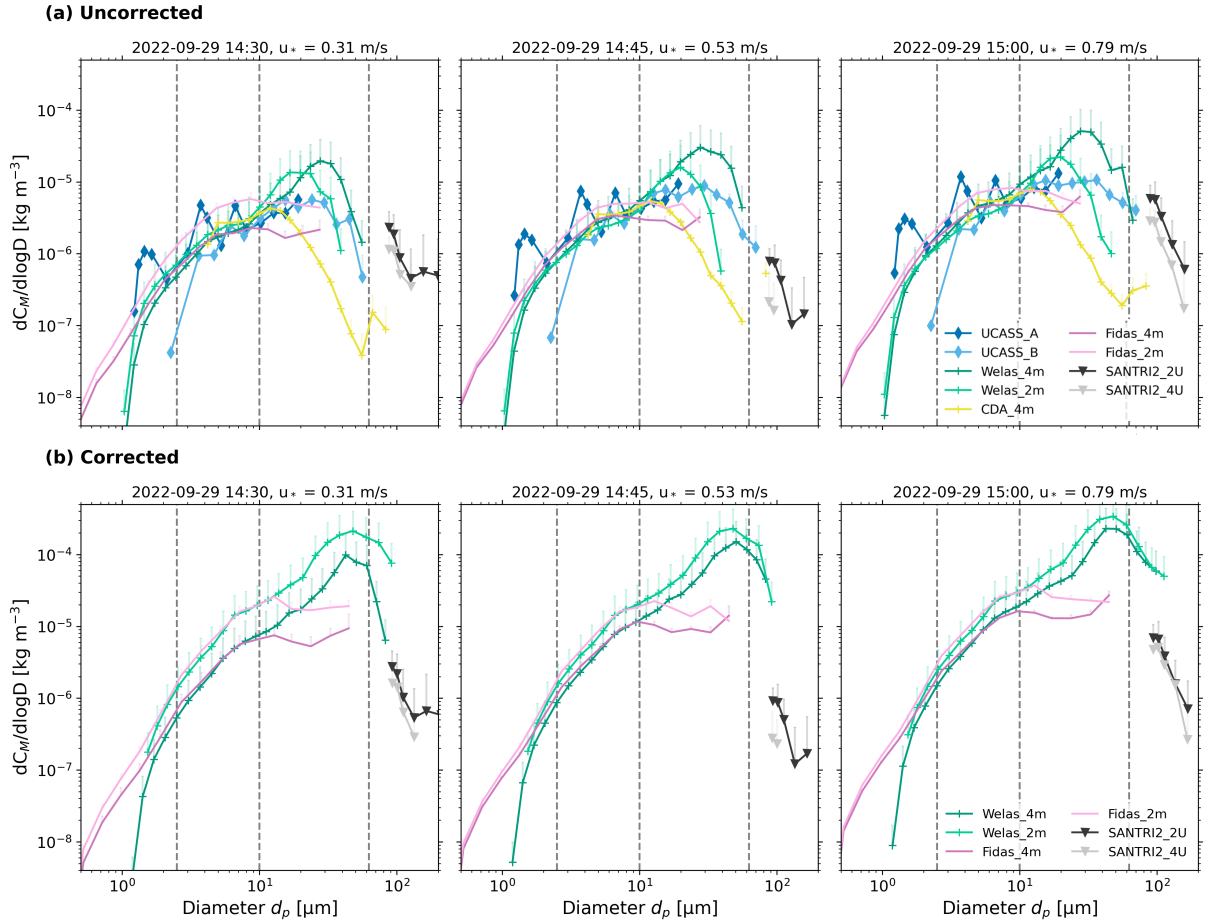

Figure 5.4.: 15 minute average size distributions of mass concentration for dusty conditions on 29 September 2022 for 3 subsequent 15-min time periods from 14:30 until 15 UTC. (a) Uncorrected PSD with optical diameters (except SANTRI2, which uses projected-area diameter) and (b) corrected PSDs with geometric diameters. Standard errors are indicated by vertical lines (only positive errors are shown). Average 4 m friction velocity, u_* for each 15-min period are indicated in the panel titles. Dashed lines indicate the size ranges of the dust size classifications (see Chapter 1).

reduced sampling efficiency of the Sigma-2 inlet in that size range or a lower sensitivity for larger particles (*e.g.*, due to saturation of the larger sampling volume during high particle concentrations), which was not the case for the other instruments. Consequently, the CDA data were also excluded from further analysis.

In certain cases, the SANTRI2 PSDs align well with the extended particle size trends observed with the other instruments (Figs. 5.4a 2022-09-29 14:45, 15:00). However, in Fig. 5.4a 2022-09-29 14:30, the two SANTRI2 units, each averaged over the five sensors, show higher mass concentration PSDs than expected, compared to measurements from the other instruments. It is important to note that the SANTRI2s recorded projected-area diameter whereas the other instruments recorded optical diameters which could potentially change the agreement between SANTRI2 and other instruments' PSDs.

5.3. Corrected aerosol spectrometer size distributions

The uncorrected PSDs with optical diameter shown in Fig. 5.4a reveal the original measurements taken by the instruments, indicating potential biases and inaccuracies due to low sampling efficiencies and variability between instruments. The data presented in this section was corrected as explained in Sects. 4.4.2-4.4.3. Here, I discuss the corrected PSD mass concentrations as shown in 5.4b and the remaining variability between instruments. Overall, the comparison between Figs. 5.4a and 5.4b highlights that the correction procedures result in more consistent concentrations across instruments, although I could not eliminate all sources of discrepancy.

After correction, Welas_2m consistently shows higher values than Welas_4m under dusty conditions, with some exceptions for particles larger than 60 µm (Fig. 5.4b 2022-09-29 14:45, 15:00). Both instruments exhibit a peak at approximately the same diameter (~50 µm). After correction, they better match the concentrations observed in the Fidas measurements, particularly for particles larger than $d_p = 1.2\,\mu m$ and up to ~10 µm. In the Fidas' mass concentrations, a plateau in measurements for particles larger than $d_p \approx 12\,\mu m$ is visible, which I attribute to potential limitations in measuring larger particles, limitations that could not be corrected by any of the correction mechanisms applied. In comparison to the uncorrected PSDs of the SANTRI2s, most of the corrected PSDs now better fit the prolongation of the other instruments. In Figs. 5.4b 2022-09-29 15:00, the two SANTRI2 present lower mass concentration PSDs than would be expected from the Welas but fit well the overall appearance. For further analysis, only the SANTRI2, Welas, and Fidas instruments were considered, as most of the differences between these instruments were resolved. They were also used for the combined overall PSDs shown in the next subsection.

5.4. Possible reasons for discrepancies between aerosol spectrometers

The observed differences in the uncorrected and corrected PSDs presented in Sects. 5.3 and 5.2 can be attributed to several instrumental factors.

The use of inlets

The use of inlets for aerosol sampling significantly influences the measurements. All instruments equipped with inlets, such as the Welas, Fidas, and CDA, experience sampling inefficiencies, particularly for larger particles, due to losses within the inlet system (Kulkarni et al., 2011). In contrast, open-path instruments without inlets, do not suffer from inlet losses, but may be more susceptible to environmental interference. The sampling efficiency, η_{sampling}, is influenced by the inlet or pipe design, flow dynamics, and particle characteristics. The inlet losses of the different instruments used here are described in Sect. 4.4.6. In the following, the efficiencies of the inlets and instruments used in this dissertation are quantitatively or qualitatively analyzed.

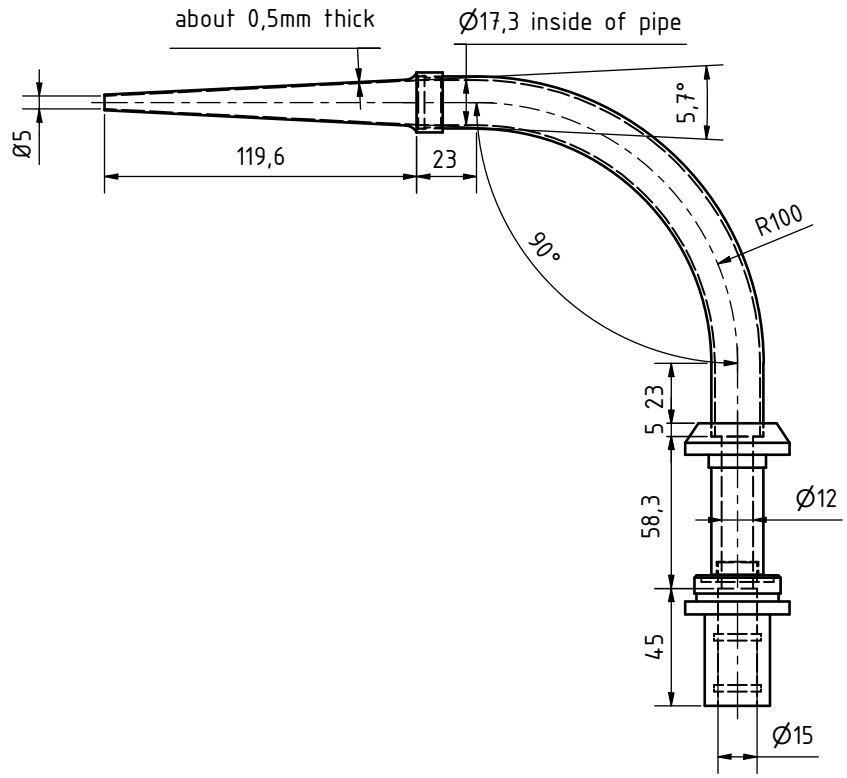

Figure 5.5.: Design of the directional inlet used for Welas and Fidas. Figure by S. Haaß.

Directional inlet of Welas and Fidas: During J-WADI, Welas and Fidas sampled the same air stream of 4.8 $\mathrm{l\,min^{-1}}$ and used the same inlet for guiding the aerosols to their corresponding measurement chambers. A directional inlet was deployed as shown in Fig. 4.6 and detailed in Fig. 5.5. In the directional inlet, particles are transported through a horizontal nozzle where the inlet undergoes enlargement, through a bend, guided through a vertical pipe piece, an IADS (Intelligent Aerosol Drying System) drying system, *i.e.*, vertical transport, and eventually reach the measurement chamber.
I calculated the sampling efficiency with the following formula:

$$\eta_{\mathrm{sampling}} = \eta_{\mathrm{inlet}} * \eta_{\mathrm{transport}} = \eta_{\mathrm{asp}} * \eta_{\mathrm{transm}} * \eta_{\mathrm{grav}} * \eta_{\mathrm{bend}}. \tag{5.1}$$

For η_{inlet}, I used the formulas introduced above for η_{transm} and η_{asp} (Eqs. 4.16, 4.17/sub-isokinetic conditions, 4.18/super-isokinetic conditions). As the Reynolds numbers for all parts of the inlet were smaller than 600, I assumed a laminar flow and that turbulent inertial deposition is negligible. The most relevant losses for the directional inlet for large particles were sedimentation losses (η_{grav}) in the horizontal part of the inlet, as they tended to settle out of the airstream due to gravity. These losses could result in underestimations of larger particle concentration. The resulting sampling efficiency η_{sampling} for different wind conditions is shown in Fig. 5.6a. For wind speeds $v \leq 5$ $\mathrm{m\,s^{-1}}$ and particle diameters $d_p \leq 5\,\mu\mathrm{m}$, the efficiency η is approximately 100%, decreasing to 0% at $d_p \approx 30\,\mu\mathrm{m}$. For wind speeds $v > 5$ $\mathrm{m\,s^{-1}}$

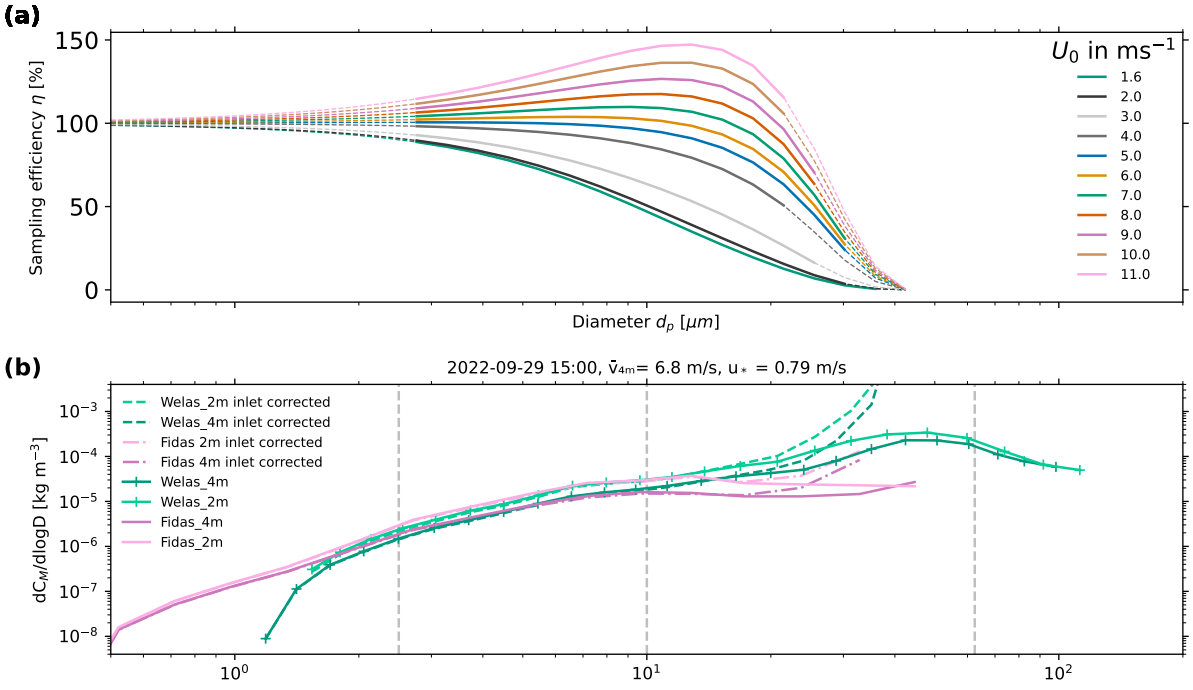

Figure 5.6.: Sampling efficiency η_{sampling} (a) for different wind conditions U_0 for the directional inlet of Welas and Fidas. Dashed curves indicate that the applied formulas may not be valid for the respective diameter range and wind conditions. (b) Example PSD (solid lines) together with the corrected PSD corrected by the sampling efficiency η_{sampling} for Welas and Fidas in dashed lines. Vertical dashed lines indicate the size ranges of the dust size classifications (see Chapter 1).

and particle diameters $d_p > 5\,\mu$m, the efficiency η increases, peaking at $d_p \approx 12\,\mu$m, and then decreases to 0% at $d_p \approx 40\,\mu$m. The peak for wind speeds $v = 11$ m s^{-1} is even at sampling efficiencies of 140%, so an oversampling of particles $d_p \approx 12\,\mu$m occurs. The peak is introduced due to sub-isokinetic conditions (Fig. 5.7), whereas the sharp decrease starting at 20 µm is mainly caused by gravitational losses in the horizontal part of the inlet and losses in the bend (Fig. 5.8). However, it should be noted that for wind speeds $U_0 > 5$ m s^{-1} and particles with $d_p > 30\,\mu$m, most of the formulas are not valid.

A similar inlet design with comparable dimensions was previously quantified by Schöberl et al. (2024). They reported cut-off diameters (defined as 50% loss) smaller than 10 µm. In contrast, my calculations showed a cut-off diameter of approximately 30 µm for $v = 5$ m s^{-1}. The lower cut-off diameters observed by Schöberl et al. (2024) may be attributed to their slightly different inlet dimensions (inner diameter = 4.527 mm), the calculation of the bend efficiency η_{bend} in degrees instead of radians (as noted in the supplementary material of Schöberl et al. 2024), or the high flow velocities and Reynold numbers associated with their airplane measurements.

By dividing the mass concentration PSDs of the Fidas and Welas instruments shown in Fig. 5.4b (2022-09-29 14:30) by the sampling efficiencies η of the directional inlet under the measurement conditions, corrected PSDs can be estimated, as shown for an example PSD in Fig. 5.6b. For the Welas, no signifi-

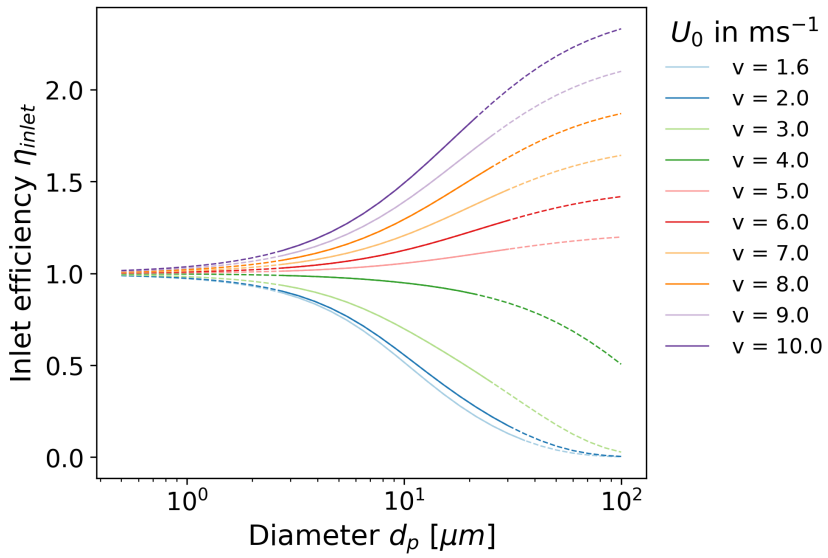

Figure 5.7.: Inlet efficiency η_{inlet} of the directional inlet for different wind conditions introducing the peak in the sampling efficiency $\eta_{sampling}$ (Eq. 5.1).

cant change in concentrations is observed for $d_p < 20\,\mu m$, not even for the oversampling which occurs at $d_p \approx 12\,\mu m$. However, for larger particle sizes, the corrected PSDs are clearly increased by several orders of magnitude compared to the uncorrected ones. A similar trend is observed for the Fidas, although most of the Fidas size range remains unaffected by large inlet inefficiencies as their size range stops before $d_p = 50\,\mu m$ and they do not show a significant peak which can be further increased. The estimated inlet efficiencies suggest that almost no particles larger than around $20\,\mu m$ should have been detected, yet the results showed the measurement of a significant number of particles in this size range. The empirically estimated inlet efficiencies, therefore, appear unrealistic. The underestimation of inlet efficiencies for large particles could potentially result from neglecting the re-emission of particles that initially settled, a process not considered in the applied formulas. Additionally, traditional deposition schemes may overestimate gravitational settling for large particles (Adebiyi et al., 2023), highlighting potential limitations in the modeled particle dynamics. To test whether other formulas or assumptions would be more in line with the detected particles in the Welas, I also applied deposition schemes other than Stokes' settling as introduced in Adebiyi et al. (2023). For example, I implemented Wu and Wang (2006) for different Corey Shape Factors (CSFs). In line with the biaxial ellipsoids considered in this dissertation and applied in the calculation of the sampling efficiencies as shown in Fig. 5.7, a CSF = 0.8 would be considered (Fig. 5.8, light orange line). This assumption leads to rapid deposition of approximately $\eta_{grav} \approx 0$ at $d_p \approx 40\,\mu m$, similar to Stokes settling (light violet line) and the settling velocity of Cheng (1997). For a CSF = 0.3 and the Wu and Wang (2006) deposition scheme, η_{grav} would fall to zero at around $d_p \approx 50\,\mu m$. Even with this low CSF, *i.e.*, highly irregular particles, the gravitational loss in the inlets is still high and does not correspond well with the amount of particles measured during J-WADI. Turbulence in the directional

inlet was not expected due to low Reynolds numbers. However, when assuming turbulent conditions for the three settling schemes implemented, η_{grav} falls to zero much later and the directional inlet would potentially measure some particles with $d_p > 60\,\mu m$.

Several formulas exist for η_{bend} (*e.g.* Pui et al., 1987; Zhang et al., 2012; Wang et al., 2024). In this study, the approach by Wang et al. (2024) was implemented to calculate the inlet efficiency, as shown in Fig. 5.8 . While the formula by Wang et al. (2024) results in higher inlet efficiencies particularly in the super-coarse and giant particle size range, combining the formulas to a unified η_{trans} leads to a rapid decrease of inlet efficiency to nearly zero for $d_p > 30\mu m$, which is against the observations as depicted in Fig. 5.9.

These results suggest that turbulence may have developed even though the Reynolds numbers did not indicate this, and that the transport or inlet efficiency might be underestimated. Additionally, it is possible that certain assumptions necessary to accurately calculate the sampling efficiencies of the system are missing.

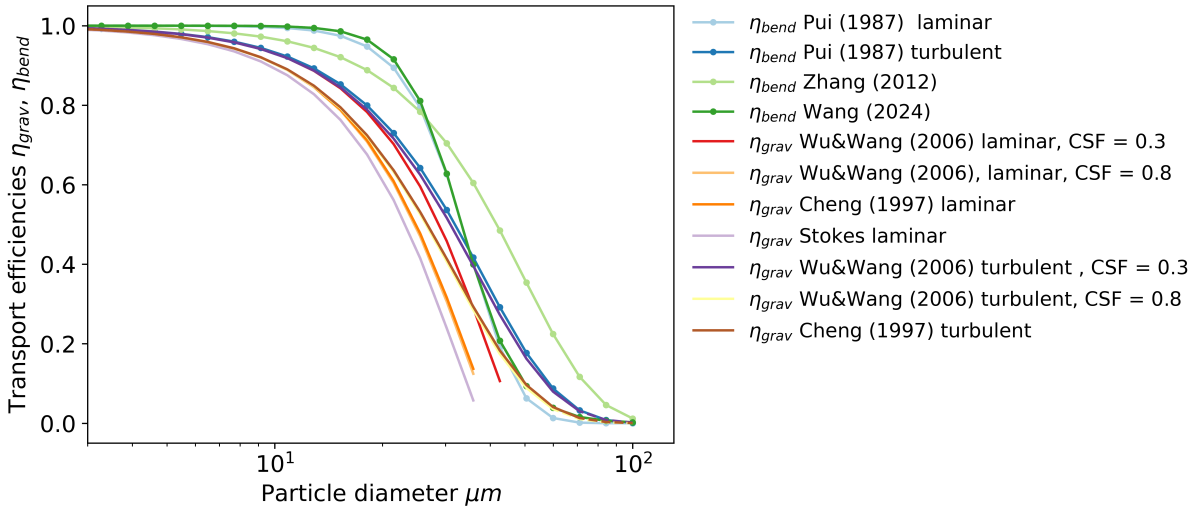

Figure 5.8.: η_{bend} and η_{grav} from different formulas and assumptions.

Furthermore, the underestimation may also stem from limitations in the applicability of the used formulas, which are not entirely suitable for this context, for instance, due to the presence of particles that are so large that the Stokes number regimes, for which the expressions are valid, is exceeded. Results from application of the formulas beyond their valid range are indicated by dashed, lighter lines in Fig. 5.6a, overlapping with diameter ranges that have low η. However, not all studies specify the validity ranges of their parameterizations, and the calculations performed in this study may therefore extend beyond their originally validated domains. The magnitude of the resulting potential error remains unknown.

Sigma-2 inlet of the CDA: The CDA used a Sigma-2 sampling head (Palas GmbH). The Association of German Engineers (VDI-2119, 2013) validated the Sigma-2 sampler after testing it in numerous investigations and concluded that it is a reliable collector for coarse and super-coarse particles (Dietze et al.,

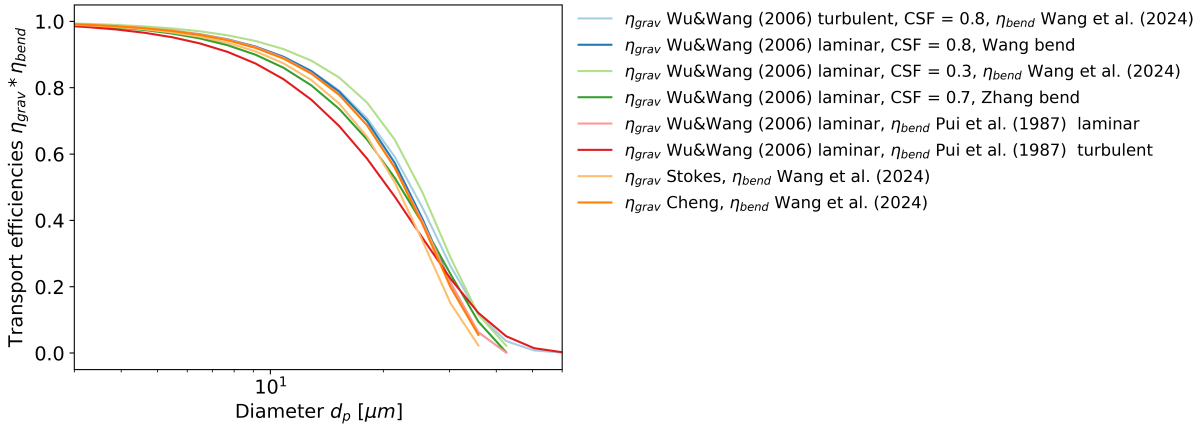

Figure 5.9.: Transport efficiency as calculated by multiplying η_{bend} and η_{grav} for different schemes.

2006; Waza et al., 2019; Rausch et al., 2022; Tian et al., 2017). However, due to the low concentrations measured for particle diameters $d_p >$ 20 µm compared to the other instruments, I suppose that substantial losses occurred from that diameter on. I assume the inlet to have less gravitational losses than the directional inlet due to missing horizontal sampling lines. In addition, I expect it to be able to sample from all horizontal angles, but to have losses due to the wire grid inside the head and the side panels between the three openings. To my knowledge, no inlet efficiency simulations or measurements were conducted and existing formulas cannot be adapted to the needs of the Sigma-2 head so that I cannot quantify η_{sampling} for the Sigma-2 inlet. Conducting own numerical inlet simulations is beyond the scope of this dissertation, but it is considered for future work.

UCASS: The UCASS is a passive instrument and in principle open-path (*i.e.* inlet-free), however its cylindrical shape may act similar to an inlet. Limited information about its sampling efficiency η is available beyond the findings of Girdwood et al. (2022), who reported low losses for droplet diameters between 3 and 10 µm. Flow dynamics simulations by Smith et al. (2019) indicated that the air velocity in the sampling area is approximately 12% higher than the ambient air velocity for an ambient wind speed of 5 m s^{-1}. Their results showed no significant turbulence inside the instrument and good sampling efficiency for particles smaller than 40 µm. Therefore, due to its large opening (5 cm on the larger side), significant losses in the nozzle are not expected.

The UCASS are also a passive system, nearly open-path where the electronics are placed in a housing with a 2.2 cm (small side) wide oval opening. When applying the formulas described in Section 4.4.6 to a simplified geometry of the UCASS (*i.e.,* assuming a round instead of a oval opening, and no electronics inside the tube to disturb the flow), as well as assuming approximately the same air flow inside and outside the instrument, I found gravitational efficiencies (η_{grav}) close to one, but substantial losses due to turbulent inertial deposition. In the large opening of the UCASS, high Reynolds numbers can develop. When applying Eq. 4.22 to a simplified geometry of the UCASS with two parts (enlargement and straight

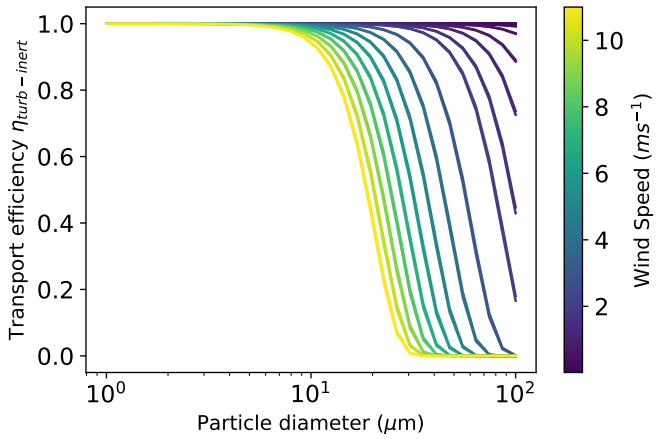

Figure 5.10.: Turbulent inertial deposition within the UCASS for different wind conditions U_0 estimated based on Eq. 4.22.

pipe: L = 4.5 cm: averaged as it increases in the opening and 9 cm and D = 4.3 cm and 6.4 cm for the different parts), I found substantial losses due to turbulent inertial deposition as shown in Fig. 5.10.

This phenomenon occurs when large particles, owing to their high inertia, are unable to follow the curved streamlines of turbulent eddies and are deposited on the walls of the instrument. For higher wind speeds around 10 m s^{-1}, inlet efficiencies rapidly decrease from approximately 90% for 11 µm particles to nearly 0% for particles of 20 µm due to the large pipe diameters, high flow rates, and resulting high Reynolds numbers (Eq. 4.22). These findings highlight a discrepancy in the turbulent flow in the UCASS between the empirical formulas and simulations, particularly for larger particles, which may stem from simplified assumptions in the modeled particle dynamics and the omission of re-suspension effects in the formulas, as partly discussed in Kulkarni et al. (2011). Based on the calculations explained above and especially due to turbulent inertial deposition, I would not expect to measure particles with diameters larger than $d_p = 20\,\mu m$. However, as these large particles were measured and the PSDs are smoother than for smaller particles, $\eta_{\text{tube, turb-inert}}$ might be underestimated by Eq. 4.22.

Given the limitations of the calculation for the directional inlet and the UCASS housing and the apparent mismatch between the theoretical/empirical estimates of inlet efficiencies and the observed particle counts, the inlet efficiencies will not be applied for the correction of the PSD in the following analysis to avoid introducing additional uncertainties, particularly for particles larger than 10 µm. Instead, the results will be interpreted with awareness of potential losses due to turbulent inertial deposition (UCASS) and gravitational settling in sampling pipes or bends (directional inlet). The inlet efficiencies of the instruments will be investigated in more detail in the future using numerical modeling of the flow dynamics in the inlets.

SANTRI2: Operating inlet-free, the SANTRI2 relies on the wind field to guide the particles through the optical path. Although this design avoids inlet-induced biases, potential turbulence effects caused by

the (quite slim) platform to which the sensors are attached can still lead to modifications of the aerosol sample seen by the sensors compared to its surrounding. Despite this, the approach offers the most direct and unaltered sampling of ambient aerosol among the J-WADI instruments, providing insights into the nearly undisturbed characteristics of large dust particles. Due to its slim design, I expect these alterations to be small.

Measurement principle differences

A second reason for the discrepancies in PSDs between instruments lies in their measurement principles, such as optical scattering (used by Welas, Fidas, CDA, and UCASS) versus the optical gate mechanism employed by SANTRI2, which introduces additional variability as it measures the projected area. Optical instruments estimate particle size based on light scattering, which can be influenced by factors such as particle shape, composition, and refractive index. The various devices based on optical scattering differ in aspects like scattering angle, sensor area, and light source, which can lead to inaccuracies, especially for non-spherical or irregularly shaped particles. In contrast, optical gate devices determine particle size by measuring the shadow cast on a photodiode, meaning the obtained 2D shape for non-spherical particles is highly dependent on their orientation when illuminated. In order to overcome these limitations, I harmonized measurements from the different devices and transformed the particle sizes to geometric diameters, assuming biaxial ellipsoids. However, some of the aforementioned causes of uncertainties, such as particle shape and refractive index, remain unresolved. The differences between the assumption of biaxial and triaxial ellipsoids are discussed in the following.

PSDs for triaxial particle assumption

Although it would be more realistic to assume triaxial ellipsoids rather than biaxial ones for geometric diameters (Huang et al., 2021), the lack of a suitable database for PSL particles with diameters $d > 50\,\mu m$ limits the applicability of this approach for the Welas, as the Meng et al. (2010) database does not cover such large particles. With the missing size range of ~$80 - 100\,\mu m$ for Welas_4m, Fig. 5.11 presents 15-minute average size distributions of mass concentration for dusty conditions on 29 September 2022, focusing on three consecutive 15-minute intervals from 14:30 until 15:00 UTC. The PSDs in Fig. 5.11c show the corrected PSDs assuming triaxial ellipsoids after the correction steps as explained in Sects. 4.4.2-4.4.3. The PSDs reveal differences, *e.g.*, in general lower mass concentrations compared to the biaxial assumption in Fig. 5.11b. Notably, the Welas size range is not entirely covered since the Meng et al. (2010) database does not include particles from around 50 µm (PSL). Especially for Welas_4m, only particles $d_p < 70\,\mu m$ are covered whereas Welas_4m covers also larger particles due to the diameter correction. The Fidas show lower mass concentrations, especially in the coarse range and in comparison to the Welas. The higher difference to the Welas might be due to the applied correction methods which may not be fully applicable for triaxial spheroids and could be further refined. Further-

more, the SANTRI2s are attributed to a smaller size range, due to the consideration of HWR = 0.45, *i.e.*, the third axis of the ellipsoid differing from the other two. Additionally, the Welas show a less smooth PSD than in Fig. 5.11a, b possibly due to the bin-wise PSD diameter correction. This is also evident for particles larger than 30 µm, where Welas_2m shows oscillating PSDs and a peak at smaller diameters than Welas_4m, likely due to low particle counts during the intercomparison period in this size range. Furthermore, the peak of both Welas size distributions shift slightly towards smaller diameters, but its position is ambiguous between 30 and 60 µm.

In Sect. 7.2, the same figures as presented in this chapter are depicted but with the assumption of triaxial instead of biaxial spheroids for the conversion from optical to geometric diameters. The overall results remain the same but the shape of the PSDs and the amount of concentration falling in each size class is differing. Especially the change in shape and peak of the PSDs underline that the discrepancies between instruments can stem from different assumption for the particle shape (and refractive index). These results demonstrate that the estimation of geometric diameters is highly sensitive to particle shape assumptions and refractive index, the latter being estimated from Di Biagio et al. (2019) but not retrieved directly from the field data. As the interpretation depends on these parameters, further research is essential to improve the reliability of geometric diameter estimates, particularly for larger particles where uncertainties remain substantial.

Additional differences

The classification of particle size bins makes use of different theoretical frameworks. For optical diameter measurements, Mie theory assuming spherical particles is commonly applied (e.g., Welas, Fidas, and CDA), whereas for the retrieval of projected area diameters, the projected area on the instrument is used. For the transformation to geometric diameters ellipsoidal particles are assumed, which are either based on databases for for different CRI (*i.e.*, sensitive to assumed CRI, *e.g.*, Gasteiger and Wiegner, 2018) or on geometric calculations as described in Sect. 4.4.3. These differing approaches influence the shape of the retrieved PSDs.

Moreover, the instruments differ in how they handle partially illuminated particles: the Welas, Fidas, and CDA avoid them by their measurement principle, the UCASSs account for this in its calculations but the SANTRI2s do not. In addition, the size ranges covered by different instruments introduce variability in accuracy towards the edges of these ranges. Instruments optimized for detecting fine particles may exhibit reduced accuracy and sensitivity for larger particles towards the edge of their size range, and vice versa. This discrepancy is particularly evident in the overlap regions where the detection capabilities of different instruments intersect, resulting in inconsistencies in PSDs.

Finally, the location of instruments can affect recorded PSDs due to proximity to emission locations, atmospheric conditions, and particle transport dynamics. Differences in height and positioning can cause variations in sheltering, turbulence, and detected dust concentrations. For Fidas and Welas, these dif-

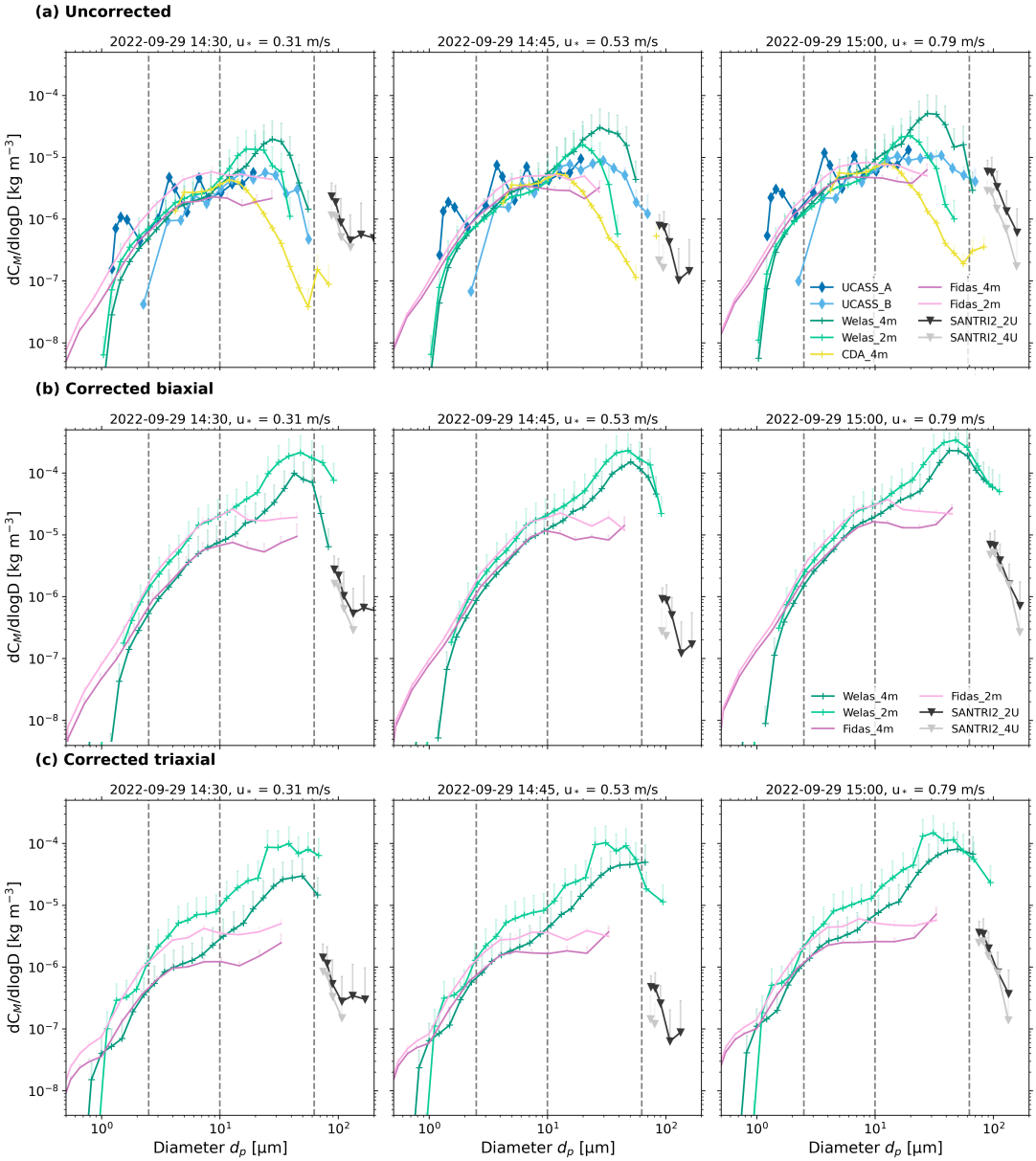

Figure 5.11.: 15 minute average size distributions of mass concentration for dusty conditions on 29 September 2022 for 3 subsequent 15-min time periods from 14:30 until 15 UTC. (a) Uncorrected PSD with optical diameters (except SANTRI2, which uses projected-area diameter) and (b) corrected PSDs with geometric diameters assuming biaxial ellipsoids. (c) Same as (b) but with geometric diameters assuming triaxial ellipsoids. Standard errors are indicated by vertical lines (only positive errors are shown). Average 4 m friction velocity, u_* for each 15-min period are indicated in the panel titles. Dashed lines indicate the size ranges of the dust size classifications (see Chapter 1).

ferences should be minimal since they share the same flow and are separated only by a tube. However, discrepancies may arise if particles are trapped in the tube connecting both instruments (Fig. 4.6b), potentially reducing counts in the Fidas, though tube clogging was not observed during the campaign. After applying my correction steps, Fidas and Welas concentrations agreed well for $d_p < 10\,\mu m$, but discrepancies arose for larger particles, with Welas concentrations being up to an order of magnitude higher at the upper limit of its size range. It is unlikely that particles with $d_p > 10\,\mu m$ continuously got trapped before reaching the sensors of the Fidas, as measurements over several weeks with the instruments were conducted, and no impacts of enhanced blockage were evident from the Fidas measurements. Therefore, I attribute most of these differences to discrepancies in the instruments' sensitivities (especially at the edges of the instruments size ranges).

Overall, these instrumental differences underscore the importance of employing a suite of complementary measurement techniques to achieve a comprehensive and robust characterization of the full PSD, particularly in the challenging super-coarse and giant particle size ranges. Understanding these differences and their implications is crucial to improving the reliability of dust measurements and developing better calibration and correction methodologies.

5.5. Variability of the PSD with u_* and stability

Fig. 5.12a shows the corrected 15-minute averaged PSDs combined across SANTRI2, Welas and Fidas (shown individually in Fig. 5.4b) over the entire measurement period and averaged within different u_* ranges similar to González-Flórez et al. (2023). The process of combining and harmonizing the concentrations of these instruments is explained in App. 4.4.4. While the mean of all PSDs in Fig. 5.12a, indicated by a dashed black line, shows the peak at around 60 µm, the categorized PSDs differ in their shape and height. As expected, higher u_* values correlate with an increase in mass concentration (dC_M) across all particle diameters (Fig. 5.12a) although the level of increase varies. However, for lower u_* values ($< 0.2\,m\,s^{-1}$, *i.e.* below the threshold friction velocity for saltation, u_{*t}), the PSDs remain largely consistent. Differences emerge at $d_p > 30\,\mu m$, where concentrations corresponding to lower u_* values decrease more rapidly–except in the $0.1\,m\,s^{-1} \leq u_* < 0.2\,m\,s^{-1}$ range where a peak at around $d_p = 60\,\mu m$ (same for $u_* > u_{*t}$) is visible–suggesting that some larger particles were already effectively lifted and detected at friction velocities ($> 0.1\,m\,s^{-1}$) and below the calculated threshold friction velocity ($u_{*t} = 0.22\,m\,s^{-1}$). For particles $d_p > 60\,\mu m$, the standard error increases significantly, casting doubt on the reliability of this relationship. Starting from $u_* \geq 0.25\,m\,s^{-1}$, which is above the threshold friction velocity, significantly higher mass concentrations are observed, although the shape of the PSD remains largely consistent as for $0.2\,m\,s^{-1} \leq u_* < 0.25\,m\,s^{-1}$. For $u_* \geq 0.35\,m\,s^{-1}$, only a small number of PSD samples is available, but the PSD for the two largest u_* categories are very similar, except for $d_p > 100\,\mu m$, where concentrations for $u_* > 0.4\,m\,s^{-1}$ fall behind those observed at lower friction velocities. The SANTRI2 were the only devices operating for $d_p > 100\,\mu m$. In this size range, the PSDs show

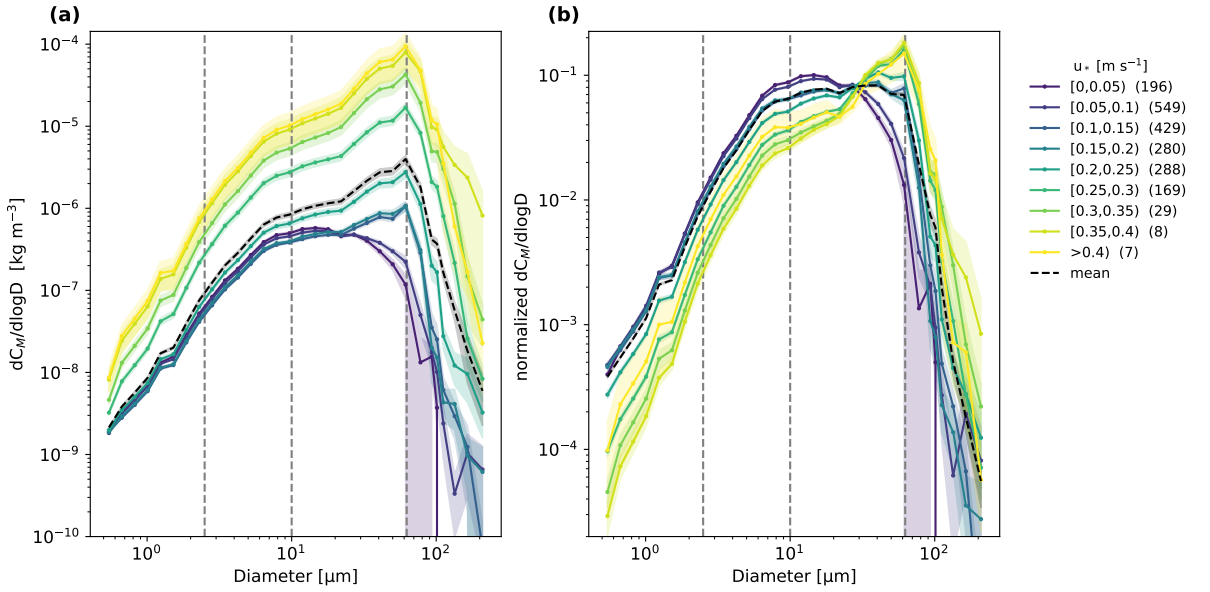

Figure 5.12.: (a) Variability of mass concentration PSD with u_* deduced from SANTRI2, Welas and Fidas over the whole campaign time. Colors indicate u_* during the 15-min averaging time period corresponding to the PSDs and the black dashed line the mean of all PSDs. Shaded areas depict the standard error of PSDs within each class across the different time steps used. Numbers in parentheses indicate the number of 15-min PSDs taken into account in each u_* range. Dashed lines indicate the size ranges of the dust size classifications (see Chapter 1). (b) Same as (a) but normalized to unity in each time interval.

generally lower concentrations at smaller u_* values, but the behavior of dC_M becomes less consistent for small u_*, either increasing or decreasing with friction velocity. Especially for $u_* < 0.05\,\mathrm{m\,s^{-1}}$, the concentrations are decreasing to almost zero at ~$d_p > 100\,\mu\mathrm{m}$. In this friction velocity range, the presence of super-coarse and giant particles is expected to be low. Additionally, these particles may not be captured by the Welas due to inlet inefficiencies. However, the open-path approach of the SANTRI2 allows for direct sampling, increasing the likelihood of detecting these (few) larger particles which might explain the abrupt change in mass concentration.

Figure 5.12b shows mass concentrations normalized to unity (15-minute PSDs were first normalized, then averaged). Here, the relative amount of the different particle sizes can be observed and shows more prominently the shift in peak mass concentrations for different u_*. The slope of the concentrations is relatively similar up to about 10 µm. However, the concentration peak shifts gradually from 12 µm to 60 µm for u_* exceeding $0.1\,\mathrm{m\,s^{-1}}$.

Variations in the normalized abundance of particles in different size ranges with varying u_* can also be observed in Fig. 5.13, which shows the total mass concentration contribution of fine, coarse, super-coarse, and giant particles across different u_* categories. At low friction velocities ($u_* < 0.2\,\mathrm{m\,s^{-1}}$), less than 10% of the mass concentration are contributed by giant particles, and approximately 60% by super-coarse particles. Below the threshold friction velocity ($u_{*t} = 0.22\,\mathrm{m\,s^{-1}}$), recorded dust might be due to intermittent releases or due to dust previously emitted and/or advected from nearby sources.

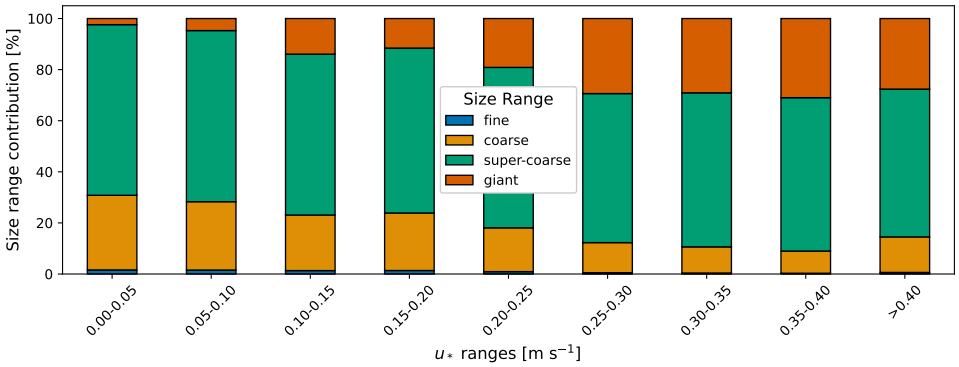

Figure 5.13.: Percentage mass concentration abundance of particle size ranges deduced from SANTRI2, Welas and Fidas over the whole campaign time with u_*.

Dust that occurred at $u_* < 0.22\,\mathrm{m\,s^{-1}}$, however, already contained a great amount of super-coarse and giant particles (see Fig. 5.13). As u_* increases up to $0.4\,\mathrm{m\,s^{-1}}$, the contribution of giant particles rises to about 25%, while super-coarse particles contribute slightly over 60%. For $u_* > 0.4\,\mathrm{m\,s^{-1}}$, the contributions of both super-coarse and giant particles decrease slightly. This behavior suggests that either the large variability for this size range, which can be observed in Fig. 5.12 (not shown in Fig. 5.13), and low statistics blur the trend or that factors other than friction velocity alone, such as deposition processes, direct entrainment of large particles, or even inlet efficiency at these sizes, may influence the concentration of larger particles in the PSD.

Earlier studies focused on the finer part of the PSD. Alfaro et al. (1997); Shao (2004); Ishizuka et al. (2008); Kok (2011a) were restricted to particles $< 10\,\mu\mathrm{m}$ or $< 20\,\mu\mathrm{m}$, so only that part of my PSD can be directly compared. The findings from the present study indicate that the shape of the mass concentration PSD is largely invariant in the size range $2 - 10\,\mu\mathrm{m}$ (see Fig. 5.12 c), supporting the conclusions of Kok (2011a) in that size range. Below $2\,\mu\mathrm{m}$, we find that the relative proportion of particle mass concentration decreases with increasing u_*. Alfaro et al. (1997); Shao (2004); Ishizuka et al. (2008) predicted a shift toward finer sizes for particles $< 10\,\mu\mathrm{m}$ or $< 20\,\mu\mathrm{m}$, whereas my results suggest a coarsening with increasing u_* both for diameters $< 2\,\mu\mathrm{m}$ and $> 10\,\mu\mathrm{m}$. It is also important to note that we analyzed the PSDs of dust concentration rather than dust emission fluxes, as done in the mentioned studies.

Fig. 5.14a shows 15-minute averaged PSDs over the entire measurement period, calculated across all instruments except CDA and UCASS and categorized into different stability regimes (Sect. 4.2). The total mass concentration across all bins is greatest during near unstable and neutral conditions, followed by unstable conditions. The lowest mass concentrations are predominantly observed at night under stable and near stable conditions when friction velocities are small (Fig. 5.1). For stable conditions, very few super-coarse and giant particles are present.

Fig. 5.14b shows the normalized PSDs. For stable conditions, smaller particles with diameters less than $20\,\mu\mathrm{m}$ are most abundant, followed by unstable, and near stable conditions. As stable stratification

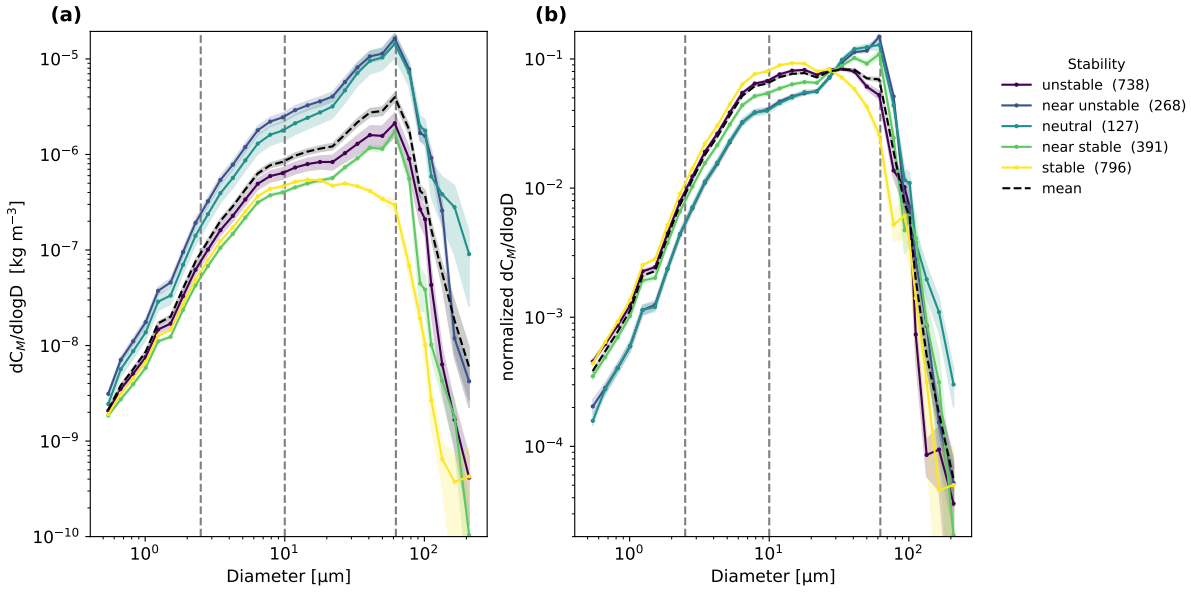

Figure 5.14.: (a) Variability of mass concentration PSD deduced from SANTRI2, Welas and Fidas over the whole campaign time with atmospheric stability. The colors indicate different stability ranges and shaded areas the standard error of PSDs within each class across different time steps, and the black line the mean of all PSD. Numbers in parentheses indicate the number of PSDs available within each stability class. Dashed lines indicate the size ranges of the dust size classifications (see Chapter 1). (b) Same as (a) but normalized to unity in each time interval.

suppresses turbulence, the lifting and transport of larger particles is limited, while allowing smaller particles to remain suspended longer. In contrast, for particles larger than 20 µm but smaller than 90 µm, the opposite trend is observed and they are more present for neutral and near (un)stable conditions. No clear trend in stability is apparent for particles larger than 90 µm in Fig. 5.14b. Further investigation is necessary to determine whether this behavior is due to instrument inaccuracies, limited particle statistics, or other reasons.

Atmospheric stability and u_* are strongly interconnected as L depends on u_* and for large u_*, conditions become increasingly neutral. To investigate the dependency of mass concentration on stability while accounting for the interdependence between z/L and u_*, Fig. 5.15 presents mass concentration as a function of u_* and colored by z/L across different particle size ranges. For $u_* < 0.2\,\mathrm{m\ s^{-1}}$, the majority of the total mass concentrations are below $10^{-6}\,\mathrm{kg\,m^{-3}}$ (Fig. 5.15a). Across all size ranges, stable conditions correspond to the lowest friction velocity values (mostly $u_* < 0.15\,\mathrm{m\ s^{-1}}$, with the smallest mass concentrations observed. With increasing $u_* > 0.1\,\mathrm{m\,s^{-1}}$, conditions become more unstable to neutral. Between $u_* = 0.1\,\mathrm{m\ s^{-1}}$ and $u_* = 0.2\,\mathrm{m\ s^{-1}}$, (near) stable and (near) unstable conditions are present. For larger u_*, mass concentrations increased sharply with slight increases in u_* (Fig. 5.15a). The majority of these data points is categorized as unstable conditions with some near unstable and near stable conditions. These near unstable time periods, however, tended to have slightly higher mass concentrations for a given u_*. For instance, for $u_* = 0.25\,\mathrm{m\ s^{-1}}$ and for near unstable conditions, mass concentrations could

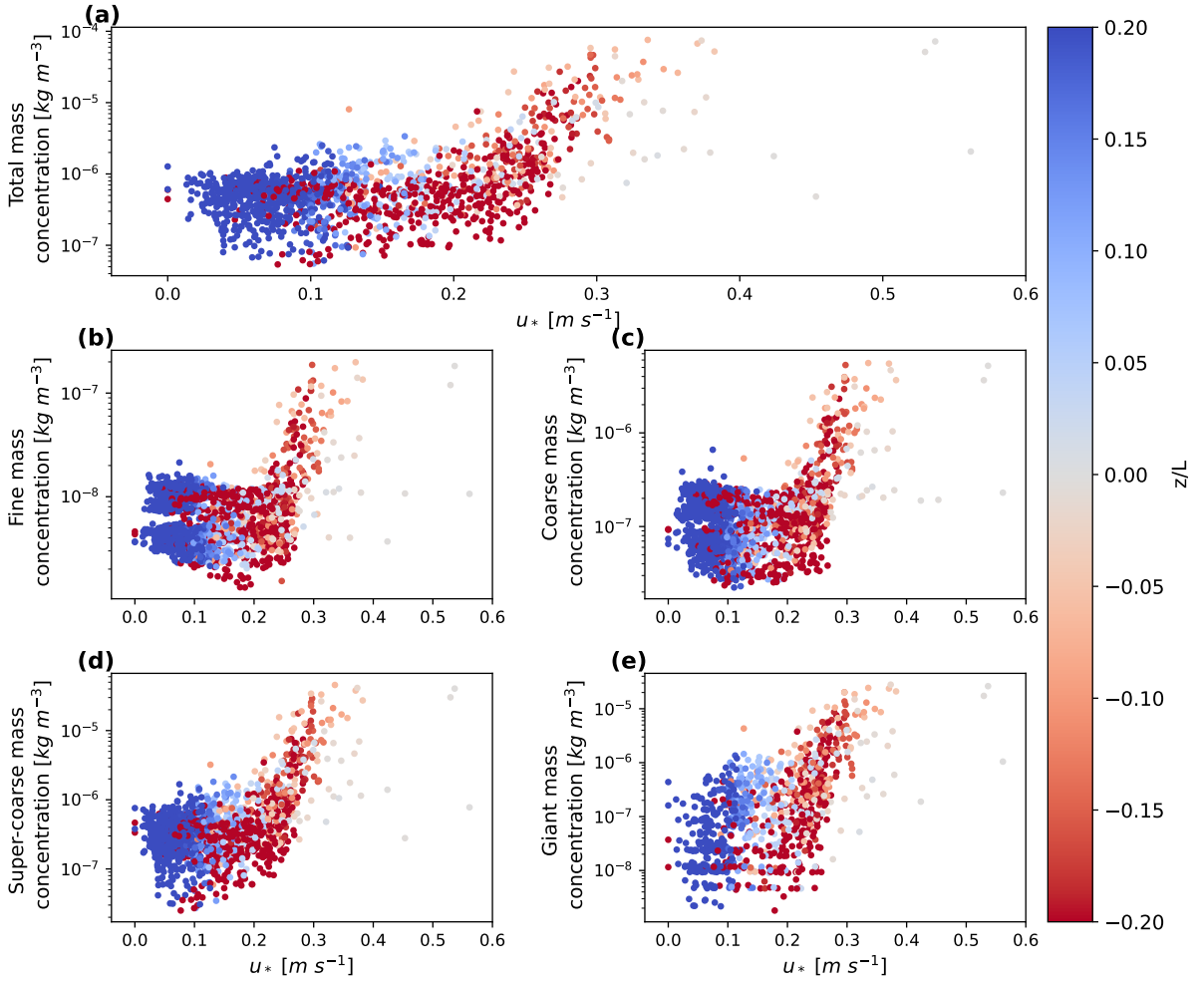

Figure 5.15.: Mass concentration deduced from SANTRI2, Welas and Fidas over the whole campaign time over u_*. The colors indicate the different stability regimes in terms of z/L for (a) total, (b) fine, (c) coarse, (d) super-coarse, and (e) giant dust mass concentration.

reach approximately one order of magnitude higher than the average for unstable conditions. However, most of the near unstable and near stable time period data points gather with the unstable conditions. For $u_* > 0.3\,\mathrm{m\ s^{-1}}$, mostly neutral conditions were registered with a potentially lower mass concentration than would be expected from the elongation of unstable conditions, but with a lack of a clear pattern due to few data points. For all size ranges (Fig. 5.15b-e), the trends for (near-) unstable and (near-) stable conditions aligns with that of the total mass concentration (Fig. 5.15a). However, for giant particles, generally less data points exists. Most data points cluster between $u_* = 0.2\,\mathrm{m\ s^{-1}}$ and $u_* = 0.4\,\mathrm{m\ s^{-1}}$ for unstable conditions. For neutral conditions, the mass concentration started to increase at higher $u_* > 0.3\,\mathrm{m\ s^{-1}}$ (Fig. 5.15e).

I observed a slight trend for increased mass concentrations for diameters $> 10\,\mu\mathrm{m}$ with near unstable followed by neutral and unstable conditions, but no clear pattern emerged. The results neither fully support nor contradict previous findings by Khalfallah et al. (2020) and Shao et al. (2020), which found

a dependency of the PSD on atmospheric stability, or González-Flórez et al. (2023) and Dupont (2022), which did not find it. However, it should be noted that these analyses were restricted to particles $< 30\,\mu m$, so only that part of my PSD can be directly compared and no direct dependency on stability is visible for this size range in the J-WADI data. Further investigation is required to fully understand these dynamics. Moreover, it is important to note that I analyzed dust concentration PSDs rather than fluxes, as done in these studies.

5.6. Comparison between PSDs from aerosol spectrometers and physical samples

To confirm the PSDs obtained with aerosol spectrometers (Sect. 5.3), I compared the results with those derived from physical samples collected using FPS and analyzed by SEM. This comparison allowed me to evaluate the accuracy of the spectrometers, particularly for larger particle sizes where instrumental biases, such as inlet efficiencies and optical corrections, might affect the measurements more than for the FPS. As the diameters from the analysis of the FPS differed in every analysis step and to make them comparable to the aerosol spectrometer data, the FPS are linearly interpolated and binned into 25 bins over the full size range of the FPS.

Fig. 5.16 presents the mass of particles deposited per mm^2 per day, normalized by dlogD from the FPS and the average across the aerosol spectrometers SANTRI2, Welas, and Fidas at different time steps. The samples and corresponding time frames are shown in Table 7.2. For comparison with the FPS samples, the number of particles deposited per unit area and their corresponding particle sizes were determined from the aerosol spectrometer measurements as outlined in Sect. 4.5 assuming a constant deposition of $v_d = 0.0007\,\mu m\,s^{-1}$ across all size ranges (corresponding to the Stokes settling velocity of particles with diameter ~2 µm). The PSDs for different time steps derived from the FPS and aerosol spectrometer show reasonable agreement (always less than an order of magnitude, mostly less than 20% deviation). However, the PSDs sometimes differ in the position of the peak which is often at $d_p \approx 60\,\mu m$ but at smaller particle sizes for the FPS (e.g. 2022-09-17). In most cases, the peak of the FPS is vague (2022-09-27) or matches the one of the aerosol spectrometer (e.g., 2022-09-21, 2022-09-24 11:03, 2022-09-26). Overall, the agreement between the PSDs obtained from different measurement techniques is quite good, considering the differences in sampling methods and instrument principles. However, discrepancies between the PSDs may be attributed to factors such as variations in sampling efficiency, changes in wind conditions, the underlying assumption on shape and orientation on the substrate or limitations in accurately capturing super-coarse and giant particles with the aerosol spectrometer setup, as discussed in Sect. 5.4. Despite these differences, the overall trends align well, reinforcing the robustness of the measurements across different techniques.

In a previous study using the same FPS in a different field experiment (Panta et al., 2023), data from the Fidas 200S aerosol spectrometer data aligned more closely with the FPS measurements (almost perfectly

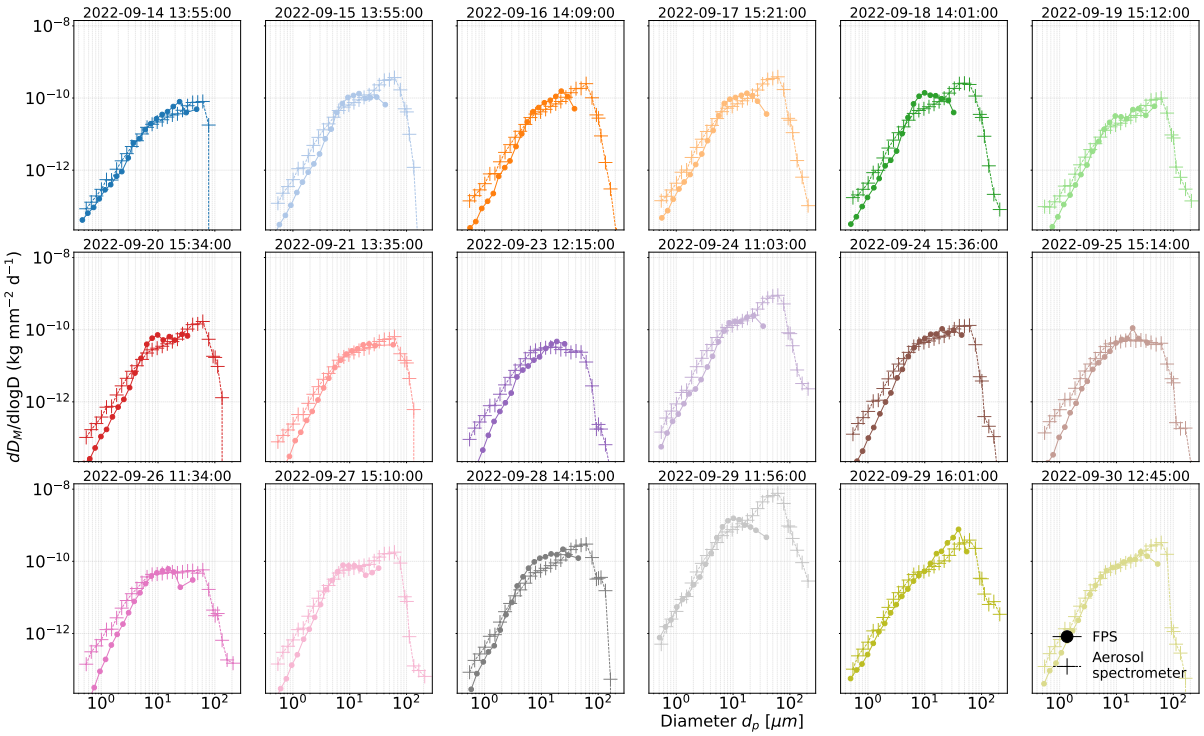

Figure 5.16.: Mean aerosol spectrometer mass deposition rates combined from SANTRI2, Welas and Fidas with the flat-plate sampler (FPS) within the sample time steps shown on top of every subplot and in Table 7.2. Error bars for FPS represent the statistical 95% confidence interval for $dD_M/dlogD$ (1.96 $\times$ standard deviation, estimated according to the Poisson distribution as square roots).

matching, deviation for $d_p \approx 1.2\,\mu m$ with less than 10 % deviation). However, in Panta et al. (2023), although the spectrometer measurements were conducted with a Fidas 200S (included in the averaged aerosol spectrometer data), a smaller size range ($d_p = 0.2 - 19\,\mu m$) was probed and a lower zoom was used for the SEM. In the smaller size range, inlet inefficiencies may have a negligible effect, as these particles are less likely to experience significant losses during sampling. Additionally, the re-binning of the FPS data in those studies was coarser, which may have reduced the observed differences.

The assumption of a constant deposition velocity to convert the aerosol spectrometer particle concentrations into deposition rates is a simplification that likely has not fully represented the actual deposition dynamics (Sect. 4.5). Larger particles are typically subject to higher gravitational settling velocities, whereas smaller particles are more influenced by atmospheric turbulence and Brownian motion. To evaluate the impact of this assumption, I tested alternative deposition velocity profiles, including those accounting for size-dependent settling relevant to large particles as described in Adebiyi et al. (2023). However, the constant deposition velocity provided the best agreement with the deposition patterns observed using the flat-plate samplers (FPS). This outcome may indicate that the rapid removal of large particles near emission sources, as estimated in Adebiyi et al. (2023), could be even more uncertain than previously thought, in line with earlier findings (van der Does et al., 2018; Adebiyi and Kok, 2020; Rat-

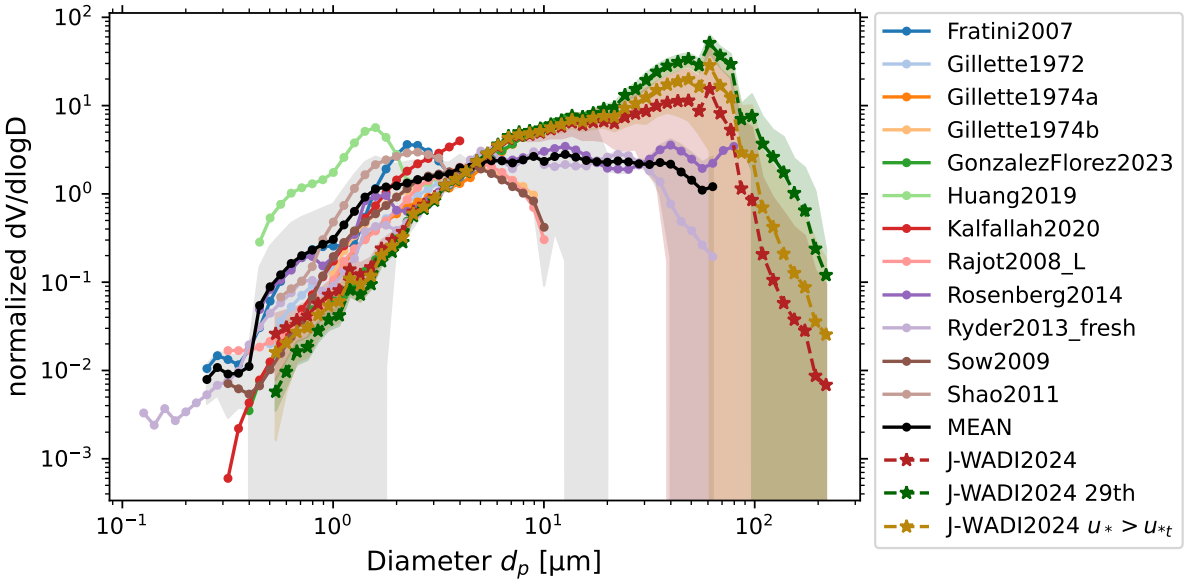

Figure 5.17.: "SOURCE" PSDs from different field campaigns within one day after emission from Formenti and Di Biagio (2024), all normalized at the integral of 1 between 1.58 and 7.1 µm before weighting by dlogD. The mean of PSDs ("MEAN"), where at least two datasets are available in the diameter range, is indicated in black and the standard deviation in gray. J-WADI results averaged over the entire campaign are shown in dark red, averaged for periods with active dust emission ($u_* > u_{*t}$) in gold and on 29 September, a particularly dusty day, during the most dusty period (between 9:30 and 17:15) in dark green with shaded areas indicating the standard deviations across time.

cliffe et al., 2024). As discussed in Sect. 4.1, the assumption that particles attain their terminal settling velocity may not hold under turbulent flow conditions. Furthermore, the FPS may inherently overestimate the abundance of large particles, since smaller particles—being more coupled to the airflow—are less likely to be deposited onto the collection surface. This could explain why assuming lower settling velocities for larger particles improves the agreement with FPS measurements. Nonetheless, a more refined approach incorporating size-dependent deposition velocities could potentially offer a more accurate representation of particle behavior. Yet, the alignment of the constant-velocity approximation with the FPS observations raises important questions regarding the underlying deposition processes of super-coarse and giant particles.

5.7. Comparative analysis of J-WADI data with other field campaigns

To contextualize the findings from the current study, I compared the results with previous research on mineral dust size distributions. Formenti and Di Biagio (2024) conducted a comprehensive analysis of mineral dust aerosol size distributions, synthesizing data from more than 50 years of in situ field observations to create a harmonized dataset. They organized dust size distributions by the stage in the dust transport life cycle: source (SOURCE, within one day after emission), mid-range transport (MRT, one to four days of transport), and long-range transport (LRT, more than four days of transport). Here, I

compare the J-WADI dataset with the Formenti and Di Biagio (2024) SOURCE dataset, acknowledging that their conversion to geometric diameters was not completely equal to the ones we applied. Most of the measurements presented in Formenti and Di Biagio (2024) were ground-based and taken at heights of a few meters above the surface, similar to J-WADI, but the data from Rosenberg et al. (2014) and Ryder et al. (2013b) are aircraft-based and at heights where smaller concentrations of larger particles are expected. The compiled campaigns are summarized in Tab. 2.1. It has to be noted that particle diameters $d_p > 30\,\mu m$ were only covered by the aircraft-based measurements and in none of the ground-based studies.

Figure 5.17 compares the SOURCE volume concentration PSDs from different field campaigns as compiled by Formenti and Di Biagio (2024). The mean for at least two PSDs from the Formenti and Di Biagio (2024) dataset is indicated in black (MEAN), with the standard deviation in gray. The averaged J-WADI data over the whole campaign, including dusty periods and non-dusty periods, are shown in dark red. As an example for dusty conditions, I also present results during daytime (10:00-15:30 UTC) on 29 September 2022, which is depicted in dark green, with shaded areas indicating the standard deviation. Data for active dust emission ($u_{*t} > 0.22\,m\,s^{-1}$, Sects. 4.3, 5.1) are indicated in gold. The averaged J-WADI data show reasonable agreement with the averaged SOURCE dataset from Formenti and Di Biagio (2024), demonstrating overall consistency in the general shape of the PSDs. However, differences are evident: For fine and coarse particles up to around 5 µm, the J-WADI PSD exhibits lower values compared to Formenti and Di Biagio (2024), while for larger particles, the J-WADI PSD is increased and extends to even larger particle diameters. This behavior becomes more pronounced in the data for active dust emission and even more in the data from 29 September, where the PSD reveals a distinct enhancement in the super-coarse and giant particle size ranges. In the averaged dataset from Formenti and Di Biagio (2024) (Fig. 5.17, black line), no clear maximum in the volume concentration PSD is observed. In contrast, a peak around 60 µm is visible in all three J-WADI datasets.

Table 5.1.: Comparison of volume size distribution percentages across different particle diameter ranges for the SOURCE dataset from Formenti and Di Biagio (2024) and from J-WADI (this study).

Dataset	$D \leq 2.5\,\mu m$	$2.5 < D \leq 10\,\mu m$	$10 < D \leq 62.5\,\mu m$	$D > 62.5\,\mu m$
SOURCE (Formenti et al., 2024)	10.8%	34.9%	52.7%	1.6%
J-WADI complete measurement period	1.3%	21.5%	63.9%	13.3%
J-WADI 29 September 2022	0.3%	7.8%	57.4%	34.5%
J-WADI $u_* > u_{*t}$	0.7%	13.7%	60.4%	25.2%

Compared to the averaged SOURCE data, the normalized and averaged J-WADI dataset suggests a shift in the emitted dust size distribution toward coarser particles (Table 5.1). While Formenti and Di Biagio (2024) reported a fine particle ($< 2.5\,\mu m$) contribution of 10.8%, the J-WADI dataset shows only 1.3%, indicating a lower proportion of fine particles in the J-WADI measurements. The fraction of 2.5 — 10 µm particles is also smaller during J-WADI (34.9% vs. 21.5%). In contrast, the J-WADI results indicate a

higher proportion of super-coarse particles (52.7% vs. 63.9%) and much higher fraction of giant particles (>62.5 µm; 1.6% vs. 13.3%).

During periods of active dust emission (i.e. for $u_* > u_{*t}$), the contributions of fine, coarse, and super-coarse particles decreased (0.7%, 1.7%, and 60.4%, respectively), whereas the percentage of giant particles increased to 25.2% (Table 5.1). This behavior is even enhanced on 29 September, a particularly dusty day, where we found even lower fine and coarse particle fractions (0.3% and 7.8%). With 57.4%, the contribution of the super-coarse range was also lower on 29 September, but more similar to SOURCE (52.7%). The giant particle fraction with 34.5% is significantly increased for 29 September in comparison to the average J-WADI data (13.3%), J-WADI active dust emission periods (25.2%), and especially the SOURCE data (1.6%). Overall, dust emission in J-WADI was characterized by a smaller proportion of smaller particles (fine, coarse) and a larger proportion of larger particles (super-coarse and giant) compared to the reference data.

For $u_* > u_{*t}$ and 29 September J-WADI data, I included measurements taken during active dust emission. These conditions are similar to aircraft campaigns as for the two datasets including $d_p > 20\,\mu m$ (Ryder et al., 2013b; Rosenberg et al., 2014), where they actively targeted dust outflow regions and therefore tended to sample elevated dust concentrations. On the other hand, the J-WADI campaign was conducted directly at an emission source, where a higher fraction of super-coarse and giant particles is expected, as these larger particles are more likely to settle out of the atmosphere before reaching greater height and distance from the source and may explain the elevated contributions of super-coarse and giant particles in my averaged data over the whole campaign. This proximity to emission sources in J-WADI may therefore explain the increased contributions of super-coarse and giant particles in my data.

6. Conclusions and Outlook

An in-depth understanding of the full size distribution of mineral dust at emission and its behavior during atmospheric transport is crucial for an accurate representation in climate models and for assessing dust impacts on the climate and Earth systems. Large particles remain significantly underrepresented in models, largely due to an incomplete understanding of their physical behavior. This challenge is further compounded by the scarcity of observational data, as the measurement of large particles involves considerable technical and conceptual difficulties. With this doctoral thesis, I contributed to advancing our understanding of the full size distribution of mineral dust at emission, especially in the super-coarse and giant range, based on measurements from J-WADI, an intensive dust field campaign conducted in Wadi Rum, Jordan.

The main outcomes obtained in this thesis are outlined in Sect. 6.1 and compared to the objectives formulated in Chapter 3 (Fig. 6.1). The subsequent Sect. 6.2 discusses potential future research based on these findings.

6.1. Conclusions

The data collected during J-WADI have provided valuable insights into the size distribution of mineral dust particles ranging from ~0.4 to 200 µm at a desert emission source in Wadi Rum, Jordan (Objective 1, Chapter 3). This study is the first to encompass such a broad range of particle diameters directly at the emission source, with a particular emphasis on super-coarse ($10 < d_p \leq 62.5\,\mu m$) and giant ($d_p > 62.5\,\mu m$) particles.

A key feature of this study was the utilization of a diverse set of aerosol spectrometers, including active, passive, and open-path devices, and their comparison with physical samples from a flat-plate sampler. The aerosol spectrometers covered different size ranges that were partly complementary to extend the overall observed size range, and partly overlapping to enable systematic intercomparison and validation. While agreement in mass concentrations was good for smaller particle sizes, discrepancies arose for particles with $d_p > 10\,\mu m$, largely due to differences in measurement principles (*e.g.*, light source and the illumination of the particles), size ranges (sensitivity limitations), and inlet effects. By applying the correction and harmonization techniques developed in Chapter 4, data from multiple instruments with overlapping size ranges could be successfully merged, resulting in coherent and robust PSDs. These methods include the correction of outliers, especially from the SANTRI2 instruments, the conversion of all data to a common diameter definition, namely the geometric diameter, systematic bias correction

Summary of main outcomes aligned with objectives

Objective 1 – Measurement: Successfully measured near-surface dust concentrations from 0.4–200 µm during J-WADI, capturing the full PSD, including super-coarse and giant particles, under varying meteorological conditions.

Objective 2 – Instrument evaluation: Identified and addressed challenges in large particle detection due to inlet inefficiencies and sensitivity limits, confirmed through cross-instrument comparison and physical sampling.

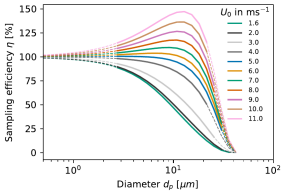

Objective 3 – Harmonization methods: Developed and applied robust methods to merge overlapping instruments, including outlier correction, diameter conversion, bias adjustment, and rebinning—yielding consistent, reliable PSDs.

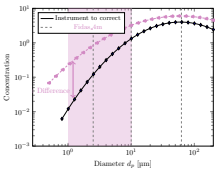

Objective 4 – Particle occurrence: Super-coarse and giant particles dominated during J-WADI with PSD peaks around 60 µm and significant contributions of up to ∼90% in the super-coarse and giant size range.

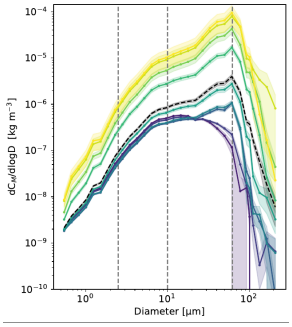

Objective 5 – PSD Variability: Demonstrated that PSD varies strongly with friction velocity and slightly with atmospheric stability, with highest large-particle concentrations under neutral and unstable conditions.

Figure 6.1.: Conclusion and alignment with objectives.

through intercomparison of identical instrument types, and subsequent bin-wise adjustment, harmonization of concentration levels by scaling all measurements to a reference instrument, and the development of a rebinning approach to unify the PSDs across different instruments. This approach offers a transferable framework for future measurement campaigns to obtain consistent and harmonized particle size distributions (Objective 3). During J-WADI, a peak in mass concentration PSD during periods of active emission was observed at around 60 µm (Objective 4), although the detection of larger particles was likely constrained by inlet inefficiencies (calculated cut-off diameter ∼30 µm for Welas, compared to no restrictions for inlet-free SANTRI2s) and instrument insensitivity near the limits of their size ranges (Objective 2). The results show that during active dust emission events, when the threshold friction velocities (u_{*t} = 0.22 m s^{-1}) was exceeded, 0.7 % of the mass concentration was found in the fine, 13.7 % in the coarse, 60.4 % in the super-coarse range and 25.2 % in the giant range during active dust emission. Data averaged over the whole campaign (including periods of calm winds) showed a significant shift to-

ward the fine and coarse size fractions (1.3%, 21.5 %, 63.9 % and 13.3 %) with larger proportions in the super-coarse and giant ranges compared to findings from previous studies as compiled in Formenti and Di Biagio (2024) (Objective 4). I found that with higher friction velocities (u_*) and under (near) unstable and neutral atmospheric stability conditions, dust concentrations were highest and the abundance of super-coarse and giant particles was largest (Objective 5). Physical samples collected using a flat-plate sampler largely confirmed the PSDs derived from aerosol spectrometers.
The results highlight the challenges in accurately quantifying giant particles but also demonstrate strategies to overcome them. Despite these challenges, the results demonstrate a remarkably high abundance of super-coarse and giant particles in emitted dust. This emphasizes the need to account for the full PSD, including super-coarse and giant particles, in future studies. By improving our knowledge of the size distribution and abundance of super-coarse and giant particles directly after their emission, the foundation for unraveling their evolution during atmospheric transport and their broader impacts on the climate system is laid. Incorporating more accurate PSDs, particularly of super-coarse and giant particles, into dust models is essential for improving predictions of long-range dust transport, cloud microphysics, and radiative forcing. These advances will ultimately enable better assessments of the environmental and climatic impacts of mineral dust.

6.2. Outlook

The work presented in this PhD thesis serves as a basis for future studies aimed at improving our understanding of the variability and mechanisms driving the full PSD at emission. Based on the insights gained, the following directions are suggested:

1. **Guidelines for measuring the full PSD:**

    - It is strongly recommended that future campaigns employ multiple instruments with overlapping size ranges to ensure full PSD coverage and compensate for limitations inherent to individual measurement principles, especially when measuring super-coarse and giant particles. This particle range should not be neglected as this work has shown. The correction and harmonization methods developed here can serve as a guideline for combining measurements from different instruments for which intercomparison periods between instruments are essential. This includes systematic outlier correction and inter-instrument comparison techniques to derive consistent PSDs across devices regardless of different instrument types.
    - For the super-coarse and giant particle range, if possible, inlet-free instruments should be used as I calculated high sampling losses for those with inlets. When conducting measurements with instruments with inlets, the expected losses should be characterized and, if possible, corrected. In this work, among the inlet-free instruments, the SANTRI2 emerged as a promising candidate for measuring super-coarse and giant particles. However, the cause of

occasional outliers needs further investigation and mitigation, particularly for the two units excluded from analysis due to an insufficient signal-to-noise ratio.

2. **J-WADI dataset in the context of super-coarse and giant particles:** The dataset of J-WADI retrieved and harmonized in this study is very valuable as it is the first which measured the full PSD directly after emission. Further analysis will provide additional information on the behavior of super-coarse and giant particles during emission and near-surface transport. For this purpose, it should be further analyzed regarding:

   - the meteorologic conditions, *e.g.*, wind lidar data or high frequency wind data collected during J-WADI to extend the knowledge of the role of turbulence in the super-coarse and giant particle dynamics.
   - the shape of particles to gain insights about the influence of shape on the dynamics in every size range regarding uplift and sustaining of super-coarse and giant particles.
   - the role of gentle topography could be explored, as one UCASS instrument was mounted on a meteorological mast on a hill downwind of the main measurement site, where the other two were positioned at the main site, once the bin classification of the UCASSs is clarified (Sect. 4.4.7).
   - the inclusion of a more realistic particle shape, *i.e.*, triaxial (in this study biaxial), once databases for giant particles are available for the conversion from optical to geometric diameter. This helps to decrease uncertainties in the harmonization of PSDs of different measurement principles, *i.e.*, different diameter types.
   - inlet and flow characterization. Both for inlets and open-path instruments, better characterization of flow dynamics is essential. Since the inlet efficiency calculations applied in this study appear to underestimate particle transmission for $d_p > 30\,\mu\text{m}$, numerical simulations should be conducted to better quantify these effects. Numerical simulations should be used to understand and correct particle losses and discrepancies between sampled and measured aerosol concentrations. Additional research is needed to better understand the influence of flat-plate sampler flow dynamics on the measured PSDs, especially for capturing the largest particles, and to refine techniques for comparing flat-plate sampler results with those from optical spectrometers.
   - emission fluxes for the full size distribution of mineral dust by calculating them from PSDs in different heights. However, for these calculations, alternative approaches beyond the flux-gradient or eddy-covariance methods need to be developed, as both methods have limitations when applied to the super-coarse and giant particle size ranges.

3. **Further harmonizing PSDs across studies:** There is a need to unify concentrations and diameter conversions from the measurements of distinct instruments to make results from different campaigns comparable across aerosol spectrometer and also physical samples to enhance comparability and reduce interpretation errors. Future research should focus on a better characterization of (1) particle shape and (2) refractive index for different size ranges of the PSD, especially super-coarse and giant particles from different source regions, to refine the conversion between varying equivalent diameters (*e.g.*, geometric, aerodynamic, and projected area). This would enable a better comparison across studies and a deeper understanding of the full PSD.

4. **Modeling applications:** The comprehensive PSD dataset collected during J-WADI should be utilized to evaluate and improve dust emission and transport parameterizations in atmospheric models, with an emphasis on better representing the super-coarse and giant particle size ranges. This lays the foundation for decreasing uncertainties regarding mineral dust impacts in atmospheric models.

7. Appendix

7.1. Selection of measurements in different stages of the mineral dust cycle

Table 7.1 provides an overview of selected field measurements in which the particle size distribution (PSD) of mineral dust was retrieved.

Table 7.1.: Selection of measurements in different stages of the mineral dust cycle: emission, transport, and deposition. The dataset was compiled by Formenti and Di Biagio (2024).

Citation	**Campaign**	**Device(s) Used**	**Diameter Type**	**Size Range (μm)**	**Location**
Gillette et al. (1972, 1974); Gillette (1974)	-	Impactors	Projected-area	1–20	Texas, Nebraska (Ground-based)
Schütz et al. (1981)	-	Microscopy	Projected-area	-	Atlantic Ocean (Ship-based)
d'Almeida (1987)	-	Microscopy	Projected-area	-	Senegal, Mali, Niger (Ground-based)
de Reus et al. (2000)	ACE-2	DMPS + OPC	Geometrical	0.02–31	Canary Islands (Airborne)
Maring et al. (2000)	-	SMPS + APS	Geometrical	0.013–15	Tenerife (Ground-based)
Formenti et al. (2001)	CLAIRE-98	Cascade impactor	Aerodynamic	0.045–8.5	Brazil (Ground-based)
Bates et al. (2002)	INDOEX	DMPS + APS	Geometrical	0.02–7	Indian Ocean (Ground-based)
Maring et al. (2003)	PRIDE	SMPS + APS	Geometrical	0.013–15	Puerto Rico (Ground-based)
Reid et al. (2003a)	PRIDE	Microscopy	Projected-area	Up to 20	Puerto Rico (Airborne)
Reid et al. (2003b)	PRIDE	Cascade impactor, OPC	Geometrical, Optical	Up to 22	Puerto Rico (Ground-based, Airborne)
Clarke et al. (2004)	ACE-Asia, TRACE-P	OPC	Optical	0.1–10	Sea of Japan (Airborne)
Fratini et al. (2007)	-	OPC	Geometrical	0.35–9.5	Gobi Desert (Ground-based)

Kobayashi et al. (2007)	-	Coulter Multisizer	Geometrical	0.4–12	Japan (Ground-based)
Otto et al. (2007)	ACE-2	DMA + OPC	Optical	0.02–31	Canary Islands (Airborne)
Chou et al. (2008)	AMMA/DABEX	Microscopy	Projected-area	0.01–10	West Africa, Sahel (Airborne)
McConnell et al. (2008)	DODO	OPCs	Optical	Up to 40	Senegal (Airborne)
Osborne et al. (2008)	AMMA/DABEX	OPC	Optical	0.1–10	Sahel (Airborne)
Rajot et al. (2008)	AMMA	OPC	Optical	Up to 30	Niger (Ground-based)
Reid et al. (2008)	UAE2	APS	Aerodynamic	Up to 15	UAE (Ground-based)
Sow et al. (2009)	-	OPC	Optical	>0.3	Niger (Ground-based)
Wagner et al. (2009)	DAPRO (SAMUM)	OPC	Geometrical	0.01–35	Portugal (Airborne)
Weinzierl et al. (2009)	SAMUM1	OPCs + CPCs	Geometrical	0.1–50	Morocco (Airborne)
Müller et al. (2010)	RHaMBLe	SMPS + APS	Geometrical	0.01–10	Cape Verde (Ground-based)
Chen et al. (2011)	NAMMA	USHAS + APS	Geometrical	0.07–5	Tropical Atlantic (Airborne)
Formenti et al. (2011)	AMMA	OPC	Geometrical	0.1–9	Niger (Airborne)
Johnson and Osborne (2011)	GERBILS	OPCs	Geometrical	0.1–60	Western Sahara (Airborne)
Kandler et al. (2011)	SAMUM2	DMPS + APS + Microscopy	Projected-area	0.04–500	Cape Verde (Ground-based)
Shao et al. (2011a)	JADE	OPC	Geometrical	0.3–8.4	Australia (Ground-based)
Weinzierl et al. (2011)	SAMUM2	OPCs	Geometrical	0.1–30	Cape Verde (Airborne)
Jung et al. (2013)	BACEX	OPC	Optical	0.1–2.5	Barbados (Airborne)
Ryder et al. (2013a,b)	FENNEC	OPC + OAP	Geometrical	0.1–100	Western Africa (Airborne)
Rosenberg et al. (2014)	FENNEC	OPC + OAP	Geometrical	0.5–300	Western Africa (Airborne)
Meloni et al. (2015)	GAMARF	OPC	Optical	0.3–20	Lampedusa, Italy (Airborne)
Denjean et al. (2016b)	Dust-ATTACk	SMPS + OPC	Geometrical	0.011–32	Puerto Rico (Ground-based)

Denjean et al. (2016a)	ChArMEx/ ADRIMED	SMPS + OPCs	Geometrical	0.01–12	Mediterranean Basin (Airborne)
Struckmeier et al. (2016)	DIAPASON	APS	Aerodynamic	0.5–20	Rome, Italy (Ground-based)
Weinzierl et al. (2017)	SALTRACE	OPCs	Geometrical	0.06–50	Atlantic Ocean (Airborne)
Moran Zuloaga et al. (2018)	GoAmazon	OPC	Optical	0.3–10	ATTO, Brazil (Ground-based)
Renard et al. (2018)	ChArMEx	OPC	Optical	-	Mediterranean Basin (Airborne)
Ryder et al. (2018)	AER-D	OPC + CIP	Geometrical	0.1–100	Cape Verde (Airborne)
Huang et al. (2019)	-	OPC	Geometrical	0.49–7	California, USA (Ground-based)
Khalfallah et al. (2020)	WIND-O-V's	OPC	Geometrical	-	Tunisia (Ground-based)
González-Flórez et al. (2023)	FRAGMENT	OPC	Geometrical	0.2–19.1	Moroccan Sahara (Ground-based)

7.2. PSD assuming triaxial ellipsoid

Here, I present the same figures as in Section 5 but instead of biaxial ellipsoid particles, I assumed triaxial ellipsoids for the transformation to geometric diameters. The overall results remain the same but especially the peak of the PSDs shifted to 50 µm (~60 µm for biaxial ellipsoids) and the shape of the PSDs differs slightly.

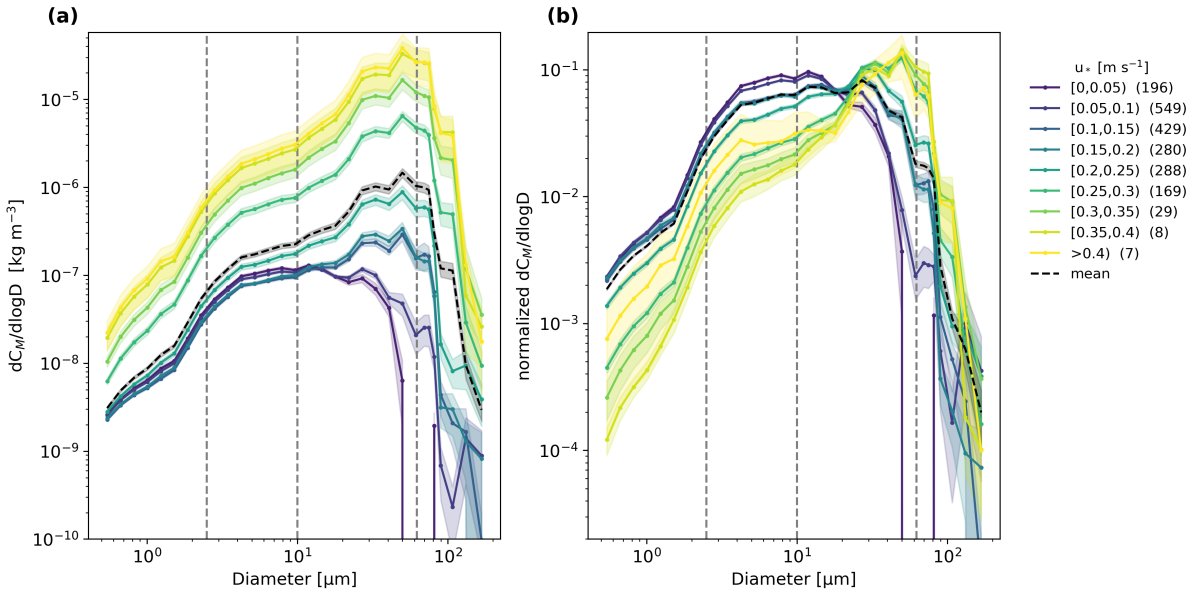

Figure 7.1.: (a) Variability of mass concentration PSD with u_* deduced from SANTRI2, Welas and Fidas assuming triaxial particles over the whole campaign time. Colors indicate u_* during the 15-min averaging time period corresponding to the PSDs. Shaded areas depict the standard error of PSDs within each class across different time steps, and the black dashed line the mean of all PSD. Numbers in parentheses indicate the number of 15-min PSDs taken into account in each u_* range. Dashed lines indicate the size ranges of the dust size classifications (Adebiyi et al., 2023). (b) Same as (a) but normalized to unity in each time interval.

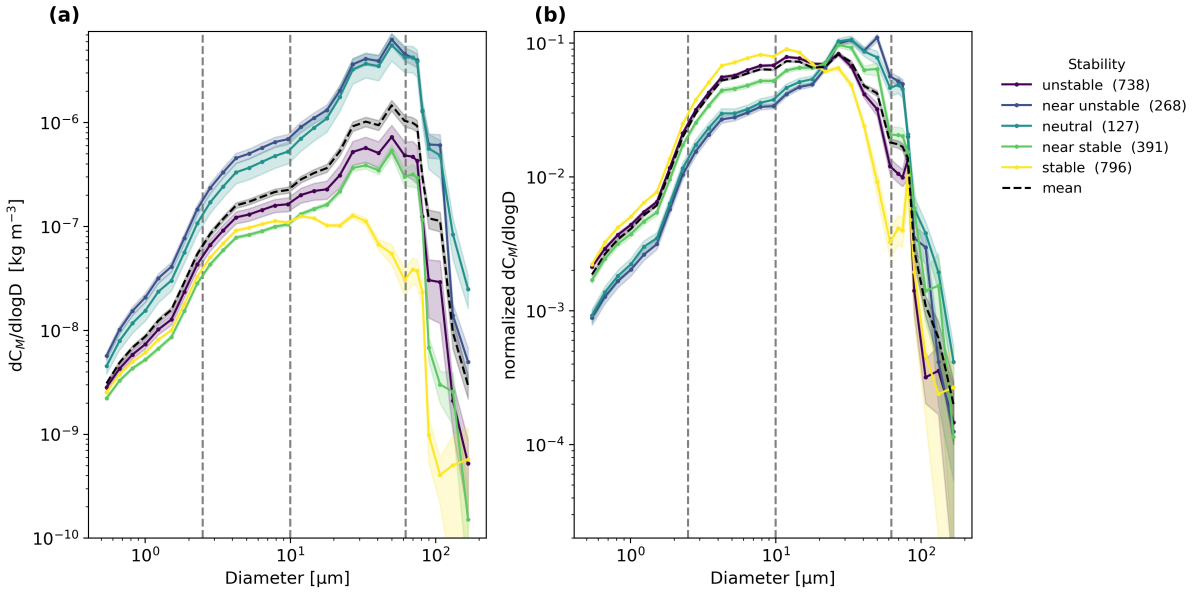

Figure 7.2.: (a) Variability of mass concentration PSD deduced from SANTRI2, Welas and Fidas assuming triaxial particles over the whole campaign time with atmospheric stability. The colors indicate different stability ranges and shaded areas the standard error of PSDs within each class across different time steps, and the black line the mean of all PSD. Numbers in parentheses indicate the number of PSDs available within each stability class. Dashed lines indicate the size ranges of the dust size classifications (Adebiyi et al., 2023). (b) Same as (a) but normalized to unity in each time interval.

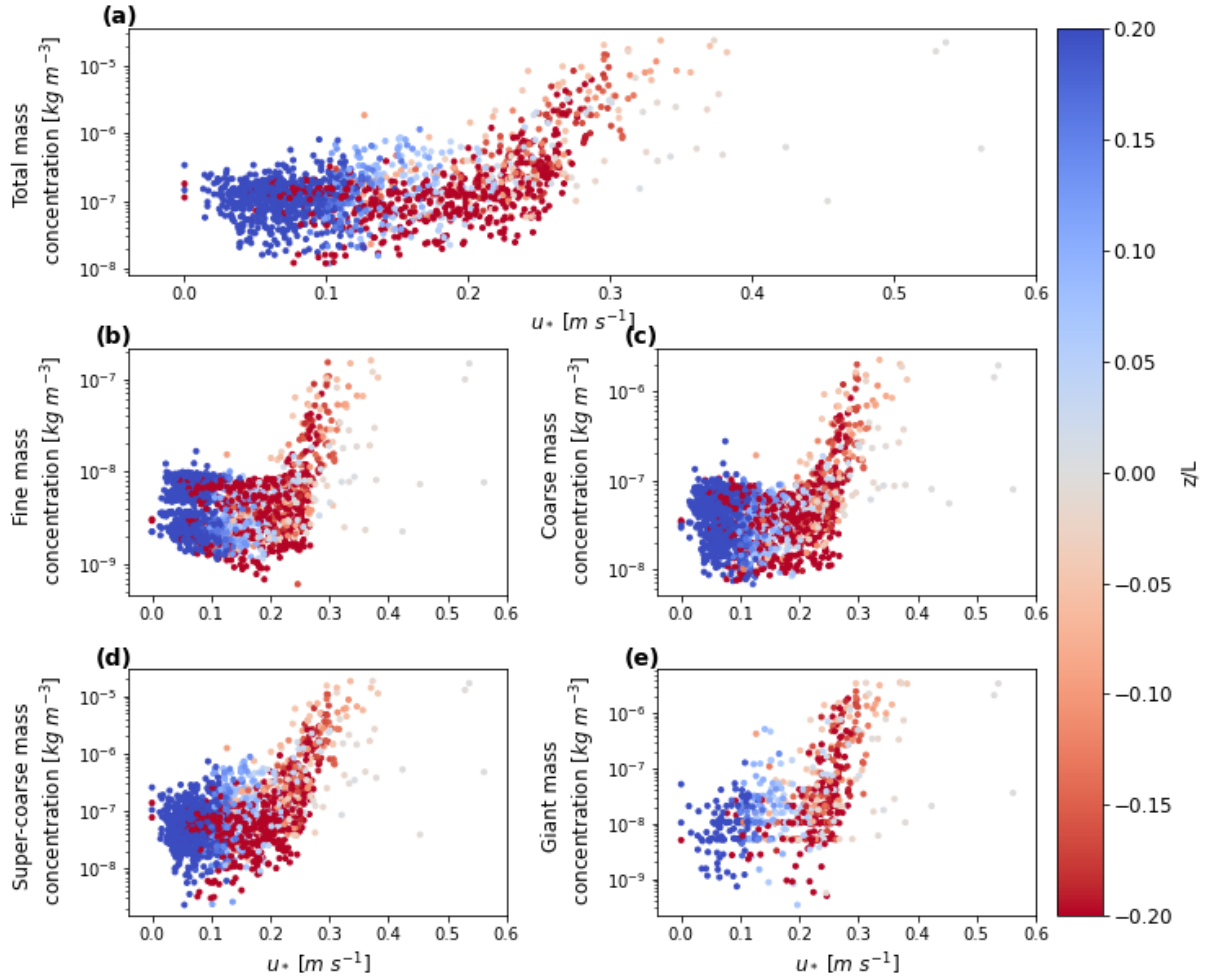

Figure 7.3.: Mass concentration deduced from SANTRI2, Welas and Fidas assuming triaxial ellipsoids over the whole campaign time over u_*. The colors indicate the different stability regimes in terms of z/L for (a) total, (b) fine, (c) coarse, (d) super-coarse, and (e) giant dust mass concentration.

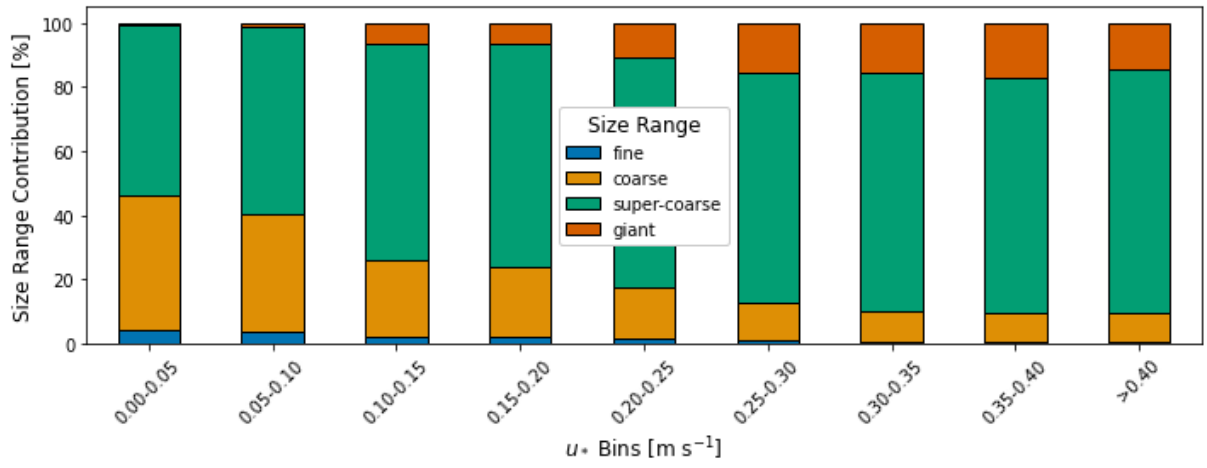

Figure 7.4.: Percentage mass concentration abundance of particle size ranges deduced from SANTRI2, Welas and Fidas assuming triaxial particles over the whole campaign time with u_*.

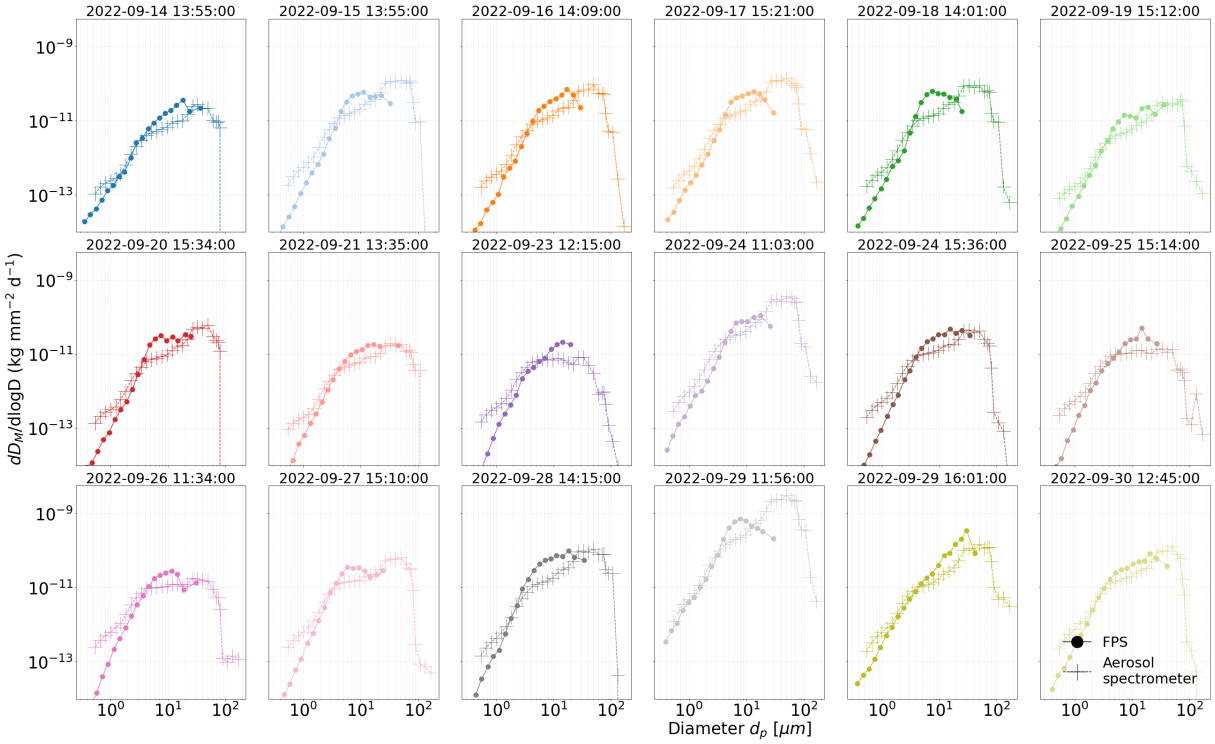

Figure 7.5.: Mean aerosol spectrometer mass deposition rates from SANTRI2, Welas and Fidas assuming triaxial ellipsoids with the flat-plate sampler (FPS) within the sample time steps shown one top of every subplot and in Table 7.2.

7.3. PSD and heat flux

Figure 7.6 illustrates the influence of heat flux on the shape of the PSDs. While no clear trend is observed overall, higher heat fluxes appear to slightly enhance the presence of particles in the 20–60µm size range. It is worth noting that for heat fluxes > 200 Wm^{-2} few data were recorded.

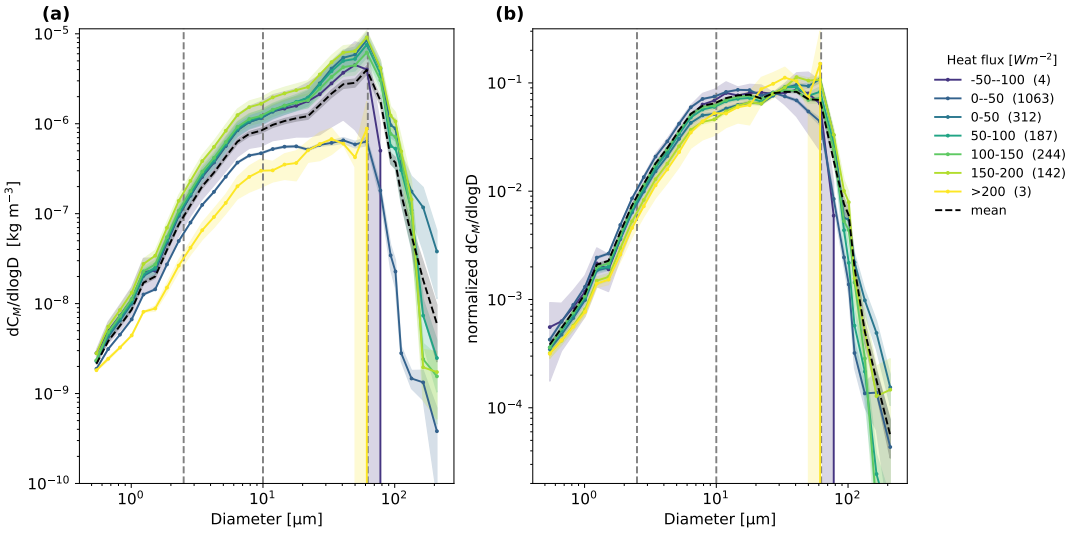

Figure 7.6.: (a) Variability of mass concentration PSD with heat flux deduced from SANTRI2, Welas and Fidas assuming triaxial particles over the whole campaign time. Colors indicate heat flux during the 15-min averaging time period corresponding to the PSDs. Shaded areas depict the standard error of PSDs within each class across different time steps, and the black dashed line the mean of all PSD. Numbers in parentheses indicate the number of 15-min PSDs taken into account in each heat flux range. Dashed lines indicate the size ranges of the dust size classifications (Adebiyi et al., 2023). (b) Same as (a) but normalized to unity in each time interval.

7.4. Time step information on the sampling periods of the FPS samples

The table below shows the sample time for each FPS sample as collected in the field. The corresponding mass deposition fluxes are shown in Figure 5.16.

Table 7.2.: Time step information on the sampling periods of the FPS samples.

sample code	start timecode (UTC)	stop timecode (UTC)	sample code	start timecode (UTC)	stop timecode (UTC)
WRS_01	12.09.2022 13:55	13.09.2022 13:55	WRS_12	24.09.2022 11:03	24.09.2022 15:36
WRS_02	13.09.2022 13:55	14.09.2022 13:55	WRS_13	24.09.2022 15:36	25.09.2022 15:14
WRS_03	14.09.2022 13:55	15.09.2022 13:55	WRS_14	25.09.2022 15:14	26.09.2022 11:32
WRS_04	15.09.2022 13:55	16.09.2022 14:09	WRS_15	26.09.2022 11:34	27.09.2022 15:02
WRS_05	16.09.2022 14:09	17.09.2022 15:21	WRS_16	27.09.2022 15:10	28.09.2022 14:15
WRS_06	17.09.2022 15:21	18.09.2022 14:01	WRS_17	28.09.2022 14:15	29.09.2022 11:56
WRS_07	18.09.2022 14:01	19.09.2022 15:12	WRS_18	29.09.2022 11:56	29.09.2022 16:01
WRS_08	19.09.2022 15:12	20.09.2022 15:34	WRS_19	29.09.2022 16:01	30.09.2022 12:45
WRS_09	20.09.2022 15:34	21.09.2022 13:35	WRS_20	30.09.2022 12:45	01.10.2022 15:54
WRS_10	21.09.2022 13:35	23.09.2022 12:15	WRS_21	01.10.2022 15:54	02.10.2022 15:23
WRS_11	23.09.2022 12:15	24.09.2022 11:03			

A. Bibliography

Adebiyi, A., J. F. Kok, B. J. Murray, C. L. Ryder, J. B. W. Stuut, R. A. Kahn, P. Knippertz, P. Formenti, N. M. Mahowald, C. P. García-Pando, M. Klose, A. Ansmann, B. H. Samset, A. Ito, Y. Balkanski, C. D. Biagio, M. N. Romanias, Y. Huang, and J. Meng, 2023: A review of coarse mineral dust in the earth system. *Aeolian Research*, **60**, 100 849.

Adebiyi, A. A. and J. F. Kok, 2020: Climate models miss most of the coarse dust in the atmosphere. *Science Advances*, **6 (15)**, URL `https://advances.sciencemag.org/content/6/15/eaaz9507`, `https://advances.sciencemag.org/content/6/15/eaaz9507.full.pdf`.

Ageitos, M. G., V. Obiso, R. L. Miller, O. Jorba, M. Klose, M. Dawson, Y. Balkanski, J. Perlwitz, S. Basart, E. D. Tomaso, J. Escribano, F. MacChia, G. Montané, N. M. Mahowald, R. O. Green, D. R. Thompson, and C. P. García-Pando, 2023: Modeling dust mineralogical composition: sensitivity to soil mineralogy atlases and their expected climate impacts. *Atmospheric Chemistry and Physics*, **23**, 8623–8657.

Albani, S., 2021: Mineral dust in PMIP simulations: A short review. *Past Global Changes Magazine*, **29 (2)**, 86–87, URL `http://dx.doi.org/10.22498/pages.29.2.86`.

Alfaro, S. C., A. Gaudichet, L. Gomes, and M. Maillé, 1997: Modeling the size distribution of a soil aerosol produced by sandblasting. *Journal of Geophysical Research: Atmospheres*, **102**, 11 239–11 249, URL `https://onlinelibrary.wiley.com/doi/full/10.1029/97JD00403https://onlinelibrary.wiley.com/doi/abs/10.1029/97JD00403https://agupubs.onlinelibrary.wiley.com/doi/10.1029/97JD00403`.

Alfaro, S. C. and L. Gomes, 2001: Modeling mineral aerosol production by wind erosion: Emission intensities and aerosol size distributions in source areas. *Journal of Geophysical Research: Atmospheres*, **106**, 18 075–18 084, URL `https://onlinelibrary.wiley.com/doi/full/10.1029/2000JD900339https://onlinelibrary.wiley.com/doi/abs/10.1029/2000JD900339https://agupubs.onlinelibrary.wiley.com/doi/10.1029/2000JD900339`.

Anaya, S. G. M., D. Althausen, M. Faust, H. Baars, B. Heinold, J. Hofer, I. Tegen, A. Ansmann, R. Engelmann, A. Skupin, B. Heese, and K. Schepanski, 2024: The implementation of dust mineralogy in cosmo5.05-muscat. *Geoscientific Model Development*, **17**, 1271–1295.

Ansell, C., H. E. Brindley, Y. Pradhan, and R. Saunders, 2014: Mineral dust aerosol net direct radiative effect during GERBILS field campaign period derived from SEVIRI and GERB. *Journal of Geophysical Research: Atmospheres*, **119 (7)**, 4070–4086, URL http://dx.doi.org/10.1002/2013JD020681.

Baddock, M., L. Boskovic, C. Strong, G. Mctainsh, J. Bullard, I. Agranovski, and R. Cropp, 2013: Iron-rich nanoparticles formed by aeolian abrasion of desert dune sand. *Geochemistry, Geophysics, Geosystems*, **14**, 3720–3729, URL https://onlinelibrary.wiley.com/doi/full/10.1002/ggge.20229https://onlinelibrary.wiley.com/doi/abs/10.1002/ggge.20229https://agupubs.onlinelibrary.wiley.com/doi/10.1002/ggge.20229.

Baddock, M., P. Ginoux, J. Bullard, and T. Gill, 2016: Do modis-defined dust sources have a geomorphological signature? *Geophysical Research Letters*, **43**, 2606–2613.

Bagnold, R. A., 1937: The transport of sand by wind. *The Geographical Journal*, **89**, 409.

———, 1941: *The physics of blown sand and desert dunes*. William Morrow New York, xx, 265 p., 16 leaves of plates : pp.

Baluchova, B., P. Bačík, and A. Mamova, 2019: The Health Impact of Mineral Dust Air Pollution on the Global and Local Scale (on the example from Slovakia). *Neuro - Endocrinology Letters*.

Banks, J. R., H. E. Brindley, M. Hobby, and J. H. Marsham, 2014: The daytime cycle in dust aerosol direct radiative effects observed in the central Sahara during the Fennec campaign in June 2011. *Journal of Geophysical Research: Atmospheres*, **119 (24)**, URL http://dx.doi.org/10.1002/2014JD022077.

Barchyn, T. E. and C. H. Hugenholtz, 2011: Comparison of four methods to calculate aeolian sediment transport threshold from field data: Implications for transport prediction and discussion of method evolution. *Geomorphology*, **129**, 190–203.

Barkley, A. E., N. E. Olson, J. M. Prospero, A. Gatineau, K. Panechou, N. G. Maynard, P. Blackwelder, S. China, A. P. Ault, and C. J. Gaston, 2021: Atmospheric transport of north african dust-bearing supermicron freshwater diatoms to south america: Implications for iron transport to the equatorial north atlantic ocean. *Geophysical Research Letters*, **48**, e2020GL090476, URL https://onlinelibrary.wiley.com/doi/full/10.1029/2020GL090476https://onlinelibrary.wiley.com/doi/abs/10.1029/2020GL090476https://agupubs.onlinelibrary.wiley.com/doi/10.1029/2020GL090476.

Bates, T. S., D. J. Coffman, D. S. Covert, and P. K. Quinn, 2002: Regional marine boundary layer aerosol size distributions in the indian, atlantic, and pacific oceans: A comparison of indoex measurements

with ace–1, ace–2, and aerosols99. *Journal of Geophysical Research*, **107**, INX2 25–1–INX2 25–15, URL https://doi.org/10.1029/2001JD001174.

Berg, J., J. Mann, A. Bechmann, M. S. Courtney, and H. E. Jørgensen, 2011: The bolund experiment, part i: Flow over a steep, three-dimensional hill. *Boundary-Layer Meteorology*, **141**, 219–243, URL https://link.springer.com/article/10.1007/s10546-011-9636-y.

Bergametti, G. and G. Forêt, 2014: Dust deposition. *Mineral Dust: A Key Player in the Earth System*, Knippertz, P. and J.-B. W. Stuut, Eds., Springer Netherlands, Dordrecht, 179–200, URL https://doi.org/10.1007/978-94-017-8978-3_8.

Betzer, P. R., K. L. Carder, R. A. Duce, J. T. Merrill, and N. W. Tindale, 1988: Long-range transport of giant mineral aerosol particles. *Nature*, **336**, 568–571.

Biagio, C. D., J. F. Doussin, M. Cazaunau, E. Pangui, J. Cuesta, P. Sellitto, M. Ródenas, and P. Formenti, 2023: Infrared optical signature reveals the source–dependency and along–transport evolution of dust mineralogy as shown by laboratory study. *Scientific Reports 2023 13:1*, **13**, 1–14, URL https://www.nature.com/articles/s41598-023-39336-7.

Bryant, R., 2013: Recent advances in our understanding of dust source emission processes. *Progress in Physical Geography Earth and Environment*, **37**, 397–421.

Bullard, J. E., M. Baddock, T. Bradwell, J. Crusius, E. Darlington, D. Gaiero, S. Gassó, G. Gisladottir, R. Hodgkins, R. McCulloch, C. McKennaNeuman, T. Mockford, H. Stewart, and T. Thorsteinsson, 2016: High-latitude dust in the Earth system. *Reviews of Geophysics*, **54 (2)**, 447–485, URL http://dx.doi.org/10.1002/2016RG000518.

Bullard, J. E., G. H. McTainsh, and C. Pudmenzky, 2004: Aeolian abrasion and modes of fine particle production from natural red dune sands: an experimental study. *Sedimentology*, **51**, 1103–1125, URL https://onlinelibrary.wiley.com/doi/full/10.1111/j.1365-3091.2004.00662.xhttps://onlinelibrary.wiley.com/doi/abs/10.1111/j.1365-3091.2004.00662.xhttps://onlinelibrary.wiley.com/doi/10.1111/j.1365-3091.2004.00662.x.

Callot, Y., B. Marticorena, and G. Bergametti, 2000: Geomorphologic approach for modelling the surface features of arid environments in a model of dust emissions: application to the sahara desert. *Geodinamica Acta*, **13**, 245–270, URL https://doi.org/10.1080/09853111.2000.11105373https://scite.ai/reports/geomorphologic-approach-for-modelling-the-VXkpaJ.

Chen, G., L. D. Ziemba, D. A. Chu, K. L. Thornhill, G. L. Schuster, E. L. Winstead, G. S. Diskin, R. A. Ferrare, S. P. Burton, S. Ismail, S. A. Kooi, A. H. Omar, D. L. Slusher, M. M. Kleb, J. S. Reid, C. H. Twohy, H. Zhang, and B. E. Anderson, 2011: Observations of saharan dust microphysical and optical

properties from the eastern atlantic during namma airborne field campaign. *Atmospheric Chemistry and Physics*, **11**, 723–740, URL https://doi.org/10.5194/acp-11-723-2011.

Chen, S., N. Jiang, J. Huang, Z. Zang, X. Guan, X. Ma, Y. Luo, J. Li, X. Zhang, and Y. Zhang, 2019: Estimations of indirect and direct anthropogenic dust emission at the global scale. *Atmospheric Environment*, **200**, 50–60.

Cheng, N.-S., 1997: Simplified settling velocity formula for sediment particle. *Journal of Hydraulic Engineering*, **123**, 149–152, URL https://ascelibrary.org/doi/abs/10.1061/%28ASCE%290733-9429%281997%29123%3A2%28149%29https://ascelibrary.org/doi/10.1061/%28ASCE%290733-9429%281997%29123%3A2%28149%29.

Chepil, W. S., 1945: Dynamics of wind erosion: I. nature of movement of soil by wind. *Soil Science*, **60**, 305–320.

Chou, C., P. Formenti, M. Maille, P. Ausset, G. Helas, M. Harrison, and S. Osborne, 2008: Size distribution, shape, and composition of mineral dust aerosols collected during the african monsoon multidisciplinary analysis special observation period 0: Dust and biomass–burning experiment field campaign in niger, january 2006. *Journal of Geophysical Research*, **113**, URL https://doi.org/10.1029/2008JD009897.

Claquin, T., M. Schulz, and Y. J. Balkanski, 1999: Modeling the mineralogy of atmospheric dust sources. *Journal of Geophysical Research: Atmospheres*, **104**, 22 243–22 256, URL https://onlinelibrary.wiley.com/doi/full/10.1029/1999JD900416https://onlinelibrary.wiley.com/doi/abs/10.1029/1999JD900416https://agupubs.onlinelibrary.wiley.com/doi/10.1029/1999JD900416.

Clarke, A. D., Y. Shinozuka, V. N. Kapustin, S. Howell, B. Huebert, S. Doherty, T. Anderson, D. Covert, J. Anderson, X. Hua, K. G. Moore, C. McNaughton, G. Carmichael, and R. Weber, 2004: Size distributions and mixtures of dust and black carbon aerosol in asian outflow: Physiochemistry and optical properties. *Journal of Geophysical Research*, **109**, URL https://doi.org/10.1029/2003JD004378.

Cuesta, J., M. Eremenko, C. Flamant, G. Dufour, B. Laurent, G. Bergametti, M. Höpfner, J. Orphal, and D. Zhou, 2015: Three-dimensional distribution of a major desert dust outbreak over east asia in march 2008 derived from iasi satellite observations. *Journal of Geophysical Research: Atmospheres*, **120**, 7099–7127, URL https://onlinelibrary.wiley.com/doi/full/10.1002/2014JD022406https://onlinelibrary.wiley.com/doi/abs/10.1002/2014JD022406https://agupubs.onlinelibrary.wiley.com/doi/10.1002/2014JD022406.

d'Almeida, G. A., 1987: On the variability of desert aerosol radiative characteristics. *Journal of Geophysical Research: Atmospheres*, **92**, 3017–3026, URL https://doi.org/10.1029/JD092iD03p03017.

de Reus, M., F. Dentener, A. Thomas, S. Borrmann, J. Ström, and J. Lelieveld, 2000: Airborne observations of dust aerosol over the north atlantic ocean during ace 2: Indications for heterogeneous ozone destruction. *Journal of Geophysical Research*, **105**, 15 263–15 275, URL https://doi.org/10.1029/2000JD900164.

Delany, A. C., A. C. Delany, D. W. Parkin, J. J. Griffin, E. D. Goldberg, and B. E. Reimann, 1967: Airborne dust collected at barbados. *Geochimica et Cosmochimica Acta*, **31**, 885–909.

Denjean, C., F. Cassola, A. Mazzino, S. Triquet, S. Chevaillier, N. Grand, T. Bourrianne, G. Momboisse, K. Sellegri, A. Schwarzenbock, E. Freney, M. Mallet, and P. Formenti, 2016a: Size distribution and optical properties of mineral dust aerosols transported in the western mediterranean. *Atmospheric Chemistry and Physics*, **16**, 1081–1104, URL https://doi.org/10.5194/acp-16-1081-2016.

Denjean, C., P. Formenti, K. Desboeufs, S. Chevaillier, S. Triquet, M. Maillé, M. Cazaunau, B. Laurent, O. L. Mayol-Bracero, P. Vallejo, M. Quiñones, I. E. Gutierrez-Molina, F. Cassola, P. Prati, E. Andrews, and J. Ogren, 2016b: Size distribution and optical properties of african mineral dust after intercontinental transport. *Journal of Geophysical Research*, **121**, 7117–7138, URL https://doi.org/10.1002/2016JD024783.

Dentener, F. J., G. R. Carmichael, Y. Zhang, J. Lelieveld, and P. J. Crutzen, 1996: Role of mineral aerosol as a reactive surface in the global troposphere. *Journal of Geophysical Research: Atmospheres*, **101**, 22 869–22 889, URL https://onlinelibrary.wiley.com/doi/full/10.1029/96JD01818https://onlinelibrary.wiley.com/doi/abs/10.1029/96JD01818https://agupubs.onlinelibrary.wiley.com/doi/10.1029/96JD01818.

Di Biagio, C., Y. Balkanski, S. Albani, O. Boucher, and P. Formenti, 2020: Direct radiative effect by mineral dust aerosols constrained by new microphysical and spectral optical data. *Geophysical Research Letters*, **47**, e2019GL086 186, URL https://onlinelibrary.wiley.com/doi/full/10.1029/2019GL086186https://onlinelibrary.wiley.com/doi/abs/10.1029/2019GL086186https://agupubs.onlinelibrary.wiley.com/doi/10.1029/2019GL086186.

Di Biagio, C., P. Formenti, Y. Balkanski, L. Caponi, M. Cazaunau, E. Pangui, E. Journet, S. Nowak, M. O. Andreae, K. Kandler, T. Saeed, S. Piketh, D. Seibert, E. Williams, and J. F. Doussin, 2019: Complex refractive indices and single-scattering albedo of global dust aerosols in the shortwave spectrum and relationship to size and iron content. *Atmospheric Chemistry and Physics*, **19**, 15 503–15 531.

Dietze, V., M. Fricker, M. Goltzsche, and E. Schultz, 2006: Air quality measurement in german health resorts - part 1: Methodology and verification. *Gefahrstoffe Reinhaltung der Luft*, **66**, 45–53.

Drakaki, E., V. Amiridis, A. Tsekeri, A. Gkikas, E. Proestakis, S. Mallios, S. Solomos, C. Spyrou, E. Marinou, C. L. Ryder, D. Bouris, and P. Katsafados, 2022: Modeling coarse and giant desert dust particles. *Atmospheric Chemistry and Physics*, **22**, 12 727–12 748.

Dubovik, O. and M. D. King, 2000: A flexible inversion algorithm for retrieval of aerosol optical properties from sun and sky radiance measurements. *Journal of Geophysical Research*, **105**, 20 673–20 696, URL https://doi.org/10.1029/2000JD900282.

Dubovik, O., A. Sinyuk, T. Lapyonok, B. N. Holben, M. Mishchenko, P. Yang, T. F. Eck, H. Volten, O. Muñoz, B. Veihelmann, W. J. van der Zande, J.-F. Leon, M. Sorokin, and I. Slutsker, 2006: Application of spheroid models to account for aerosol particle non sphericity in remote sensing of desert dust. *Journal of Geophysical Research*, **111**, D11 208, URL https://doi.org/10.1029/2005JD006619.

Dufresne, J.-L., C. Gautier, P. Ricchiazzi, and Y. Fouquart, 2002: Longwave scattering effects of mineral aerosols. *Journal of The Atmospheric Sciences - J ATMOS SCI*, **59**, 1959–1966.

Dupart, Y., S. M. King, B. Nekat, A. Nowak, A. Wiedensohler, H. Herrmann, G. David, B. Thomas, A. Miffre, P. Rairoux, B. D'Anna, and C. George, 2012: Mineral dust photochemistry induces nucleation events in the presence of so2. *Proceedings of the National Academy of Sciences of the United States of America*, **109**, 20 842–20 847, URL https://www.pnas.org/doi/abs/10.1073/pnas.1212297109.

Dupont, J. et al., 2015: Near-surface dust flux enrichment in small articles during erosion events. *Geophysical Research Letters*, **42 (12)**.

Dupont, S., 2022: On the influence of thermal stratification on emitted dust flux. *Journal of Geophysical Research: Atmospheres*, **127**, e2022JD037 364, URL https://onlinelibrary.wiley.com/doi/full/10.1029/2022JD037364https://onlinelibrary.wiley.com/doi/abs/10.1029/2022JD037364https://agupubs.onlinelibrary.wiley.com/doi/10.1029/2022JD037364.

Dupont, S., M. Klose, M. R. Irvine, C. González-Flórez, A. Alastuey, J.-M. Bonnefond, P. Dagsson-Waldhauserova, A. Gonzalez-Romero, T. Hussein, E. Lamaud, H. Meyer, A. Panta, X. Querol, K. Schepanski, S. V. Palacio, A. Wieser, J. Yus-Díez, K. Kandler, and C. P. García-Pando, 2024: Impact of dust source patchiness on the existence of a constant dust flux layer during aeolian erosion events. *Journal of Geophysical Research: Atmospheres*, **129**, e2023JD040 657, URL https://onlinelibrary.wiley.com/doi/full/10.1029/2023JD040657https://onlinelibrary.wiley.com/doi/abs/10.1029/2023JD040657https://agupubs.onlinelibrary.wiley.com/doi/10.1029/2023JD040657.

Dupont, S., J. L. Rajot, E. Lamaud, G. Bergametti, M. Labiadh, B. Khalfallah, C. Bouet, B. Marticorena, and R. Fernandes, 2021: Comparison between eddy-covariance and flux-gradient

size-resolved dust fluxes during wind erosion events. *Journal of Geophysical Research: Atmospheres*, **126**, e2021JD034 735, URL https://onlinelibrary.wiley.com/doi/full/10.1029/2021JD034735https://onlinelibrary.wiley.com/doi/abs/10.1029/2021JD034735https://agupubs.onlinelibrary.wiley.com/doi/10.1029/2021JD034735.

Durán, O., P. Claudin, and B. Andreotti, 2011: On aeolian transport: Grain-scale interactions, dynamical mechanisms and scaling laws. *Aeolian Research*, **3**, 243–270.

Etyemezian, V., G. Nikolich, W. G. Nickling, J. King, and J. A. Gillies, 2017: Analysis of an optical gate device for measuring aeolian sand movement. *Aeolian Research*, **24**, 65–79, URL https://doi.org/10.1016/j.aeolia.2016.11.005.

Falkovich, A. H., G. Schkolnik, E. Ganor, and Y. Rudich, 2004: Adsorption of organic compounds pertinent to urban environments onto mineral dust particles. *Journal of Geophysical Research: Atmospheres*, **109**, 2208, URL https://onlinelibrary.wiley.com/doi/full/10.1029/2003JD003919https://onlinelibrary.wiley.com/doi/abs/10.1029/2003JD003919https://agupubs.onlinelibrary.wiley.com/doi/10.1029/2003JD003919.

Fernandes, R., S. Dupont, and E. Lamaud, 2019: Investigating the role of deposition on the size distribution of near-surface dust flux during erosion events. *Aeolian Research*, **37**, 32–43.

Fletcher, B., 1976a: The erosion of dust by an airflow. *Journal of Physics D: Applied Physics*, **9**, 913, URL https://iopscience.iop.org/article/10.1088/0022-3727/9/6/005https://iopscience.iop.org/article/10.1088/0022-3727/9/6/005/meta.

———, 1976b: The incipient motion of granular materials. *Journal of Physics D: Applied Physics*, **9**, 2471, URL https://iopscience.iop.org/article/10.1088/0022-3727/9/17/007https://iopscience.iop.org/article/10.1088/0022-3727/9/17/007/meta.

Formenti, P., M. O. Andreae, L. Lange, G. Roberts, J. Cafmeyer, I. Rajta, W. Maenhaut, B. N. Holben, P. Artaxo, and J. Lelieveld, 2001: Saharan dust in brazil and suriname during the large–scale biosphere–atmosphere experiment in amazonia (lba)–cooperative lba regional experiment (claire) in march 1998. *Journal of Geophysical Research*, **106**, 14 919–14 934, URL https://doi.org/10.1029/2000JD900827.

Formenti, P. and C. Di Biagio, 2024: Large synthesis of in situ field measurements of the size distribution of mineral dust aerosols across their life cycles. *Earth System Science Data*, **16**, 4995–5007, URL https://essd.copernicus.org/articles/16/4995/2024/.

Formenti, P., L. Schütz, Y. Balkanski, K. Desboeufs, M. Ebert, K. Kandler, A. Petzold, D. Scheuvens, S. Weinbruch, and D. Zhang, 2011: Recent progress in understanding physical and chemical properties of african and asian mineral dust. *Atmospheric Chemistry and Physics*, **11**, 8231–8256.

Fratini, G., P. Ciccioli, A. Febo, A. Forgione, and R. Valentini, 2007: Size–segregated fluxes of mineral dust from a desert area of northern china by eddy covariance. *Atmospheric Chemistry and Physics*, **7**, 2839–2854, URL https://doi.org/10.5194/acp-7-2839-2007.

Froyd, K. D., P. Yu, G. P. Schill, C. A. Brock, A. Kupc, C. J. Williamson, E. J. Jensen, E. Ray, K. H. Rosenlof, H. Bian, A. S. Darmenov, P. R. Colarco, G. S. Diskin, T. P. Bui, and D. M. Murphy, 2022: Dominant role of mineral dust in cirrus cloud formation revealed by global-scale measurements. *Nature Geoscience 2022 15:3*, **15**, 177–183, URL https://www.nature.com/articles/s41561-022-00901-w.

Fuchs, N., 1964: The mechanics of aerosols. pergamon, oxford.

Fécan, F., B. Marticorena, and G. Bergametti, 1999: Parametrization of the increase of the aeolian erosion threshold wind friction velocity due to soil moisture for arid and semi-arid areas. *Annales Geophysicae*, **17**, 149–157, URL https://angeo.copernicus.org/articles/17/149/1999/.

Gasteiger, J. and M. Wiegner, 2018: Mopsmap v1.0: a versatile tool for the modeling of aerosol optical properties. *Geoscientific Model Development*, **11 (7)**, 2739–2762, URL https://gmd.copernicus.org/articles/11/2739/2018/.

Gaston, C. J., 2020: Re-examining Dust Chemical Aging and Its Impacts on Earth's Climate. *Accounts of Chemical Research*, **53 (5)**, 1005–1013, URL http://dx.doi.org/10.1021/acs.accounts.0c00102.

Gillette, D. A., 1974: On the production of soil wind erosion having the potential for long range transport. *Journal de Recherche Atmosphérique*, **8**, 734–744.

Gillette, D. A., I. H. Blifford, and C. R. Fenster, 1972: Measurements of aerosol size distributions and vertical fluxes of aerosols on land subject to wind erosion. *Journal of Applied Meteorology*, **11**, 977–987, URL https://doi.org/10.1175/1520-0450(1972)011<0977:MOASDA>2.0.CO;2.

Gillette, D. A., D. W. Fryrear, J. B. Xiao, P. Stockton, D. Ono, P. J. Helm, T. E. Gill, and T. Ley, 1997: Large-scale variability of wind erosion mass flux rates at owens lake: 1. vertical profiles of horizontal mass fluxes of wind-eroded particles with diameter greater than 50 μm. *Journal of Geophysical Research: Atmospheres*, **102 (D22)**, 25 977–25 987, URL https://agupubs.onlinelibrary.wiley.com/doi/abs/10.1029/97JD00961, https://agupubs.onlinelibrary.wiley.com/doi/pdf/10.1029/97JD00961.

Girdwood, J., H. Ballington, C. Stopford, R. Lewis, and E. Hesse, 2025: Calibration of optical particle spectrometers using mounted fibres. *Atmospheric Measurement Techniques*, **18 (1)**, 305–317, URL https://amt.copernicus.org/articles/18/305/2025/.

Girdwood, J., H. R. Smith, W. Stanley, Z. Ulanowski, C. Stopford, C. Chemel, K. Doulgeris, D. Brus, D. A. Campbell, and R. Mackenzie, 2020: Design and field campaign validation of a multi-rotor unmanned aerial vehicle and optical particle counter. *Atmospheric Measurement Techniques*, **13 (12)**, 6613–6630, URL `https://doi.org/10.5194/amt-13-6613-2020`.

Girdwood, J., W. Stanley, C. Stopford, and D. Brus, 2022: Simulation and field campaign evaluation of an optical particle counter on a fixed-wing UAV. *Atmospheric Measurement Techniques*, **15 (7)**, 2061–2076, URL `https://doi.org/10.5194/amt-15-2061-2022`.

Gkikas, A., E. Proestakis, V. Amiridis, S. Kazadzis, E. D. Tomaso, A. Tsekeri, E. Marinou, N. Hatzianastassiou, and C. P. Garciá-Pando, 2021: Modis dust aerosol (midas): A global fine-resolution dust optical depth data set. *Atmospheric Measurement Techniques*, **14**, 309–334.

Gomes, L., G. Bergametti, G. Coude-Gaussen, and P. Rognon, 1990: Submicron desert dusts: a sandblasting process. *Journal of Geophysical Research*, **95**.

González-Flórez, C., M. Klose, A. Alastuey, S. Dupont, J. Escribano, V. Etyemezian, A. Gonzalez-Romero, Y. Huang, K. Kandler, G. Nikolich, A. Panta, X. Querol, C. Reche, J. Yus-Díez, and C. P. García-Pando, 2023: Insights into the size-resolved dust emission from field measurements in the moroccan sahara. *Atmospheric Chemistry and Physics*, **23**, 7177–7212.

González-Romero, A., C. González-Flórez, A. Panta, J. Yus-Díez, P. Córdoba, A. Alastuey, N. Moreno, M. Hernández-Chiriboga, K. Kandler, M. Klose, R. N. Clark, B. L. Ehlmann, R. N. Greenberger, A. M. Keebler, P. Brodrick, R. Green, P. Ginoux, X. Querol, and C. P. García-Pando, 2024a: Characterization of the particle size distribution, mineralogy, and fe mode of occurrence of dust-emitting sediments from the mojave desert, california, usa. *Atmospheric Chemistry and Physics*, **24**, 9155–9176.

González-Romero, A., C. González-Flórez, A. Panta, J. Yus-Díez, P. Córdoba, A. Alastuey, N. Moreno, K. Kandler, M. Klose, R. N. Clark, B. L. Ehlmann, R. N. Greenberger, A. M. Keebler, P. Brodrick, R. O. Green, X. Querol, and C. P. García-Pando, 2024b: Probing iceland's dust-emitting sediments: Particle size distribution, mineralogy, cohesion, fe mode of occurrence, and reflectance spectra signatures. *Atmospheric Chemistry and Physics*, **24**, 6883–6910.

González-Romero, A., C. González-Flórez, A. Panta, J. Yus-Díez, C. Reche, P. Córdoba, N. Moreno, A. Alastuey, K. Kandler, M. Klose, C. Baldo, R. N. Clark, Z. Shi, X. Querol, and C. P. García-Pando, 2023: Variability in sediment particle size, mineralogy, and fe mode of occurrence across dust-source inland drainage basins: the case of the lower drâa valley, morocco. *Atmospheric Chemistry and Physics*, **23**, 15 815–15 834.

Goossens, D., C. Nolet, V. Etyemezian, L. Duarte-Campos, G. Bakker, and M. Riksen, 2018: Field testing, comparison, and discussion of five aeolian sand transport measuring devices operating on

different measuring principles. *Aeolian Research*, **32**, 1–13, URL https://doi.org/10.1016/j.aeolia.2018.01.001.

Goudie, A. and N. Middleton, 2001: Saharan dust storms: nature and consequences. *Earth-Science Reviews*, **56 (1)**, 179–204, URL https://www.sciencedirect.com/science/article/pii/S0012825201000678.

Goudie, A. S. and N. J. Middleton, 2006: Desert dust in the global system. *Desert Dust in the Global System*, 1–287.

Gouesbet, G., 2019: Generalized lorenz–mie theories and mechanical effects of laser light, on the occasion of arthur ashkin's receipt of the 2018 nobel prize in physics for his pioneering work in optical levitation and manipulation: A review. *Journal of Quantitative Spectroscopy and Radiative Transfer*, **225**, 258–277.

Greeley, R., M. R. Balme, J. D. Iversen, S. Metzger, R. Mickelson, J. Phoreman, and B. White, 2003: Martian dust devils: Laboratory simulations of particle threshold. *Journal of Geophysical Research: Planets*, **108**, 5041, URL https://onlinelibrary.wiley.com/doi/full/10.1029/2002JE001987https://onlinelibrary.wiley.com/doi/abs/10.1029/2002JE001987https://agupubs.onlinelibrary.wiley.com/doi/10.1029/2002JE001987.

Green, R. O., N. Mahowald, C. Ung, D. R. Thompson, L. Bator, M. Bennet, M. Bernas, N. Blackway, C. Bradley, J. Cha, P. Clark, R. Clark, D. Cloud, E. Diaz, E. B. Dor, R. Duren, M. Eastwood, B. L. Ehlmann, L. Fuentes, P. Ginoux, J. Gross, Y. He, O. Kalashnikova, W. Kert, D. Keymeulen, M. Klimesh, D. Ku, H. Kwong-Fu, E. Liggett, L. Li, S. Lundeen, M. D. Makowski, A. Mazer, R. Miller, P. Mouroulis, B. Oaida, G. S. Okin, A. Ortega, A. Oyake, H. Nguyen, T. Pace, T. H. Painter, J. Pempejian, C. P. Garcia-Pando, T. Pham, B. Phillips, R. Pollock, R. Purcell, V. Realmuto, J. Schoolcraft, A. Sen, S. Shin, L. Shaw, M. Soriano, G. Swayze, E. Thingvold, A. Vaid, and J. Zan, 2020: The earth surface mineral dust source investigation: An earth science imaging spectroscopy mission. *IEEE Aerospace Conference Proceedings*.

Guha, A., 2008: Transport and deposition of particles in turbulent and laminar flow. *Annual Review of Fluid Mechanics*, **40**, 311–341, URL https://www.annualreviews.org/content/journals/10.1146/annurev.fluid.40.111406.102220.

Hangal, S. and K. Willeke, 1990: Overall efficiency of tubular inlets sampling at 0–90 degrees from horizontal aerosol flows. *Atmospheric Environment. Part A. General Topics*, **24**, 2379–2386.

Harper, J. M., D. Harvey, T. Huang, J. McGrath, D. Meer, and J. C. Burton, 2022: The lifetime of charged dust in the atmosphere. *PNAS Nexus*, **1**.

He, C., K. Liou, Y. Takano, F. Chen, and M. Barlage, 2019: Enhanced Snow Absorption and Albedo Reduction by DustSnow Internal Mixing: Modeling and Parameterization. *Journal of Advances in Modeling Earth Systems*, **11 (11)**, 3755–3776, URL http://dx.doi.org/10.1029/2019MS001737.

Heisel, M., B. Chen, J. F. Kok, and M. Chamecki, 2021: Gentle topography increases vertical transport of coarse dust by orders of magnitude. *Journal of Geophysical Research: Atmospheres*, **126**, e2021JD034 564, URL https://onlinelibrary.wiley.com/doi/full/10.1029/2021JD034564https://onlinelibrary.wiley.com/doi/abs/10.1029/2021JD034564https://agupubs.onlinelibrary.wiley.com/doi/10.1029/2021JD034564.

Heyder, J. and J. Gebhart, 1977: Gravitational deposition of particles from laminar aerosol flow through inclined circular tubes. *Journal of Aerosol Science*, **8**, 289–295.

Hinds, W. C., 1999: *Aerosol technology: properties, behavior, and measurement of airborne particles*. John Wiley & Sons, Chichester, 504 pp.

Hinds, W. C. and Y. Zhu, 2022: *Aerosol technology: properties, behavior, and measurement of airborne particles*. John Wiley & Sons.

Hoose, C. and O. Möhler, 2012: Heterogeneous ice nucleation on atmospheric aerosols: A review of results from laboratory experiments. *Atmospheric Chemistry and Physics*, **12**, 9817–9854.

Huang, J., J. Liu, B. Chen, and S. Nasiri, 2015: Detection of anthropogenic dust using calipso lidar measurements. *Atmospheric Chemistry and Physics*, **15**, 11 653–11 665.

Huang, J., T. Wang, W. Wang, Z. Li, and H. Yan, 2014: Climate effects of dust aerosols over East Asian arid and semiarid regions. *Journal of Geophysical Research: Atmospheres*, **119 (19)**, URL http://dx.doi.org/10.1002/2014JD021796.

Huang, Y., A. A. Adebiyi, P. Formenti, and J. F. Kok, 2021: Linking the different diameter types of aspherical desert dust indicates that models underestimate coarse dust emission. *Geophysical Research Letters*, **48**, e2020GL092 054, URL https://onlinelibrary.wiley.com/doi/full/10.1029/2020GL092054https://onlinelibrary.wiley.com/doi/abs/10.1029/2020GL092054https://agupubs.onlinelibrary.wiley.com/doi/10.1029/2020GL092054.

Huang, Y., J. F. Kok, K. Kandler, H. Lindqvist, T. Nousiainen, T. Sakai, et al., 2020: Climate models and remote sensing retrievals neglect substantial desert dust asphericity. *Geophysical Research Letters*, **47**, e2019GL086 592, URL https://doi.org/10.1029/2019GL086592.

Huang, Y., J. F. Kok, R. L. Martin, N. Swet, I. Katra, T. E. Gill, R. L. Reynolds, and L. S. Freire, 2019: Fine dust emissions from active sands at coastal oceano dunes, california. *Atmospheric Chemistry and Physics*, **19**, 2947–2964, URL https://doi.org/10.5194/acp-19-2947-2019.

Huneeus, N., M. Schulz, Y. Balkanski, J. Griesfeller, J. Prospero, S. Kinne, S. Bauer, O. Boucher, M. Chin, F. Dentener, T. Diehl, R. Easter, D. Fillmore, S. Ghan, P. Ginoux, A. Grini, L. Horowitz, D. Koch, M. C. Krol, W. Landing, X. Liu, N. Mahowald, R. Miller, J.-J. Morcrette, G. Myhre, J. Penner, J. Perlwitz, P. Stier, T. Takemura, and C. S. Zender, 2011: Global dust model intercomparison in aerocom phase i. *Atmospheric Chemistry and Physics*, **11 (15)**, 7781–7816, URL https://acp.copernicus.org/articles/11/7781/2011/.

Ishizuka, M., M. Mikami, J. Leys, Y. Yamada, S. Heidenreich, Y. Shao, and G. H. McTainsh, 2008: Effects of soil moisture and dried raindroplet crust on saltation and dust emission. *Journal of Geophysical Research: Atmospheres*, **113**, URL https://onlinelibrary.wiley.com/doi/full/10.1029/2008JD009955https://onlinelibrary.wiley.com/doi/abs/10.1029/2008JD009955https://agupubs.onlinelibrary.wiley.com/doi/10.1029/2008JD009955.

Iversen, J. D., J. B. Pollack, R. Greeley, and B. R. White, 1976: Saltation threshold on mars: The effect of interparticle force, surface roughness, and low atmospheric density. *Icarus*, **29**, 381–393.

Iversen, J. D. and B. R. White, 1982: Saltation threshold on earth, mars and venus. *Sedimentology*, **29**, 111–119, URL https://onlinelibrary.wiley.com/doi/full/10.1111/j.1365-3091.1982.tb01713.xhttps://onlinelibrary.wiley.com/doi/abs/10.1111/j.1365-3091.1982.tb01713.xhttps://onlinelibrary.wiley.com/doi/10.1111/j.1365-3091.1982.tb01713.x.

Jeong, G. Y., 2024: Microanalysis and mineralogy of Asian and Saharan dust. *Journal of Analytical Science and Technology*, **15 (1)**, URL http://dx.doi.org/10.1186/s40543-024-00425-5.

Jeong, G. Y., J. Y. Kim, J. Seo, G. M. Kim, H. C. Jin, and Y. Chun, 2014: Long-range transport of giant particles in asian dust identified by physical, mineralogical, and meteorological analysis. *Atmospheric Chemistry and Physics*, **14**, 505–521.

Jickells, T. D., Z. An, K. H. Andersen, A. R. Baker, G. Bergametti, N. Brooks, J. Cao, P. W. Boyd, R. A. Duce, K. A. Hunter, H. Kawahata, N. Kubilay, J. LaRoche, P. S. Liss, N. M. Mahowald, J. M. Prospero, A. Ridgwell, I. Tegen, and R. Torres, 2005: Global iron connections between desert dust, ocean biogeochemistry, and climate. *Science*, **308**, 67–71.

Johnson, B. T. and S. R. Osborne, 2011: Physical and optical properties of mineral dust aerosol measured by aircraft during the gerbils campaign. *Quarterly Journal of the Royal Meteorological Society*, **137**, 1117–1130, URL https://doi.org/10.1002/qj.777.

Johnson, K. S. and N. Meskhidze, 2013: Atmospheric dissolved iron deposition to the global oceans: effects of oxalate-promoted fe dissolution, photochemical redox cycling, and dust mineralogy. *Geoscientific Model Development Discussions*, **6 (3)**.

Journet, E., Y. Balkanski, and S. P. Harrison, 2014: A new data set of soil mineralogy for dust-cycle modeling. *Atmospheric Chemistry and Physics*, **14**, 3801–3816.

Jung, E., B. Albrecht, J. M. Prospero, H. H. Jonsson, and S. M. Kreidenweis, 2013: Vertical structure of aerosols, temperature, and moisture associated with an intense african dust event observed over the eastern caribbean. *Journal of Geophysical Research*, **118**, 4623–4643, URL https://doi.org/10.1002/jgrd.50352.

Kalashnikova, O. V. and R. A. Kahn, 2008: Mineral dust plume evolution over the atlantic from misr and modis aerosol retrievals. *Journal of Geophysical Research: Atmospheres*, **113 (D24)**, URL https://agupubs.onlinelibrary.wiley.com/doi/abs/10.1029/2008JD010083, https://agupubs.onlinelibrary.wiley.com/doi/pdf/10.1029/2008JD010083.

Kaly, F., B. Marticorena, B. Chatenet, J. L. Rajot, S. Janicot, A. Niang, H. Yahi, S. Thiria, A. Maman, A. Zakou, B. S. Coulibaly, M. Coulibaly, I. Koné, S. Traoré, A. Diallo, and T. Ndiaye, 2015: Variability of mineral dust concentrations over west africa monitored by the sahelian dust transect. *Atmospheric Research*, **164-165**, 226–241.

Kandler, K., N. Benker, U. Bundke, E. Cuevas, M. Ebert, P. Knippertz, S. Rodríguez, L. Schütz, and S. Weinbruch, 2007: Chemical composition and complex refractive index of saharan mineral dust at izaña, tenerife (spain) derived by electron microscopy. *Atmospheric Environment*, **41**, 8058–8074.

Kandler, K., K. Schneiders, M. Ebert, M. Hartmann, S. Weinbruch, M. Prass, and C. Pöhlker, 2018: Composition and mixing state of atmospheric aerosols determined by electron microscopy: Method development and application to aged saharan dust deposition in the caribbean boundary layer. *Atmospheric Chemistry and Physics*, **18**, 13 429–13 455.

Kandler, K., L. Schütz, S. Jäckel, K. Lieke, C. Emmel, D. Müller-Ebert, M. Ebert, D. Scheuvens, A. Schladitz, B. Šegvić, A. Wiedensohler, and S. Weinbruch, 2011: Ground–based off–line aerosol measurements at praia, cape verde, during the saharan mineral dust experiment: microphysical properties and mineralogy. *Tellus B*, **63**, 459–474, URL https://doi.org/10.1111/j.1600-0889.2011.00546.x.

Kandler, K., L. Schütz, C. Deutscher, M. Ebert, H. Hofmann, S. Jäckel, R. Jaenicke, P. Knippertz, K. Lieke, A. Massling, A. Petzold, A. Schladitz, B. Weinzierl, A. Wiedensohler, S. Zorn, and S. Weinbruch, 2009: Size distribution, mass concentration, chemical and mineralogical composition and derived optical parameters of the boundary layer aerosol at tinfou, morocco, during samum 2006. *Tellus, Series B: Chemical and Physical Meteorology*, **61**, 32–50.

Karydis, V. A., A. P. Tsimpidi, A. Pozzer, M. Astitha, and J. Lelieveld, 2016: Effects of mineral dust on global atmospheric nitrate concentrations. *Atmospheric Chemistry and Physics*, **16**, 1491–1509.

Khalfallah, B., C. Bouet, M. T. Labiadh, S. C. Alfaro, G. Bergametti, B. Marticorena, S. Lafon, S. Chevaillier, A. Féron, P. Hease, T. H. des Tureaux, S. Sekrafi, P. Zapf, and J. L. Rajot, 2020: Influence of atmospheric stability on the size distribution of the vertical dust flux measured in eroding conditions over a flat bare sandy field. *Journal of Geophysical Research: Atmospheres*, **125**, e2019JD031 185, URL https://onlinelibrary.wiley.com/doi/full/10.1029/2019JD031185https://onlinelibrary.wiley.com/doi/abs/10.1029/2019JD031185https://agupubs.onlinelibrary.wiley.com/doi/10.1029/2019JD031185.

Klingmüller, K., J. Lelieveld, V. A. Karydis, and G. L. Stenchikov, 2019: Direct radiative effect of dust–pollution interactions. *Atmospheric Chemistry and Physics*, **19 (11)**, 7397–7408, URL http://dx.doi.org/10.5194/ACP-19-7397-2019.

Klingmüller, K., V. A. Karydis, S. Bacer, G. L. Stenchikov, and J. Lelieveld, 2020: Weaker cooling by aerosols due to dust-pollution interactions. *Atmospheric Chemistry and Physics*, **20**, 15 285–15 295.

Klose, M., T. E. Gill, V. Etyemezian, G. Nikolich, Z. G. Zadeh, N. P. Webb, and R. S. Van Pelt, 2019: Dust emission from crusted surfaces: Insights from field measurements and modelling. *Aeolian Research*, **40**, 1–14, URL https://doi.org/10.1016/j.aeolia.2019.05.001.

Klose, M. and Y. Shao, 2012: Stochastic parameterization of dust emission and application to convective atmospheric conditions. *Atmospheric Chemistry and Physics*, **12**, 7309–7320.

Klose, M., Y. Shao, X. Li, H. Zhang, M. Ishizuka, M. Mikami, and J. F. Leys, 2014: Further development of a parameterization for convective turbulent dust emission and evaluation based on field observations. *Journal of Geophysical Research: Atmospheres*, **119 (17)**, 10 441–10 457, URL https://agupubs.onlinelibrary.wiley.com/doi/abs/10.1002/2014JD021688, https://agupubs.onlinelibrary.wiley.com/doi/pdf/10.1002/2014JD021688.

Knippertz, P. and M. C. Todd, 2012: Mineral dust aerosols over the sahara: Meteorological controls on emission and transport and implications for modeling. *Reviews of Geophysics*, **50 (2)**.

Kobayashi, H., K. Arao, T. Murayama, K. Iokibe, R. Koga, and M. Shiobara, 2007: High–resolution measurement of size distributions of asian dust using a coulter multisizer. *Journal of Atmospheric and Oceanic Technology*, **24**, 194–205, URL https://doi.org/10.1175/JTECH1965.1.

Kok, J., 2011a: Does the size distribution of mineral dust aerosols depend on the wind speed at emission? *Atmospheric Chemistry and Physics*, **11**, 10 149–10 156.

Kok, J. F., 2011b: A scaling theory for the size distribution of emitted dust aerosols suggests climate models underestimate the size of the global dust cycle. *Proceedings of the National Academy of Sciences of the United States of America*, **108**, 1016–1021, URL https://www.pnas.org/doi/abs/10.1073/pnas.1014798108.

Kok, J. F., A. A. Adebiyi, S. Albani, Y. Balkanski, R. Checa-Garcia, M. Chin, P. R. Colarco, D. S. Hamilton, Y. Huang, A. Ito, M. Klose, L. Li, N. M. Mahowald, R. L. Miller, V. Obiso, C. P. García-Pando, A. Rocha-Lima, and J. S. Wan, 2021: Contribution of the world's main dust source regions to the global cycle of desert dust. *Atmospheric Chemistry and Physics*, **21**, 8169–8193.

Kok, J. F., N. M. Mahowald, G. Fratini, J. A. Gillies, M. Ishizuka, J. F. Leys, M. Mikami, M. S. Park, S. U. Park, R. S. V. Pelt, and T. M. Zobeck, 2014: An improved dust emission model - part 1: Model description and comparison against measurements. *Atmospheric Chemistry and Physics*, **14**, 13 023–13 041.

Kok, J. F., E. Parteli, T. Michaels, and D. Francis, 2012: The physics of wind-blown sand and dust. *Reports on progress in physics. Physical Society (Great Britain)*, **75**, 106 901.

Kok, J. F., D. Ridley, Q. Zhou, R. Miller, C. Zhao, C. Heald, D. Ward, S. Albani, and K. Haustein, 2017: Smaller desert dust cooling effect estimated from analysis of dust size and abundance. *Nature Geoscience*, **10**.

Kok, J. F., T. Storelvmo, V. A. Karydis, A. A. Adebiyi, N. M. Mahowald, A. T. Evan, C. He, and D. M. Leung, 2023: Mineral dust aerosol impacts on global climate and climate change. *Nature Reviews Earth & Environment*, **4 (2)**, 71–86, URL `https://doi.org/10.1038/s43017-022-00379-5`.

Kok, J. F., D. S. Ward, N. M. Mahowald, and A. T. Evan, 2018: Global and regional importance of the direct dust-climate feedback. *Nature Communications 2018 9:1*, **9**, 1–11, URL `https://www.nature.com/articles/s41467-017-02620-y`.

Korte, L. F., G. J. A. Brummer, M. V. D. Does, C. V. Guerreiro, R. Hennekam, J. A. V. Hateren, D. Jong, C. I. Munday, S. Schouten, and J. B. W. Stuut, 2017: Downward particle fluxes of biogenic matter and saharan dust across the equatorial north atlantic. *Atmospheric Chemistry and Physics*, **17**, 6023–6040.

Kotsyfakis, M., S. Zarogiannis, and E. Patelarou, 2019: The health impact of Saharan dust exposure. *International Journal of Occupational Medicine and Environmental Health*, URL `http://ijomeh.eu/pdf-110732-43709?filename=Thehealthimpactof.pdf`.

Kuhli, M., M. Weiss, and H. Steckel, 2010: Characterisation of solution-based pressurised metered-dose inhaler aerosols with an optical particle counter. *European Journal of Pharmaceutics and Biopharmaceutics*, **75**, 393–398.

Kulkarni, P., P. A. Baron, and K. Willeke, 2011: Aerosol measurement: Principles, techniques, and applications: Third edition. *Aerosol Measurement: Principles, Techniques, and Applications: Third Edition*.

Kumar, P., I. N. Sokolik, and A. Nenes, 2011: Cloud condensation nuclei activity and droplet activation kinetics of wet processed regional dust samples and minerals. *Atmospheric Chemistry and Physics*, **11**, 8661–8676.

Kuwano, A., A. T. Evan, B. Walkowiak, and R. Frouin, 2024: Quantifying the dust direct radiative effect in the southwestern United States: findings from multiyear measurements. *Atmospheric Chemistry and Physics*, **24 (17)**, 9843–9868, URL http://dx.doi.org/10.5194/acp-24-9843-2024.

Leys, J., G. McTainsh, C. Strong, S. Heidenreich, and K. Biesaga, 2008: Dustwatch: using community networks to improve wind erosion monitoring in australia. *Earth Surface Processes and Landforms*, **33**, 1912–1926, URL https://onlinelibrary.wiley.com/doi/full/10.1002/esp.1733https://onlinelibrary.wiley.com/doi/abs/10.1002/esp.1733https://onlinelibrary.wiley.com/doi/10.1002/esp.1733.

Li, L., N. M. Mahowald, R. L. Miller, C. Pérez García-Pando, M. Klose, D. S. Hamilton, M. G. Ageitos, P. Ginoux, Y. Balkanski, R. O. Green, O. Kalashnikova, J. F. Kok, V. Obiso, D. Paynter, and D. R. Thompson, 2021: Quantifying the range of the dust direct radiative effect due to source mineralogy uncertainty. *Atmospheric Chemistry and Physics*, **21**, 3973–4005.

Liu, B. Y. and J. K. Agarwal, 1974: Experimental observation of aerosol deposition in turbulent flow. *Journal of Aerosol Science*, **5**, 145–155.

Liu, B. Y., Z. Q. Zhang, and T. H. Kuehn, 1989: A numerical study of inertial errors in anisokinetic sampling. *Journal of Aerosol Science*, **20**, 367–380.

Longueville, F., P. Ozer, S. Doumbia, and S. Henry, 2012: Desert dust impacts on human health: an alarming worldwide reality and a need for studies in West Africa. *International Journal of Biometeorology*, URL https://orbi.uliege.be/bitstream/2268/123853/1/IJB2013_De%20Longueville%20-%20Ozer%20-%20Doumbia%20-%20Henry.pdf.

Mahowald, N., S. Albani, J. F. Kok, S. Engelstaeder, R. Scanza, D. S. Ward, and M. G. Flanner, 2014: The size distribution of desert dust aerosols and its impact on the earth system. *Aeolian Research*, **15**, 53–71, URL https://www.sciencedirect.com/science/article/pii/S1875963713000736.

Maring, H., D. L. Savoie, M. A. Izaguirre, L. Custals, and J. S. Reid, 2003: Mineral dust aerosol size distribution change during atmospheric transport. *Journal of Geophysical Research*, **108**, URL https://doi.org/10.1029/2002JD002536.

Maring, H., D. L. Savoie, M. A. Izaguirre, C. McCormick, R. Arimoto, J. M. Prospero, and C. Pilinis, 2000: Aerosol physical and optical properties and their relationship to aerosol composition in the free troposphere at izaña, tenerife, canary islands, during july 1995. *Journal of Geophysical Research*, **105**, 14 677–14 700, URL https://doi.org/10.1029/2000JD900106.

Marker, B. R., 2012: Mineral dust: An overview. *Episodes*, **35 (2)**, 337–341, URL http://dx.doi.org/10.18814/EPIIUGS/2012/V35I2/005.

Marticorena, B., 2014: Dust production mechanisms. *Mineral Dust: A Key Player in the Earth System*, Knippertz, P. and J.-B. W. Stuut, Eds., Springer Netherlands, Dordrecht, 93–120, URL https://doi.org/10.1007/978-94-017-8978-3_5.

Marticorena, B. and G. Bergametti, 1995: Modeling the atmospheric dust cycle: 1. design of a soil-derived dust emission scheme. *Journal of Geophysical Research: Atmospheres*, **100**, 16 415–16 430, URL https://onlinelibrary.wiley.com/doi/full/10.1029/95JD00690https://onlinelibrary.wiley.com/doi/abs/10.1029/95JD00690https://agupubs.onlinelibrary.wiley.com/doi/10.1029/95JD00690.

McConnell, C. L., E. J. Highwood, H. Coe, P. Formenti, B. Anderson, S. Osborne, S. Nava, K. Desboeufs, G. Chen, and M. a. J. Harrison, 2008: Seasonal variations of the physical and optical characteristics of saharan dust: Results from the dust outflow and deposition to the ocean (dodo) experiment. *Journal of Geophysical Research*, **113**, URL https://doi.org/10.1029/2007JD009606.

McKenna-Neuman, C. and W. G. Nickling, 1989: A theoretical and wind tunnel investigation of the effect of capillary water on the entrainment of sediment by wind. *Canadian Journal of Soil Science*, **69**, 79–96.

Meloni, D., A. di Sarra, G. Brogniez, C. Denjean, L. De Silvestri, T. Di Iorio, P. Formenti, J. L. Gómez-Amo, J. Gröbner, N. Kouremeti, G. Liuzzi, M. Mallet, G. Pace, and D. M. Sferlazzo, 2018: Determining the infrared radiative effects of Saharan dust: a radiative transfer modelling study based on vertically resolved measurements at Lampedusa. *Atmospheric Chemistry and Physics*, **18 (6)**, 4377–4401, URL http://dx.doi.org/10.5194/ACP-18-4377-2018.

Meloni, D., W. Junkermann, A. d. Sarra, M. Cacciani, L. D. Silvestri, T. D. Iorio, V. Estellés, J. L. Gómez-Amo, G. Pace, and D. M. Sferlazzo, 2015: Altitude–resolved shortwave and longwave radiative effects of desert dust in the mediterranean during the gamarf campaign: Indications of a net daily cooling in the dust layer. *Journal of Geophysical Research*, **120**, 3386–3407, URL https://doi.org/10.1002/2014JD022312.

Meng, J., Y. Huang, D. M. Leung, L. Li, A. A. Adebiyi, C. L. Ryder, N. M. Mahowald, and J. F. Kok, 2022: Improved parameterization for the size distribution of emitted dust aerosols reduces model underestimation of super coarse dust. *Geophysical Research Letters*, **49**, e2021GL097 287, URL https://onlinelibrary.wiley.com/doi/full/10.1029/2021GL097287https://onlinelibrary.wiley.com/doi/abs/10.1029/2021GL097287https://agupubs.onlinelibrary.wiley.com/doi/10.1029/2021GL097287.

Meng, Z., P. Yang, G. W. Kattawar, L. Bi, K. N. Liou, and I. Laszlo, 2010: Single-scattering properties of tri-axial ellipsoidal mineral dust aerosols: A database for application to radiative transfer calculations. *Journal of Aerosol Science*, **41**, 501–512.

Menut, L., G. Siour, B. Bessagnet, F. Couvidat, E. Journet, Y. Balkanski, and K. Desboeufs, 2020: Modelling the mineralogical composition and solubility of mineral dust in the mediterranean area with chimere 2017r4. *Geoscientific Model Development*, **13**, 2051–2071.

Meskhidze, N., W. L. Chameides, and A. Nenes, 2005: Dust and pollution: A recipe for enhanced ocean fertilization? *Journal of Geophysical Research: Atmospheres*, **110**, 1–23, URL https://onlinelibrary.wiley.com/doi/full/10.1029/2004JD005082https://onlinelibrary.wiley.com/doi/abs/10.1029/2004JD005082https://agupubs.onlinelibrary.wiley.com/doi/10.1029/2004JD005082.

Meyer, H., K. Kandler, S. Dupont, J. Escribano, J. Girdwood, G. Nikolich, A. Alastuey, V. Etyemezian, C. G. Flórez, A. González-Romero, T. Hussein, M. Irvine, P. Knippertz, O. Möhler, X. Querol, C. Stopford, F. Vogel, F. Weis, A. Wieser, C. P. García-Pando, and M. Klose, 2025a: From fine to giant: Multi-instrument assessment of the dust particle size distribution at an emission source during the J-WADI field campaign, submitted.

Meyer, H., K. Kandler, S. Dupont, J. Escribano, J. Girdwood, G. Nikolich, A. Alastuey, V. Etyemezian, C. González-Flórez, A. GONZALEZ ROMERO, T. Hussein, M. Irvine, P. Knippertz, O. Möhler, X. Querol, C. Stopford, F. Vogel, F. Weis, A. Wieser, C. Pérez García-Pando, and M. Klose, 2025b: Data presented in meyer et al. 2025 "from fine to giant: Multi-instrument assessment of the dust particle size distribution at an emission source during the j-wadi field campaign". URL https://doi.org/10.5281/zenodo.15112651.

Meyer, H., K. Kandler, S. Dupont, J. Escribano, J. Girdwood, G. Nikolich, A. Alastuey, V. Etyemezian, C. González-Flórez, A. González-Romero, T. Hussein, M. Irvine, P. Knippertz, O. Möhler, X. Querol, C. Stopford, F. Vogel, F. Weis, A. Wieser, C. P. García-Pando, and M. Klose, 2026: From fine to giant: multi-instrument assessment of the dust particle size distribution at an emission source during the j-wadi field campaign. *Atmospheric Measurement Techniques*, **19**, 21–61, URL https://amt.copernicus.org/articles/19/21/2026/.

Min, Q.-L., R. Li, B. Lin, E. Joseph, S. Wang, Y. Hu, V. Morris, and F. Chang, 2009: Evidence of mineral dust altering cloud microphysics and precipitation. *Atmospheric Chemistry and Physics*, **9 (9)**, 3223–3231, URL http://dx.doi.org/10.5194/ACP-9-3223-2009.

Moore, J. K. and O. Braucher, 2008: Sedimentary and mineral dust sources of dissolved iron to the world ocean. *Biogeosciences*, **5**, 631–656.

Müller, K., S. Lehmann, D. van Pinxteren, T. Gnauk, N. Niedermeier, A. Wiedensohler, and H. Herrmann, 2010: Particle characterization at the cape verde atmospheric observatory during the 2007 rhamble intensive. *Atmospheric Chemistry and Physics*, **10**, 2709–2721, URL https://doi.org/10.5194/acp-10-2709-2010.

Ndour, M., B. D'Anna, C. George, O. Ka, Y. Balkanski, J. Kleffmann, K. Stemmler, and M. Ammann, 2008: Photoenhanced uptake of no2 on mineral dust: Laboratory experiments and model simulations. *Geophysical Research Letters*, **35**, URL https://onlinelibrary.wiley.com/doi/full/10.1029/2007GL032006https://onlinelibrary.wiley.com/doi/abs/10.1029/2007GL032006https://agupubs.onlinelibrary.wiley.com/doi/10.1029/2007GL032006.

Nemuc, A., S. Basart, A. Tobías, S. Nickovic, F. Barnaba, S. Kazadzis, L. Mona, V. Amiridis, A. Vukovic, I. Christel, P. D. Waldhauserová, and A. Monteiro, 2020: Cost Lecture 2019 AE GM Barcelona: International Network to Encourage the Use of Monitoring and Forecasting Dust Products (InDust). *Europaeum Review*.

Nenes, A., B. Murray, and A. Bougiatioti, 2014: Mineral dust and its microphysical interactions with clouds. *Mineral Dust: A Key Player in the Earth System*, 287–325, URL https://link.springer.com/chapter/10.1007/978-94-017-8978-3_12.

Nickovic, S., A. Vukovic, M. Vujadinovic, V. Djurdjevic, and G. Pejanovic, 2012: Technical note: High-resolution mineralogical database of dust-productive soils for atmospheric dust modeling. *Atmospheric Chemistry and Physics*, **12**, 845–855.

Niemand, M., O. Möhler, B. Vogel, H. Vogel, C. Hoose, P. Connolly, H. Klein, H. Bingemer, P. DeMott, J. Skrotzki, and T. Leisner, 2012: A particle-surface-area-based parameterization of immersion freezing on desert dust particles. *Journal of the Atmospheric Sciences*, **69 (10)**, 3077 – 3092, URL https://journals.ametsoc.org/view/journals/atsc/69/10/jas-d-11-0249.1.xml.

Obiso, V., M. G. Ageitos, C. P. García-Pando, J. P. Perlwitz, G. L. Schuster, S. E. Bauer, C. D. Biagio, P. Formenti, K. Tsigaridis, and R. L. Miller, 2024: Observationally constrained regional variations of shortwave absorption by iron oxides emphasize the cooling effect of dust. *Atmospheric Chemistry and Physics*, **24**, 5337–5367.

Oerlemans, J., R. Giesen, and M. Van Den Broeke, 2009: Retreating alpine glaciers: increased melt rates due to accumulation of dust (Vadret da Morteratsch, Switzerland). *Journal of Glaciology*, **55 (192)**, 729–736, URL http://dx.doi.org/10.3189/002214309789470969.

Osborne, S. R., B. T. Johnson, J. M. Haywood, A. J. Baran, M. a. J. Harrison, and C. L. McConnell, 2008: Physical and optical properties of mineral dust aerosol during the dust and biomass–burning experiment. *Journal of Geophysical Research*, **113**, URL https://doi.org/10.1029/2007JD009551.

Ott, D. K. and T. M. Peters, 2008: A shelter to protect a passive sampler for coarse particulate matter, pm10 − 2.5. *Aerosol Science and Technology*, **42**, 299–309, URL https://www.tandfonline.com/doi/abs/10.1080/02786820802054236.

Otto, S., M. de Reus, T. Trautmann, A. Thomas, M. Wendisch, and S. Borrmann, 2007: Atmospheric radiative effects of an in situ measured saharan dust plume and the role of large particles. *Atmospheric Chemistry and Physics*, **7**, 4887–4903, URL https://doi.org/10.5194/acp-7-4887-2007.

Otto, S., T. Trautmann, and M. Wendisch, 2011: On realistic size equivalence and shape of spheroidal Saharan mineral dust particles applied in solar and thermal radiative transfer calculations. *Atmospheric Chemistry and Physics*, **11 (9)**, 4469–4490, URL http://dx.doi.org/10.5194/ACP-11-4469-2011.

Panta, A., K. Kandler, A. Alastuey, C. González-Flórez, A. González-Romero, M. Klose, X. Querol, C. Reche, J. Yus-Díez, and C. P. García-Pando, 2023: Insights into the single-particle composition, size, mixing state, and aspect ratio of freshly emitted mineral dust from field measurements in the moroccan sahara using electron microscopy. *Atmospheric Chemistry and Physics*, **23**, 3861–3885.

Perlwitz, J. P., C. P. García-Pando, and R. L. Miller, 2015a: Predicting the mineral composition of dust aerosols - part 1: Representing key processes. *Atmospheric Chemistry and Physics*, **15**, 11 593–11 627.

———, 2015b: Predicting the mineral composition of dust aerosols - part 2: Model evaluation and identification of key processes with observations. *Atmospheric Chemistry and Physics*, **15**, 11 629–11 652.

Prospero, J. M., 1996: *Saharan Dust Transport Over the North Atlantic Ocean and Mediterranean: An Overview*. Springer, Dordrecht, 133-151 pp., URL https://link.springer.com/chapter/10.1007/978-94-017-3354-0_13.

Prospero, J. M., R. A. Glaccum, and R. T. Nees, 1981: Atmospheric transport of soil dust from africa to south america. *Nature 1981 289:5798*, **289**, 570–572, URL https://www.nature.com/articles/289570a0.

Pui, D. H., F. Romay-Novas, and B. Y. Liu, 1987: Experimental study of particle deposition in bends of circular cross section. *Aerosol Science and Technology*, **7**, 301–315, URL https://www.researchgate.net/publication/245323787_Experimental_Study_of_Particle_Deposition_in_Bends_of_Circular_Cross_Section.

Pye, K., 1987: *Aeolian Dust and Dust Deposits*. Academic Press, London, UK.

Rajot, J. L., P. Formenti, S. Alfaro, K. Desboeufs, S. Chevaillier, B. Chatenet, A. Gaudichet, E. Journet, B. Marticorena, S. Triquet, A. Maman, N. Mouget, and A. Zakou, 2008: Amma dust experiment: An

overview of measurements performed during the dry season special observation period (sop0) at the banizoumbou (niger) supersite. *Journal of Geophysical Research*, **113**, URL https://doi.org/10.1029/2008JD009906.

Ratcliffe, N. G., C. L. Ryder, N. Bellouin, S. Woodward, A. Jones, B. Johnson, B. Weinzierl, L.-M. Wieland, and J. Gasteiger, 2024: Long range transport of coarse mineral dust: an evaluation of the met office unified model against aircraft observations. *EGUsphere*, **2024**, 1–32, URL https://egusphere.copernicus.org/preprints/2024/egusphere-2024-806/.

Raupach, M. R., D. A. Gillette, and J. F. Leys, 1993: The effect of roughness elements on wind erosion threshold. *Journal of Geophysical Research: Atmospheres*, **98**, 3023–3029, URL https://onlinelibrary.wiley.com/doi/full/10.1029/92JD01922https://onlinelibrary.wiley.com/doi/abs/10.1029/92JD01922https://agupubs.onlinelibrary.wiley.com/doi/10.1029/92JD01922.

Rausch, J., D. Jaramillo-Vogel, S. Perseguers, N. Schnidrig, B. Grobéty, and P. Yajan, 2022: Automated identification and quantification of tire wear particles (twp) in airborne dust: Sem/edx single particle analysis coupled to a machine learning classifier. *Science of The Total Environment*, **803**, 149 832.

Reicher, N., C. Budke, L. Eickhoff, S. Raveh-Rubin, I. Kaplan-Ashiri, T. Koop, and Y. Rudich, 2019: Size-dependent ice nucleation by airborne particles during dust events in the eastern mediterranean. *Atmospheric Chemistry and Physics*, **19**, 11 143–11 158.

Reid, E. A., J. S. Reid, M. M. Meier, M. R. Dunlap, S. S. Cliff, A. Broumas, K. Perry, and H. Maring, 2003a: Characterization of african dust transported to puerto rico by individual particle and size segregated bulk analysis. *Journal of Geophysical Research*, **108**, URL https://doi.org/10.1029/2002JD002935.

Reid, J. S., H. H. Jonsson, H. B. Maring, A. Smirnov, D. L. Savoie, S. S. Cliff, E. A. Reid, J. M. Livingston, M. M. Meier, O. Dubovik, and S. C. Tsay, 2003b: Comparison of size and morphological measurements of coarse mode dust particles from africa. *Journal of Geophysical Research: Atmospheres*, **108**, 8593, URL https://onlinelibrary.wiley.com/doi/full/10.1029/2002JD002485https://onlinelibrary.wiley.com/doi/abs/10.1029/2002JD002485https://agupubs.onlinelibrary.wiley.com/doi/10.1029/2002JD002485.

Reid, J. S., E. A. Reid, A. Walker, S. Piketh, S. Cliff, A. A. Mandoos, S.-C. Tsay, and T. F. Eck, 2008: Dynamics of southwest asian dust particle size characteristics with implications for global dust research. *Journal of Geophysical Research*, **113**, URL https://doi.org/10.1029/2007JD009752.

Renard, J.-B., F. Dulac, P. Durand, Q. Bourgeois, C. Denjean, D. Vignelles, B. Couté, M. Jeannot, N. Verdier, and M. Mallet, 2018: In situ measurements of desert dust particles above the western

mediterranean sea with the balloon–borne light optical aerosol counter/sizer (loac) during the charmex campaign of summer 2013. *Atmospheric Chemistry and Physics*, **18**, 3677–3699, URL https://doi.org/10.5194/acp-18-3677-2018.

Rizza, U., K. Kandler, M. Eknayan, G. Passerini, E. Mancinelli, S. Virgili, M. Morichetti, M. Nolle, K. Eleftheriadis, V. Vasilatou, and P. Ielpo, 2021: Investigation of an intense dust outbreak in the mediterranean using xmed-dry network, multiplatform observations, and numerical modeling. *Applied Sciences 2021, Vol. 11, Page 1566*, **11**, 1566, URL https://www.mdpi.com/2076-3417/11/4/1566/htmhttps://www.mdpi.com/2076-3417/11/4/1566.

Rosenberg, P. D., D. J. Parker, C. L. Ryder, J. H. Marsham, L. Garcia-Carreras, J. R. Dorsey, I. M. Brooks, A. R. Dean, J. Crosier, J. B. McQuaid, and R. Washington, 2014: Quantifying particle size and turbulent scale dependence of dust flux in the sahara using aircraft measurements. *Journal of Geophysical Research: Atmospheres*, **119 (12)**, 7577–7598, URL https://agupubs.onlinelibrary.wiley.com/doi/abs/10.1002/2013JD021255, https://agupubs.onlinelibrary.wiley.com/doi/pdf/10.1002/2013JD021255.

Ryder, C., E. Highwood, A. Walser, P. Seibert, A. Tipka, and B. Weinzierl, 2019: Coarse and giant particles are ubiquitous in saharan dust export regions and are radiatively significant over the sahara. *Atmospheric Chemistry and Physics*, **19**, 15 353–15 376.

Ryder, C. L., E. J. Highwood, T. M. Lai, H. Sodemann, and J. H. Marsham, 2013a: Impact of atmospheric transport on the evolution of microphysical and optical properties of saharan dust. *Geophysical Research Letters*, **40**, 2433–2438, URL https://doi.org/10.1002/grl.50482.

Ryder, C. L., E. J. Highwood, P. D. Rosenberg, J. Trembath, J. K. Brooke, M. Bart, A. Dean, J. Crosier, J. Dorsey, H. Brindley, J. Banks, J. H. Marsham, J. B. McQuaid, H. Sodemann, and R. Washington, 2013b: Optical properties of saharan dust aerosol and contribution from the coarse mode as measured during the fennec 2011 aircraft campaign. *Atmospheric Chemistry and Physics*, **13**, 303–325.

Ryder, C. L., F. Marenco, J. K. Brooke, V. Estelles, R. Cotton, P. Formenti, J. B. McQuaid, H. C. Price, D. Liu, P. Ausset, P. D. Rosenberg, J. W. Taylor, T. Choularton, K. Bower, H. Coe, M. Gallagher, J. Crosier, G. Lloyd, E. J. Highwood, and B. J. Murray, 2018: Coarse–mode mineral dust size distributions, composition and optical properties from aer–d aircraft measurements over the tropical eastern atlantic. *Atmospheric Chemistry and Physics*, **18**, 17 225–17 257, URL https://doi.org/10.5194/acp-18-17225-2018.

Ryder, C. L., J. B. McQuaid, C. Flamant, P. D. Rosenberg, R. Washington, H. E. Brindley, E. J. Highwood, J. H. Marsham, D. J. Parker, M. C. Todd, J. R. Banks, J. K. Brooke, S. Engelstaedter, V. Estelles, P. Formenti, L. Garcia-Carreras, C. Kocha, F. Marenco, H. Sodemann, C. J. Allen, A. Bourdon,

M. Bart, C. Cavazos-Guerra, S. Chevaillier, J. Crosier, E. Darbyshire, A. R. Dean, J. R. Dorsey, J. Kent, D. O'Sullivan, K. Schepanski, K. Szpek, J. Trembath, and A. Woolley, 2015: Advances in understanding mineral dust and boundary layer processes over the sahara from fennec aircraft observations. *Atmospheric Chemistry and Physics*, **15**, 8479–8520.

Sanwlani, N. and R. Das, 2022: Understanding haze: modeling size-resolved mineral aerosol from satellite remote sensing. *Remote Sensing*, **14**, 761.

Scanza, R. A., N. Mahowald, S. Ghan, C. S. Zender, J. F. Kok, X. Liu, Y. Zhang, and S. Albani, 2015: Modeling dust as component minerals in the community atmosphere model: Development of framework and impact on radiative forcing. *Atmospheric Chemistry and Physics*, **15**, 537–561.

Schade, H., E. Kunz, F. Kameier, and C. O. Paschereit, 2007: Strömungslehre. *Strömungslehre*.

Schepanski, K., 2018: Transport of mineral dust and its impact on climate. *Geosciences*, **8 (5)**.

Scheuvens, D. and K. Kandler, 2014: On composition, morphology, and size distribution of airborne mineral dust. *Mineral Dust: A Key Player in the Earth System*, Knippertz, P. and J.-B. W. Stuut, Eds., Springer Netherlands, Dordrecht, 15–49, URL https://doi.org/10.1007/978-94-017-8978-3_2.

Schulz, M., J. M. Prospero, A. R. Baker, F. Dentener, L. Ickes, P. S. Liss, N. M. Mahowald, S. Nickovic, C. P. García-Pando, S. Rodríguez, M. Sarin, I. Tegen, and R. A. Duce, 2012: Atmospheric transport and deposition of mineral dust to the ocean: Implications for research needs. *Environmental Science and Technology*, **46**, 10 390–10 404, URL https://pubs.acs.org/doi/abs/10.1021/es300073u.

Schütz, L., R. Jaenicke, and H. Pietrek, 1981: Saharan dust transport over the north atlantic ocean. *Desert Dust*, Péwe, T. L., Ed., Geological Society of America, Special Paper, Vol. 186, 87–100, URL https://doi.org/10.1130/SPE186-p87.

Schöberl, M., M. Dollner, J. Gasteiger, P. Seibert, A. Tipka, and B. Weinzierl, 2024: Characterization of the airborne aerosol inlet and transport system used during the a-life aircraft field experiment. *Atmospheric Measurement Techniques*, **17**, 2761–2776.

Seinfeld, J. H. and S. N. Pandis, 1998: *Atmospheric chemistry and physics from air pollution to climate change*. Wiley.

Shao, Y., 2004: Simplification of a dust emission scheme and comparison with data. *Journal of Geophysical Research*, **109**, URL https://api.semanticscholar.org/CorpusID:58906477.

———, 2008: *Physics and modelling of wind erosion*. Springer Nature, URL https://doi.org/10.1007/978-1-4020-8895-7.

Shao, Y., M. Ishizuka, M. Mikami, and J. F. Leys, 2011a: Parameterization of size-resolved dust emission and validation with measurements. *Journal of Geophysical Research: Atmospheres*, **116 (D8)**, URL https://agupubs.onlinelibrary.wiley.com/doi/abs/10.1029/2010JD014527, https://agupubs.onlinelibrary.wiley.com/doi/pdf/10.1029/2010JD014527.

Shao, Y. and M. Klose, 2016: A note on the stochastic nature of particle cohesive force and implications to threshold friction velocity for aerodynamic dust entrainment. *Aeolian Research*, **22**, 123–125.

Shao, Y. and H. Lu, 2000: A simple expression for wind erosion threshold friction velocity. *Journal of Geophysical Research: Atmospheres*, **105**, 22 437–22 443, URL https://onlinelibrary.wiley.com/doi/full/10.1029/2000JD900304https://onlinelibrary.wiley.com/doi/abs/10.1029/2000JD900304https://agupubs.onlinelibrary.wiley.com/doi/10.1029/2000JD900304.

Shao, Y., M. R. Raupach, and P. A. Findlater, 1993: Effect of saltation bombardment on the entrainment of dust by wind. *Journal of Geophysical Research: Atmospheres*, **98 (D7)**, 12 719–12 726, URL https://agupubs.onlinelibrary.wiley.com/doi/abs/10.1029/93JD00396, https://agupubs.onlinelibrary.wiley.com/doi/pdf/10.1029/93JD00396.

Shao, Y., K. H. Wyrwoll, A. Chappell, J. Huang, Z. Lin, G. H. McTainsh, M. Mikami, T. Y. Tanaka, X. Wang, and S. Yoon, 2011b: Dust cycle: An emerging core theme in earth system science. *Aeolian Research*, **2**, 181–204.

Shao, Y., J. Zhang, M. Ishizuka, M. Mikami, J. Leys, and N. Huang, 2020: Dependency of particle size distribution at dust emission on friction velocity and atmospheric boundary-layer stability. *Atmospheric Chemistry and Physics*, **20**, 12 939–12 953.

Shi, T., J. Cui, Y. Chen, Y. Zhou, W. Pu, Q. Chen, X. Zhang, and X. Wang, 2020: Enhanced light absorption and reduced snow albedo due to internally mixed mineral dust in grains of snow. *Atmospheric Chemistry and Physics*, URL http://dx.doi.org/10.5194/acp-2020-985.

Shi, Z., M. D. Krom, T. D. Jickells, S. Bonneville, K. S. Carslaw, N. Mihalopoulos, A. R. Baker, and L. G. Benning, 2012: Impacts on iron solubility in the mineral dust by processes in the source region and the atmosphere: A review. *Aeolian Research*, **5**, 21–42.

Skonieczny, C., A. Bory, V. Bout-Roumazeilles, W. Abouchami, S. J. Galer, X. Crosta, A. Diallo, and T. Ndiaye, 2013: A three-year time series of mineral dust deposits on the west african margin: Sedimentological and geochemical signatures and implications for interpretation of marine paleo-dust records. *Earth and Planetary Science Letters*, **364**, 145–156.

Smith, H. R., Z. Ulanowski, P. H. Kaye, E. Hirst, W. Stanley, R. Kaye, A. Wieser, C. Stopford, M. Kezoudi, J. Girdwood, R. Greenaway, and R. Mackenzie, 2019: The Universal Cloud and Aerosol

Sounding System (UCASS): a low-cost miniature optical particle counter for use in dropsonde or balloon-borne sounding systems. *Atmospheric Measurement Techniques*, **12 (12)**, 6579–6599, URL https://doi.org/10.5194/amt-12-6579-2019.

Sokolik, I. N., 2015: Aerosols | dust. *Encyclopedia of Atmospheric Sciences: Second Edition*, 48–52.

Song, Q., Z. Zhang, H. Yu, J. F. Kok, C. D. Biagio, S. Albani, J. Zheng, and J. Ding, 2022: Size-resolved dust direct radiative effect efficiency derived from satellite observations. *Atmospheric Chemistry and Physics*, **22**, 13 115–13 135.

Sow, M., S. C. Alfaro, J. L. Rajot, and B. Marticorena, 2009: Size resolved dust emission fluxes measured in niger during 3 dust storms of the amma experiment. *Atmospheric Chemistry and Physics*, **9**, 3881–3891, URL https://doi.org/10.5194/acp-9-3881-2009.

Stout, J. E., 1998: Effect of averaging time on the apparent threshold for aeolian transport. *Journal of Arid Environments*, **39**, 395–401.

Struckmeier, C., F. Drewnick, F. Fachinger, G. P. Gobbi, and S. Borrmann, 2016: Atmospheric aerosols in rome, italy: sources, dynamics and spatial variations during two seasons. *Atmospheric Chemistry and Physics*, **16**, 15 277–15 299, URL https://doi.org/10.5194/acp-16-15277-2016.

Sullivan, R. C., S. A. Guazzotti, D. A. Sodeman, and K. A. Prather, 2007: Direct observations of the atmospheric processing of asian mineral dust. *Atmospheric Chemistry and Physics*, **7**, 1213–1236.

Taylor, M., S. Kazadzis, and E. Gerasopoulos, 2014: Multi-modal analysis of aerosol robotic network size distributions for remote sensing applications: dominant aerosol type cases. *Atmospheric Measurement Techniques*, **7 (3)**, 839–858, URL https://amt.copernicus.org/articles/7/839/2014/.

Tegen, I. and I. Fung, 1994: Modeling of mineral dust in the atmosphere: Sources, transport, and optical thickness. *Journal of Geophysical Research: Atmospheres*, **99**, 22 897–22 914, URL https://onlinelibrary.wiley.com/doi/full/10.1029/94JD01928https://onlinelibrary.wiley.com/doi/abs/10.1029/94JD01928https://agupubs.onlinelibrary.wiley.com/doi/10.1029/94JD01928.

Tegen, I., A. A. Lacis, and I. Fung, 1996: The influence on climate forcing of mineral aerosols from disturbed soils. *Nature 1996 380:6573*, **380**, 419–422, URL https://www.nature.com/articles/380419a0.

Textor, C., M. Schulz, S. Guibert, S. Kinne, S. E. Bauer, Y. Balkanski, T. Berntsen, T. Berglen, O. Boucher, M. Chin, F. Dentener, T. Diehl, H. Feichter, D. Fillmore, S. Ghan, P. Ginoux, S. Gong, A. Grini, J. Hendricks, L. Horrowitz, I. Isaksen, T. Iversen, A. Kirkevag, D. Koch, J. E. Kristjansson, M. Krol, A. Lauer, J. F. Lamarque, X. Liu, V. Montanaro, G. Myhre, J. Penner, G. Pitari, S. Reddy,

O. Seland, P. Stier, T. Takemura, and X. Tie, 2006: Analysis and quantification of the diversities of aerosol life cycles within aerocom. *Atmos. Chem. Phys.*, **6**, 1777–1813.

Thomas, J. W., 1958: Gravity settling of particles in a horizontal tube. *Journal of the Air Pollution Control Association*, **8**, 32–34, URL https://www.tandfonline.com/doi/abs/10.1080/00966665.1958.10467825.

Tian, Z., V. Dietze, F. Sommer, A. Baum, U. Kaminski, J. Sauer, C. Maschowski, P. Stille, K. Cen, and R. Gieré, 2017: Coarse-particle passive-sampler measurements and single-particle analysis by transmitted light microscopy at highly frequented motorways. *Aerosol and Air Quality Research*, **17**, 1939–1953, URL https://aaqr.org/articles/aaqr-17-02-oa-0064.

Torres, B. and D. Fuertes, 2021: Characterization of aerosol size properties from measurements of spectral optical depth: a global validation of the grasp-aod code using long-term aeronet data. *Atmospheric Measurement Techniques*, **14 (6)**, 4471–4506, URL https://amt.copernicus.org/articles/14/4471/2021/.

Torres-Padrón, M. E., M. D. Gelado-Caballero, C. Collado-Sánchez, V. F. Siruela-Matos, P. J. Cardona-Castellano, and J. J. Hernández-Brito, 2002: Variability of dust inputs to the canigo zone. *Deep Sea Research Part II: Topical Studies in Oceanography*, **49**, 3455–3464.

Usher, C. R., A. E. Michel, and V. H. Grassian, 2003: Reactions on mineral dust. *Chemical Reviews*, **103**, 4883–4939, URL https://pubs.acs.org/doi/abs/10.1021/cr020657y.

van der Does, M., P. Knippertz, P. Zschenderlein, R. Giles Harrison, and J.-B. W. Stuut, 2018: The mysterious long-range transport of giant mineral dust particles. *Science Advances*, **4 (12)**, URL https://advances.sciencemag.org/content/4/12/eaau2768, https://advances.sciencemag.org/content/4/12/eaau2768.full.pdf.

Varga, G., C. Cserháti, J. Kovács, J. Szeberényi, and B. Bradák, 2014: Unusual saharan dust events in the carpathian basin (central europe) in 2013 and early 2014. *Weather*, **69**, 309–313, URL https://onlinelibrary.wiley.com/doi/full/10.1002/wea.2334https://onlinelibrary.wiley.com/doi/abs/10.1002/wea.2334https://rmets.onlinelibrary.wiley.com/doi/10.1002/wea.2334.

Varga, G., P. Dagsson-Walhauserová, F. Gresina, and A. Helgadottir, 2021: Saharan dust and giant quartz particle transport towards iceland. *Scientific Reports 2021 11:1*, **11**, 1–12, URL https://www.nature.com/articles/s41598-021-91481-z.

Veghte, D. P. and M. A. Freedman, 2014: Facile Method for Determining the Aspect Ratios of Mineral Dust Aerosol by Electron Microscopy. *Aerosol Science and Technology*, **48 (7)**, 715–724, URL http://dx.doi.org/10.1080/02786826.2014.920484.

Veghte, D. P., J. E. Moore, L. Jensen, and M. A. Freedman, 2015: Influence of shape on the optical properties of hematite aerosol. *Journal of Geophysical Research: Atmospheres*, **120 (14)**, 7025–7039, URL http://dx.doi.org/10.1002/2015JD023160.

von Holdt, J. R., F. D. Eckardt, M. C. Baddock, and G. F. Wiggs, 2019: Assessing landscape dust emission potential using combined ground-based measurements and remote sensing data. *Journal of Geophysical Research: Earth Surface*, **124**, 1080–1098, URL https://doi.org/10.1029/2018jf004713https://scite.ai/reports/assessing-landscape-dust-emission-potential-PQremZK.

Wagner, F., D. Bortoli, S. Pereira, M. J. Costa, A. M. Silva, B. Weinzierl, M. Esselborn, A. Petzold, K. Rasp, B. Heinold, and I. Tegen, 2009: Properties of dust aerosol particles transported to portugal from the sahara desert. *Tellus B*, **61**, 297–306, URL https://doi.org/10.1111/j.1600-0889.2008.00393.x.

Wang, S., C.-W. Lin, S.-H. Huang, and C.-C. Chen, 2024: Aerosol deposition in 90-degree bends: An enhanced empirical equation and a design concept of reducing losses. *Aerosol Science and Technology*, **58**, 475–484, URL https://www.tandfonline.com/doi/full/10.1080/02786826.2024.2316832.

Warren, S. G., 1984: Impurities in Snow: Effects on Albedo and Snowmelt (Review). *Annals of Glaciology*, **5**, 177–179, URL http://dx.doi.org/10.3189/1984AoG5-1-177-179.

Waza, A., K. Schneiders, J. May, S. Rodríguez, B. Epple, and K. Kandler, 2019: Field comparison of dry deposition samplers for collection of atmospheric mineral dust: Results from single-particle characterization. *Atmospheric Measurement Techniques*, **12**, 6647–6665.

Webb, N. P., S. L. LeGrand, B. F. Cooper, E. M. Courtright, B. L. Edwards, C. Felt, J. W. V. Zee, and N. P. Ziegler, 2021: Size distribution of mineral dust emissions from sparsely vegetated and supply-limited dryland soils. *Journal of Geophysical Research: Atmospheres*, **126**.

Webb, N. P. and C. Strong, 2011: Soil erodibility dynamics and its representation for wind erosion and dust emission models. *Aeolian Research*, **3**, 165–179.

Weiden, S. L. V. D., F. Drewnick, and S. Borrmann, 2009: Particle loss calculator – a new software tool for the assessment of the performance of aerosol inlet systems. *Atmospheric Measurement Techniques*, **2**, 479–494, URL www.atmos-meas-tech.net/2/479/2009/.

Weinzierl, B., A. Ansmann, J. M. Prospero, D. Althausen, N. Benker, F. Chouza, M. Dollner, D. Farrell, W. K. Fomba, V. Freudenthaler, J. Gasteiger, S. Groß, M. Haarig, B. Heinold, K. Kandler, T. B. Kristensen, O. L. Mayol-Bracero, T. Müller, O. Reitebuch, D. Sauer, A. Schäfler, K. Schepanski,

A. Spanu, I. Tegen, C. Toledano, and A. Walser, 2017: The saharan aerosol long–range transport and aerosol–cloud–interaction experiment: Overview and selected highlights. *Bulletin of the American Meteorological Society*, **98**, 1427–1451, URL https://doi.org/10.1175/BAMS-D-15-00142.1.

Weinzierl, B., A. Petzold, M. Esselborn, M. Wirth, K. Rasp, K. Kandler, L. Schütz, P. Koepke, and M. Fiebig, 2009: Airborne measurements of dust layer properties, particle size distribution and mixing state of saharan dust during samum 2006. *Tellus B*, **61**, 96–117, URL https://doi.org/10.1111/j.1600-0889.2008.00392.x.

Weinzierl, B., D. Sauer, M. Esselborn, A. Petzold, A. Veira, M. Rose, S. Mund, M. Wirth, A. Ansmann, M. Tesche, S. Gross, and V. Freudenthaler, 2011: Microphysical and optical properties of dust and tropical biomass burning aerosol layers in the cape verde region—an overview of the airborne in situ and lidar measurements during samum–2. *Tellus B*, **63**, 589–618, URL https://doi.org/10.1111/j.1600-0889.2011.00566.x.

Welti, A., F. Lüönd, O. Stetzer, and U. Lohmann, 2009: Influence of particle size on the ice nucleating ability of mineral dusts. *Atmospheric Chemistry and Physics*, **9 (18)**, 6705–6715, URL http://dx.doi.org/10.5194/ACP-9-6705-2009.

Willeit, M. and A. Ganopolski, 2018: The importance of snow albedo for ice sheet evolution over the last glacial cycle. *Climate of the Past*, **14 (5)**, 697–707, URL http://dx.doi.org/10.5194/CP-14-697-2018.

Wittmann, M., C. D. Groot Zwaaftink, L. Steffensen Schmidt, S. Guðmundsson, F. Pálsson, O. Arnalds, H. Björnsson, T. Thorsteinsson, and A. Stohl, 2017: Impact of dust deposition on the albedo of Vatnajökull ice cap, Iceland. *The Cryosphere*, **11 (2)**, 741–754, URL http://dx.doi.org/10.5194/TC-11-741-2017.

Woodward, X., A. Kostinski, S. China, C. Mazzoleni, and W. Cantrell, 2015: Characterization of Dust Particles' 3d Shape and Roughness with Nanometer Resolution. *Aerosol Science and Technology*, **49 (4)**, 229–238, URL http://dx.doi.org/10.1080/02786826.2015.1017550.

Wright, J., B. Smith, and B. Whalley, 1998: Mechanisms of loess-sized quartz silt production and their relative effectiveness: laboratory simulations. *Geomorphology*, **23**, 15–34.

Wu, W. and S. S. Y. Wang, 2006: Formulas for sediment porosity and settling velocity. *Journal of Hydraulic Engineering*, **132**, 858–862, URL https://ascelibrary.org/doi/abs/10.1061/%28ASCE%290733-9429%282006%29132%3A8%28858%29https://ascelibrary.org/doi/10.1061/%28ASCE%290733-9429%282006%29132%3A8%28858%29.

Yus-Díez, J., M. Pandolfi, A. Alastuey, C. González-Flórez, J. Escribano, A. González-Romero, M. Ivančič, M. Rigler, M. Klose, K. Kandler, et al., 2023: Quantifying variations in multi-wavelength optical properties of freshly-emitted saharan dust from the lower drâa valley, moroccan sahara.

Zhang, H. and X. Li, 2014: Review of the field measurements and parameterization for dust emission during sand-dust events. *Journal of Meteorological Research*, **28**, 903–922, URL https://link.springer.com/article/10.1007/s13351-014-3296-z.

Zhang, P., R. M. Roberts, and A. Bénard, 2012: Computational guidelines and an empirical model for particle deposition in curved pipes using an eulerian-lagrangian approach. *Journal of Aerosol Science*, **53**, 1–20.

Zhang, Z. Q. and B. Y. Liu, 1989: On the empirical fitting equations for aspiration coefficients for thin-walled sampling probes. *Journal of Aerosol Science*, **20**, 713–720.

Zhou, Y., R. C. Levy, L. A. Remer, S. Mattoo, Y. Shi, and C. Wang, 2020: Dust aerosol retrieval over the oceans with the modis/viirs dark-target algorithm: 1. dust detection. *Earth and Space Science*, **7**, e2020EA001 221, URL https://onlinelibrary.wiley.com/doi/full/10.1029/2020EA001221https://onlinelibrary.wiley.com/doi/abs/10.1029/2020EA001221https://agupubs.onlinelibrary.wiley.com/doi/10.1029/2020EA001221.

Zimmermann, F., S. Weinbruch, L. Schütz, H. Hofmann, M. Ebert, K. Kandler, and A. Worringen, 2008: Ice nucleation properties of the most abundant mineral dust phases. *Journal of Geophysical Research: Atmospheres*, **113**, URL https://onlinelibrary.wiley.com/doi/full/10.1029/2008JD010655https://onlinelibrary.wiley.com/doi/abs/10.1029/2008JD010655https://agupubs.onlinelibrary.wiley.com/doi/10.1029/2008JD010655.

Zingg, A. W., 1952: Wind tunnel studies of the movement of sedimentary material. *Proc. 5th Hydraulics Conf., IAHR*, 111–135, URL https://cir.nii.ac.jp/crid/1572261549350606592.

B. List of Figures

C. List of Tables

D. Abbreviations

PSD Particle size distribution i

J-WADI Jordan Wind Erosion and Dust Investigation i

DOD Dust Optical Depth 7

AOD Aerosol Optical Depth 7

OPC Optical Particle Counter 18

HWR Height-to-width ratio 15

AR Aspect ratio 15

SEM Scanning Electron Microscopy 19

DMPS Differential Mobility Particle Sizer 23

APS Aerodynamic Particle Sizer 23

SMPS Scanning Mobility Particle Sizer 23

MRT Mid-range transport 24

LRT Long-range transport 24

OAP Optical Array Probe 24

CSF Corey Shape Factor 65

PSL Polystyrene latex spheres 44

FPS Flat-Plate Sampler 67

GLMT Generalized Lorenz-Mie Theory

TFEM Time Fraction Equivalence Method

MOST Monin-Obukhov Similarity Theory

EC Eddy Covariance

AERONET AErosol RObotic NETwork

Acknowledgments

Between dust storms and data gaps, this PhD journey has been as turbulent as the wind conditions needed for dust entrainment. Now that the dust settles, I am immensely grateful to everyone who helped me weather it. What follows is a deeply heartfelt thank you to those who walked, ran, climbed with me, and occasionally carried me through the past years.

First and foremost, I would like to express my deepest gratitude to my first supervisor, TT-Prof. Dr. Martina Klose. Martina, your academic expertise, continuous encouragement, even in times when things looked unpromising, and always open door were crucial in helping me reach this point. I sincerely thank you for your detailed feedback on multiple versions of this and other manuscripts, and for your overall guidance throughout the past four years. I am also grateful for the opportunity to have been the first employee and PhD candidate in your group and for the chance to engage in outreach activities.

I would also like to extend my sincere thanks to my second supervisor, Prof. Dr. Peter Knippertz. Thank you, Peter, for sharing your knowledge, for maintaining an overarching view of the broader scientific context (instead of observing every dust particle individually), and for offering fresh perspectives that helped shape the direction of this research.

Among the most memorable experiences of my PhD journey was the participation in two field campaigns, where the data of this thesis was collected. This would not have been possible without the J-WADI and Iceland teams. Especially, I want to thank Prof. Dr. Konrad Kandler and Prof. Dr. Carlos Pérez García-Pando for invaluable feedback, connecting dots, and clarifying many open questions. Thank you Konrad and Carlos! I would additionally like to thank you and the rest of the team for conducting fieldwork together, for laughing, crying, sweating together, for carpool karaoke, saving instruments from glacier floodings, and keeping tents from flying away. Most importantly, I am deeply grateful for the scientific exchange–your feedback, the many meetings, and your input into the data analyses were invaluable and form the backbone of this thesis. Through all of this, with and without the chaos, you not only made the experience unforgettable but also helped to improve the science.

I am also deeply grateful to my colleagues and peers, whose presence shaped both the academic and personal aspects of this journey. A heartfelt thanks goes to my working group–for collaboratively advancing the science, for group dinners, and for shared excursions. Sebastian, thank you for your quiet yet steadfast support, for shared beverages, and for our philosophical conversations. Katharina, thank you for coffee breaks, moaning sessions, organizing the PhD seminar, co-working, and always being there to listen and support. Felix, thank you for sharing beverages, music, and some worldviews.

A big thanks goes also to my friends, who sustained me in ways no academic training ever could: Dana, thank you for your empowering energy, for always listening, planning and structuring together, checking on me, and helping me stay grounded. Katharina, thank you for your encouragement and motivation. Clara, thank you for showing me how to dare–both of you, thank you for being Pendejas. Lisa, thank you for making me laugh, for countless shared experiences and phone calls, "die Wahrheit", and for believing in me ever since we met in middle school. Simon, thank you for walking this PhD path alongside me, for bringing in fun and depth in equal measure. Katrin, thank you for being a clever and quiet supporter, a perceptive listener, and for creatively seeing new perspectives. Gavide, thank you for maintaining a running connection and support. Jan: thank you for being by my side. For proofreading, for supporting me through every phase, meal prep many months before the (dust-) storm of the PhD began, and for postcards and food deliveries from the Antarctic: your presence (even if not always in the same physical place) made all the difference. Simon2, thank you so much for helping me organize the code and data and for supporting me in moving forward with the publication, and much much more.

Another big thanks goes to my family, whose presence was a stabilizing force throughout this process: Laura, thank you for supporting me especially during the writing phase, for co-working sessions, proof-reading, discussing the big life questions, and for calming me down: you are truly the practical sibling. Papa, thank you for always helping me navigate adult challenges and grounding me by comparing your projects with my PhD work, and for teaching me how to deal with people. Mama, thank you for loving me unconditionally, for never expecting anything other than for me to be myself, for your kindness, for showing me that one does not have to fit a mold and, of course, for raising me.

Finally, I acknowledge the use of ChatGPT (OpenAI), which supported me not only in refining the wording of certain sections of this manuscript but also in enhancing creativity, for example, by generating the figure below, which was part of the science slam contributions I gave during the final year of my PhD phase, which brought me to the exciting experience to present in front of 850 people.

Figure D.1.: The secret journeys of desert sands. Figure created by ChatGPT.